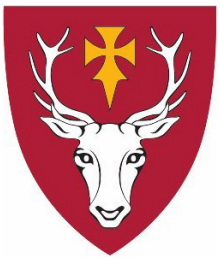
Spatial and Temporal Variability in the Uranian Atmosphere



Arjuna James

Hertford College



University of Oxford

A thesis presented for the degree of

Doctor of Philosophy

Michaelmas 2023

Acknowledgements

First and foremost, I would like to express my sincere gratitude to Prof. Patrick Irwin for his diligent supervision and guidance throughout this endeavour. Your commitment to your graduate students is admirable, and your consistency, come rain or shine, in being available for weekly meetings is truly invaluable. I am grateful for your patience and understanding in my periods of difficulty and spans of being stuck in the proverbial mud. Thank you for keeping faith in my ability to persevere come crunch time. I would also like to thank the wider planetary research group during my time in AOPP, including Juan Alday, Jake Taylor, Kevin Olsen, Jack Dobinson, Jingxuan Yang, Charlie Alexander and Shubham Kulkarni, who all helped me along the journey in some way and contributed to making my DPhil experience an enjoyable one.

Thank you to my collaborators who helped to greatly improve the main publication of my DPhil with their comments and suggestions, and who also made conference trips that much more fulfilling. Namely, Prof. Leigh Fletcher, Prof. Nick Teanby, Dr. Amy Simon, Dr. Mike Wong, Dr. Mike Roman, Dr. Daniel Toledo and Dr. Glenn Orton.

A huge shoutout to my two longstanding office mates Burtie Spry and Rowan Curtis, with whom I had the pleasure of sharing many great conversations, laughs, and positive memories during my time at AOPP. I couldn't have asked for two better human beings

to share a workspace with. Thank you for inspiring me to work harder and reach higher by simply being yourselves. Thank you to Prof. Neil Bowles for reliably spicing up the work day with his frequent trips to our office, bearing interesting and/or hilarious stories, and offering extremely useful advice to me on several occasions. I would also like to thank the wider AOPP community for making the department a pleasant environment to work within, with a special shoutout to the wonderful coffee club folks for providing all members of the department with consumables. Last but not least, on a departmental front, I would like to thank the graduate administrative team for providing invaluable support throughout my DPhil for all issues, large and small.

I would also like to thank Hertford College for affording me many opportunities to enhance my personal development, and entrusting me with a role as a Junior Dean. In particular I would like to thank the Welfare team, the Porters, the Catering team and the Accommodation team for their help and service during my time working at the college.

Next, I would like to give a huge shoutout to the incredible people that I have met along the way during my Oxford experience. These individuals truly made my time here special, and were an essential part of negotiating the COVID-19 pandemic. In particular Ngoni Mugwisi, Prince Abudu, Lewis Hammond, Alex Smit, Rowan Curtis, Kevin Tang, Mesi Vegh, Rasched Haidari, Dan Qureshi, Attayah Douglas, Elena Gallina, Marcus Sefranek, David Quartey, Femi Nylander, and the entire Hertford College 2019/2020 MCR committee, and many more I will save naming.

I would also like to thank and acknowledge the many teachers and mentors I have met and known along the way on my academic journey. In particular Tony Simpson, Christopher Lumsden, Grahame Smart, Godwin Kanton, Samuel Addo, Prof. Mark Green, Prof. Dylan Owen, Prof. Malcolm Fairbairn, Dr. Emilie Steinmark, and Prof. Klaus Suhling.

Finally, a thank you to my entire extended family, lots of love and gratitude to my three older siblings who laid down the blueprint for success in each of their respective journeys, setting a shining example for me to follow, and most importantly, I would like to express my deepest gratitude to my mum, firstly for her unflagging dedication to her children over the years, and secondly for her unwavering support throughout my journey so far in life. None of this would have been possible without you.

Table of Contents

Acknowledgements i

List of Abbreviations vii

Abstract xiii

1 Introduction 1

1.1 Overview of Uranus 2

1.2 Formation, Evolution and Internal Structure 4

1.2.1 Forming an Ice Giant 4

1.2.2 The Evolution of Uranus 7

1.2.3 Internal Structure 9

1.3 The Atmosphere of Uranus 11

1.3.1 Temperature 11

1.3.2 Composition 14

1.3.2.1 Troposphere 14

1.3.2.2 Stratosphere 18

1.3.3 Vertical Aerosol Models 20

1.3.4 Dynamics . . . 26
1.3.4.1 Radiative Forcing . . . 26
1.3.4.2 Zonal Structure . . . 27
1.3.4.3 General Circulation Models . . . 30
1.3.5 Discrete Features . . . 31
1.3.6 Spatial & Temporal Variability . . . 33
1.3.6.1 Latitudinal Variability . . . 33
1.3.6.2 Seasonal Change . . . 37
1.4 Scientific Questions . . . 39
1.5 Thesis Outline . . . 40

2 Instrumentation & Data Reduction 41
2.1 HST/WFC3 . . . 41
2.1.1 Observation Methodology & Data Reduction . . . 43
2.2 HST/STIS . . . 45
2.2.1 Observation Methodology . . . 48
2.2.2 Data Reduction . . . 49
2.3 VLT/MUSE . . . 52
2.3.1 Observation Methodology . . . 54
2.3.2 Data Reduction . . . 55
2.3.2.1 Calibration . . . 55
2.3.2.2 Deconvolution . . . 58

3 Radiative Transfer & Retrieval Theory 62
3.1 Radiative Transfer . . . 63
3.1.1 Origin of the Spectrum . . . 63

3.1.1.1 Collision-Induced Absorption 64
3.1.1.2 Rayleigh Scattering 65
3.1.1.3 Raman Scattering 66
3.1.2 Radiative Transfer Equation 67
3.1.2.1 Line-by-line Method 69
3.1.2.2 Correlated-k Approximation 71
3.1.3 Mie Theory 72
3.1.3.1 Kramers-Kronig Relations 74
3.2 Retrieval Theory 75
3.2.1 Statistical Methods 77
3.2.1.1 Optimal Estimation 77
3.2.1.2 Markov Chain Monte Carlo 79
3.2.1.3 Nested Sampling 81
3.2.1.4 Method Comparison 83
3.3 NEMESIS 85
3.3.1 Noise & Smoothing 86
3.3.2 Minnaert Limb-darkening Model 88
3.3.3 Quality Control 89

4 The Evolution of Uranus' Polar Hood **92**
4.1 Minnaert Analysis with HST/WFC3 92
4.2 CH_4 Retrievals with HST/STIS 102
4.3 Latitudinal Retrievals 110
4.3.1 HST/WFC3 110
4.3.2 HST/STIS 116

4.4 Mechanisms 133
4.5 Summary 140

5 Variability within the Uranian Atmosphere 143

5.1 Latitudinal Retrieval Analysis with VLT/MUSE 143
5.2 Spatial & Temporal Variability 155
5.2.1 Aerosol-2 Pressure 156
5.2.2 Aerosol Opacity 158
5.2.2.1 Aerosol-1 158
5.2.2.2 Aerosol-2 161
5.2.2.3 Aerosol-3 162
5.2.3 Aerosol-2 Imaginary Refractive Index Spectrum 164
5.2.4 Cloud-top CH_4 VMR 166
5.3 Summary 168

6 Conclusions & Future Work 173

6.1 Uranus: The North Polar Hood 173
6.2 Uranus: Spatial & Temporal Variability 180
6.3 Conclusions & Discussion 187
6.4 Future Work 192

Bibliography 196

List of Abbreviations

ACS . . . . . Advanced Camera for Surveys

ALMA . . . . . Atacama Large Millimeter Array

AO . . . . . Adaptive Optics

AU . . . . . Astronomical Unit

C_2H_2 . . . . . Acetylene

C_2H_4 . . . . . Ethylene

C_2H_6 . . . . . Ethane

C_4H_2 . . . . . Diacetylene

CCD . . . . . Charge-Coupled Device

CCN . . . . . Cloud Condensation Nuclei

CH_4 . . . . . Methane

CIA . . . . . Collision-Induced Absorption

CO . . . . . Carbon Monoxide

CO_2 ..... Carbon Dioxide

CTE ..... Charge Transfer Efficiency

DALR ..... Dry Adiabatic Lapse Rate

ECCM ..... Equilibrium Cloud Condensation Model

EM ..... Electromagnetic

ESO ..... European Southern Observatory

FITS ..... Flexible Image Transport System

FOV ..... Field of View

FWHM ..... Full Width at Half Maximum

H_2 ..... Hydrogen

H_2O ..... Water

H_2S ..... Hydrogen Sulfide

He ..... Helium

HRC ..... High Resolution Camera

HST ..... Hubble Space Telescope

IFU ..... Integral Field Unit

IR ..... Infrared

IRIS ..... Infrared Interferometer Spectrometer and Radiometer

IRLOS ..... Infrared Low Order Sensor

IRTF . . . . . Infrared Telescope Facility

ISAC . . . . . Infrared Spectrometer and Array Camera

LTE . . . . . Local Thermodynamic Equilibrium

MAMA . . . . . Multi-Anode Microchannel Array

MCMC . . . . . Markov Chain Monte Carlo

MSM . . . . . Mode Selection Mechanism

MUSE . . . . . Multi Unit Spectroscopic Explorer

NASA . . . . . National Aeronautics and Space Administration

NEMESIS . . . . . Non-linear optimal Estimator for MultivariatE spectral analySIS

NFM . . . . . Near-Field Mode

NIFS . . . . . Near-infrared Integral-Field Spectrograph

NH_3 . . . . . Ammonia

NH_4SH . . . . . Ammonium Hydrosulfide

NIR . . . . . Near Infrared

NIRC2 . . . . . Near Infrared Camera 2

NS . . . . . Nested Sampling

O_2 . . . . . Oxygen

OE . . . . . Optimal Estimation

OPAL . . . . . Outer Planet Atmospheres Legacy

OTF . . . . . Optical Transfer Function

PDF . . . . . Probability Density Function

PH_3 . . . . . Phosphine

PSF . . . . . Point Spread Function

PSN . . . . . Protosolar Nebula

RTE . . . . . Radiative Transfer Equation

SALR . . . . . Saturated Adiabatic Lapse Rate

SINFONI . . . . . Spectrograph for INtegral Field Observations in the Near Infrared

SNR . . . . . Signal to Noise Ratio

STIS . . . . . Space Telescope Imaging Spectrograph

STScI . . . . . Space Telescope Science Institute

SVP . . . . . Saturation Vapour Presuure

UV . . . . . Ultraviolet

UVIS . . . . . Ultraviolet and Visible

VLA . . . . . Very Large Array

VLT . . . . . Very Large Telescope

VMR . . . . . Volume Mixing Ratio

WCOG . . . . . Weighted-Center-Of-Gravity

WFC3 . . . . . Wide-Field Camera 3

WFM . . . . . Wide-Field Mode

WFS . . . . . Wavefront Sensor

Abstract

VLT/MUSE, HST/STIS and HST/WFC3 observations of Uranus in the visible/near-infrared were employed to probe spatial and temporal variability within its atmosphere. A Minnaert analysis of Uranus' north polar hood reveals a temporal brightening of this feature, predominantly caused by physical changes within the atmosphere, as opposed to any brightening effects caused by changes in viewing geometry as Uranus' orbit progresses towards northern summer solstice in 2030. A reduction in the temporal rate of brightening was also provisionally observed. The holistic aerosol model [Irwin et al., 2022] was applied to latitudinal retrieval analyses on the three datasets, determining an increase in the integrated opacity (τ), and a reduction in the imaginary refractive index spectrum (n_i) longwards of 0.6 μm, of the 1 – 2-bar haze (aerosol-2) layer north of $\sim$40°N to be the predominant cause of the hood's brightening. The single-scattering albedo of the aerosol-2 layer in the 60 – 70°N latitude band at 0.8 μm is observed to increase from $\sim$0.958 $\pm$ 0.002 in 2012, to $\sim$0.973 $\pm$ 0.002 in 2015, and to $\sim$0.9918 $\pm$ 0.0002 in 2021 from HST/STIS and VLT/MUSE retrieval analyses. Between the 2012 and 2015 STIS observations, the average increase in τ_2 was 1.09 $\pm$ 0.08 at 0.8 μm, a $\sim$33% increase. An average increase in τ for the deep haze (aerosol-1) layer north of $\sim$45°N of 0.6 $\pm$ 0.1 at 0.8 μm ($\sim$56% increase), and an average decrease in polar cloud-top methane (CH_4) VMR from 40 – 80°N of 0.0019 $\pm$ 0.0003 ($\sim$10% decrease) were also found between 2012 and 2015. A further reduction in polar cloud-top CH_4 was found from analysis of the 2021 VLT/MUSE observation contrary to Sromovsky et al. [2019]'s conclusion of a general latitudinal stability. The 1 – 2-bar haze layer altitude is observed to be very stable, providing evidence for it lying within a region of static stability [Irwin et al., 2022]. The results

were found to be consistent with a temporal slowing of a stratospheric meridional circulation exhibiting downwelling at the poles.

Chapter 1

Introduction

The spirit at the very core of the scientific endeavour is encapsulated in the history of the seventh planet farthest from the Sun, namely Uranus. This cold, distant world, discovered by William Herschel in 1781 and originally named *Georgium Sidus* (George's Star) after King George III, has a complex and evolving history. Uranus progressively evolved from a common star, to an icy comet, before finally settling for life as a planet. In reality, of course, Uranus was not the object undergoing this evolution, but instead humanity's perception of this distant, cold world. Prior to its official discovery, it was observed on several occasions by different astronomers and misidentified as a common star [Bourtembourg, 2013]. The rise of technology brought with it the telescope, enabling this 'star' to be distinguished as a wanderer upon the backdrop of the static constellations. Although proclaimed as an icy comet from the depths of the Solar System by its founder, the status of this wandering object was immediately put up for debate. With the lack of any sign of a tail or coma, calculations revealing a circular orbit were enough to turn the tide in favour of the planet categorisation.

The journey from ignorance to enlightenment is often traversed in stages, with a better approximation to the truth attained with each step. In the case of Uranus, a diligent community arrived at a consensus on the true nature of this pale blue-green dot in the night sky, by careful consideration of an evolving body of evidence.

1.1 Overview of Uranus

Lying at an average orbital distance of 19.19 AU from the Sun, Uranus is barely visible to the naked eye from Earth, hence its relatively late discovery in 1781. Compared to the five classical planets of the Solar System, namely Mercury, Venus, Mars, Jupiter and Saturn, it is a relatively poorly understood world. Table 1.1 gives a summary of Uranus' bulk and orbital parameters compared with those of the Earth.

Table 1.1: A comparison of the orbital and bulk parameters of Uranus and the Earth.

Parameter	Earth	Uranus
Sidereal orbit period (yr)	1	84
Sidereal rotation period (hr)	23.9345	17.24
Average solar distance (AU)	1.0	19.19
Mass (10^{24} kg)	5.97	86.8127 ± 0.0040^{a}
Relative mass	1	14.54
Orbital eccentricity	0.0167	0.0469
Obliquity (°)	23.44	97.77 [1]
Equatorial radius (1 bar) (km)	6378.1	25559 ± 4^{b}
Mean density (g/cm^3)	5.513	1.270
Solar irradiance (Wm^{-2})	1361.0	3.69
Black-body temperature (K)	254.0	58.1
Mean temperature (1 bar) (K)	288	76 ± 2^{c}
Bond albedo	0.306	0.300 ± 0.049^{d}
Heat flux ratio	1.0	1.06 ± 0.08^{d}

[1] Values sourced from (https://nssdc.gsfc.nasa.gov/planetary/factsheet/uranusfact.html) unless labelled otherwise. [a] Jacobson [2014], [b] Archinal et al. [2018], [c] Lindal et al. [1987], [d] Pearl et al. [1990].

Uranus is the third largest planet of the Solar System by size and makes up one half of the so-called 'ice giant' category of Solar System planets, the other being Neptune. The name derives from the fact that, unlike their gas giant counterparts Jupiter and Saturn, whose mass is predominantly in the form of hydrogen (H_2) and helium (He) gas, the bulk of the ice giant mass stems from heavier elements and consists mostly of volatile materials (i.e., ice-forming elements such as oxygen and carbon). The 'ice' moniker is a consequence of the high likelihood that these elements were originally accreted in the form of ices, or as gas trapped within water ice [Boss et al., 2002]. However, similar to the gas giants, Uranus' observable atmosphere is predominantly composed of H_2 and He, with the planet also shrouded by a global system of cloud and haze layers. The blue-green appearance of the planet is largely due to the relatively high abundance of methane (CH_4) within its atmosphere, and the nature of its absorption bands in the visible and near-infrared (NIR), resulting in more absorption of light at the red end of the spectrum than the blue end. Akin to nitrogen in Earth's atmosphere, Rayleigh scattering in Uranus' upper atmosphere also contributes to its characteristic blue-green colour.

Traversing the Solar System at a relatively large distance from the Earth, space mission travel times to Uranus are long, with favourable launch windows optimising for mission travel time coming few and far between. As a result, to date, the Uranian system has only been visited by a single spacecraft, NASA's *Voyager 2* mission [Stone and Miner, 1986]. Launched in 1977, the spacecraft reached Uranus for a fly-by encounter at the beginning of 1986, with initial observations appearing to reveal a featureless, pale blue-green ball of gas with very little dynamical activity. This picture slowly began to evolve over time with the continued observation of Uranus from space and, with the relatively recent advent of adaptive optics, from the ground, across a broad range of wavelengths.

The totality of observations from *Voyager 2* and beyond have granted a window into the unique zonal wind patterns, the composition-pressure profiles of molecules, the spatial variability of molecules, and much more for this distant cold world [Stone and Miner, 1986].

1.2 Formation, Evolution and Internal Structure

1.2.1 Forming an Ice Giant

The formation process of Uranus (and its ice giant partner Neptune) has remained an active area of research over the past few decades and remains so at the time of writing (e.g., Pollack et al. [1996], Dodson-Robinson and Bodenheimer [2010], Helled and Bodenheimer [2014], Frelikh and Murray-Clay [2017], Mousis et al. [2020], Miguel and Vazan [2023]). Unlike their terrestrial and gas giant counterparts, there exist a number of unanswered questions within the leading ice giant formation models. With an ever-growing catalogue of discovered exoplanets showing that Uranus and Neptune-sized planets are abundant in other solar systems [Batalha et al., 2013, Petigura et al., 2018], the desire for a consistent model of formation continues to grow.

In the standard core accretion formation model, an initially gradual accumulation of material via collisions occurs, starting from sub-micron-sized dust grains through to kilometre-sized planetesimals, until a solid core of mass $\sim$10 $M_\oplus$ ($M_\oplus$ = Earth mass) is formed, which then accretes a massive gaseous envelope from the solar nebula in a process named 'runaway gas accretion' [Boss, 2003, Müller et al., 2018, Atreya et al., 2020]. The entire formation process requires several million years or more [Boss, 2003]. However, young stars typically lose their gas discs within a few million years in regions

of low-mass star formation [Briceño et al., 2001], but this time is significantly less in regions of massive star formation [Bally et al., 1998]. This indicates that core accretion might only be viable in relatively long-lived protoplanetary discs [Boss, 2003].

The disc (gravitational) instability formation model, by contrast, has the planet forming directly from the disc, triggered by a gravitational instability where regions of slightly higher density in the protoplanetary disc lead to the formation of clumps of gas and dust [Boss et al., 2002, Boss, 2003]. Under the right conditions, these clumps will contract under the influence of gravity and become progressively more dense until they form planets, with the whole formation process taking on the order of thousands of years [Boss et al., 2002, Boss, 2003]. This is much faster than core accretion and allows for the possibility of planet formation in very short-lived protoplanetary discs. However, the conditions required for the clumps to contract (e.g., a cooling of the midplane of the disc as the clumps form, clumps being robust enough to survive tidal forces etc.) present a limiting factor to this model [Boss, 2007]. The core accretion model has prevailed as the more favourable of the two formation models and is seen as the standard planetary formation scenario; however, work on the disc instability model remains active [Helled and Bodenheimer, 2014, Müller et al., 2018].

The *in situ* formation of the ice giants by core accretion poses significant hurdles. The first of which is the fact that, for the case of Uranus, lying at a current average orbital distance of $\sim$19.2 AU, it would require on the order of 50 million years to form, simply as a consequence of the lower density of the protoplanetary disc at such distances [Pollack et al., 1996]. This is much larger than the expected 1 – 5 million year lifetime of the Sun's protoplanetary disc [Atreya et al., 2020]. This is compounded by the fact that any proposed migration of planetary embryos from the inner Solar System out to this distance

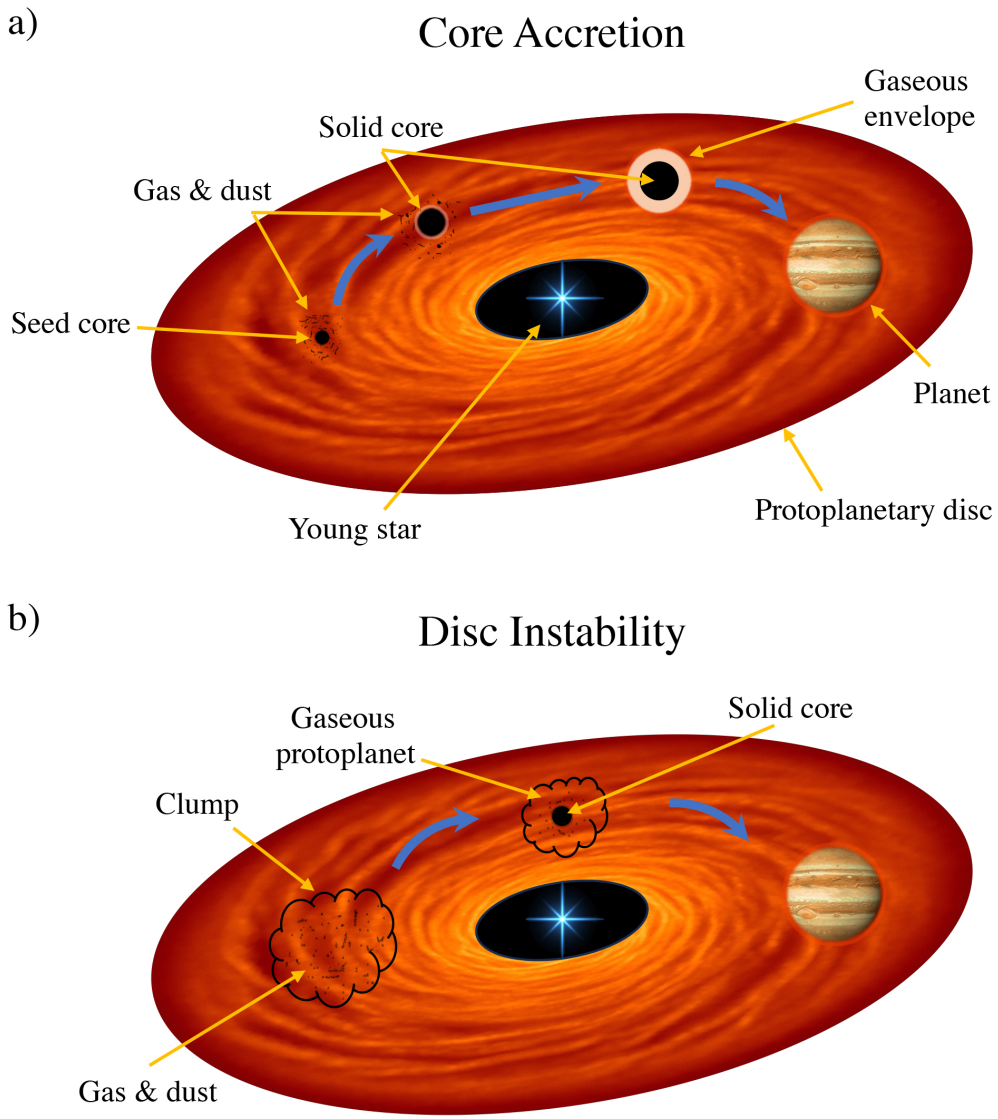


Figure 1.1: Schematic diagram of the two leading planet formation models: a) core accretion and b) disc (gravitational) instability. Note, object sizes are not to scale.

run the risk of encountering Saturn or Jupiter, resulting in their ejection from the disc on hyperbolic orbits, removal by direct impact with the gas giants, or injection into elliptical comet-like orbits [Boss, 2003]. In summation, the *in situ* formation of Uranus by core accretion is an unlikely scenario.

However, a plausible and simple alternative solution to this problem has the ice giants forming between Jupiter and Saturn before being gravitationally scattered, or migrating, outward to their current orbital positions, where the formation process then concludes [Thommes et al., 1999, 2002, Tsiganis et al., 2005]. Despite this neat solution, many unanswered questions remain that do not fit into the standard core accretion picture (e.g., ice giant cores are $\gtrsim 10\ M_\oplus$ but runaway gas accretion doesn't appear to have occurred), these are collectively referred to as the 'fine tuning' problem [Frelikh and Murray-Clay, 2017, Helled et al., 2020]. A number of sub-models, such as the pebble accretion model and planet merger model, have been proposed to attempt to answer some of these questions, but ultimately *in situ* measurements of the atmospheric composition are required to favour one model over another and advance work on this degenerate problem [Helled et al., 2020].

1.2.2 The Evolution of Uranus

Uranus possesses a number of unique physical parameters when compared to its giant planet counterparts, hinting at an uncommon evolution history. The most notable of these are its large obliquity of 97.8°, and its low heat flux ratio of 1.06 (the ratio between emitted radiation and the incident solar radiation), denoting a relatively low source of internal heat. To put this in context, Neptune, the second of the ice giant planets, has an obliquity of 28.3°, comparable to that of the other solar system planets, and a heat flux

ratio of 2.61 [Pearl and Conrath, 1991], the largest of the four giant planets. Although the ice giant planets share a number of similarities (e.g., mass, radius), these two metrics clearly hint at very different evolution histories for these two distant worlds.

A long-standing plausible explanation for Uranus' extreme tilt is a giant impact shortly after its formation [Safronov, 1966]. Many studies have since worked on this hypothesis, simulating the many impact scenarios that reproduce the observables as well as the Uranian moon system, which orbits on the rotational plane of Uranus (e.g., Slattery et al. [1992], Podolak and Helled [2012], Kegerreis et al. [2018], Reinhardt et al. [2020], Rufu and Canup [2022]). Ultimately, these studies confirmed that an oblique impact is able to alter Uranus' rotation period, alter its obliquity, and eject enough material to create a disc from which its regular satellites are able to form [Helled et al., 2020].

An alternative explanation, shedding the requirement for a giant impact, cites planetary migration as the source of Uranus' large obliquity [Boué and Laskar, 2010]. This scenario, however, does require particular conditions to be met, for example, an orbiting satellite during Uranus' migration outward and a temporarily large orbital inclination (i.e., a large angle with respect to the rotational plane of the Sun and protoplanetary disc) [Boué and Laskar, 2010]. These conditions result in the giant impact hypothesis being the more favourable of the two models, in addition to the fact that it aids formation models by providing more mass to the planet [Helled et al., 2020].

The question of Uranus' low internal source of heat is a non-trivial one, requiring a better understanding of Uranus' interior structure, evolution and composition to find a robust solution [Helled et al., 2020]. With the bulk of Uranus' structure expected to be fluid, the atmospheric and interior compositions are closely linked [Helled et al., 2020], however, there are still many unanswered questions about the deep composition. For example,

what the deep abundance of ammonia is, which appears to be depleted in the troposphere of the atmosphere [de Pater et al., 1989]. A better understanding of Uranus' interior is required to shed light on how the internal heat flux is transported, providing insight into the planet's formation and evolution history [Helled et al., 2020].

1.2.3 Internal Structure

Interior models of Uranus are based upon the available observational constraints (e.g., mass, radius, rotation rate, etc.). One important metric for constructing interior models is the gravity field, which provides an important constraint on the interior density profile of a planet [Helled et al., 2020]. Due to a limited number of constraints, the interior model becomes a degenerate problem in which a number of competing models fit the available data well. There are currently two main models for Uranus' interior, which can be summarised as the 'solid rocky core' model and 'diffuse core' model. The solid rocky core model consists of an outer atmospheric envelope, predominantly composed of H_2 and He, followed by a large layer of ices below, and finally a small, solid rocky core at the centre. The diffuse core model, on the other hand, consists of the same outer atmospheric envelope, but followed by a large layer of ices mixed with rocks, with a gradual transition between ice and rock with depth [Nettelmann et al., 2013, Helled et al., 2020]. Within these two models, the boundary between the atmosphere and layer below can either be a distinct phase boundary or a gradual transition [Helled et al., 2020]. A schematic diagram of these two models is given in Fig. 1.2.

As previously mentioned, *Voyager 2* is the only spacecraft to have visited Uranus in its 1986 fly-by encounter. As a consequence, the gravitational coefficients describing its gravity field are not very well constrained when compared to, for example, Jupiter, which

has a dedicated spacecraft, Juno, oriented in a polar orbit to enable robust measurements [Militzer et al., 2022]. Such measurements unlock the degeneracy between competing models and, in the case of Jupiter, reveal a diffuse core [Militzer et al., 2022]. Therefore, a dedicated space mission to Uranus is necessary to further constrain the gravity field and shed light on the nature of its core.

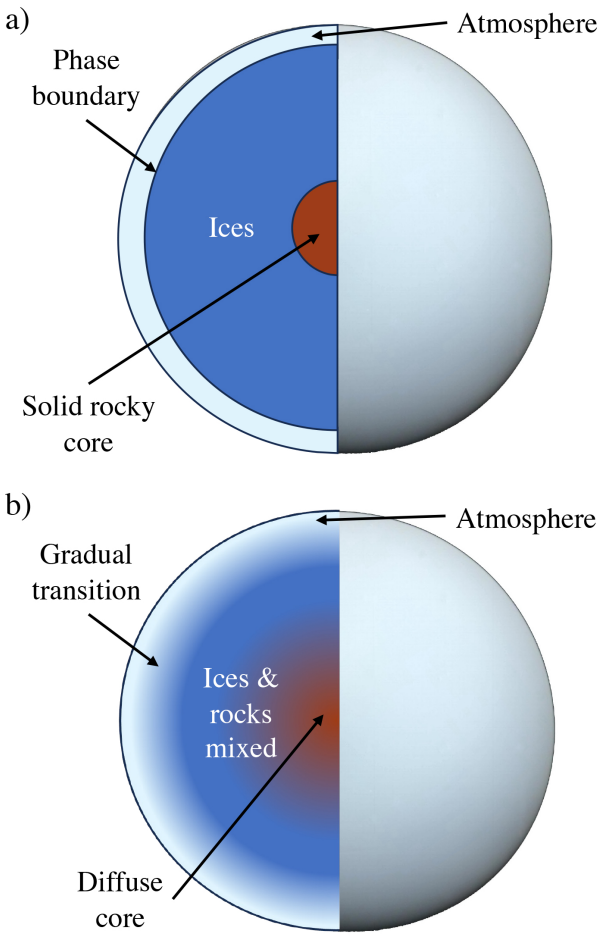


Figure 1.2: Schematic diagram of the two leading interior models of Uranus: a) the solid rocky core model and b) the diffuse core model. Note the examples of the phase boundary in a) in which there is a hard boundary between the atmospheric layer and the ice layer, whereas in b) there is a gradual transition between these layers.

Though these two models are the front-runners, it is important to note that an alternative

model, consistent with the observational constraints, also exists. This model calls into question the moniker of 'ice giant' by proposing that the interior is mostly composed of rocks (by mass) leading to a 'rock giant' classification instead [Teanby et al., 2020]. The interior structure differs from the models described above in that the H_2-He envelope is much larger and the rocky content below is much larger [Helled et al., 2020]. There are a number of arguments against this model, such as the existence of Uranus' magnetic field or its orbital distance being more favourable for icy material, which are still open for debate [Teanby et al., 2020, Helled et al., 2020]. However, some observational data, such as the lack of tropospheric carbon monoxide (CO) detected in Uranus' atmosphere, an indicator of interior ice content, favour the rock giant picture [Teanby et al., 2020]. The true nature of Uranus' interior is yet to be determined at the time of writing.

1.3 The Atmosphere of Uranus

1.3.1 Temperature

Atmospheres are stratified based upon the method of heat transport occurring at a given pressure level. At pressures where the infrared (IR) optical depth (i.e., the natural log of the ratio of incident to transmitted power) to space is high, heat cannot efficiently escape via radiation. As a result, parcels of air rise convectively, expanding and cooling adiabatically as they do so, assuming thermal contact with neighboring air masses can be neglected [Irwin, 2009]. This results in a transfer of heat upwards. The temperature at pressure levels contained in this zone is governed by the dry adiabatic lapse rate (DALR) (for the scenario of no condensation), defined in Eqn. 1.1. This describes the decrease in temperature with height (equally the decrease in temperature with decreasing pressure)

of a parcel of dry air lifted by a reversible adiabatic process through an atmosphere in hydrostatic equilibrium (i.e., when external forces are balanced by the pressure-gradient force) [Irwin, 2009]. This region of the atmosphere is named the troposphere

$$\frac{dT}{dz} = -\frac{\bar{m}}{C_p}g = -\frac{g}{c_p} = -\Gamma_d \tag{1.1}$$

where T is the temperature, z is the altitude, $\bar{m}$ is the mean molecular weight of the atmosphere, C_p is the molar heat capacity at constant pressure, g is the gravitational constant of the planet, c_p is the specific heat capacity at constant pressure, and Γ_d is the DALR. If condensation is occurring though, the saturated adiabatic lapse rate (SALR) instead applies, which is a slightly more complex process that results in Eqn. 1.1 being multiplied by a factor involving the latent heat of vaporisation of the condensing molecule(s).

At lower pressures, the IR optical depth to space becomes progressively smaller, leading to radiation becoming more efficient than convection at transporting heat. A plot of the temperature-pressure profiles of the two ice giant planets is shown in Fig. 1.3, at equatorial latitudes for Uranus and mid-southern latitudes for Neptune. It can be seen that the temperatures decrease with height up to a certain level, known as the tropopause, where they are then approximately constant before increasing again. The region above the tropopause where temperature is observed to increase with height is known as the stratosphere.

Radio occultation observations captured by *Voyager 2* detected a tropopausal temperature near the 100-mbar level of 53 $\pm$ 1K for Uranus [Lindal et al., 1987]. Above the tropopause, Lindal et al. [1987] found that the gas temperature reached 114 $\pm$ 10K near the 0.5-mbar level of the stratosphere. In this case, the increase in temperature is due to

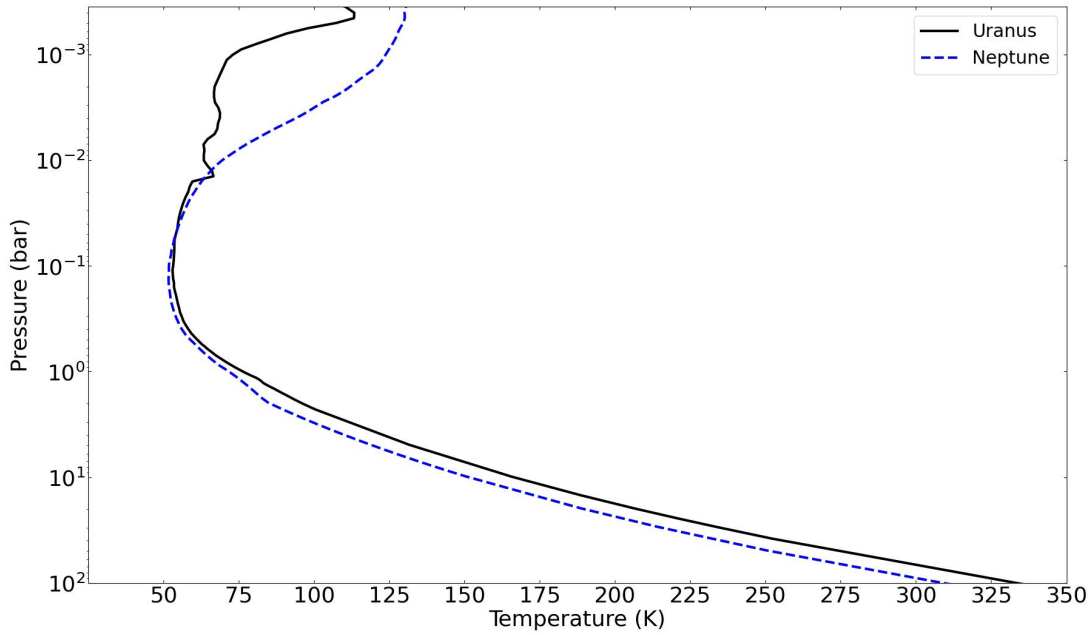


Figure 1.3: A comparison of the temperature-pressure profiles of Uranus and Neptune [Lindal et al., 1987, Irwin, 2009]. The tropopause for both planets is found at the ∼100-mbar level. Note the discrete bumps in temperature indicating layers of hydrocarbon aerosol absorption [Lindal et al., 1987].

absorption of solar radiation in the ultraviolet (UV) through to the IR, mainly by CH_4 and its photodissociation products [Irwin, 2009]. Lindal et al. [1987] also detected several warm layers, indicating the absorption of solar radiation by hydrocarbon aerosols.

From Fig. 1.3, we see that Neptune has a significantly higher stratospheric temperature at the 0.5-mbar level, despite being at a much greater orbital distance, with a value of $\sim$130K [Lindal et al., 1990, Lindal, 1992]. This indicates much more absorption of solar radiation, largely due to higher abundances of CH_4 in the stratosphere than Uranus [Baines and Hammel, 1994, Baines et al., 1995]. The tropospheric temperature profiles of the ice giants are very similar despite the large difference in orbital distance. This is a result of the aforementioned contrast in the source of internal heat between the two planets.

1.3.2 Composition

1.3.2.1 Troposphere

The bulk of Uranus' observable atmosphere is composed of a mix of H_2 and He gas. The volume mixing ratio (VMR) of a gas (i.e., the ratio of the number density of the given gas to the total number density of the atmosphere) is denoted f_X for gas X, and for He, this was found from the analysis of *Voyager 2* data to be 0.152 ± 0.033, corresponding to a mass fraction of $Y_{He} = 0.262 \pm 0.048$ [Conrath et al., 1987]. This value is consistent with the protosolar nebula (PSN) mass fraction of $Y_{PSN,He} = 0.275$, indicating that there is no significant loss of He from the atmosphere taking place, akin to the process of helium 'rain' out in the gas giant atmospheres [Conrath et al., 1991].

A molecule of hydrogen can occupy one of two spin states, named ortho-hydrogen and

para-hydrogen. At high temperatures (T $\gtrsim$ 300 K), the para-H_2 fraction (f_p) of H_2 gas tends to an equilibrium value of $f_{p,eq} = \frac{n_{para}}{n_{total}} = 0.25 = f_{deep}$. Such temperatures are found in the deep troposphere of Uranus at ∼100 bar (see Fig. 1.3). For temperatures below ∼300 K, the equilibrium fraction, $f_{p,eq}$, begins to increase with decreasing temperature [Irwin, 2009]. Due to the cool temperatures found in the upper region of Uranus' troposphere ($p < 5$ bar), $f_{p,eq} > 0.25$ here. For a given pressure level, any deviation of f_p from the equilibrium value, $f_{p,eq}$, defined by the temperature found at that level, provides insight into how vigorous the vertical motion within the troposphere is. The difference, $f_{p,eq} - f_p$, can therefore be used as a metric to estimate the vigor of vertical motion. If f_p is closer to the deep equilibrium value f_{deep} = 0.25 than $f_{p,eq}$ at the pressure level being probed, this indicates vigorous vertical convection, mixing deep, warm equilibrium H_2 with this cooler gas [Irwin, 2009]. Conrath et al. [1998] probed the para-H_2 fraction using *Voyager 2* data, examining the 0.1 – 1 bar region. It was found that the average difference from equilibrium (i.e., $f_{p,eq} - f_p$) across latitudes was 0.02, the smallest of the four giant planets, indicating relatively sluggish vertical convection. It is important to note that aerosols catalyse the conversion of ortho-H_2 to para-H_2, meaning an understanding of Uranus' aerosol distribution is a key factor in interpreting the observed f_p profile [Irwin, 2009]. This will be revisited in Section 1.3.2.2.

The next most abundant molecule in the Uranian atmosphere is CH_4. Its documented abundance has been a continuously developing story over the past few decades. Early analyses of *Voyager 2* radio occultation data, recorded at a limited range of latitudes (2 – 7°S), resulted in a VMR for the nominal model of Lindal et al. [1987] of 2.3% at $p \simeq$ 1.3 bar. However, several models with varying temperature profiles below ∼1 bar were analysed by the group, producing upper and lower bounds for f_{CH_4}, spanning ∼1.1 –

4%. Baines et al. [1995] later found, utilising disc-averaged hydrogen quadrupole observations from the Very Large Array (VLA) observatory, and the *Voyager 2* thermal profile of Lindal et al. [1987], a value of $1.6^{+0.7}_{-0.5}$%, in agreement with the value found by Lindal et al. [1987]. These results supported the notion that cloud-top f_{CH_4} was uniform with latitude and constant below the CH_4 condensation level ($\sim$1.2 bar). With the advent of adaptive optics technology enabling robust correction for atmospheric distortion, Sromovsky and Fry [2007] re-examined the picture for Uranus using ground-based observations from the Keck observatory in Hawaii. Analysing latitudes of 45°S, 12°S and 35°N, they found that a number of values for f_{CH_4} spanning 1.3 – 4% fit the data well, with each favoured value having its pros and cons. Karkoschka and Tomasko [2009] found a similar range of 1.4 – 3.2% for the deep CH_4 abundance analysing HST/STIS observations from a number of southern latitudes spanning 15 – 60°S, this opened up a new discussion which will be covered in Section 1.3.6.

Other notable molecules in the troposphere include ammonia (NH_3), for which de Pater and Massie [1985] constrained the VMR to 3 – 9 $\times$ 10^{-6} in the upper troposphere using ground-based microwave observations. They also constrained the hydrogen sulfide (H_2S) deep tropospheric abundance to 10 – 30 $\times$ solar, i.e., a VMR of $\sim$0.38 – 1.13 $\times$ 10^{-3}, providing early signs that H_2S could be the more abundant of the two molecules that are predicted to react together to form ammonium hydrosulfide (NH_4SH), depleting the less abundant of the two molecules. Irwin et al. [2018] were the first to report a direct, unambiguous detection of cloud-top H_2S, noting abundances of 4 – 8 $\times$ 10^{-6}, placing a lower limit of 1.0 – 2.5 $\times$ 10^{-5} below the cloud layer, and confirming it to be more abundant than NH_3. The upper tropospheric mixing ratio of phosphine (PH_3) has been constrained by Encrenaz et al. [1996] to an upper limit of 2 $\times$ 10^{-6} from ground-

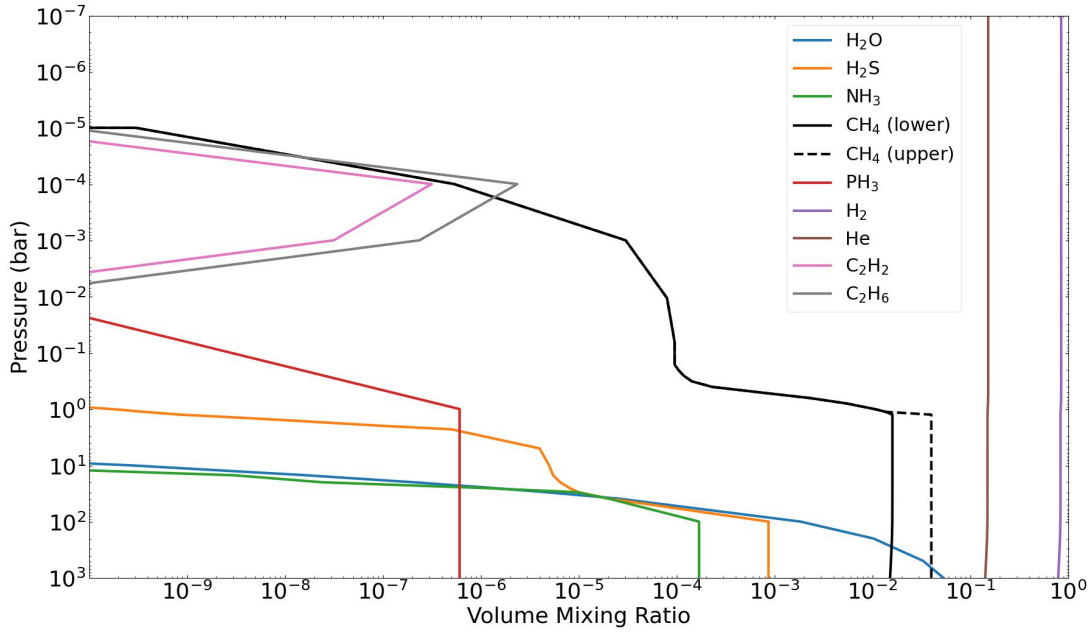


Figure 1.4: A plot of the mixing ratio-pressure profiles for molecules detected in the Uranian atmosphere [Irwin, 2009, Irwin et al., 2018, Molter et al., 2021]. Two deep CH_4 profiles are included representing the lower ($\sim$1.4%) and upper ($\sim$4%) bounds on the deep abundance [Sromovsky and Fry, 2007, Karkoschka and Tomasko, 2009].

based millimetre and HST IR observations, which was later constrained to $p < 3.1$ bar [Encrenaz et al., 2004]. Carbon monoxide (CO), again from ground-based millimetre observations and HST IR observations, was detected in the upper troposphere giving an upper limit for the VMR of 2×10^{-8} above 3.1 bar [Encrenaz et al., 2004]. Finally, water (H_2O), a molecule that models predict is abundant in the deep troposphere ($\sim$4% VMR at $p > 200$ bar [Cavalié et al., 2017]) has eluded detection thus far, except in the very upper troposphere, where quantities are consistent with an external source [Feuchtgruber et al., 1997]. This is very likely due to a strong depletion of gas-phase H_2O as water condenses at deeper levels [Moses et al., 2020].

Fig. 1.4 displays the abundance-pressure profiles in the troposphere and stratosphere for

data available on the molecules detected and constrained in the atmosphere of Uranus. The relevant molecules included in the work of this thesis are CH_4, which is the dominant absorber in the visible/NIR, and H_2 & He, which provide significant collision-induced absorption, discussed later in Section 1.3.6.1.

1.3.2.2 Stratosphere

It was previously mentioned that aerosols can catalyse the conversion of ortho-H_2 to para-H_2, and therefore play an important role in interpreting the f_p profile of Uranus. Building on the aforementioned work within the troposphere, Fouchet et al. [2003] studied f_p in the stratosphere in the 1 – 10 mbar region. They found that f_p lies close to equilibrium, noting an anti-correlation between the size of the departure from thermodynamic equilibrium and the abundance of aerosols, confirming their expected influence [Irwin, 2009].

Due to the cool temperatures observed in the upper troposphere of Uranus, its tropopause is predicted to act as a cold trap for CH_4, preventing significant quantities from rising up into the stratosphere [Irwin, 2009]. Early ground-based observations by Orton et al. [1987] placed an upper bound on the stratospheric abundance, finding $f_{CH_4} < 1 \times 10^{-5}$. Not long after, Yelle et al. [1989], analysing *Voyager 2* UV observations, found a VMR of $\sim 3 \times 10^{-7}$ between 3 and 5 mbar, and $\sim 1 - 3 \times 10^{-7}$ for p $<$ 3 mbar, significantly smaller than the upper bound given by Orton et al. [1987]. More recent analysis of mid-IR observations from the Spitzer space telescope found the best fit to the data for $f_{CH_4} = 1.6 \times 10^{-5}$ at the tropopause [Orton et al., 2014b]. This work was furthered using far-IR observations from the Herschel space observatory, finding the tropopausal CH_4 abundance to lie at $\sim 4 \times 10^{-4}$ [Lellouch et al., 2015]. This value is $\sim$6 larger than

that found by Orton et al. [2014b], seemingly in conflict. However, Lellouch et al. [2015] note that this conflict can be reconciled if f_{CH_4} decreases rapidly from the tropopause level of $p \sim 100$ mbar to the 2-mbar level. In contrast, Neptune has a mid-stratospheric $f_{CH_4} = 1.15 \times 10^{-3}$ [Lellouch et al., 2015], providing more evidence for the scenario of sluggish vertical convection on Uranus, tying into the picture painted by work on the ortho-/para-H_2 ratio [Baines and Bergstralh, 1986, Baines et al., 1995, Conrath et al., 1998, Fouchet et al., 2003].

Photolysis of CH_4, via the absorption of UV photons, is constantly occurring in the Uranian stratosphere, depleting the molecule [Atreya, 1990]. CH_4 photolysis leads to photochemistry, splitting up the constituent parts of the molecule and recombining them to form new hydrocarbons. Small abundances of these hydrocarbons have been detected within the stratosphere, some notable examples include acetylene (C_2H_2), ethane (C_2H_6), ethylene (C_2H_4) and diacetylene (C_4H_2) [Orton et al., 1987, Pollack et al., 1987, Yelle et al., 1989, Bandy et al., 1992, Encrenaz et al., 1998, Moses et al., 2018]. These hydrocarbons play an important role in the production of the observed haze layers in Uranus' stratosphere (e.g., Romani and Atreya [1988], Moses et al. [1995]), discussed in Section 1.3.3. Carbon dioxide (CO_2) has also been detected in very small quantities at the same pressure levels as these hydrocarbons, suggesting an external source of oxygen (O_2) [Orton et al., 2014b].

One final molecule worth noting is CO. CO was first detected in Uranus' atmosphere using the Infrared Spectrometer and Array Camera (ISAC) instrument on the Very Large Telescope (VLT), for which a mixing ratio of 3 $\times 10^{-8}$ at the tropopause and above provided the best fit to the data [Encrenaz et al., 2004]. Cavalié et al. [2014] later utilised Herschel observations and found a slightly lower VMR of 7.1 – 9.0 $\times 10^{-9}$ fit their data

best. This is significantly less than the corresponding mixing ratio of 0.6 – 2.5 $\times 10^{-6}$ in Neptune's atmosphere [Hesman et al., 2007, Fletcher et al., 2010], indicating the contrast in vertical convection between the two ice giant atmospheres. Similar to the case of CO_2, the presence of CO suggests an external source of O_2 in the atmosphere of Uranus, e.g., from the infall of ring material.

1.3.3 Vertical Aerosol Models

The aerosol layers within the Uranian atmosphere are an almagamation of those predicted from theory, and those detected from observation. An example of the theoretical side is a simple class of models named Equilibrium Cloud Condensation Models (ECCMs) [Weidenschilling and Lewis, 1973]. They are based upon a set of simple assumptions about a parcel of gas rising within the atmosphere, with the picture as follows. The parcel rises from the warm, deep interior without mixing with the surrounding gas. The temperature decreases as it rises, resulting in the saturated VMR reducing with altitude, eventually becoming equal to the VMR of the gas in the parcel. At this pressure level, gas begins to condense from the parcel, which can be accelerated by the presence of cloud condensation nuclei (CCN), to form aerosols. As the parcel continues to rise, more gas condenses out, with the VMR of the parcel mirroring the gas' saturated VMR curve, which continues to decrease with altitude as temperature continues to decrease. It is assumed that the aerosols are left behind and fall through the atmosphere as the parcel rises further. On reaching the tropopause, beyond which temperature begins to rise again, the VMR of the parcel essentially becomes fixed, as the aerosols are no longer available to re-evaporate. Therefore, the tropopause acts as a cold trap for gases that condense in the troposphere, limiting their stratospheric abundances [Irwin, 2009]. The level at which

the parcel's VMR intersects the saturated VMR curve determines the base pressure of the modelled aerosol layer, meaning a higher deep VMR leads to a deeper cloud base [Irwin, 2009].

Some of the assumptions of ECCMs, such as the lack of mixing with the surrounding gas, are not very realistic, resulting in the models being able to provide reliable predictions for cloud base pressures, but not for the vertical extent of the cloud or its optical thickness (e.g., Irwin [2009]). In the atmosphere of Uranus, ECCMs predict a large H_2O aerosol layer based in the 100 – 1000 bar region, dependent on the deep abundance of H_2O. Above this, based at ∼40 bar, lies an NH_4SH layer produced by the combination of NH_3 and H_2S. This is followed by an H_2S ice layer based between 2 – 8 bar. Finally, a CH_4 ice cloud based at ∼1.5 bar is predicted [Irwin, 2009].

Observations in the visible and NIR are able to probe down to a few bars, limited by the opacity of the overlying aerosol layers, gaseous absorption, and Rayleigh scattering towards the blue end of the visible spectrum. As a result, the deep layers ($p \gtrsim 10$ bar) cannot be probed directly via remote sensing, and are therefore informed from theoretical aerosol models and deep composition models. The initial analysis of *Voyager 2* data revealed an optically thick tropospheric cloud with top pressure between 2.4 – 3.2 bar, a thin CH_4 cloud centred at ∼1.2 bar, and the detection of an upper tropospheric haze with top pressure ∼0.67 bar [Baines and Bergstralh, 1986, Lindal et al., 1987]. When analysing the tropospheric cloud aerosols, Baines and Bergstralh [1986] found that the single-scattering albedo darkened steeply longwards of ∼0.6 μm, a characteristic of UV-irradiated H_2S ice crystals, providing a hint for the cloud's composition. The CH_4 cloud was found to have a very thin visible optical depth, potentially indicating that aerosols grow and precipitate rapidly, leading to low visible reflectance [Irwin, 2009].

Later studies began to dispute the observed CH_4 cloud. Sromovsky et al. [2006] preferred a 2-cloud model between 2 – 6 bar, finding a significant peak in aerosol scattering near 2 bar and either near 6 bar or distributed between 3 and 6 bar for the deep cloud. They found only a small contribution at the location of the putative CH_4 cloud near 1.25 bar. Irwin et al. [2007] also favoured a 2-cloud model, but with the clouds based at 2 bar and $\sim$8 – 10 bar, later noting the absence of the expected CH_4 cloud at 1.2 – 1.3 bar [Irwin et al., 2009]. Sromovsky and Fry [2008] confirmed a lack of significant cloud particle scattering near 1.2 bar from spectral and HST observations, casting more doubt on the existence of a stable cloud layer here. The work of Karkoschka and Tomasko [2009] favoured a 2-cloud model with a probable H_2S tropospheric cloud at $\sim$3 bar and an extended tropospheric haze at $\sim$1.4 bar. They explicitly stated that their data was able to exclude a significant cloud layer at the CH_4 condensation level (1.2 bar). Further work by Sromovsky et al. [2011] explored a more complex 5-cloud model, while Irwin et al. [2012] favoured a 2-cloud model, similar to that of Karkoschka and Tomasko [2009], with an extended tropospheric haze. Tice et al. [2013] & Irwin et al. [2015] continued to develop this 2-cloud parameterisation, with Sromovsky et al. [2019] also favouring the simpler 2-layer model after exploring more complex models with additional layers [Sromovsky et al., 2014, 2019]. As previously mentioned, Irwin et al. [2018] then provided the first unequivocal detection of gaseous H_2S above the main Uranian cloud deck, providing the first direct evidence that the tropospheric cloud is indeed composed of H_2S ice. Later, Sromovsky et al. [2019] found tentative signs of a deeper cloud layer in the 9 – 11 bar region. Including this layer in their models improved their fits, especially in the 0.54 – 0.67 μm region. They proposed a composition of NH_4SH, but noted that further work is certainly needed to confirm the existence of this aerosol layer.

CH_4 photochemistry, important between 0.1 – 10 mbar, produces hydrocarbons such as C_2H_6, C_2H_2, C_2H_4, and polyacetylenes ($C_{2n}H_2$, n = 2, 3, 4...) [Irwin, 2009]. Models predict a C_4H_2 ice layer at $p > 0.1$ mbar, a C_2H_2 ice layer at $p > 2.5$ mbar, and a C_2H_6 ice layer at $p > 15$ mbar [Irwin, 2009]. Upon condensing, these haze particles combine to form larger particles, and eventually fall under the force of gravity, forming an optically thin extended haze layer. Due to the gravitational fall out, the haze layers tend to thin out at pressures greater than ∼30 mbar [Irwin, 2009]. Initial analysis of *Voyager 2* data confirmed the presence of a stratospheric haze in the ∼1 – 100 mbar region (e.g., Orton et al. [1987], Marley and McKay [1999]), with aerosols within early models having mean radii between 0.10 – 0.15 μm, and number densities between 1 – 3 particles.cm^{-3} [Pollack et al., 1987]. Baines and Bergstralh [1986] detected an upper tropospheric haze, extending between ∼0.67 – 1.2 bar, with optical depth $0.4 < \tau < 1.0$ at 0.6435 μm, indicating the coalescence and gravitational descent of stratospheric aerosols. Rages et al. [1991] then reported the presence of haze in the lower stratosphere and upper troposphere, confirming the earlier detections, and found that the particle radii reduced from ∼0.2 μm at ∼1.4 bar to ∼0.02 μm at 1 mbar in their model. The previously mentioned work of Karkoschka and Tomasko [2009], with its extended tropospheric haze based at 1.4 bar (preferred for its simplicity), favoured mean particle radii of 0.1 μm. Their model fixed the real refractive index of the aerosols to 1.4 and parameterised the imaginary refractive index, allowing for a large value in the UV region of the spectrum to maintain sufficient absorption, and a much smaller value in the visible region.

A similar approach was employed in later work, modelling the particles using Henyey-Greenstein (HG) functions with asymmetry parameter g = 0.7, and allowing the imaginary refractive index to vary [Irwin et al., 2012, Tice et al., 2013, Irwin et al., 2015]. Once

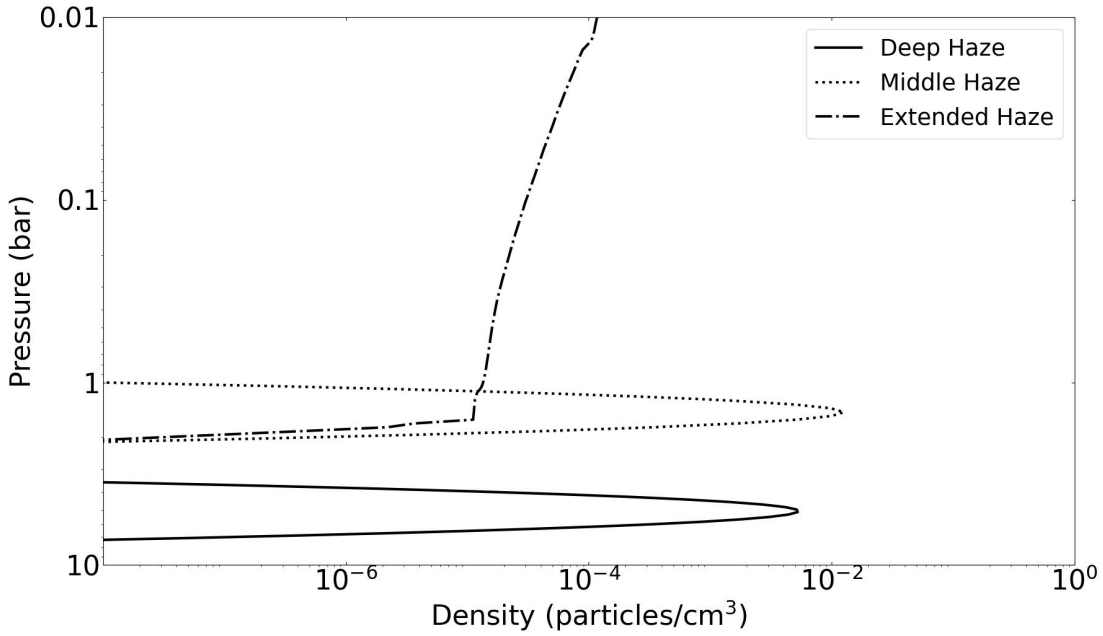


Figure 1.5: Plot of particle density against pressure demonstrating the vertical aerosol model of Irwin et al. [2022, 2023a] for Uranus. The vertical profiles plotted were retrieved using a disc-averaged HST/STIS 2015 observations.

again a mean radius of $\sim$0.1 μm was favoured, however, the models fitted best with the haze base pressure fixed at the top of the tropospheric cloud ($\sim$1 bar) [Tice et al., 2013, Irwin et al., 2015]. Sromovsky et al. [2019] then explored modelling non-spherical haze particles using simple HG functions, resulting in asymmetry parameters much smaller than that of Tice et al. [2013] & Irwin et al. [2012, 2015], ranging from 0.43 $\pm$ 0.04 at 10°N to 0.26 – 0.39 at 60°N. Toledo et al. [2019] provided a microphysical treatment for haze formation, simulating observations from VLT/SINFONI (Integral Field Unit Spectrometer) and HST/WFC3. By coupling the simulations to the NEMESIS radiative transfer code, they found haze particles at the tropopause level ($\sim$100 mbar) with mean radius $\sim$0.2 μm and a density of $\sim$2.9 particles.cm^{-3}, with the haze production rate in the stratosphere lying between $\sim 3 \times 10^{-16} - 3 \times 10^{-15}$ kg.m^{-2}.s^{-1}.

Most recently, Irwin et al. [2022] developed a robust 3-layer aerosol model, common to both ice giant atmospheres, after thorough analysis applying the Minnaert limb-darkening model to observations spanning 0.3 – 2.5 μm sourced from HST/STIS, HST/WFC3, NASA's Infrared Telescope Facility SpeX (IRTF/SpeX) instrument, and the Gemini Observatory's Near-Infrared Integral Field Spectrometer (Gemini/NIFS) instrument. This model was later improved by Irwin et al. [2023a], consisting of a deep haze layer centred at $\sim$5 bar, assumed to be composed of a mixture of H_2S ice and photochemical haze, a photochemical haze layer centred near the CH_4 condensation level (1 – 2 bar) assumed to be a mixture of photochemical haze and CH_4 ice (this layer is trapped in a region of static stability caused by the rapid drop of molecular weight at the CH_4 condensation level due to it being an abundant gas in the upper troposphere), and finally an extended photochemical haze layer extending from this level up through to the stratosphere where the haze particles are produced. The only significant change from the previous iteration of the model is the deep haze layer, which was changed from a diffuse layer lying mainly between 4 – 7 bar to a compact layer centered at $\sim$5 bar. Irwin et al. [2023a] found this change to significantly improve latitudinal retrieval analyses, resulting in smoothly varying latitudinal profiles as opposed to the previously less physically plausible oscillating profiles. This model is displayed in Fig. 1.5. Irwin et al. [2022] suggest that CH_4 condensing onto the haze particles at the base of the 1 – 2-bar aerosol layer forms ice/haze particles that grow rapidly and quickly precipitate, as proposed by Carlson et al. [1988], subsequently re-evaporating at deeper levels causing the release of the haze particles at their core, which can then act as CCN for H_2S ice formation.

1.3.4 Dynamics

1.3.4.1 Radiative Forcing

The circulation of a given planetary atmosphere is largely driven by a combination of internal heating from below, and solar heating from above. Therefore, having a measure of how a planet's internal heat flux compares to its incident solar flux, parameters that have been experimentally measured for the ice giants, should provide some insight into its circulation. Uranus' energy balance was found from *Voyager 2*'s Infrared Interferometer Spectrometer and Radiometer (IRIS) to be $E = 1.06 \pm 0.08$ [Pearl et al., 1990], i.e., its internal heat source accounts for only 6% of its total energy flux, the smallest fraction of the four giants planets. Based on this number alone, we expect Uranus' circulation to be sluggish and predominantly driven by solar forcing.

Another important factor in the circulation of an atmosphere is the obliquity of the planet. Uranus stands out with its large $\sim 98^\circ$ tilt, meaning that during a Uranian year, both poles will receive direct sunlight from overhead, and both poles experience a night that is half a Uranian year long [Irwin, 2009]. When *Voyager 2* encountered Uranus, it was close to southern summer solstice, resulting in virtually only the southern hemisphere being illuminated. This was approximately the case in the decade leading up to the *Voyager 2* fly-by, with its atmosphere appearing static and featureless. Thus, Flasar et al. [1987] expected to find a temperature gradient between the illuminated south pole and the equator of $\sim$7K. However, looking at the 500 – 1000 mbar region, they found almost no temperature difference at all. The pole-to-pole temperature contrast was also examined in the 500 – 1000 mbar region, expected to be of the order $\sim$10K, but once again almost no difference at all was found [Flasar et al., 1987]. These results suggested

efficient redistribution of absorbed solar heat via meridional (and zonal) circulation.

Uranus moved through its northern spring equinox in 2007, causing a significant change in solar forcing, leading to large scale changes in the dynamics of the atmosphere. CH_4 windows (i.e., regions of the spectrum lying outside of CH_4 absorption bands, allowing deeper pressures to be probed) dimmed in brightness in the south and brightened in the north, with the bright 'collar' at 45°S declining in brightness whilst a similar one developed at 45°N and began to brighten, and discrete cloud features were seen at midlatitudes (∼30°N & 30°S) [Norwood and Chanover, 2009, Sromovsky et al., 2009, Irwin et al., 2009, 2010]. Such findings led Sromovsky et al. [2009] to conclude that the asymmetric band structure of Uranus is a delayed response to solar forcing, with a surprisingly short delay of only a few years. Now as Uranus progresses towards northern summer solstice, the change in solar forcing once again presents an opportunity to study the resulting changes in atmospheric dynamics [Sromovsky et al., 2012a, Irwin et al., 2017, Toledo et al., 2018, Sromovsky et al., 2019].

1.3.4.2 Zonal Structure

The gas giant atmospheres, especially Jupiter, have zonal structures that are clearly seen in the visible, with bright bands (zones) and dark bands (belts) alternating as one moves away from the equator in the latitudinal direction. These are found to be regions of alternating prograde and retrograde flow (Fig. 1.6) [Sanchez-Lavega et al., 2000, Porco et al., 2003]. Uranus, and its ice giant counterpart Neptune, also exhibit a latitude-dependent zonal wind structure. The pattern of the zonal winds, however, appears to be much less complex, and among other differences, visible bright and dark bands are not as easily seen (Fig. 1.7).

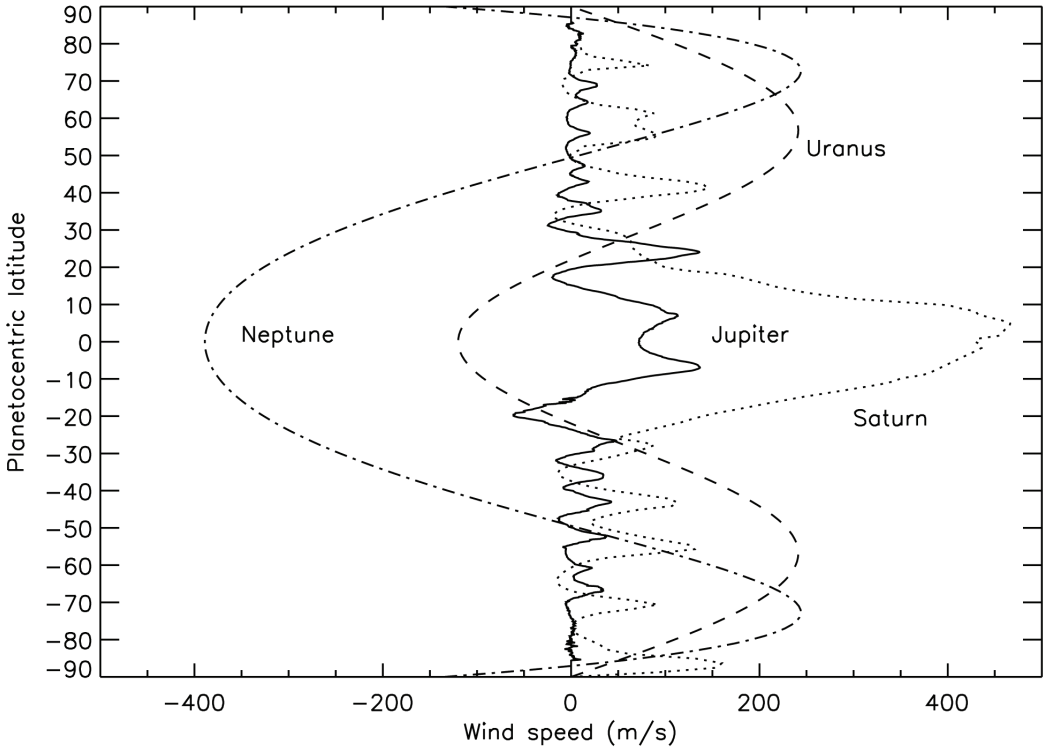


Figure 1.6: A comparison of the zonal wind velocities of the four giant planets: Jupiter (*solid*) [Porco et al., 2003], Saturn (*dotted*) [Sanchez-Lavega et al., 2000], Uranus (*dashed*) [Hammel et al., 2001] and Neptune (*dashed-dotted*) [Sromovsky et al., 1993]. This figure is the original work of Irwin [2009] and is included with the author's permission.

Both Ice Giants have high speed retrograde equatorial jets and prograde midlatitude jets, very different to the numerous alternating belts and zones of the gas giants [Lindal et al., 1987, Sromovsky et al., 1993, Hammel et al., 2001]. The ice giant midlatitude jets have much larger wind speeds than their gas giant counterparts, on the order of 200 ms^{-1}, with the equatorial jet wind speeds of Uranus and Neptune being comparable to those of Jupiter and Saturn respectively (Fig. 1.6). Sromovsky and Fry [2005], extending the zonal wind observations of Uranus up to 60°N, confirmed the existence of a slight north-south asymmetry in the midlatitude jets. The cause of this asymmetry is yet to be confirmed, but is thought to be a permanent feature of the atmosphere [Sromovsky et al., 2009].

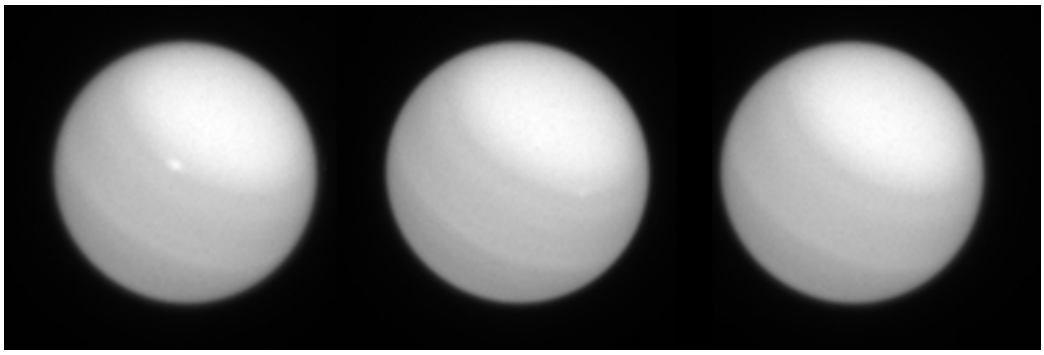


Figure 1.7: Three HST/WFC3 images captured by the Outer Planet Atmospheres Legacy (OPAL) programme [Simon et al., 2015] between 25/10/2017 - 27/10/2017 using the 0.657 μm filter. A large faint banded structure can be observed. The north pole is at the top right of each image, encircled by the north polar 'hood'. A bright convective storm can be seen at the edge of the polar hood.

Simulation work has been carried out to try and uncover the nature of the zonal wind structures of the ice giants. Lian and Showman [2010] made the first breakthrough by probing the effect of large-scale latent heating of the atmosphere via the condensation of H_2O vapour. They were able to reproduce the correct number of jets (3) and the retrograde direction of the equatorial jet, finding that large H_2O abundances always favour a

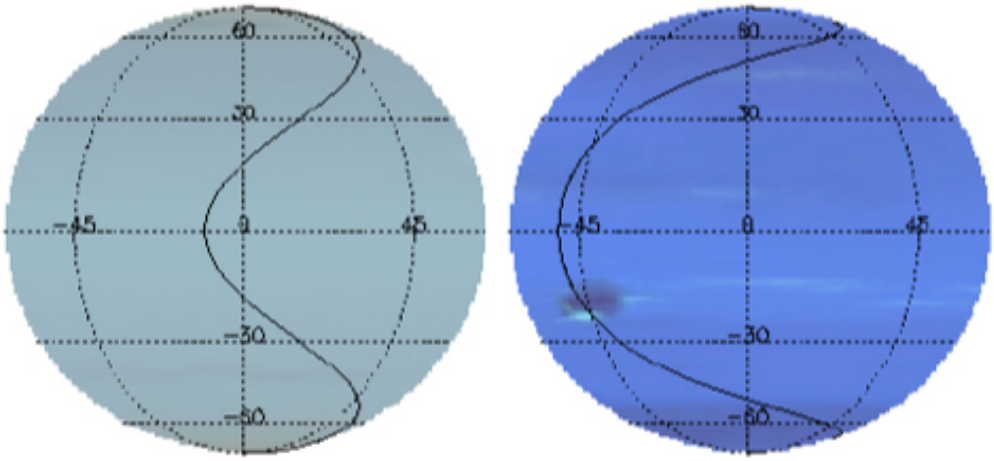


Figure 1.8: A comparison of the zonal wind velocities of the ice giant planets Uranus [Hammel et al., 2001] and Neptune [Sromovsky et al., 1993] superimposed onto each planet's disc. Wind speeds are converted to degrees longitude. Labelled numbers are degrees of latitude and longitude, not velocity. This figure is the original work of Irwin [2009] and is included with the author's permission.

retrograde equatorial jet. This work was built upon by Soderlund et al. [2013], who investigated whether or not the zonal winds are a consequence of 3-dimensional turbulence excited in planetary-scale H_2O layers. They also incorporated magnetic field observations in their modelling work. Simulations were successful in matching observations by producing zonal jets with retrograde flow at the equator, and even extended to predicting local equatorial peaks in internal heat fluxes due to equatorial upwelling [Soderlund et al., 2013].

1.3.4.3 General Circulation Models

The similarities between the zonal wind velocities of Uranus and Neptune suggest some commonality between the general circulation of the ice giants, confounded by the stark contrast compared to the zonal winds of the Gas Giants, Jupiter and Saturn. General

circulation models (GCMs), such as EPIC [Dowling et al., 1998, 2006] and DYNAMICO [Dubos et al., 2015], have been successfully applied to the gas giant atmospheres to model many of the observed features, including the zonal structure of belts and zones (e.g., Sayanagi and Showman [2007], Palotai and Dowling [2008], Guerlet et al. [2014], Cosentino et al. [2017]). The literature on GCMs for the ice giant atmospheres, however, is scarce. The EPIC and DYNAMICO GCMs have been applied to explore seasonal change and eddy activity in Uranus' atmosphere in preliminary work [Sussman, 2011, Milcareck et al., 2021], but many questions still remain unanswered about this atmosphere's underlying general circulation.

Speculative models of the tropospheric and stratospheric circulation have been proposed (e.g., Karkoschka and Tomasko [2009], Sromovsky et al. [2014], Fletcher et al. [2020]) that are consistent with the observed phenomena in Uranus' atmosphere, including latitudinal mixing ratio gradients in molecules such as CH_4 [Karkoschka and Tomasko, 2009, Sromovsky et al., 2014], H_2S and NH_3 [de Pater et al., 1991, Molter et al., 2021], the distribution and transport of haze [Toledo et al., 2019], and hemispherical asymmetries in convective activity and cloud formation [Sromovsky et al., 2012a, de Pater et al., 2015, Sromovsky et al., 2015]. These models mainly consist of stacked circulation cells that result in downwelling at the poles and upwelling at equatorial and midlatitudes in the upper troposphere. An example is shown in Fig. 1.9.

1.3.5 Discrete Features

Many discrete features have been observed in the Uranian atmosphere over the past few decades at various locations and epochs, ranging from a dark spot, small-scale convective clouds, and convective storm systems (e.g., Irwin et al. [2007], Sromovsky and Fry

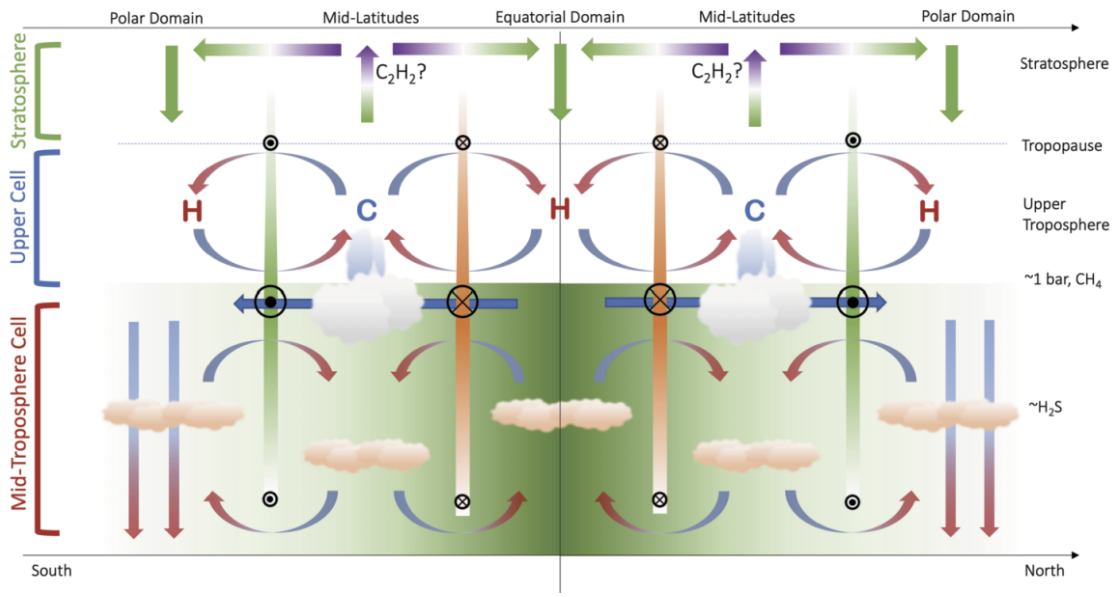


Figure 1.9: A schematic diagram of Fletcher et al. [2020]'s proposed meridional circulation of the Uranian atmosphere from the mid-troposphere to the lower stratosphere. Arrows indicate the direction of travel of gas, with the labels 'H' representing hotter gas and 'C' representing colder gas relatively speaking. Figure adapted from Fletcher et al. [2020]'s Figure 8.

[2007], Irwin et al. [2009], Hammel et al. [2009], Sromovsky et al. [2009], Irwin et al. [2011], Sromovsky et al. [2012b], Irwin et al. [2017]). The dark spot was discovered in 2006, similar in appearance to the Great Dark Spot (GDS) on Neptune, at 28°N (see Fig. 1.10) [Hammel et al., 2009]. It was observed to have a 5° width and 2° height, circling the planet ∼20 ms^{-1} faster than bright features located at the same latitude [Hammel et al., 2009]. Irwin et al. [2022] were able to explain the ice giant dark spot phenomenon within the framework of their holistic vertical aerosol model as a darkening of their deep haze layer. They noted that this could be the result of an uplift of chromophores (molecules responsible for colour) from below this level, or equally from the sublimation of H_2S ice into the vapour state, due to anomalously warm temperatures, revealing the darker CCN photochemical haze cores [Irwin et al., 2022].

1.3.6 Spatial & Temporal Variability

1.3.6.1 Latitudinal Variability

The breakthrough work of Karkoschka and Tomasko [2009] provided a shift in thinking with regard to Uranus' CH_4 abundance. Building on the work of Sromovsky and Fry [2007], they identified a more reliable technique for probing cloud-top CH_4 mixing ratio. Using HST Space Telescope Imaging Spectrograph (STIS) observations obtained in 2002, they explicitly contradicted the assumption of latitudinal uniformity in cloud-top f_{CH_4}. Their results showed a reduction in f_{CH_4} with latitude by a factor of ∼2 as the region being probed moved from Uranus' equator to its pole, retrieving values of 3.2% within 20° of the equator and 1.4% at latitudes south of 50°S. They noted that the absolute values of f_{CH_4} depend on the temperature profile used, but the latitudinal gradient is independent of this. This new method utilised H_2 collision-induced absorption (CIA) to

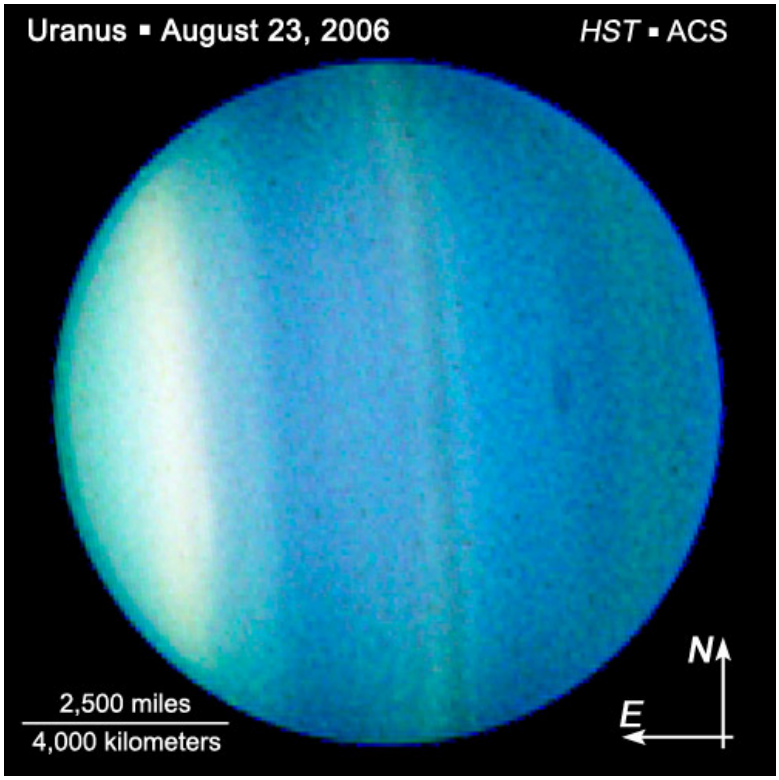


Figure 1.10: An image of Uranus captured using HST's Advanced Camera for Surveys (ACS) High Resolution Camera (HRC) (https://hubblesite.org/contents/media/images/2006/47/2000-Image.html?Tag=Uranus). The dark spot can be seen to the right of the centre of the disc [Hammel et al., 2009].

break the degeneracy between variations in aerosol opacity and f_{CH_4}. In the 500 – 1000 nm spectral region, CH_4 is the dominant absorber, except for a small window between 818 – 832 nm where H_2 CIA dominates. If latitudinal features in CH_4 absorption bands also appear in this region dominated by H_2 CIA absorption, they must be due to aerosol opacity, but if they do not appear in this region, we can be confident that they are due to variations in cloud-top CH_4 mixing ratio [Karkoschka and Tomasko, 2009].

Irwin et al. [2009] put the results of Karkoschka and Tomasko [2009] to the test using data from the United Kingdom Infrared Telescope in combination with the radiative transfer retrieval code NEMESIS, probing the vertical cloud structure around northern spring equinox (2006 – 2008) in the NIR J-band (1.17 – 1.31 μm) and H-band (1.45 – 1.65 μm). A change in the deep value ($\sim$3 – 4 bar) of f_{CH_4}, from 4% near to the equator to $\sim$1 – 2% near to the poles, resulted in little difference in their spectral fits, meaning their conclusions were consistent with latitudinally-dependent cloud-top f_{CH_4}. Sromovsky et al. [2011] reached a similar conclusion from a re-analysis of the *Voyager 2* occultation observations of Lindal et al. [1987] and novel analysis of 2002 HST/STIS observations. They examined potential f_{CH_4}-pressure profiles, finding the best quality retrieval fits were obtained for f_{CH_4} depleted to depths of 3 – 4 bars at 60°S and 1.5 – 2 bar at 45°S, suggesting that below a particular latitude-dependent depletion pressure (p_d), the mixing ratio of CH_4 reaches the deep value of $\sim$4% at all latitudes. This work provided further support for the conclusion of Karkoschka and Tomasko [2009], with recent studies solidifying these results (e.g, Tice et al. [2013], Sromovsky et al. [2014], Irwin et al. [2017], Toledo et al. [2018], Sromovsky et al. [2019], James et al. [2023]).

In addition to CH_4, the H_2S, NH_3 and H_2 abundance also appear to display latitudinal variability in the Uranian atmosphere. de Pater et al. [1989] found latitudinal variations

in the brightness temperature from radio observations, interpreting this as latitudinal variation in the NH_3 abundance, with the VMR largest ($\sim 2 \times 10^{-6}$) in the equatorial region ($< 30 - 40°$) at altitudes where the temperature is $145 < T < 240$ K (i.e., $7 \lesssim p \lesssim 30$ bar from Fig. 1.3), less in the midlatitudes ($1 - 2 \times 10^{-7}$) at altitudes where $145 < T < 220$ K (i.e., $7 \lesssim p \lesssim 25$ bar from Fig. 1.3), and smallest (10^{-7}) in the polar region ($>70°$) down to altitudes where $T \sim 280$ K (i.e., down to $p \sim 55$ bar from Fig. 1.3). They later noted, utilising Very Large Array (VLA) microwave observations, that the abundance of NH_3 appeared to be homogeneous in latitude below the level of cloud formation, similar to the case of CH_4 [de Pater et al., 1991]. The most likely explanation given for the latitudinal variation was attributed to dynamical processes within the atmosphere, leading de Pater et al. [1991] to predict an equivalent effect on other gases such as H_2S. More recently, Molter et al. [2021] utilised Atacama Large Millimeter Array (ALMA) and VLA observations of Uranus, obtained between 2015 and 2018, to probe pressures from $\sim$1 to $\sim$50 bar. Analysis revealed the north polar region to be very bright at all observed wavelengths northwards of $\sim$50°N. This was attributed to strong depletions in both NH_3 and H_2S, extending down to the NH_4SH layer, when compared to the equatorial region [Molter et al., 2021]. Modelling was consistent with an NH_3 abundance of $4.7^{+2.1}_{-1.8} \times 10^{-7}$ and an H_2S abundance of $< 1.9 \times 10^{-7}$ between $\sim$20 and $\sim$50 bar, whereas the equator and midlatitudes were consistent with deep abundances of $1.7^{+0.7}_{-0.4} \times 10^{-4}$ for NH_3 and $8.7^{+3.1}_{-1.5} \times 10^{-4}$ for H_2S [Molter et al., 2021]. The most likely explanation for the depletions was a large-scale downwelling in the north polar vortex region from $\sim$0.1 to $\sim$50 bar.

Lastly a slight hemispherical asymmetry in the zonal winds of Uranus at the midlatitudes has been observed, where southern winds are $\sim$20 ms^{-1} more westward than the corre-

sponding winds in the north [Sromovsky et al., 2009, 2012b]. An underlying explanation has yet to be put forward for this asymmetry, which is thought to be a permanent feature of the atmosphere and not linked to the season [Sromovsky et al., 2009].

1.3.6.2 Seasonal Change

Since the *Voyager 2* fly-by encounter in 1986, Uranus has progressed from southern summer solstice (1985) to northern spring equinox (2007), and is currently on its approach to northern summer solstice (2030) at the time of writing. Having covered almost half a Uranian year, observations have been able to closely track seasonal changes within the atmosphere (e.g., Lindal et al. [1987], Sromovsky and Fry [2007, 2008], Irwin et al. [2009], Karkoschka and Tomasko [2009], Irwin et al. [2010, 2012], Tice et al. [2013], Sromovsky et al. [2014], Toledo et al. [2018], Sromovsky et al. [2019]). The most notable of these changes occurred a few years prior to, during, and a few years after the 2007 equinox, marking the transition between increasing illumination of the northern hemisphere and decreasing illumination of the southern hemisphere.

On the approach to equinox, the south polar hood, a large bright 'cap' enshrouding the south polar region down to ∼45°S latitude and across all longitudes, began to diminish in brightness, eventually reducing down to a circumpolar collar at ∼45°S, which itself diminished in brightness through equinox [Irwin et al., 2009]. A similar circumpolar collar formed in the northern hemisphere at ∼45°N through equinox, concurrent with the continued diminishing brightness of the southern collar, which eventually vanished [Sromovsky et al., 2009, Irwin et al., 2009, 2010]. The collars are thought to be a delayed response to solar forcing, but with a surprisingly short delay of only a few years [Sromovsky et al., 2009, Irwin et al., 2009]. The northern polar collar then appeared to

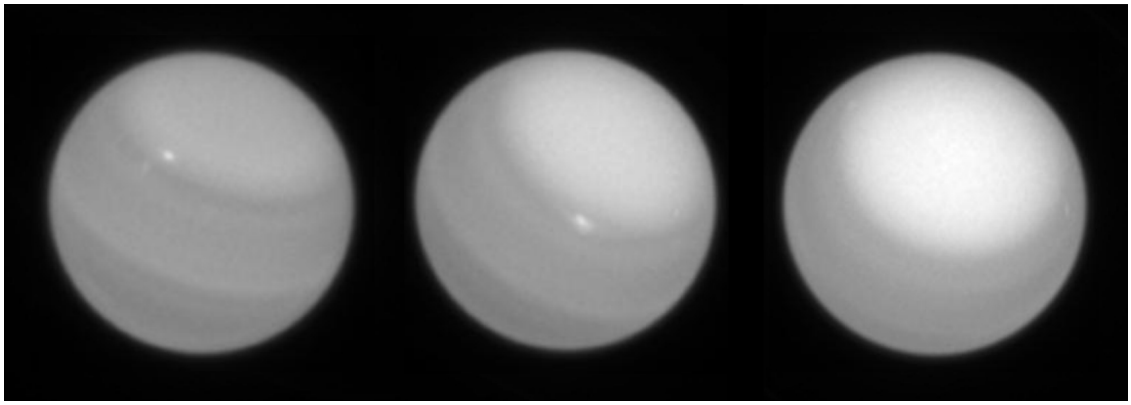


Figure 1.11: HST/WFC3 images in the 0.845 μm filter from 2014 (*left*), 2018 (*middle*) and 2022 (*right*), displaying the brightening of the north polar hood as Uranus approaches northern summer solstice (in 2030). An example of the convective storm activity, which peaked during equinox, can be seen in the midlatitudes at the top left of the 2014 disc. The north pole is at the top right of the disc for 2014 and 2018, and at the top middle for 2022. Image brightness has been scaled to that of the 2022 image.

extend northward over time, resulting in a north polar hood [Irwin et al., 2017, Toledo et al., 2018], similar to that observed in the southern polar region prior to equinox (e.g., Karkoschka and Tomasko [2009]). Sromovsky and Fry [2008] proposed that the collar is a result of increased aerosol scattering within a tropospheric cloud layer near 2 bar, leading to questions about the source of the polar hood. From analysis of NIR VLT/SINFONI observations in the H-band, Toledo et al. [2018] concluded that the bright appearance of the hood is mainly a result of the depletion in cloud-top f_{CH_4} at polar hood latitudes, rather than from latitudinal variation of the optical properties or abundance of aerosols. The subsequent observed brightening of the newly formed north polar hood (e.g., Irwin et al. [2011, 2017]) thus desired an explanation, seemingly stemming from either a further reduction in polar f_{CH_4} or from changes in aerosol scattering properties. Sromovsky et al. [2019] utilised HST/STIS, Keck Near Infrared Camera 2 (Keck/NIRC-2) and IRTF/SpeX observations to address this question, finding the depletion in f_{CH_4} to be generally stable over time, and an increase in aerosol scattering to be responsible for the

polar hood brightening. They did, however, note that the persistent latitudinal gradient in upper tropospheric CH_4 contributes to the northern polar region appearing brighter relative to the equator and midlatitudes [Sromovsky et al., 2019].

The 2007 equinox also produced a marked increase in convective storm activity at mid-latitudes [Sromovsky and Fry, 2007, Sromovsky et al., 2009, Irwin et al., 2009], which has since declined [de Pater et al., 2015, Irwin et al., 2016, 2017]. This increase in activity is likely a consequence of the change in solar forcing at this critical season of transition in the Uranian atmosphere [Sromovsky et al., 2009, Irwin et al., 2009].

1.4 Scientific Questions

Despite the significant progress that has been made in understanding the planet Uranus, there are many questions yet to be answered on the nature of this planet and its atmosphere. There are five main scientific questions that this investigation aims to address:

1. **What physical changes are responsible, if any, for the observed temporal brightening of Uranus' north polar hood?** (Chapter 4)

2. **What is the underlying mechanism driving the physical changes, if any, responsible for the temporal brightening of Uranus' north polar hood?** (Chapter 4)

3. **How do the aerosol layers of Uranus' atmosphere change with latitude and time?** (Chapter 5)

4. **Is the latitudinal profile of cloud-top CH_4 VMR stable over long timescales ($\gtrsim$ 3 years)?** (Chapter 5)

5. **Does the depletion in polar cloud-top CH_4 VMR exhibit interseasonal variability?** (Chapter 5)

1.5 Thesis Outline

This thesis presents retrieval analysis work on the atmosphere of Uranus carried out using observations from three data sources: HST/WFC3, HST/STIS and VLT/MUSE.

In Chapter 2, the telescopes and instruments used to obtain the data are described in detail, including the methodology and techniques used to obtain the observations. A description of the data reduction processes for the different datasets will also be given in detail. Chapter 3 will cover the underlying physics and background theory behind radiative transfer and retrieval theory, including a comprehensive deep dive into the NEMESIS radiative transfer code, and how it was used for the analysis. The Minnaert limb-darkening model, utilised to great effect in this work, will also be described in detail.

Chapters 4 & 5 will comprise the analysis, results and discussion of the investigation. Chapter 4 analyses the HST/WFC3 and HST/STIS datasets to investigate Uranus' polar hood feature, tracking its development and seeking an explanation behind its observed brightening. Chapter 5 employs a novel VLT/MUSE observation and, again, the HST/STIS and HST/WFC3 datasets to probe general variability in the Uranian atmosphere, both latitudinally and temporally, with a focus on the cloud-top CH_4 mixing ratio profile over time.

Chapter 6 will then present the conclusions of the investigation and explore ideas for future work that could build on the results presented in this thesis.

Chapter 2

Instrumentation & Data Reduction

The following Sections provide a description of the sources of data used in this investigation. This includes a description of the telescope used, the instrument utilised, and the data reduction process for each unique dataset.

2.1 HST/WFC3

The Hubble Space Telescope (HST) is a low Earth orbit space telescope with functional imaging stretching from the UV to the IR regions of the electromagnetic spectrum. It was launched in 1990 and remains operational at the time of writing. HST contains a number of instruments used for observing, one of which is its Wide Field Camera 3 (WFC3), an upgrade from its predecessor the Wide Field and Planetary Camera 2 (itself an upgrade from the Wide Field and Planetary Camera 1).

The WFC3 instrument possesses two channels, one for ultraviolet and visible light (UVIS) and the other for near-infrared light (NIR). Only the UVIS channel was used for imag-

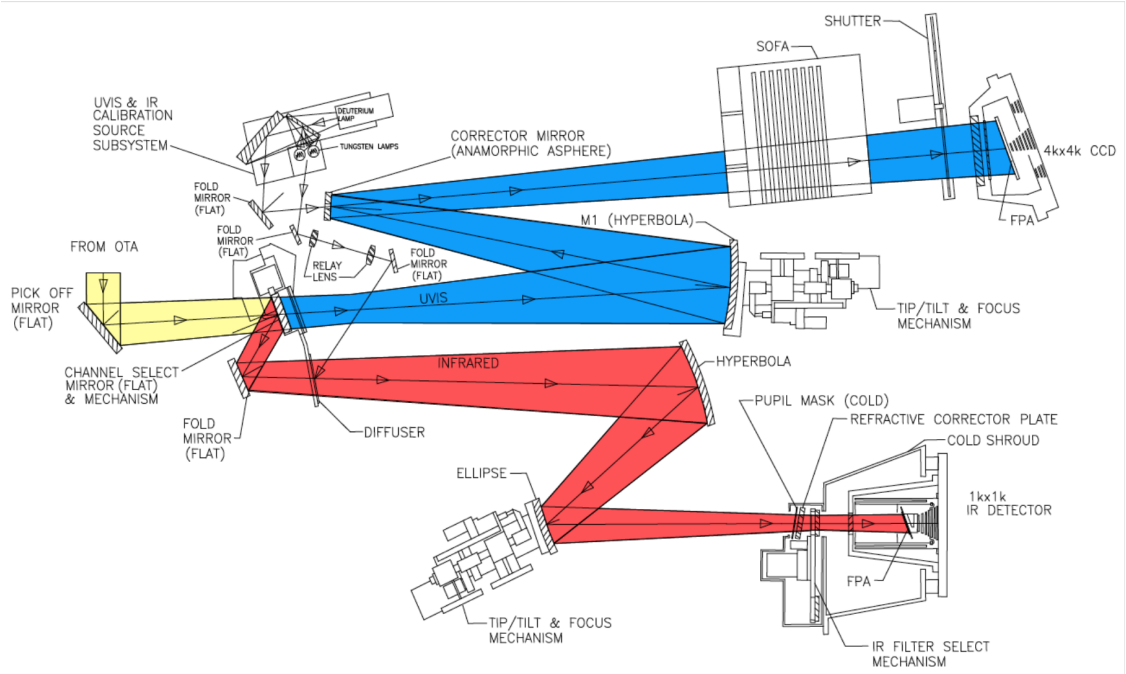


Figure 2.1: A diagram of the WFC3 instrument optical setup and its sequence of operation [Sohn et al., 2011].

ing when collecting the dataset used in this investigation. The UVIS channel consists of two butted 4096 $\times$ 2051 thinned, back-illuminated charge-coupled device (CCD) detectors to support imaging between 200 and 1000 nm. The detectors are silicon-based, 16 megapixel, high sensitivity, low noise array CCDs. In general, CCDs function by converting the energy of incident photons into electrical charge. The amount of electrical charge produced is recorded for each pixel on the device, which is eventually reconfigured into an image. The UVIS channel has a 0.0395″ $\times$ 0.0395″ pixel scale and a 162″ $\times$ 162″ field of view (FOV).

UVIS contains several narrow-band, medium-band, and wide-band filters with which imaging can be carried out. Seven of these were utilised to obtain the observations in the dataset, consisting of narrow-band and medium-band filters only. These are described in

Table 2.1 and displayed in Fig. 2.2.

Table 2.1: The seven UVIS filters used by the Outer Planet Atmospheres Legacy programme to obtain observations of Uranus.

Name (Aperture)	λ_0 (nm)	FWHM (nm)
F467M (UVIS)	467	21.5
F547M (UVIS)	547	70.9
FQ619N (UVIS)	619	6.1
F657N (UVIS)	657	12.1
FQ727N (UVIS2)	727	6.4
F763M (UVIS)	763	70.9
F845M (UVIS)	845	87.6

HST/WFC3 images are displayed in Fig. 2.3 from each UVIS filter for the 2015 and 2021 datasets used for analysis. Uranus' orbit can be seen to be progressing towards northern summer solstice, occurring in 2030, via the north polar hood at the upper right of the disc moving further into view.

2.1.1 Observation Methodology & Data Reduction

The Outer Planet Atmospheres Legacy (OPAL) programme is the initiative responsible for recording, calibrating and processing the HST/WFC3 dataset into a usable format for studying seasonal variability in the atmospheres of Jupiter, Saturn, Uranus and Neptune. OPAL began recording yearly global maps of the giant planets in 2014 and is currently an ongoing initiative. The dataset used here consists of sets of yearly observations of Uranus spanning 2015 – 2021. Each set of observations were captured $\sim$1 year apart during 8 HST orbits covering two full rotations of the planet. Images were navigated using an ellipsoid limb-fitting technique with equatorial and polar radii of 25,559 km and 24,973 km, respectively. The FQ727N data were fringe corrected post-pipeline using images of the dark sky to remove streaks and artefacts (e.g., stemming from scattered starlight

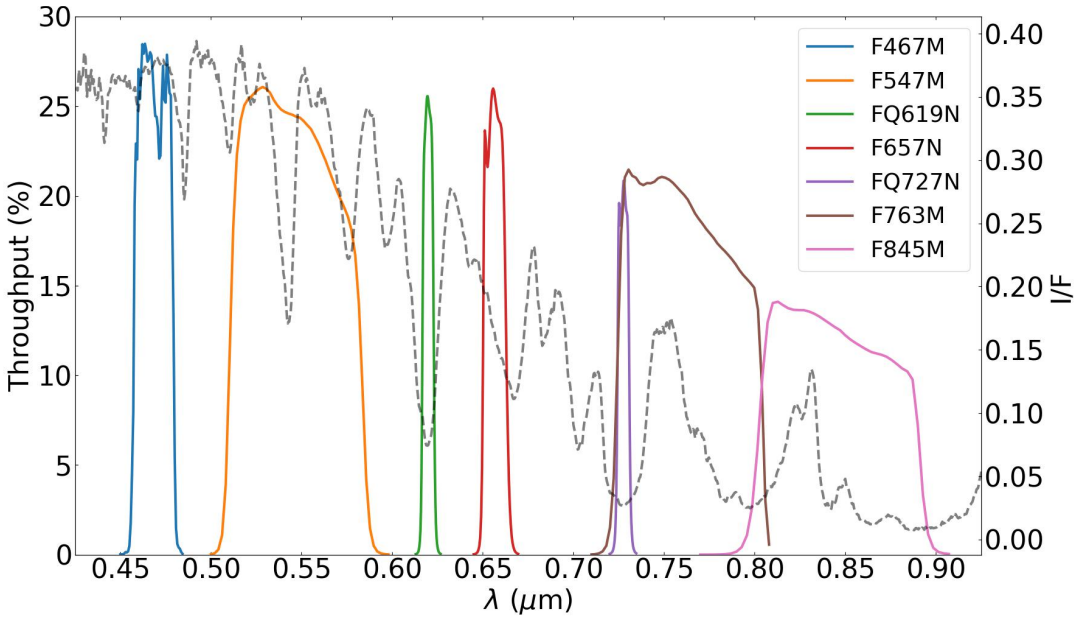


Figure 2.2: The seven UVIS filters used for 2015 – 2021 observations of Uranus on a plot of throughput against wavelength in microns. The dashed grey line displays the disc-averaged reflectivity (I/F) spectrum of a 2015 HST/STIS observation of Uranus as a reference for the spectral features captured by each filter.

or thin-film interference effects in the detector), resulting in a $\sim$1.1% correction. Data were photometrically calibrated in accordance with the latest WFC3 calibration pipeline update, accounting for new time-dependent inverse sensitivities [Calamida et al., 2021], resulting in a $\sim$0.3 – 0.8% correction to the pre-2021 observations (dependent on the filter and epoch).

The calibration pipeline is a lengthy procedure for which a brief summary is given here. Firstly, a correction for the charge transfer efficiency (CTE) is made, due to a degradation in the CCDs over time. A simple noise model is then calculated for each pixel of the image and stored in an 'error' array. A table of known bad pixels on the detector is then read in, flagging their positions. Overscan regions are then used to provide a measure of the bias level at the time of the exposure, which is subtracted from the data. The image is

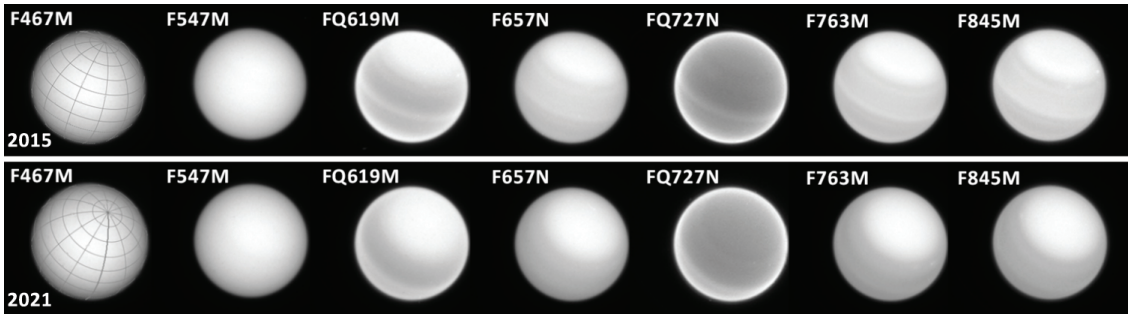


Figure 2.3: HST/WFC3 images in the seven UVIS filters for the 2015 (*top*) and 2021 (*bottom*) datasets. The 0.467-μm images include superimposed latitude-longitude grids with spacing of 30° between lines of longitude and 15° between lines of latitude. The north pole is at the upper right of the disc and is seen to move further into view over the 6-year timespan.

then bias-corrected by subtracting the bias image. A particular type of bad pixel known as 'sink' pixels, which affect the output of neighbouring pixels, are also flagged and their impact is corrected. The image is then multiplied by the gain to convert the units into electrons. The image is then dark-corrected by first scaling then subtracting the dark reference image. Next, the image is corrected for pixel quantum efficiency, known as flat-fielding, using the flat reference file. After flat-fielding, the photometric keywords (e.g., PHOTFLAM), containing the values of the inverse sensitivities, are populated using precomputed tables. Finally, a flux normalisation of the UVIS1 and UVIS2 detectors is performed to ensure that the flux correction is uniform over both detectors [Calamida et al., 2022].

2.2 HST/STIS

The Space Telescope Imaging Spectrograph (STIS) is another instrument onboard HST. STIS is a medium resolution spectrograph containing three large-format (1024 $\times$ 1024 pixel) two-dimensional detectors operating from the UV to the NIR region of the electro-

magnetic spectrum. The first of these detectors is a thinned, backside-illuminated CCD, named the STIS/CCD, with 0.05078″ × 0.05078″ pixels and a 52″ × 52″ square FOV, operating from 164 to 1030 nm. The second is a Cs_2Te Multi-Anode Microchannel Array (MAMA) detector, named the STIS/NUV-MAMA, with 0.0245″ × 0.0248″ pixels, and a 25″ × 25″ square FOV, operating in the near-UV from 160 to 310 nm. Finally, a solar-blind CsI MAMA, named the STIS/FUV-MAMA, is included with ∼0.025″ × 0.025″ pixels, and a 25″ × 25″ square FOV, operating in the far-UV from 115 to 170 nm [Sohn et al., 2011]. The observations used in this investigation were obtained using solely the STIS/CCD.

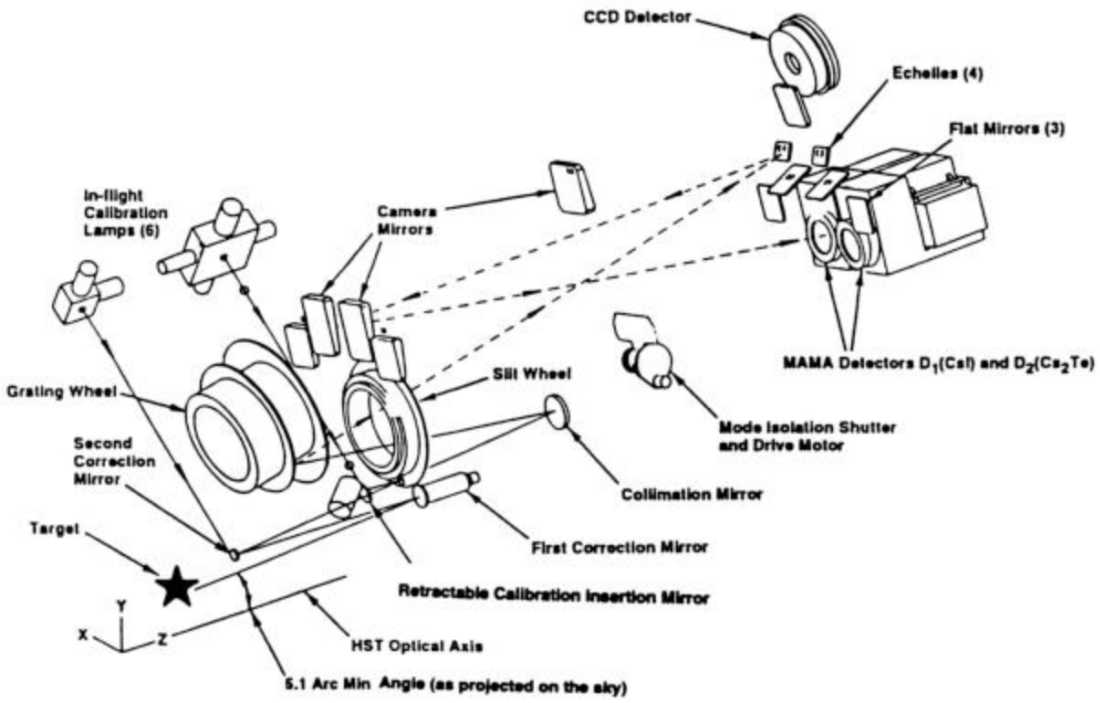


Figure 2.4: A diagram of the STIS instrument optical setup and its sequence of operation [Sohn et al., 2011].

STIS possesses a number of different slits and gratings with which to perform long-slit spectroscopy. The long slits have widths 0.05, 0.1, 0.2, 0.5 and 2.0 arcseconds in the

dispersion direction, and lengths of 52″ as projected on the CCD detector. There are 10 first-order gratings available covering the full spectral range, providing resolving powers of ∼500 – 17,000 from the UV at 115 nm through the NIR at ∼1000 nm. A slit wheel and a grating wheel allow switching between these different elements. The slit wheel contains apertures and slits for spectroscopy as well as apertures for imaging. Slit-wheel positioning is repeatable to very high precision: ±7.5 and ±2.5 milliarcseconds in the spatial and spectral directions, respectively. The grating wheel, named the Mode Selection Mechanism (MSM), contains the first-order gratings, the prism, and the mirrors used for imaging. The MSM is a nutating wheel that can orient optical elements in three dimensions, permitting the selection of one of its many optical elements as well as adjustment of the tip and tilt angles of the selected grating or mirror. For some gratings, only a portion of the spectral range of the grating falls on the detector in any one exposure. These gratings can be scanned (tilted by the MSM) so that different segments of the spectral format are moved onto the detector for different exposures. For these gratings a set of pre-specified central wavelengths, corresponding to specific MSM positions (i.e., grating tilts), has been defined. The grating wheel exhibits non-repeatability which is corrected for in post-observation data processing using simultaneously obtained comparison-lamp exposures [Sohn et al., 2011].

The gratings utilised to obtain this dataset were the G430L, covering 290 – 570 nm with a 0.273 nm/pixel dispersion, and the G750L, covering 524 – 1027 nm with a 0.492 nm/pixel dispersion [Sromovsky et al., 2014]. The system throughput of these gratings is displayed in Fig. 2.5.

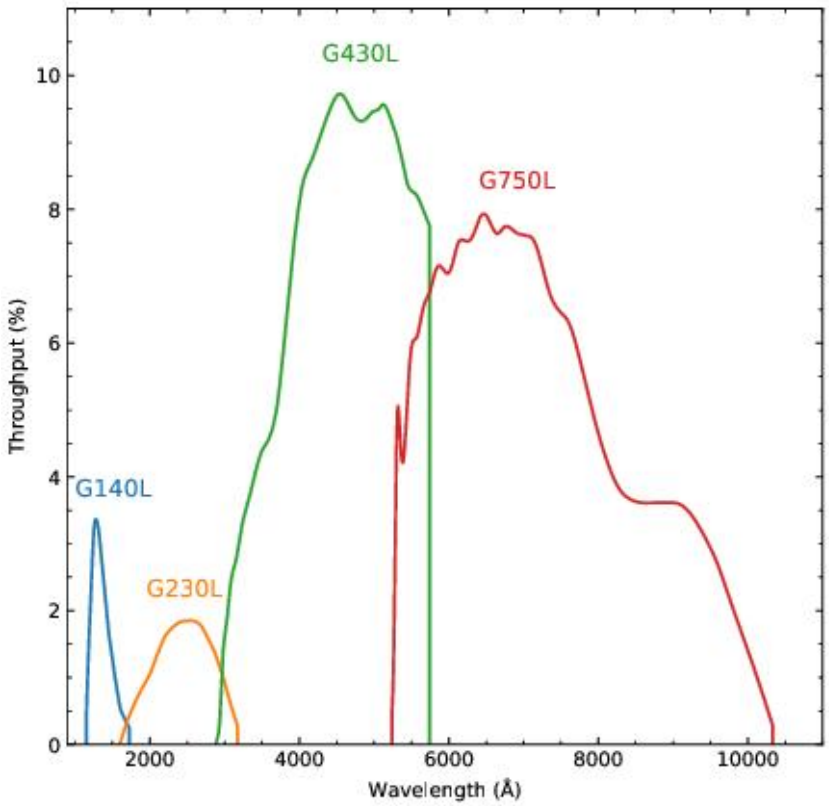


Figure 2.5: A plot of throughput against wavelength in Angstroms for the gratings used by the STIS/CCD. G430L and G750L were the two gratings utilised to obtain the observations in the HST/STIS dataset [Sohn et al., 2011].

2.2.1 Observation Methodology

Observations of Uranus were both made using 4 HST orbits, three of them devoted to STIS spatial mosaics and one orbit devoted to WFC3 support imaging, captured on 27 – 28 September 2012 (2012-09-27-21:38:11 – 2012-09-28-01:15:31 UT) [Sromovsky et al., 2014] and 10 October 2015 (14:09:48 – 17:44:54 UT) [Sromovsky et al., 2019]. STIS is a long-slit spectrometer, but the $52'' \times 0.10''$ long-slit was aligned with the planet's polar axis and stepped across the disc at intervals of $0.152''$ from centre to edge for the G430L grating (because Uranus has no high spatial resolution center-to-limb fea-

tures at these wavelengths, interpolation was used to fill in the missing columns of the mosaic), and stepped by 0.0562″ intervals for the G750L grating, forming a "cube" of half the planet, where at each location on the disc a complete spectrum covering 300.4 – 1020.0 nm was recorded at a resolution of 1 nm, sampled every 0.4 nm.

2.2.2 Data Reduction

To reduce and calibrate the observations, flat-fielded science images, fringe flats, and WAVECALS (exposures of arc sources used for wavelength calibration) from the Space Telescope Science Institude (STScI) STIS data processing pipeline were input into a rather extensive post-processing suite described in Appendix A of Sromovsky et al. [2014], of which a summary is provided here. Firstly, pixels affected by cosmic rays and other defects were identified and cleaned in the images using interpolation. Afterwards, long wavelength fringing was removed from the G750L grating images by dividing by normalised fringe flats, obtained simultaneously with the science observations, with a final correction later applied for slit throughput as a function of the image row. The CCD efficiency of transferring charge is not perfect (typically $\sim$0.99995 instead of 1.0). This results in a point source imaged at the top and bottom of the chip differing in apparent brightness (fainter at the top) due to charge loss (or trapped charge) during the readout, named Charge Transfer Efficiency (CTE) loss. CTE has the added effect of faint sources being more affected than bright ones. In order to obtain the correct "sky" background with respect to the planet's disc, dependent on the telescope's point spread function (PSF) (i.e., the response of a focused optical imaging system to a point source) under ideal conditions, a correction accounting for CTE effects must be applied to the sky background. A column-by-column deconvolution was used to achieve this, following the method of

Karkoschka and Tomasko [2009] used for 2002 HST/STIS observations of Uranus.

Next, in order to correct for scattered light, a spectral image deconvolution was performed, mainly targeting "Red Halo" CCD substrate scattering. This was performed following the method of Karkoschka and Tomasko [2009]. A correction to the distortion of spectral lines, causing them to be curved, was applied using STScI parameters [Sohn et al., 2011], with first-order terms being adjusted according to the 2012 and 2015 measured spectral calibration data [Sromovsky et al., 2014]. Spectral calibration was then performed. The red shift stemming from the motion of Uranus about its orbit was taken into account based on the location being examined, as a result of the changing Earth-Uranus distance and HST's orbit around the Earth. Due to HST being in space, vacuum wavelengths were used for calibration. A spectral resolution adjustment was then performed, with the blue range being smoothed and the red range being slightly sharpened to obtain 1 nm resolution throughout. Spectra are sharper near the limb of Uranus due to the slit not being evenly illuminated, which was also accounted for.

The disc was then navigated, first fitting the red-range data of the acquisition image by convolving it with the spectral sensitivity distribution, moving each slit in both axes to obtain the best fit. The red-range navigation was then adjusted using deep methane absorption bands as a guide. The blue range was navigated by comparing profiles with the red range using overlapping spectral regions [Sromovsky et al., 2014]. At this stage, the aforementioned interpolation to fill in the mosaic was performed, using the same method as Karkoschka and Tomasko [2009], to produce $0.05''$ sampling from the original $0.15''$ sampling. A spatial resampling was then carried out to match that of Karkoschka and Tomasko [2009] (using cubic interpolation), providing an angular scale of $0.0277''$/pixel.

Finally, a deconvolution was performed in order to mitigate the effects of diffraction. The

deconvolution used monochromatic PSFs generated by *Tiny Tim*, a software dedicated to simulating HST PSFs [Krist, 1995], including corrections to account for the lower sample frequency in the slit stepping direction. Features of the HST PSF were removed for each wavelength using this *Tiny-Tim*-generated PSF. The blue (< 530 nm) and red (> 540 nm) ranges of the data were combined following Karkoschka and Tomasko [2009]. The cub-

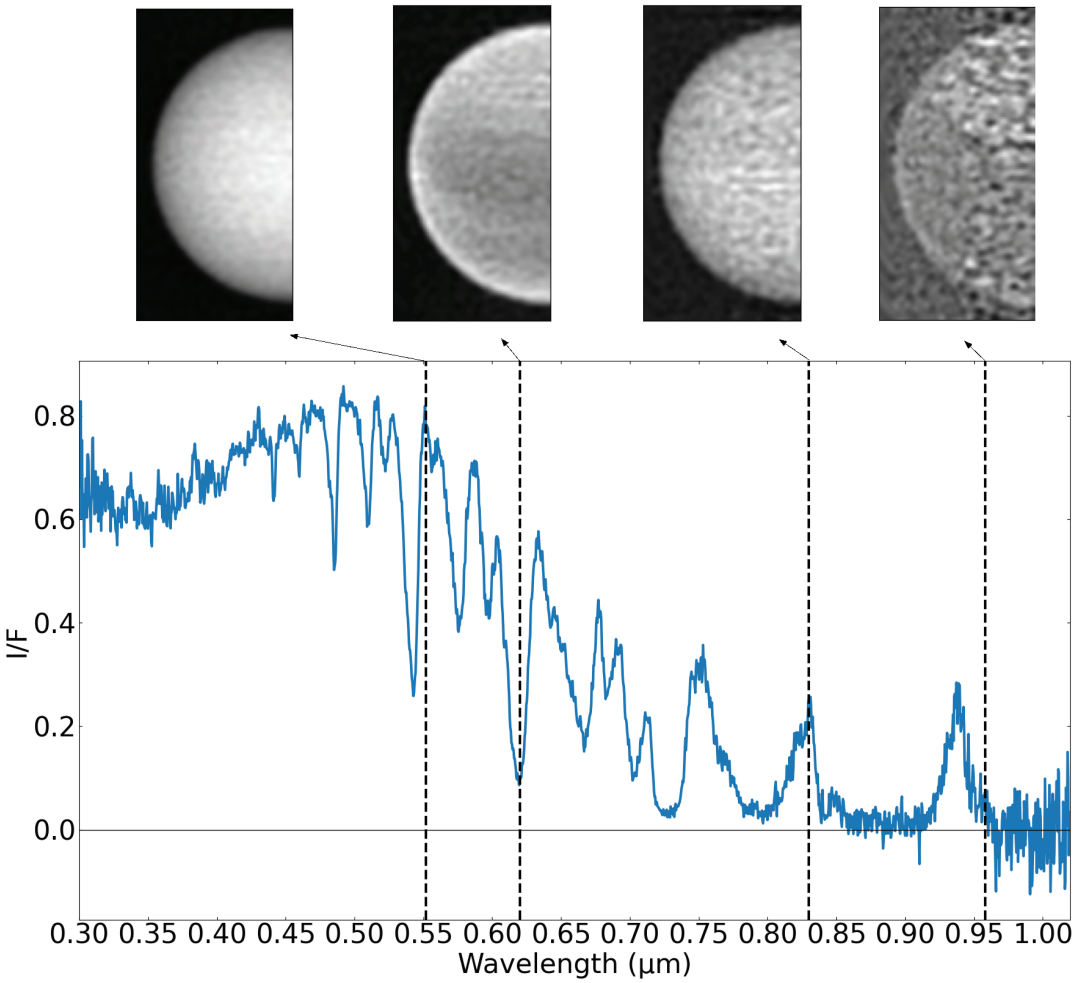


Figure 2.6: A plot of the 2015 HST/STIS reflectivity spectrum extracted from a point at the centre of the disc, demonstrating an increase in noise longwards of $\sim$0.95 μm. Images at 0.552 μm, 0.62 μm, 0.83 μm and 0.958 μm are included, covering representative wavelengths from both methane-absorbing and continuum regions, and visually demonstrating a degradation in image quality.

es produced from this were then photometrically corrected using HST/WFC3 support images. The disc-averaged I/F was found for both images, and by comparing the uncalibrated STIS synthetic disc-averaged I/F to the corresponding WFC3 values, a correction function was constructed to photometrically calibrate the STIS cubes [Sromovsky et al., 2014].

It should be noted that for the 2015 cube, an error in the program resulted in half of the half-disc being covered with STIS's nominal 0.05″ slit instead of the 0.15″ slit. This produced a higher spectral resolution at the cost of a significant reduction in signal to noise ratio. Uranus rotated more than 45° over the course of these observations, resulting in the assumption of a high degree of zonal symmetry in Uranus' atmosphere being embedded from the outset [Sromovsky et al., 2019].

Finally, the 2012 and 2015 observations are both significantly effected by noise longwards of $\sim$0.95 μm, leading to low a signal-to-noise ratio (SNR), demonstrated by Fig. 2.6. As a result, it was decided to omit this region of the spectrum from the analysis to avoid any skewing of our retrieval results.

2.3 VLT/MUSE

The Multi Unit Spectroscopic Explorer (MUSE) is one of many instruments at the European Southern Observatory's (ESO) Very Large Telescope (VLT) facility in Chile. MUSE is a large-format integral-field spectrograph, operating in the nominal (N) 480 – 930 nm wavelength range, with a modular structure composed of 24 identical Integral Field Unit (IFU) modules [Bacon et al., 2010]. MUSE is also capable of being run in extended (E) mode, extending the wavelength range to 465 – 930 nm. The instrument

records 300 × 300 pixel "cubes", where each 3-dimensional pixel, or "spaxel", contains a complete visible/NIR spectrum, boasting a spectral resolving power of between ∼2000 – 4000 [Bacon et al., 2010]. MUSE is endowed with two viewing modes: a Wide-Field Mode (WFM) with a 59.9″ × 60″ FOV, and a Narrow-Field Mode (NFM) with a 7.42″ × 7.43″ FOV, which uses adaptive optics (AO) via four laser guide stars to attain a spatial resolution of < 0.1″ [Bacon et al., 2010]. The 578 – 605 nm region of the spectrum is reserved for the operation of the laser guide stars and is thus excluded from AO observations. It is important to correct for a number of factors at such high spatial resolution, including differential atmospheric refraction between different wavelengths. To achieve this, MUSE uses an atmospheric dispersion compensator that reduces residual shifts between wavelengths to less than a pixel [Bacon et al., 2010]. Observations of Uranus were obtained in 2021 using NFM-AO-N for which a list of observational parameters are given in Table 2.2.

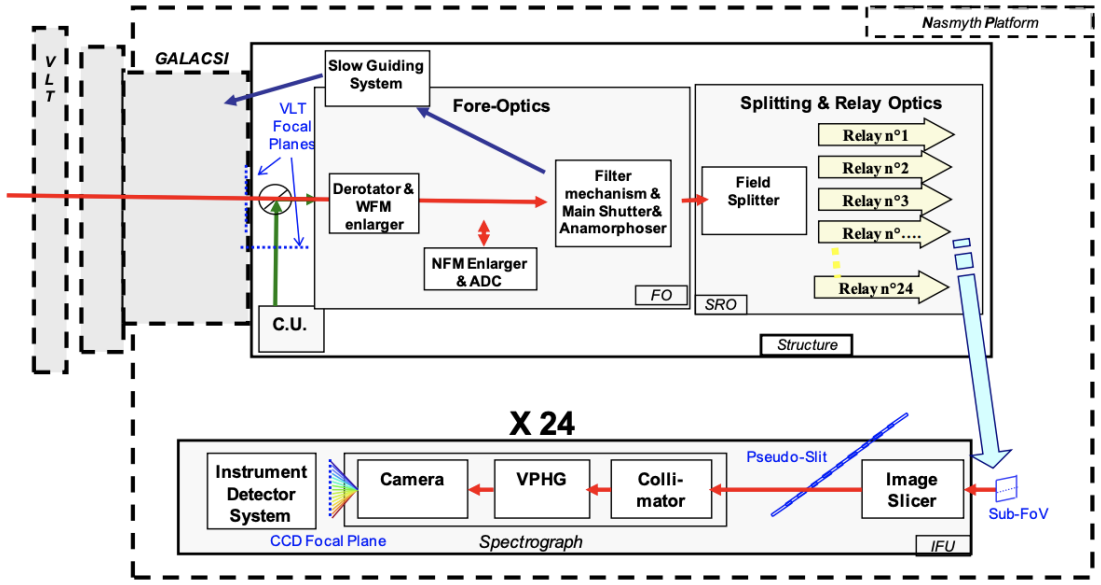


Figure 2.7: A diagram of the MUSE instrument optical setup and its sequence of operation [Bacon et al., 2010].

Table 2.2: VLT/MUSE instrument observational parameters for the nominal Narrow-Field Mode [Bacon et al., 2010].

Simultaneous spectral range	480 – 930 nm
Resolving power	1740 @ 480 nm
	3450 @ 930 nm
Narrow-Field Mode (NFM)	
Field of View	$7.42'' \times 7.43''$
Spatial sampling	$0.025''$/pixel
Spatial resolution (FWHM)	$0.055 - 0.080''$
Strehl ratio @ 0.75 μm	10 – 30%
Limiting magnitude in 1hr	R_{AB} = 22.3 mag
Limiting flux in 1hr	2.3×10^{-21} J.s^{-1}.m^{-2}
Limiting surface brightness in 1hr	R_{AB} = 17.3 mag arcsec^{-2}

2.3.1 Observation Methodology

Observations of Uranus were obtained in NFM-AO-N on 25 October 2021 05:19:29 UT. Due to Uranus' large angular size at this time ($\sim$3.75$''$), exceeding the recommended target size of 3$''$ (enabling robust tracking), the observation had to be carried out in designated visitor mode (reserved for non-typical observation runs) with an AO specialist on hand. The observation was carried out using the Large Scale for the Wavefront Sensor (WFS), equipped with a FOV of $5'' \times 5''$ but still requiring some room for margin within this. WFS was originally designed for observations of the extended cores of galaxies with a gaussian-like profile. For example, to measure an object position at 500 Hz on the WFS, the image is multiplied by a Gaussian whose shape automatically adjusts to the object Gaussian size, the so-called weighted-center-of-gravity (WCOG) method. As Uranus' profile is more of a step function, this WCOG adjustment was disabled and replaced by a simpler threshold of the noisy pixels, whereby all values below 3σ of the Infrared Low Order Sensor (IRLOS) detector noise (sub-electron readout noise) are forced to 0. This method was previously proven in commissioning mode observations of

Neptune to provide much better performance.

2.3.2 Data Reduction

2.3.2.1 Calibration

The MUSE raw data comes in multi-extension Flexible Image Transport System (FITS) files, where each of the 24 CCD images (4224 $\times$ 4240 pixels) is stored in one extension. Uranus observations were collected from ESO's La Silla Paranal data portal with processed calibrations already applied to the raw data via ESO's MUSE calibration pipeline [Weilbacher et al., 2020]. A summary of the calibration for the relevant NFM-AO-N observations is given below, described by Weilbacher et al. [2020], for which a flow chart of the full calibration pipeline is displayed in Fig. 2.8 for reference.

First a basic processing is performed. The input to this first step is the raw Uranus exposure, along with its corresponding illumination flat-field exposure, and several calibration files covered below. A pre-reduced pixel table is the final output of this basic processing.

Each individual CCD performs the following process internally, such that it is repeated 24 times. The image is loaded from the raw data and saturated pixels are automatically detected and marked (values = 0 or $>$ 65,500). Overscan regions of the CCDs are then analysed, determining a bias correction prior to the subtraction of the master bias image. The units of the CCD are then converted to electrons using the CCD gain. The master dark is then subtracted from the science image to provide a dark correction, which is then divided by the master lamp flat-field image. The twilight sky cube is then used to propagate the relative IFU flux level. A pixel table for the science image was then created by assigning coordinates to each CCD pixel. This is achieved using the requisite input

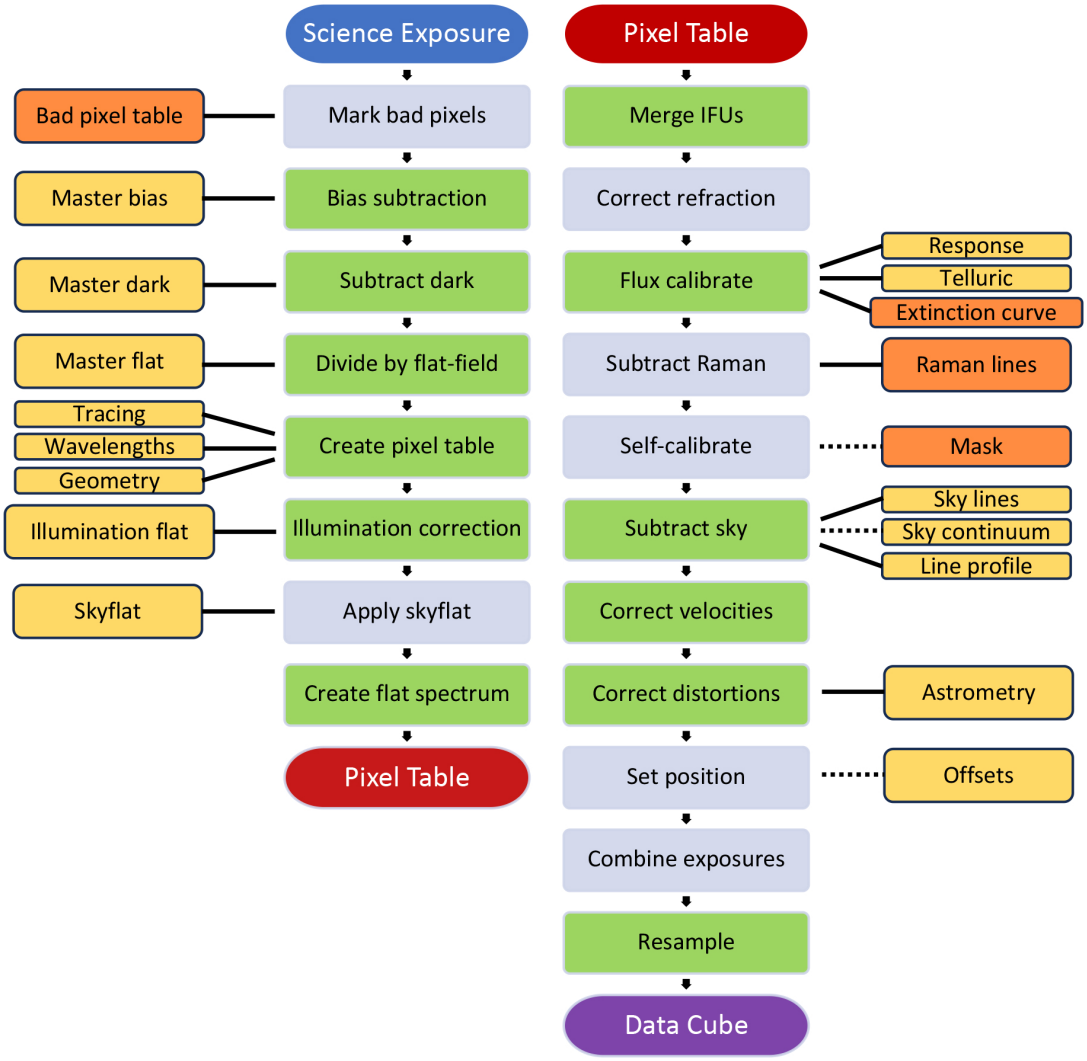


Figure 2.8: Flow charts displaying the full step-by-step process involved in ESO's MUSE data calibration pipeline [Weilbacher et al., 2020]. *Left:* Shows the basic processing from raw science data to the intermediate pixel table. *Right:* Shows the post-processing from the pixel table to the final data cube. The steps performed in the calibration of our dataset are highlighted in green; additional optional steps within the pipeline are highlighted in light grey. Manually created input files are highlighted in orange; calibration files are highlighted in yellow. Inputs that are required are connected with solid lines, and inputs that are not required are connected with dotted lines. Flow charts are adapted from Fig. 1 of Weilbacher et al. [2020].

calibrations, wavelength calibration table, geometry table and trace table. The pixel table is then cropped to the useful wavelength range, in this case 480 – 930 nm.

A pixel table is also created for the raw illumination flat-field exposure using the same steps as for the science image. This exposure is then used to determine a correction for the relative illumination between all slices of one IFU [Weilbacher et al., 2020]. This correction removes achromatic variations of the illumination, due to the image slicer illumination varying with temperature and time during a night of observation, greatly improving the uniformity of the flux across the field [Weilbacher et al., 2020]. To finalise the basic science processing, the master twilight sky cube (collected at evening twilight) is interpolated to the coordinate of each pixel in the pixel table. The pixel table is then corrected by dividing by this interpolated twilight sky cube, removing the contribution of the sky brightness.

Following the basic processing, a science post-processing is carried out, taking the pre-reduced pixel tables as input and outputting the reduced data cube.

Firstly, a single table is created by merging the pixel tables from all IFUs, accounting for the relative efficiency of each IFU (measured from twilight sky exposures) [Weilbacher et al., 2020]. All lamp-flat spectra were averaged, with the resulting lamp-flat mean spectrum being smoothed over features such as interference filter fringes and telluric absorption, preventing the small-scale variations corrected for by flat-fielding being reintroduced. The science image is subsequently divided by this smoothed mean lamp-flat spectrum. NFM has a built-in atmospheric dispersion corrector (ADC), meaning no correction is necessary to account for this. The merged pixel table is then flux calibrated to convert the pixel table into units of flux, utilising an atmospheric extinction curve. Afterwards, a telluric correction spectrum is applied to account for atmospheric absorption.

Sky lines and line profile calibration files are then used to carry out sky subtraction. The sky spectrum that is subtracted is reconstructed by feeding in the fraction of the exposure that is sky-dominated to the pipeline. The motion of the telescope (i.e., its radial velocity with respect to Uranus) is then corrected for. The astrometric calibration file is then used to correct the spatial coordinates, transforming the pixel table into spherical coordinates via a linear transformation, rotation, and then a spherical projection. The spherical coordinates are then rotated onto the celestial coordinates of the observed centre of the field [Weilbacher et al., 2020]. The final step is to resample the data from the exposure into a data cube. A drizzle-like algorithm [Fruchter and Sosey, 2009] is used to conserve the flux during this process [Weilbacher et al., 2020]. This combines multiple dithered exposures (images taken with slight offsets) into a single, high-resolution image with improved sampling and reduced noise. Drizzle distributes pixel values based on their fractional overlap with output pixels, preserving flux and reduces artificial edge effects.

2.3.2.2 Deconvolution

The calibrated observations were then deconvolved using the MODIFIED-CLEAN deconvolution algorithm developed by Dr. Jack Dobinson, and described in detail by Irwin et al. [2023a]. This algorithm was successfully applied to Neptune MUSE observations, enabling the first ground-based observation of a dark spot within its atmosphere [Irwin et al., 2023a].

The MODIFIED-CLEAN algorithm is an altered version of the CLEAN deconvolution algorithm [Giovannelli and Coulais, 2005], whereby instead of selecting only the brightest pixel in a given image, it selects all pixels above a given threshold, t_s, treating each

one as an extended source. The iterative scheme for MODIFIED-CLEAN is given by Eqn. 2.1

$$\begin{aligned} \tilde{O}_0(\underline{x}) &= \underline{0}, \\ I_n(\underline{x}) &= I(\underline{x}) - (R * \tilde{O}_n)(\underline{x}), \\ x_s &= \{x_i; I_n(x_i) > t_s; x_i \in \underline{x}\}, \\ \tilde{O}_{n+1}(\underline{x}) &= \tilde{O}_n(\underline{x}) + g_{loop} I_n(x_s) \end{aligned} \tag{2.1}$$

where $\tilde{O}(\underline{x})$ is an estimate of the true signal, i.e., what we would measure with a perfect instrument, $\underline{x}$ is a vector defining the position of a pixel, $R(\underline{x})$ is the response function, i.e., the PSF, $I(\underline{x})$ is the observational data recorded by the instrument, i.e., $\tilde{O}(\underline{x})$ after passing through $R(\underline{x})$ and being degraded by noise, $I_n(\underline{x})$ is the data after the n^{th} iteration of the deconvolution, and g_{loop} is the loop-gain, i.e., the fraction of the brightest pixel added to the components, $\tilde{O}(\underline{x})$, at each iteration, which was set to 0.5.

Due to the unique nature of the measurement (i.e., a large, bright object with angular diameter exceeding MUSE's recommended size), a standard-star observation was not simultaneously obtained. The PSF was therefore simulated using the work of Fétick et al. [2019] as a guide, modelling the power spectral density of the atmosphere plus AO system, finding the optical transfer function (OTF) of that system, and combining it with the telescope's non-AO diffraction limited OTF to return the combined PSF. This PSF was then normalised, such that it summed to 1, had an odd number of rows/columns, was centered on the brightest pixel, and contained no undefined numbers (NaNs), infinities (INFs), or negative values. Before deconvolving the observation, the cube was interpolated over any NaNs and INFs using python's *scipy.interpolate.griddata* package, and

finally passed through a singular spectrum analysis (SSA) filtering algorithm [Ghil et al., 2002] to remove artefacts from the image.

The threshold t_s was then determined by choosing an initial threshold, t_i, from successive applications of '*Otsu*' thresholding [Otsu, 1996, Sankur and Sezgin, 2004]. This technique divides a set into two different classes (bright and dark) by choosing a dividing threshold, t_{otsu}, in such a way that the variance between the two classes is minimised [Otsu, 1996]. A factor was then applied, t_{factor}, manually set to 0.3, to the interval between t_i, which was set to -1 here, and the maximum of the data, leading to Eqn. 2.2.

$$t_s = max[I_n(\underline{x})]t_{factor} + (1 - t_{factor})t_i \tag{2.2}$$

MODIFIED-CLEAN was then run, with the completion criteria being set to when the root mean square (RMS) value of the residual is reduced to 1% of the original value, or the absolute brightest pixel is reduced to 1% of the original value, or 5,000 iterations are reached [Irwin et al., 2023a]. One of the main objectives of the MODIFIED-CLEAN algorithm is to remove the 'halo glow' of the AO system [Irwin et al., 2023a]. Therefore, once the deconvolution is complete, the usual practice of reconvolving the final CLEAN-components with a 'clean beam' was not performed. Circumventing this step avoids our Minnaert limb-darkening fits to the deconvolved data being adversely effected. A comparison of the standard calibrated observation to the deconvolved observation at 0.615 μm is shown in Fig. 2.9.

Finally, a latitude-longitude grid was fitted to the deconvolved disc using a disc-fitting routine within MODIFIED-CLEAN, enabling the extraction and analysis of individual latitude bands to be performed.

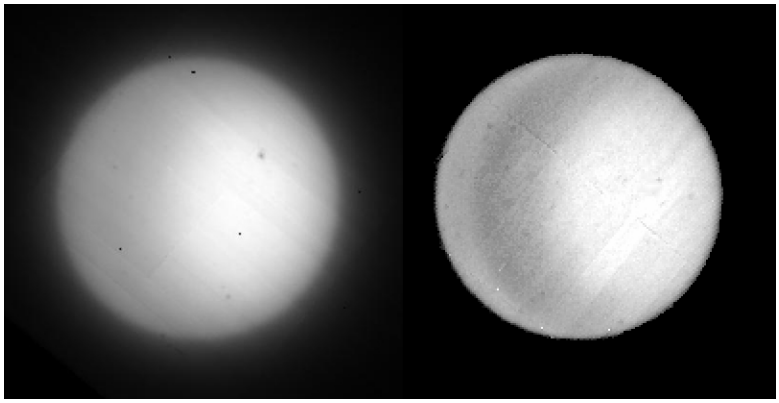


Figure 2.9: A comparison of the 0.615 μm standard calibrated MUSE observation of Uranus (*left*) with the same image deconvolved using the MODIFIED-CLEAN algorithm (*right*).

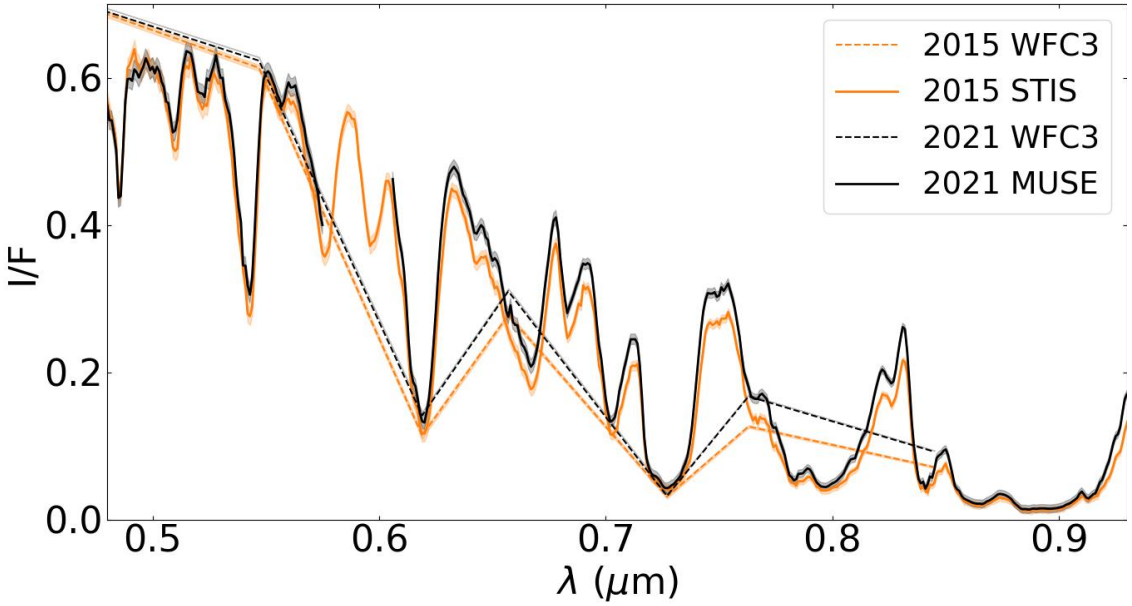


Figure 2.10: A comparison of the disc-averaged HST/WFC3 (2015 & 2021), HST/STIS (2015) and VLT/MUSE (2021) datasets. It can be seen that there is good agreement between the reflectivity values, suggesting accurate calibrations of each dataset.

The three datasets are plotted together in Fig. 2.10 for easy comparison, demonstrating the consistency between the results of the different data processing and calibration pipelines.

Chapter 3

Radiative Transfer & Retrieval Theory

At the core of the work carried out in this investigation lies the general purpose radiative transfer and retrieval code NEMESIS, the **N**on-linear optimal **E**stimator for **M**ultivariat**E** spectral analy**SIS** [Irwin et al., 2008]. NEMESIS was utilised to perform atmospheric retrievals, the process of retrieving the atmospheric properties of a planet from an observed spectrum. Therefore, an in depth review is presented here of the background theory of radiative transfer, the physics underlying the transfer of electromagnetic (EM) radiation and its interaction with matter, and retrieval theory, the statistical methods and physics (e.g., radiative transfer) underlying retrievals. Finally, a relevant description of NEMESIS is given, along with the methods used to perform the retrievals in this work.

3.1 Radiative Transfer

3.1.1 Origin of the Spectrum

To retrieve the atmospheric properties of a planet, one first needs observational data in the form of a spectrum, i.e., a profile of intensity against wavelength (frequency) for the EM radiation stemming from the target atmosphere. For the planets of the Solar System, this is typically dominated by reflected sunshine at visible wavelengths. Each atmospheric spectrum contains a unique set of absorption (and emission) features, which, as a consequence of being caused by the interaction between light and the constituent molecules of the atmosphere, act as a fingerprint for the atmosphere's chemical composition.

EM radiation undergoes absorption, emission and scattering as it passes through an atmosphere, altering its original state in vacuum. Each type of molecule within a given atmosphere possesses a number of energy modes, each with its own discrete energy levels, and each containing varying degrees of freedom, which almagamate to define an individual molecule's energy state at a given time. These are the electronic, vibrational and rotational energy modes. Each of these modes operates at a different energy scale (i.e., the energy delta between energy levels are at different scales) and is characterised by different processes. In general, the electronic modes have energy level differences equivalent to photon energies in the near-UV and visible portion of the EM spectrum, and they occur when the electrons of the molecule's atoms are excited or de-excited to different energy states; the vibrational modes have energy level differences corresponding to photon energies in the IR region of the spectrum, and they occur when the bending and stretching patterns of the bonds between the atoms in the molecule change; the rotational modes have energy level differences corresponding to photon energies in the

far-IR/microwave region of the spectrum, and they occur when the rotation about a given axis of the molecule changes. These modes are largely independent and are altered by the absorption or emission of photons with energies equivalent to the energy delta between the different states of the given mode.

A photon is able to impact different energy modes at the same time for a given interaction (i.e., an absorption or emission), leading to, for example, vibrational-rotational modes. For the visible/NIR observations of Uranus considered in this investigation, these vibrational-rotational modes dominate the spectrum, and therefore play an important role in the fitting process. Note, molecules also possess translational energy, i.e., motion in each of the three spatial dimensions, which is continuous as opposed to discrete. This energy can lead to a broadening of spectral features as a result of the apparent change in wavelength (frequency) of an EM wave with respect to a moving observer, termed the Doppler effect. This requires motion with respect to the line of sight of the observer and is dubbed Doppler broadening. At the cool temperatures ($\sim$50 – 100 K) found in Uranus' upper troposphere, the Doppler broadening effect is weak. The presence of other molecules in a gas, leading to collisions and interactions between molecules via small-scale forces (e.g., Van der Waals forces), also leads to a broadening effect, dubbed pressure broadening.

3.1.1.1 Collision-Induced Absorption

In addition to the absorption features associated with vibrational-rotational energy transitions via the absorption of visible and NIR photons, inelastic collisions between molecules can also induce the absorption of photons. In the gas phase, collisions between molecules often induce transitory dipole moments within homonuclear diatomic molecules (e.g.,

H_2) that are otherwise unable to interact with EM radiation. These transitory dipole moments enable the molecules to temporarily interact with IR photons, leading to absorption. Due to Heisenberg's uncertainty principle, the short-lived nature of these induced dipoles leads to a broad wavelength (frequency), smooth absorption profile. This phenomenon is known as collision-induced absorption (CIA). CIA is typically weak, however, if the abundance of the homonuclear diatomic molecule is large, CIA can become significant in the NIR region of the spectrum [Irwin, 2009]. In the case of Uranus, the abundance of H_2 in the observable atmosphere is large ($\sim$85%), and the abundance of He is significant ($\sim$15%), such that H_2-H_2 and H_2-He collisions produce significant absorption in the NIR region [Irwin, 2009]. As described in Section 1.3.6, CIA is a key determinant in Karkoschka and Tomasko [2009]'s method of distinguishing cloud-top methane (CH_4) mixing ratio from variations in aerosol opacity.

3.1.1.2 Rayleigh Scattering

In addition to the absorption of photons, the scattering of light also occurs within atmospheres. Scattering of photons can either be elastic (i.e., the kinetic energy of the photon is conserved), or inelastic (i.e., kinetic energy of the photon is not conserved). The elastic scattering of photons from particles of much smaller size than the wavelength of light is dubbed Rayleigh scattering. This originates from the polarisability of the 'air' molecules, enabling an electric dipole to be induced that radiates at the same wavelengths (frequency) as the incident light. This results in radiation being emitted at the same wavelength (frequency), which is the scattered light that is observed. As a result of Rayleigh scattering being inversely proportional to the fourth power of the wavelength of incident light (i.e., $\propto \lambda^{-4}$), it dominates at the blue end of the spectrum before dropping off rapidly at longer wavelengths.

3.1.1.3 Raman Scattering

The inelastic scattering of photons is termed Raman scattering. This type of scattering occurs when the absorption of a photon excites a molecule into a higher energy state, which in turn relaxes back to a state that differs from the original mode. Raman scattering effects can usually be neglected, being significant only in the UV region of the EM spectrum. However, in the case of Uranus, identifiable solar spectrum features are observed as being shifted to longer wavelengths in the spectrum of its atmosphere due to Raman scattering associated with rotational transitions of H_2 molecules [Sromovsky and Fry, 2005]. As our observations are in the visible/NIR, Stokes Raman scattering, whereby scattered photons are of longer wavelength than incident photons, are important. Raman scattering originating from UV photons causes a cascade effect to longer wavelengths, with the scattered photons that are of longer wavelength also undergoing Raman scattering themselves, producing even longer wavelength scattered photons. This results in the effect becoming significant up to $\sim$0.55 μm, meaning it must be accounted for when analysing the datasets used in this investigation.

The polarisation of the incident light is also an important factor when considering Raman scattering. Polarised light places limitations on the accessible Raman modes, resulting in a lesser effect [Sromovsky and Fry, 2005]. For example, unpolarised light (i.e., light polarised randomly in all directions) enables all modes of Raman scattering to be accessible, whereas light polarised in a single direction restricts the accesible modes, resulting in a lesser effect and, in turn, a weaker signature in the observed spectrum. It is therefore important that polarisation is also accounted for.

3.1.2 Radiative Transfer Equation

By adopting a few simple assumptions and approximations, an equation can be derived to describe radiative transfer within an atmosphere. Such an equation takes the incoming radiance (i.e., the radiant flux per unit solid angle) at the top of the atmosphere and returns the outgoing radiance exiting the top of the atmosphere. A very simple radiative transfer equation (RTE) can be derived by adopting the following assumptions: 1) only single scattering of photons occurs within the atmosphere, 2) the absorption coefficient of the atmosphere has no dependence on wavelength (frequency), 3) for radiation that is emitted from the atmosphere at angles close to the vertical (near-nadir viewing), the atmosphere can be approximated as plane-parallel (i.e., composed of flat parallel layers), and 4) local thermodynamic equilibrium (LTE) exists (i.e., temperature varies in space and time slowly enough such that, for a given point, it is in equilibrium in some local neighborhood about that point). These are collectively known as a 'gray' atmosphere, and lead to the RTE (Eqn. 3.1)

$$I_{\tilde{\nu}_1}(\mu) = I_{\tilde{\nu}_0} T_{\tilde{\nu}}(\mu, z_0, z_1) + \int_{z_0}^{z_1} B_{\tilde{\nu}}(z) \frac{dT_{\tilde{\nu}}}{dz} dz \tag{3.1}$$

where $I_{\tilde{\nu}_1}$ is the spectral radiance leaving the top of the atmosphere, $\mu = cos\theta$, where θ is the angle to the vertical or zenith angle, $I_{\tilde{\nu}_0}$ is the spectral radiance incident upwards at altitude z_0 and angle θ, $T_{\tilde{\nu}}$ is the transmission from z_0 to z_1 at angle θ, $B_{\tilde{\nu}}$ is the Planck function at wavenumber $\tilde{\nu}$ and altitude z where the temperature is $t(z)$, and the derivative of the transmission with respect to z is known as the transmission weighting function [Irwin, 2009].

Nadir (θ = 0) or near-nadir viewing geometries provide low vertical resolution with a full

width at half maximum (FWHM) roughly equal to the pressure scale height. This becomes an issue for probing the profiles of gas abundances that vary quickly with altitude. One way to increase vertical resolution is to view the limb of the planet. The RTE is very similar to the previous one, but instead we integrate directly along the path l [Irwin, 2009].

$$I_{\tilde{\nu}_1} = \int_{l_0}^{l_1} B_{\tilde{\nu}}(l) \frac{dT_{\tilde{\nu}}}{dl} dl = \int_{z_0}^{z_1} B_{\tilde{\nu}}(z) K'_{\tilde{\nu}} dz \tag{3.2}$$

$$K'_{\tilde{\nu}} = \frac{dT_{\tilde{\nu}}}{dl} \frac{dl}{dz}$$

As well as increasing vertical resolution, limb-viewing makes the detection of trace atmospheric gases much easier since the path lengths are much longer. The downside is that the plane-parallel approximation is no longer valid, and it places more constraints on the telescope being used, i.e., we need an orbiting spacecraft with good pointing accuracy and a narrow field of view [Irwin, 2009].

In the case of a real atmosphere, photons can be scattered multiple times, negating the assumption of single scattering only. Eqn. 3.1 must therefore be altered to account for this, giving a multiple-scattering RTE (Eqn. 3.3)

$$\mu \frac{dI_{\tilde{\nu}}(\tau_{\tilde{\nu}}, \mu, \phi)}{d\tau_{\tilde{\nu}}} = I_{\tilde{\nu}}(\tau_{\tilde{\nu}}, \mu, \phi) - \frac{\varpi_0(\tau_{\tilde{\nu}})}{4\pi} \int_0^{2\pi} \int_{-1}^{1} p(\tau_{\tilde{\nu}}; \mu, \phi; \mu', \phi') I_{\tilde{\nu}}(\tau_{\tilde{\nu}}, \mu', \phi') d\mu' d\phi' \tag{3.3}$$

where thermal emission is assumed to be negligible and $I_{\tilde{\nu}}$ is the radiance, $\tau_{\tilde{\nu}}$ is the optical depth of the atmosphere, $\varpi_0(\tau_{\tilde{\nu}})$ is the single-scattering albedo for aerosols and

gas at a particular level in the atmosphere, $p(\tau_{\tilde{\nu}}; \mu, \phi; \mu', \phi')$ is the phase function at the atmospheric level of optical depth $\tau_{\tilde{\nu}}$, incident zenith angle defined by $\mu' = \cos\theta'$, where θ' is the zenith angle, and incident azimuth angle, ϕ', and scattered in the direction described by $\mu = \cos\theta$ and ϕ, where θ is the zenith angle [Irwin, 2009].

3.1.2.1 Line-by-line Method

In order to solve the RTE (Eqn. 3.3), one first needs a model atmosphere of the target planet containing the vertical abundance profiles of the gases measured from available data sources (or informed guesses if data is not available). For this model, the positions and strengths of each of the absorption lines for every gas within the model is needed. Given the absorption coefficients of the numerous gases and aerosols within the atmosphere, the emerging radiance can be calculated. As the line strengths and linewidths are functions of both temperature and pressure, and since atmospheres are inhomogeneous in both of these, the monochromatic transmission at wavenumber $\tilde{\nu}$ of a path through an atmosphere [$T_{12}(\tilde{\nu})$], between two levels z_1 and z_2, at zenith angle θ is given by

$$T_{12}(\tilde{\nu}) = exp\left(-\frac{1}{\mu}\int_{z_1}^{z_2} n(z)\left(\sum_j q_j(z)\sum_i k_{ij}(\tilde{\nu}, p(z), T(z))\right)dz\right) \tag{3.4}$$

where $n(z)$ is the number density of the atmosphere at altitude z, $p(z)$ is the atmospheric pressure at altitude z, $T(z)$ is the atmospheric temperature at altitude z, $q_j(z)$ is the mole fraction of gas j at altitude z, the summation over i is over all the absorption lines of gas j that contribute to the optical depth at wavenumber $\tilde{\nu}$, and k_{ij} are the absorption coefficients, dependent on wavenumber, pressure and temperature. Databases exist (e.g., HITRAN [Rothman et al., 2005]) that contain lists of the molecular absorption lines for different gases. For each line of each gas, k_{ij} must be calculated from the line strengths

and lineshape, both functions of temperature and pressure. Though they are very accurate, since thousands of absorption lines may contribute to the absorption at a particular wavelength, line-by-line calculations are computationally expensive and relatively slow.

The absorption coefficient $k(\nu)$ is a rapidly varying function of ν; therefore a very small step size in ν is required to accurately calculate the mean transmission. When calculating the mean transmission within a spectral interval, however, the parts of the interval that are highly or poorly absorbing do not matter, only their fraction. Thus, we can reorder the coefficients from low absorption to high absorption without changing the integral. The resulting spectrum is called the k-distribution, $k(g)$, and is a smoothly varying function of g, which is the fraction of the spectral interval, varying between 0 and 1 (e.g., Irwin [2009]). This leads to the mean transmission $\bar{T}(m)$

$$\bar{T}(m) = \int_0^1 e^{-k(g)m} dg \simeq \sum_{i=1}^{N} e^{-k_i m} \Delta g_i \tag{3.5}$$

where m is the absorber amount (i.e., number density), k_i is the k-distribution calculated at each of the N quadrature points, and Δg_i are the quadrature weights [Irwin, 2009]. The quadrature points and weights here use the Gauss-Legendre quadrature scheme [Goody and Yung, 1989]. The gaussian quadrature summation here is approximately equal to the integral when generalised in the limit of small intervals [Lacis and Oinas, 1991]. Once the wavelength range and resolution of the data being forward-modelled is known, the k-distributions can be calculated for the gases found in a given planetary atmosphere at a range of pressures and temperatures, and stored in look-up tables for quick calculation. However, it is important to note that when using these k-tables for several gases, a given spectral interval may contain lines from several different gases, which may or may not be

spectrally correlated. If there is no spectral correlation between the lines of the different gases, the k-tables can be combined together in a straightforward manner (i.e., multiplying each gas' k-distribution by its path amount and re-ordering the absorptions in order of increasing strength [Eqn. 3.6]). For the case where the lines are spectrally correlated, however, this combining of the k-tables only provides an approximation, resulting in a degree of uncertainty entering the picture. In the work carried out later in this thesis, only CH_4 and hydrogen CIA are significant sources of gaseous absorption in the region of Uranus' atmosphere being probed, meaning there is no need to combine k-tables.

Observational spectra have limited spectral resolution due to instrument limitations, meaning the transmissions calculated above need to be integrated over the instrument function [Irwin, 2009]. For cases in which the resolution does not justify a full line-by-line treatment, we can use k-distributions to reduce calculation times. However, when calculating the transmission for inhomogeneous atmospheres (e.g., the atmosphere of Uranus) using k-distributions, we need to combine the k-distributions of the component sub-paths using the correlated-k approximation, described in the following section.

3.1.2.2 Correlated-k Approximation

The correlated-k method approximates the mean transmission calculation for a path of absorber amount (number density) m in an inhomogeneous atmosphere (e.g., Irwin [2009]). To find the transmission of an inhomogeneous path, we split it up into smaller sub-paths, with each being individually approximated as being homogeneous. The correlated-k approximation assumes that the high and low absorbing parts of the k-distributions of the different sub-paths are correlated with each other, hence, they can be multiplied together as though they were monochromatic to determine the mean trans-

mission of the inhomogeneous path [Irwin, 2009]

$$\bar{T} \simeq \sum_{i=1}^{N} exp\left(\sum_{j=1}^{M} k_{ij} m_j\right) \Delta g_i \tag{3.6}$$

where the path has been split into M sub-paths.

The correlated-k approximation is typically found to have a similar accuracy to other approximation models (e.g., the band model approximation), with a huge advantage being that thermal emission, as well as scattering calculations, can also be summed in the same way [Irwin, 2009].

3.1.3 Mie Theory

Mie theory was developed in 1908 to describe electromagnetic scattering by homogeneous spherical particles [Mishchenko and Travis, 2008]. In order to accommodate photon scattering interactions of spherical particles in an atmosphere in the general case, Mie theory was adopted. The probability that a photon is scattered in a particular direction is described by a function named the phase function $p(\theta)$. Regardless of direction, the probability that a photon is absorbed or scattered by a particle depends on the absorption and scattering cross-sections, σ_{abs} and σ_{sca}, of the particle. These both depend on a number of parameters including the particle composition, mean particle radius, particle shape and wavelength of light (λ). The extinction cross-section is given by the formula $\sigma_{ext} = \sigma_{sca} + \sigma_{abs}$, and the single-scattering albedo ϖ is found from the ratio below [Irwin, 2009].

$$\varpi = \frac{\sigma_{sca}}{\sigma_{ext}} \tag{3.7}$$

When the particle size is much smaller than λ, Rayleigh scattering occurs, where scattering particles typically behave as simple dipoles. Dipole scatterers have zero absorption cross-sections and are therefore purely scattering, with scattering cross-sections proportional to λ^{-4} [Irwin, 2009]. When λ is of comparable size to the particle, the calculation of $p(\theta)$ and σ_{ext} becomes complex. Given spherical, liquid aerosols and knowledge of the complex refractive index $(n_r + in_i)$ as a function of λ, we can use Mie theory to solve Maxwell's equations analytically and determine the scattering properties. This enables the calculation of Q_{ext}, i.e., the ratio between the extinction cross-section and the geometric cross-sectional area of the particles, ϖ, and $p(\theta)$, all as functions of λ.

For the case of non-spherical particles, e.g., ice crystals, a number of methods exist for calculating the scattering properties. In reality, to first order, when ice crystals are randomly oriented, they are largely indistinguishable from spherical aerosols with identical mean radius [Irwin, 2009]. If the ice crystals align though, e.g., due to dynamics, the approximation breaks down. No simple expression for $p(\theta)$ exists for the case of non-spherical or spherical particles. Having a simple form representing $p(\theta)$ that utilises parameterisation, however, can be useful. Radiative transfer models can then use this to approximate the real phase functions of the particles [Irwin, 2009]. The double Henyey-Greenstein (HG) representation, shown in Eqn. 3.8, is an example of this

$$p(\theta) = \left\{ f \frac{1 - g_1^2}{(1 + g_1^2 - 2g_1 cos\theta)^{3/2)}} + (1 - f) \frac{1 - g_2^2}{(1 + g_2^2 - 2g_2 cos\theta)^{3/2}} \right\} \tag{3.8}$$

where g_1 is the asymmetry of the forward-scattering lobe (varying between 0 and 1), g_2 is the asymmetry of the back-scattering lobe (varying between 0 and -1), and f is the fractional contribution of the forward-scattering part (between 0 and 1). The NEMESIS

retrieval code, used for this investigation, approximates phase functions using these double HG phase functions. This not only reduces computation time but also averages over phase function features such as the rainbow and glory that we do not expect to see from non-spherical randomly-oriented ice particles [Irwin, 2009].

3.1.3.1 Kramers-Kronig Relations

In order to find the complex refractive index as a function of λ, allowing the application of Mie Theory, we make use of the Kramers-Kronig relations. These are bidirectional mathematical relations connecting the real and imaginary parts of a complex function that is analytic. In atmospheric physics, these relations can be applied to calculate the refractive index of an aerosol layer. By assuming the value of the real part of the refractive index at some reference wavelength, we can retrieve the aerosol's absorption coefficient $\kappa(\lambda)$ as a function of wavelength [equivalent to the imaginary refractive index, $n_i(\lambda)$], and use these relations to reconstruct the real refractive index (n_r) spectrum in the relevant wavelength range. This is an important parameterisation that contains the absorption characteristics of the retrieved aerosols within a NEMESIS model, revealing at which wavelength ranges they are more or less absorbing, where a smaller value for κ (n_i) indicates less absorption. These relations were utilised to develop the imaginary refractive index spectra within the holistic vertical aerosol model for Uranus [Irwin et al., 2022, 2023a]. They are also employed in the retrieval work of this thesis to examine the spatial and temporal variability of the imaginary refractive index spectra.

3.2 Retrieval Theory

Retrieval theory describes the inverse method underlying the 'retrieval' approach of analysing a spectrum to produce an atmospheric model. It is known as an 'inverse' method as it involves reverse-engineering the measured spectrum to determine the characteristics of its root cause, the atmosphere. The atmospheric models produced include parameters such as the vertical profiles of composition, aerosol structure and temperature to name a few. The general approach makes use of 'forward-modelling', the practice of producing a synthetic spectrum for a model atmosphere as seen from the observer (a telescope in space or on the surface of the Earth). This synthetic spectrum can then be compared to the observed spectrum, with the essence of retrieval theory being to minimise the difference between these two spectra. This is achieved by altering the atmospheric model (composition, temperature, aerosol distribution, etc.), producing a new synthetic spectrum with this updated model and again comparing this to the observed spectrum, and iterating until specific convergence quality criteria are achieved.

For a set of radiances represented by the measurement vector $\mathbf{y}$, i.e., containing the observed spectrum, with errors defined by the vector ϵ, we can define a state vector $\mathbf{x}$ representing the atmospheric conditions to be retrieved at each level of the atmosphere (i.e., composition, temperature etc.). The forward model $\mathbf{F}(\mathbf{x}_n)$, encapsulating the physics of the atmosphere and measurement [Rodgers, 2000], thus relates $\mathbf{x}$ to $\mathbf{y}$ via Eqn. 3.9.

$$\mathbf{y} = \mathbf{F}(\mathbf{x}) + \epsilon \tag{3.9}$$

It is convenient to linearise the problem about a reference state $\mathbf{x}_0$ [Rodgers, 2000]. This

can be achieved by performing a Taylor expansion of Eqn. 3.9, leading to Eqn. 3.10

$$\mathbf{y} - \mathbf{F}(\mathbf{x}) = \frac{\partial \mathbf{F}(\mathbf{x})}{\partial \mathbf{x}}(\mathbf{x} - \mathbf{x}_0) + \epsilon = \mathbf{K}(\mathbf{x} - \mathbf{x}_0) + \epsilon \tag{3.10}$$

where $\mathbf{K}$ is the Jacobian or kernel, an $m \times n$ matrix containing the partial derivatives of each forward model element with respect to each state vector element [Rodgers, 2000]. With the kernel in hand, we can use a least-squares approach to minimise the difference between the forward model and the measured spectrum by minimising a 'cost function', ϕ

$$\phi = (\mathbf{y} - \mathbf{F}(\hat{\mathbf{x}}))^T \mathbf{S}_\epsilon^{-1} (\mathbf{y} - \mathbf{F}(\hat{\mathbf{x}})) \tag{3.11}$$

where $\mathbf{S}_\epsilon = E\{\epsilon\epsilon^T\}$ is the error covariance matrix (where E is the expected value operator), and $\hat{\mathbf{x}}$ is an approximation to $\mathbf{x}$, the true state vector [Rodgers, 2000]. The solution to $\hat{\mathbf{x}}$ is then given by Eqn. 3.12

$$\begin{aligned} \hat{\mathbf{x}} &= (\mathbf{K}^T \mathbf{S}_\epsilon^{-1} \mathbf{K})^{-1} \mathbf{K}^T \mathbf{S}_\epsilon^{-1} \mathbf{y} \\ &= \hat{\mathbf{S}} \mathbf{K}^T \mathbf{S}_\epsilon^{-1} \mathbf{y} \end{aligned} \tag{3.12}$$

where $\hat{\mathbf{S}} = (\mathbf{K}^T \mathbf{S}_\epsilon^{-1} \mathbf{K})^{-1}$ is the covariance matrix [Rodgers, 2000].

Without any further constraint, the inverse method of retrieval theory results in a plethora of solutions that will provide a good fit to the measured spectrum, satisfying the quality criteria. This denotes the fact that this is an ill-posed problem, i.e., we are trying to calculate an infinite set of parameters with a finite set of measurements. In addition, small changes in the observed spectrum can lead to significant changes in the retrieved

parameter profiles, meaning errors on the measured spectrum can be amplified and lead to unphysical oscillations in retrieved vertical parameter profiles. This is known as an ill-conditioned problem. Thus, in order to produce physically plausible solutions that are also likely solutions, we must employ statistical methods to further constrain the problem.

3.2.1 Statistical Methods

3.2.1.1 Optimal Estimation

One such technique used to add additional constraint to the retrieval problem is Optimal Estimation (OE). This method invokes atmospheric state parameters obtained from measurements (e.g., from previous space missions), or estimates informed by previous studies, as *a priori* knowledge of the system in the form of an *a priori* state vector $\mathbf{x}_a$, with corresponding error covariance matrix $\mathbf{S}_a$ [Irwin, 2009]. The cost function of Eqn. 3.11 can then be modified to give Eqn. 3.13, incorporating this *a priori* knowledge.

$$\phi = (\mathbf{y} - \mathbf{F}(\hat{\mathbf{x}}))^T \mathbf{S}_\epsilon^{-1} (\mathbf{y} - \mathbf{F}(\hat{\mathbf{x}})) + (\hat{\mathbf{x}} - \mathbf{x}_a)^T \mathbf{S}_a^{-1} (\hat{\mathbf{x}} - \mathbf{x}_a) \tag{3.13}$$

This modified cost function encapsulates the closeness of fit of the synthetic spectrum to the measured spectrum, whilst also taking into account the degree to which the solution strays from the *a priori* state vector, $\mathbf{x}_a$. Thus, the optimal solution is found by minimising Eqn. 3.13, i.e., by obtaining the closest fit between the synthetic spectrum and the measured spectrum, whilst simultaneously not straying too far from $\mathbf{x}_a$. The degree to which the solution is able to deviate from $\mathbf{x}_a$ depends on the *a priori* errors ($\mathbf{S}_a$) and the errors on the measurements ($\mathbf{S}_\epsilon$) [Irwin, 2009].

When applied to a linear problem, e.g., temperature retrievals [Irwin, 2009], the optimal solution [Rodgers, 2000] is found to be

$$\hat{\mathbf{x}} = \mathbf{x}_a + (\mathbf{K}^T\mathbf{S}_\epsilon^{-1}\mathbf{K} + \mathbf{S}_a^{-1})^{-1}\mathbf{K}^T\mathbf{S}_\epsilon^{-1}(\mathbf{y} - \mathbf{K}\mathbf{x}_a) \tag{3.14}$$

with covariance matrix given by $\hat{\mathbf{S}} = \mathbf{S}_a - \mathbf{S}_a\mathbf{K}^T(\mathbf{K}\mathbf{S}_a\mathbf{K}^T + \mathbf{S}_\epsilon)^{-1}\mathbf{K}\mathbf{S}_a$.

However, when it comes to atmospheric retrievals we are often faced with a non-linear problem. For a linear retrieval, for example a temperature retrieval with the spectrum in units of radiance, the rate of change of radiance with temperature (i.e., the $\mathbf{K}$-matrix elements) is not strongly dependent on the temperature profile itself, meaning the best-fit profile is straightforward to obtain in one step [Irwin, 2009]. This is not the case for retrievals of vertical aerosol layer properties or atmospheric composition. The atmospheric transmission is significantly affected by small changes in the profiles of these parameters, which inexorably affects the $\mathbf{K}$-matrix, meaning these retrievals must be calculated iteratively, i.e., they are non-linear. If the $\mathbf{K}$-matrix needs to be recalculated for each iteration, this becomes computationally expensive [Irwin, 2009]. To make this iterative process more efficient, an extension of OE to the non-linear case is desirable.

The iterative scheme for non-linear OE leading to the optimal solution [Irwin, 2009], $\mathbf{x_{n+1}}$, is thus given by Eqn. 3.15

$$\begin{aligned}\mathbf{x}_{n+1} &= \mathbf{x}_a + \mathbf{S}_a\mathbf{K}_n^T(\mathbf{K}_n^T\mathbf{S}_a\mathbf{K}_n^T + \mathbf{S}_\epsilon)^{-1}((\mathbf{y} - \mathbf{y}_n) - \mathbf{K}_n(\mathbf{x}_a - \mathbf{x}_n)) \\ \mathbf{x}_{n+1} &= \mathbf{x}_a + \mathbf{G}_n(\mathbf{y} - \mathbf{y}_n) + \mathbf{A}_n(\mathbf{x}_a - \mathbf{x}_n)\end{aligned} \tag{3.15}$$

where the subscript n denotes the number of iterations performed, $\mathbf{G}_n = (\mathbf{K}^T\mathbf{S}_\epsilon^{-1}\mathbf{K} +$

$\mathbf{S}_a^{-1})^{-1}\mathbf{K}^T\mathbf{S}_\epsilon^{-1}$ is the gain matrix containing the partial derivatives of the state with respect to the measurement, and $\mathbf{A}_n = \mathbf{G}_n\mathbf{K}_n$ is the averaging kernel matrix. The *a priori* state vector, $\mathbf{x}_a$, ensures that the retrieval remains subject to its constraints at each iteration [Irwin, 2009].

The more prior knowledge of the system one has, the more reliable the OE algorithm becomes. However, OE can still be employed for systems with underconstrained *a priori* knowledge (e.g., Uranus' atmosphere). In this case, great care must be taken when analysing the retrieval results. This can be achieved using a number of OE's built-in diagnostic tools that assess the quality of a solution. The averaging kernel matrix, $\mathbf{A}$, quantifies the balance between the fraction of the retrieved value that stems from the measurement, $\mathbf{y}$, as opposed to the *a priori*, $\mathbf{x}_a$, and the number of degrees of freedom, ν, reveals the balance of the error variance and the degree of the fit to the data, encapsulated in the reduced-χ^2 parameter, $\chi^2_\nu = \frac{\chi^2}{\nu}$. For a given solution, a general guiding rule of thumb is that a value of $\chi^2_\nu \simeq 1$ indicates a well-balanced, good quality solution, whereas $\chi^2_\nu < 1$ signifies an overestimation of the error variance or an over-fitting of the data, and $\chi^2_\nu > 1$ indicates an underestimation of the error variance or an under-fitting of the data.

3.2.1.2 Markov Chain Monte Carlo

The inverse problem can be tackled using a Bayesian approach. By representing the measurement $\mathbf{y}$ as a probability density function (PDF), we can find a relation to the PDF of the state vector $\mathbf{x}$. The forward model $\mathbf{F}(\mathbf{x})$ then maps a point in state space into a region in measurement space determined by the PDF of the measurement error ϵ [Rodgers, 2000]. Alternatively, a given measurement $\mathbf{y}$ could be the result of a mapping

from a region of the state parameter space described by some PDF, as opposed to stemming from an individual point. Typically, we have some prior information about the state that we can describe using a PDF, which can be used to constrain the solution [Rodgers, 2000].

Bayes' theorem can tell us how the PDF of the measurement maps into the state parameter space, taking into account prior knowledge, via Eqn. 3.16

$$P(\mathbf{x}|\mathbf{y}) = \frac{P(\mathbf{y}|\mathbf{x})P(\mathbf{x})}{P(\mathbf{y})} \tag{3.16}$$

where $P(\mathbf{x}|\mathbf{y})$ is the posterior PDF of the state when the measurement is given (where | denotes 'event conditional on'), $P(\mathbf{x})$ is the prior PDF describing prior knowledge of the state, $P(\mathbf{y}|\mathbf{x})$ is a PDF describing the knowledge of $\mathbf{y}$ that would be obtained if the state were $\mathbf{x}$, i.e., the likelihood distribution (this penalises improbable fits to the measurement $\mathbf{y}$), and $P(\mathbf{y})$ is a PDF describing the marginal likelihood, or evidence, which in essence is a normalisation factor needed to compare different Bayesian models [Rodgers, 2000].

Markov Chain Monte Carlo (MCMC) is a statistical method that utilises Bayesian inference, an application of Bayes' theorem, by combining the Monte Carlo method with a Markov Chain. The Monte Carlo method is a process of repeated random sampling of a parameter space, in this case generating repeated random spectra from state vectors to compare to the measured spectrum. A Markov Chain is a random process that describes a sequence of possible events within a state parameter space, whereby the probability of each event occurring only depends on the state that was attained by the previous event, i.e., the current state. Therefore, the Markov Chain is effectively a distribution describing the likelihood of one state transitioning into another.

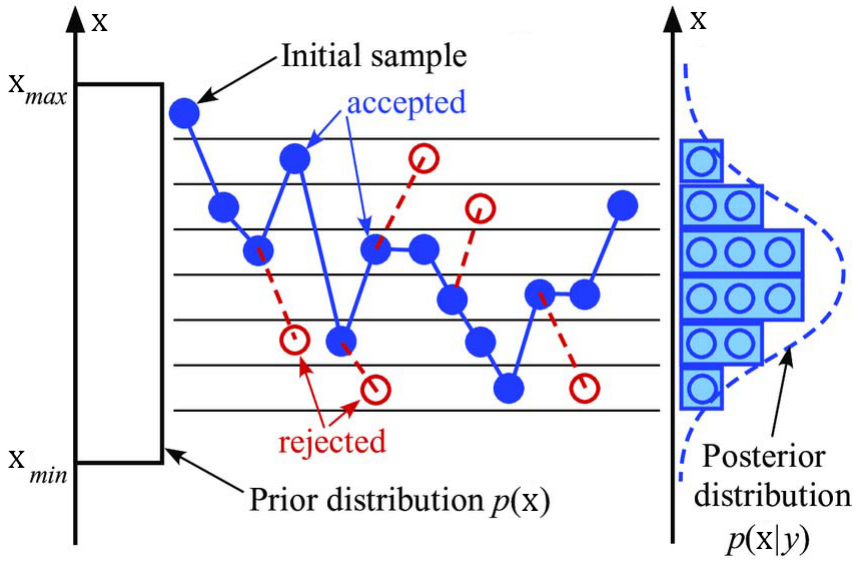


Figure 3.1: A schematic diagram of a simplified rendering of the Metropolis-Hastings MCMC algorithm [Hastings, 1970]. Here, for the Markov Chain, the transition to the next event has a probability of either being accepted or rejected, with rejections resulting in the event being discarded. The diagram is adapted from Fig. 9 of Tomic et al. [2019].

Thus, MCMC utilises these two techniques to randomly sample the state parameter space and iteratively improve the posterior PDF. Various algorithms exist that carry out MCMC, e.g., emcee [Foreman-Mackey et al., 2013] and Metropolis-Hastings [Hastings, 1970].

3.2.1.3 Nested Sampling

Another statistical method that utilises Bayesian inference is Nested Sampling (NS) [Skilling, 2006]. NS estimates the posterior PDF, $P(\mathbf{x}|\mathbf{y})$, from Bayes' theorem (Eqn. 3.16) of a set of parameters, $\mathbf{x}$, given a set of data, $\mathbf{y}$.

NS operates by initialising a set of points in the state parameter space, termed live points, that are randomly sampled from the prior PDF, $P(\mathbf{x})$. The algorithm then iteratively evaluates the likelihood at each of the live points and removes the one with the lowest

likelihood, call this L_{min}, replacing it with a new live point that is drawn from the prior PDF, such that its likelihood, $L(\mathbf{y}|\mathbf{x})$, satisfies $L(\mathbf{y}|\mathbf{x}) > L_{min}$. This iterative procedure returns progressively smaller regions, or 'volumes', within the prior PDF. The process continues until a particular stopping criterion is met, resulting in a final volume whereby $L(\mathbf{y}|\mathbf{x}) > L_{min}$, where here L_{min} is the likelihood of the final live point that was removed. This result can then be mapped into one-dimensional (1D) space, greatly simplifying a high dimensional problem. Mathematically speaking, the marginal likelihood, $P(\mathbf{y})$, denoted Z is given by

$$Z = \int L(\mathbf{y}|\mathbf{x})P(\mathbf{x})d^n\mathbf{x} \tag{3.17}$$

where n is the number of dimensions. By substituting the prior volume, $X = P(\mathbf{x})d^n\mathbf{x}$, we can transform Eqn. 3.17 into

$$X(\lambda) = \int_{L(\mathbf{y}|\mathbf{x})>\lambda} P(\mathbf{x})d^n\mathbf{x} \tag{3.18}$$

Finally, by defining the inverse of Eqn. 3.18 as the likelihood of $X(\lambda)$ as $L(X(\lambda)) = \lambda$ [Skilling, 2006], we obtain a 1D integral for the marginal likelihood from Eqn. 3.19

$$Z = \int_0^1 L(X)dX \tag{3.19}$$

A simple graphical example of the result of a NS run is shown in Fig. 3.2, showing a comparison between the regions of increasing likelihood and how they map onto the integral of Eqn. 3.19.

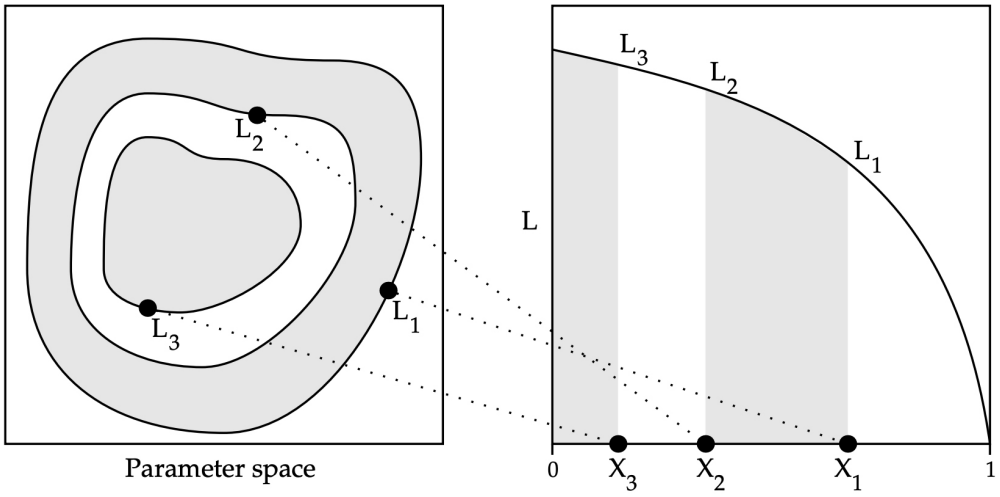


Figure 3.2: Plots showing the result of a Nested Sampling run. The plot on the left displays three distinct regions with increasing likelihoods L_1 through L_3, and on the right a plot of how they map onto $L(X)$ and the integral of Eqn. 3.19. Figure from Skilling [2006].

3.2.1.4 Method Comparison

NS has several advantages over other Bayesian inference methods such as MCMC. Firstly, the ability to map a high dimensional problem into 1D space, i.e., to efficiently explore complex, multi-modal posterior distributions, is unique to this method. For example, MCMC can struggle to handle degeneracies between parameters in highly dimensional problems, which can result in an inefficient exploration of the parameter space and convergence to local optimal solutions as opposed to the desired global solution. NS can also be used to estimate the marginal likelihood, which can be difficult with other methods. MCMC is also able to estimate this but it can become very computationally expensive. The marginal likelihood is a very useful parameter as it allows direct comparison between different models [Garland, 2018]. NS is therefore the more desirable technique of the two in most cases.

OE has clear weaknesses when compared to the Bayesian inference methods. Firstly, the OE algorithm requires *a priori* knowledge in order to constrain the set of possible solutions, and in the case of underconstrained *a priori* knowledge, great care must be taken to ensure the validity of solutions. In contrast, NS and MCMC are not limited by *a priori* knowledge as they are capable of exploring the entire parameter space. Additionally, the solution produced by the OE algorithm provides an optimal balance between the terms of the cost function, minimising its value. However, this process is susceptible to converging to local optimal solutions instead of the desired global solution. This is similar to the case of MCMC, however, due to OE's reliance on *a priori* knowledge, it is more prone to converging to local minima in the cost function parameter space. A range of *a priori* values must therefore be considered for OE retrievals.

Despite these weak points, OE does have a major advantage over the Bayesian inference methods – time efficiency. The main strength of the OE algorithm, especially in the case of multiple-scattering reflected sunshine problems that require many forward-model calculations (e.g., planetary atmosphere retrievals), is its computational efficiency. OE is not very computationally expensive, with retrievals converging within $\sim$15 iterations for the aforementioned type of problems, leading to retrieval times on the order of minutes to hours. This is very fast relative to NS or MCMC retrievals. NS, the more efficient of the two Bayesian inference techniques discussed, is typically applied to the retrieval problem for exoplanet atmospheres (e.g., Taylor [2022]), with a typical retrieval requiring on the order of $\sim$20,000 iterations to converge. This leads to retrieval times of approximately

$$T \simeq n_{iter} \times n_{\lambda} \times T_{spec} \tag{3.20}$$

where T is the retrieval time, n_{iter} is the number of iterations, n_λ is the number of wavelength data points and T_{spec} is the average time required for a single forward-model calculation, typically $\sim$1 – 120 s with the NEMESIS retrieval code (described in Section 3.3). Therefore, it can be seen that the number of wavelengths in the dataset is crucial in the feasibility of using the NS method. The datasets contained in this investigation typically have in the region of $\sim$500 data points, leading to retrieval times of $T \simeq 115$ days using the lower bound of T_{spec}, and times of $T \simeq 38$ years for the upper bound of T_{spec} for NS, far too long to be feasible for this investigation. In fact, the exoplanet retrievals described above use a simple non-scattering thermal emission forward model, whereas the forward model used for this work uses a multiple-scattering model, which is more computationally taxing, meaning T_{spec} lies closer to the upper bound. MCMC retrievals, being more computationally expensive than NS, would require even longer run times. As a result, the atmospheric retrievals for Uranus' atmosphere were carried out using OE with the NEMESIS radiative transfer retrieval code.

3.3 NEMESIS

The Non-linear optimal Estimator for MultivariatE spectral analySIS (NEMESIS) is a radiative transfer retrieval algorithm developed by Irwin et al. [2008]. NEMESIS is a continuously evolving entity catered towards performing planetary atmospheric retrievals, especially those involving multiple-scattering reflected sunshine calculations, for which non-linear optimal estimation and the correlated-k approximation are utilised. The iterative scheme of Eqn. 3.15 is modified within the code, following the Levenberg-Marquardt algorithm [Levenberg, 1944, Marquardt, 1963] to implement a 'damped least-squares' iterative scheme, with damping parameter λ, leading to Eqn. 3.21

$$\mathbf{x}_{n+1}^{'} = \mathbf{x}_n + \frac{\mathbf{x}_{n+1} - \mathbf{x}_n}{1 + \lambda} \tag{3.21}$$

where $\mathbf{x}_{n+1}^{'}$ is the modified state vector, and λ is initially set to a value of 1. This modified scheme operates as follows. A forward-model spectrum is calculated using $\mathbf{x}_{n+1}^{'}$, then: a) if this is found to reduce the cost function, ϕ, $\mathbf{x}_n$ is replaced by $\mathbf{x}_{n+1}^{'}$, λ is multiplied by an arbitrary factor of 0.3 and the next iteration is initiated, or, b) if this is found to increase ϕ, λ is multiplied by an arbitrary factor of 10 and a new $\mathbf{x}_{n+1}^{'}$ is found. The damping parameter λ will therefore tend to zero as the optimal solution is approached.

3.3.1 Noise & Smoothing

The *a priori* state vector for planetary retrievals is often limited to a best guess due to a lack of *in situ* data, meaning we need to estimate the *a priori* error covariance matrix. The measurement covariance matrix, $\mathbf{S}_\epsilon$, is known from the noise level of the instrument used to collect the data, or from the standard deviation of the measurements themselves [Irwin, 2009].

Forward model errors also need to be estimated and added to $\mathbf{S}_\epsilon$, dubbed forward-modelling noise. For example, for the case of Uranus, the CH_4 absorption coefficients used in our models are those of Karkoschka and Tomasko [2010], formed from a combination of CH_4 transmission measurement sources including HST (Jupiter), Huygens (Titan) and the laboratory. These cover the wavelength range analysed and are used to inform the predicted CH_4 coefficients in the atmosphere of Uranus. As these are not direct measurements of the atmosphere in question though, an element of uncertainty inevitably enters the frame. This is one such source that is accounted for in the forward-

modelling noise. Other sources include the forward errors introduced in our assumed atmospheric parameterisation. Failing to account for these leads to the retrievals returning large χ^2_ν values, making it very difficult to interpret the retrieved atmospheric parameters and errors.

In the ideal case, we want the errors in $\mathbf{S}_\epsilon$ and in the *a priori* covariance matrix, $\mathbf{S}_a$, to have equal weighting [Irwin, 2009]. Generally, $\mathbf{S}_a$ is constructed by setting the diagonal elements to the square of the estimated *a priori* errors (chosen from reasonable guesses), and, when retrieving continuous vertical profiles, setting the off-diagonal elements by assuming an amount of cross-correlation (e.g., Rodgers [2000]) using Eqn. 3.22 [Irwin et al., 2008]

$$S_{ij} = (S_{ii}S_{jj})^{\frac{1}{2}} exp\left(-\frac{ln|\frac{p_i}{p_j}|}{c}\right) \tag{3.22}$$

where c, typically set to 1.5, is the 'correlation length', i.e., a measure of how correlated the different pressure levels are (in this case the number of scale heights over which the profile can be said to be fairly correlated), and p_i and p_j represent the pressures at the i^{th} and j^{th} levels [Irwin et al., 2008].

A selection of appropriate *a priori* errors is therefore key to producing a well-balanced retrieval. Errors being too large lead to NEMESIS minimising the cost function, ϕ, at any cost. This leads to large retrieval errors that are untenable and large, unphysical oscillations in the retrieved vertical profile. Setting the *a priori* errors too small results in the retrieved profile barely changing from the *a priori* profile, with retrieval errors being similarly small. We therefore need to undergo a process of tuning the *a priori* errors such that an intermediate, well-conditioned case is obtained, whereby a good fit to the

measured spectrum is found, whilst simultaneously providing a sufficient degree of vertical smoothing via $\mathbf{S}_a$ (i.e., retrieving a profile devoid of large, unphysical oscillations) [Irwin et al., 2008].

3.3.2 Minnaert Limb-darkening Model

An empirical law was discovered by Minnaert [1941] when analysing reflected light from the lunar surface, relating the dependence of the brightness observed on the incident and emission angles. When this Minnaert law is applied to the case of reflected sunshine from planetary atmospheres, the observed reflectivity from a given location can be well approximated, which has been applied to the case of Jupiter [Pérez-Hoyos et al., 2020], Neptune [Irwin et al., 2021] and Uranus [James et al., 2023]. The application of Minnaert's law enables one to account for centre-to-limb variations in the observed planet's disc, accurately approximating the apparent darkening or brightening of the planet's limb due to variations in gas abundances, cloud and temperature with respect to the distance from the centre of the disc in an absorbing atmosphere. Minnaert's law is given by Eqn. 3.23

$$\frac{I}{F} = \left(\frac{I}{F}\right)_0 \mu_0^k \mu^{k-1} \tag{3.23}$$

where $\left(\frac{I}{F}\right)_0$ is the nadir-viewing reflectivity, μ and μ_0 are the cosines of the emission and solar incidence angles, respectively, and k is the limb-darkening parameter, for which a value of $k > 0.5$ indicates limb-darkening, and a value of $k < 0.5$ indicates limb-brightening. The Minnaert law can be re-expressed as the following

$$\mu \frac{I}{F} = \left(\frac{I}{F}\right)_0 (\mu\mu_0)^k \tag{3.24}$$

allowing an exponential regression of the form $y = ax^b$ to be performed, with exponent $b = k$ and multiplication factor $a = \left(\frac{I}{F}\right)_0$, the so-called Minnaert parameters. Uranus is sufficiently distant from the Earth and the Sun such that the solar and viewing zenith angles can be approximated to be the same (i.e., $\mu = \mu_0$), simplifying the equation further. This very simple but powerful tool provides further constraint to radiative transfer retrievals, requiring them to simultaneously fit the radiance/reflectivity spectrum *and* the centre-to-limb variations. Another advantage of the Minnaert limb-darkening model is that, due to Eqn. 3.24 producing a linear fit in log space, extrapolation can be performed such that spectra need only be simulated at two zenith angles (NEMESIS typically uses five zenith angles in a Gauss-Lobatto quadrature scheme [Irwin et al., 2008]) in order to constrain the nadir spectrum and limb-darkening. This increases computational efficiency and significantly reduces retrieval times.

3.3.3 Quality Control

As discussed in Section 3.2.1.1, great care must be taken to gain trust and confidence in the retrieval results of systems with underconstrained *a priori* knowledge when using OE. This is the case for the atmosphere of Uranus, for which no *in situ* probe measurements exist. As a result, our *a priori* state vector is predominantly informed by studies using the *Voyager 2* data (e.g., Lindal et al. [1987]) and results obtained from retrieval analyses of ground-based and space-based telescope observations (e.g. Karkoschka and Tomasko [2009], Sromovsky et al. [2014], Irwin et al. [2022]).

A number of techniques are used to carry out this vetting process, making use of some of OE's diagnostics mentioned in Section 3.2.1.1:

- **Testing a range of *a priori* values** – It is paramount when undertaking a retrieval analysis to initially test a large range of *a priori* values for the parameter(s) being retrieved. Values spanning several orders of magnitude can be used as a starting point with the retrieved value or profile used as a guide to home in on an appropriate value. When retrieving several parameters, which are often correlated to some degree, this should be performed in a fashion that explores all combinations of the different *a priori* values chosen for the parameters. This should be carried out choosing a consistent fractional *a priori* error (for the investigated parameters) that is large enough to give the parameters the freedom to move away from the *a priori* (e.g., 100% fractional errors). This is an effective way to explore the parameter space of the cost function, ϕ, allowing multiple minima to be found (if they exist), which can then be compared.

- **Assessing the χ^2_ν value** – Once a retrieval has been appropriately tuned, with the error covariance matrices deemed to be well-balanced, the reduced-χ^2 of the retrieval is then used to assess this. A value on the order of $\chi^2_\nu \simeq 1$ is sought to confirm the quality of the retrieval.

- **Selectively fixing parameters** – For retrievals containing multiple free parameters, it is a useful exercise to fix each of the free parameters individually, in combination with each other, and altogether, and re-run the retrieval. Comparison of the resulting retrieved profiles can provide insight into the degree to which each parameter affects the results, rendering changes in certain parameters inconsequential.

- **Bracket retrievals** – Another method used to assess the retrieval results is performed by creating two copies of the retrieval being tested and manipulating the *a priori* profile of the parameter in question. One copy has the *a priori* profile set very large compared to the original retrieval (e.g., increased by a factor of 10), with the other copy's *a priori* profile set very small (e.g., decreased by a factor of 10), and both copies are given the same fractional *a priori* error. The retrievals are then run to see if their resulting profiles converge in some region of the parameter space lying between their two *a priori* profiles, before each tends back to their respective *a priori*. Convergence provides support for the original solution, indicating the region where maximum information is contained in the parameter space. This is known as a 'bracket' retrieval.

Chapter 4

The Evolution of Uranus' Polar Hood

In this Chapter, the first set of results and analysis of this thesis are presented. HST/WFC3 and HST/STIS observations are analysed to investigate the temporal evolution of Uranus' north polar hood feature and examine its observed brightening, with the aim of finding the main cause(s) within the chosen vertical aerosol model. This Chapter is a more in depth account of the work presented in James et al. [2023], which is the original work of the author.

4.1 Minnaert Analysis with HST/WFC3

To begin the analysis of the HST/WFC3 dataset, the Minnaert limb-darkening model was first applied to the entire dataset. In order to carry this out, for each image used, the disc was split into bands of latitude of width 10°, which were stepped across the entire visible disc using a step size of 5°. The data in each band were individually plotted on a graph of $\mu\frac{I}{F}$ vs $\mu\mu_0$, from which a fit to the Minnaert equation (Eqn. 3.24) was

performed, returning the Minnaert parameters $\left(\frac{I}{F}\right)_0$ and k. The output of this process contains the Minnaert parameter profiles as functions of latitude, ϕ, for each image, covering the seven spectral filters within each year's dataset. This enables a year-on-year comparison of the latitudinal variations in the nadir reflectivity, $\left(\frac{I}{F}\right)_0(\lambda)$, and limb-darkening parameter, $k(\lambda)$, for each filter. An example of the Minnaert fits for the 2015 data is displayed in Fig. 4.1, where the data has been limited to $\mu\mu_0 > 0.09$. Table 4.1 presents the retrieved reflectivity values from the NEMESIS fits of Fig. 4.1 along with their errors.

The data on the Minnaert plot of Fig. 4.1 begins to deviate from a linear trend as $\mu\mu_0$ becomes small, i.e., as we approach the edge of the disc, due to a mixing with space causing 'dilution' of the signal [Irwin et al., 2021]. Limiting the data to $\mu\mu_0 > 0.09$ avoids these edge effects whilst capturing 4 of the 5 zenith angles in NEMESIS' quadrature scheme, including 61.45° and 0.00° used in later retrievals.

The Minnaert model relies on the limb of the planet being captured to accurately fit centre-to-limb variations. Here, the high northern latitudes lack the coverage in zenith angle to capture the limb of the planet. Thus, at some cutoff latitude, the bands defined above will no longer capture the limb, making it difficult to accurately fit k, the limb-darkening parameter, resulting in additional uncertainty in the fit (e.g., the 2015 cutoff latitude band is centred at 60°N, and the 2021 cutoff latitude band is centred at 35°N). This element of uncertainty was addressed by scaling the errors on the Minnaert parameters, found from the square root of the diagonals of the covariance matrices returned by the fits to Eqn. 3.24, with respect to latitude. This was achieved by implementing a scaling factor that uses the number of datapoints within each latitude band on the $\mu\frac{I}{F}$ *vs* $\mu\mu_0$ Minnaert plot as a marker of the zenith angle coverage. It was also normalised such

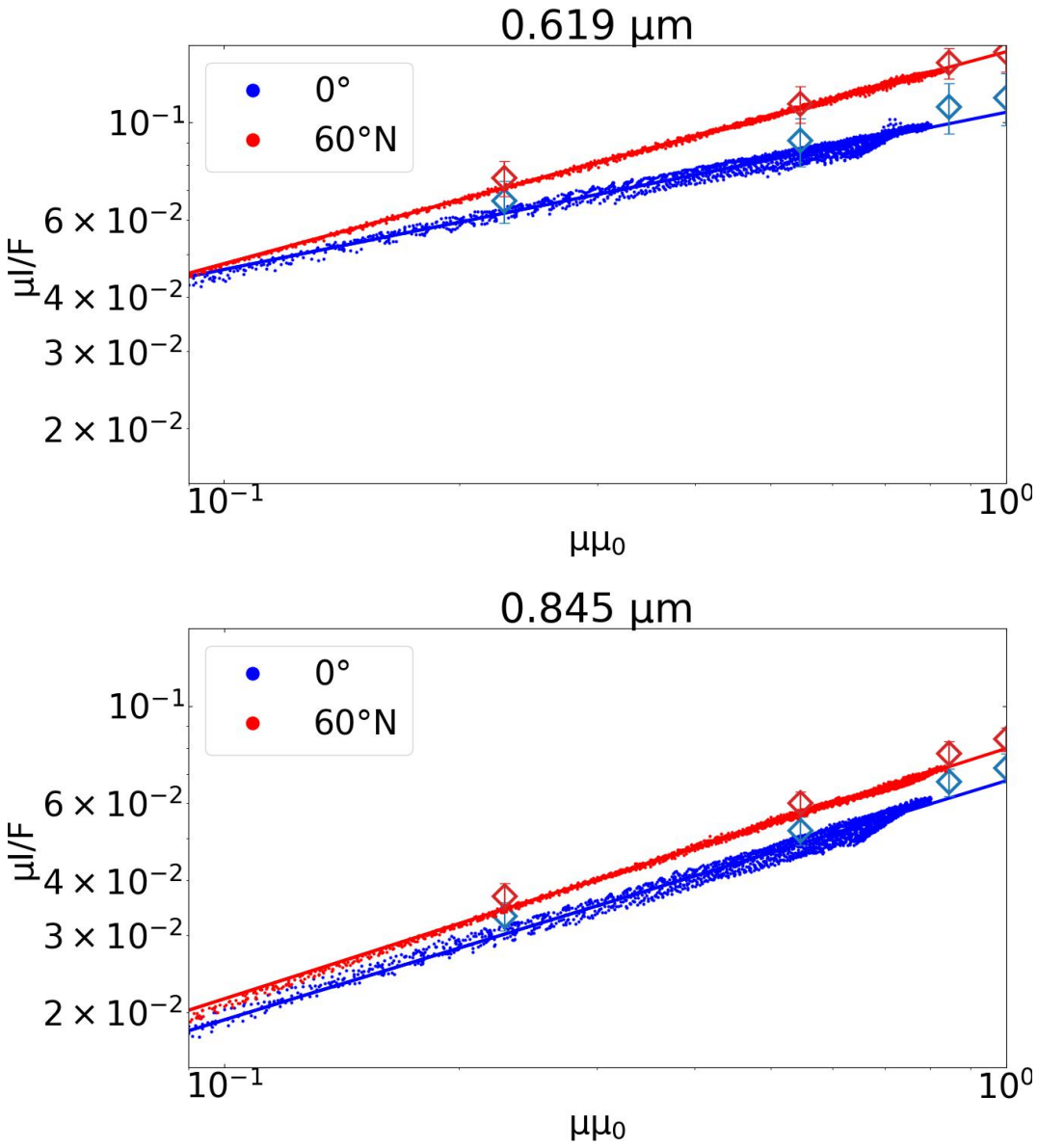


Figure 4.1: Minnaert plot showing the linear fits to the 2015 HST/WFC3 data for the 0.619-μm and 0.845-μm filters at two 10°-wide latitude bands centred at 0° (blue) and 60°N (red). Solid lines represent the fits to each latitude band. Diamonds represent the simulated reflectivity values from our best-fit model to the data, presented later in Section 4.3.1, at 0° (blue) and 60°N (red) for the four zenith angles in the NEMESIS quadrature scheme lying within the $\mu\mu_0 > 0.09$ range (0.0°, 21.145°, 42.3729° and 61.45°), demonstrating that they obey the linear Minnaert relation. The equations of the linear fits in log space, in the form $\mu\frac{I}{F} = (\frac{I}{F})_0 \mu\mu_0^k$, are as follows; for the 0.619-μm filter, $\mu\frac{I}{F} = 0.105\mu\mu_0^{0.359}$ at 0°, and $\mu\frac{I}{F} = 0.145\mu\mu_0^{0.484}$ at 60°N; for the 0.845-μm filter, $\mu\frac{I}{F} = 0.067\mu\mu_0^{0.545}$ at 0°, and $\mu\frac{I}{F} = 0.080\mu\mu_0^{0.571}$ at 60°N.

Table 4.1: Table presenting the Minnaert parameters $\mu\mu_0$ and $\mu\frac{I}{F}$ of retrievals on the 2015 HST/WFC3 observation in Fig. 4.1.

Wavelength (μm)	Latitude (°)	$\mu\mu_0$	$\mu\frac{I}{F}$	$\Delta\mu\frac{I}{F}$
0.619	0.0	1.000	0.1139	0.0154
0.619	0.0	0.846	0.1084	0.0143
0.619	0.0	0.546	0.0908	0.0114
0.619	0.0	0.228	0.0663	0.0073
0.845	0.0	1.000	0.0773	0.0055
0.845	0.0	0.846	0.0670	0.0048
0.845	0.0	0.546	0.0519	0.0038
0.845	0.0	0.228	0.0332	0.0024
0.619	60.0	1.000	0.1450	0.0143
0.619	60.0	0.846	0.1138	0.0111
0.619	60.0	0.546	0.1103	0.0105
0.619	60.0	0.228	0.0746	0.0068
0.845	60.0	1.000	0.0839	0.0052
0.845	60.0	0.846	0.0780	0.0049
0.845	60.0	0.546	0.0599	0.0039
0.845	60.0	0.228	0.0369	0.0025

that for the band with the largest number of datapoints it equals unity, and thus as we move away from the centre of the disc the factor increases. Eqn. 4.1 defines this scaling factor

$$f_{\phi_b} = \sqrt{\frac{d_{max}}{d}} \tag{4.1}$$

where f_{ϕ_b} is the scaling factor (where $f_{\phi_b} \geq 1$) for the considered latitude band ϕ_b, d is the number of datapoints on the Minnaert plot for the latitude band being considered, and d_{max} is the maximum number of datapoints on the Minnaert plot found within any one of the visible latitude bands. This scaling method is also applied to later retrieval work, where the errors being scaled are instead the estimated measurement errors (see Section 4.3). Alternatively, to account for the lack of accuracy in fitting k at high latitudes, one can fix k to the average value of all latitudes north of the limb cutoff latitude [Irwin et al., 2023b].

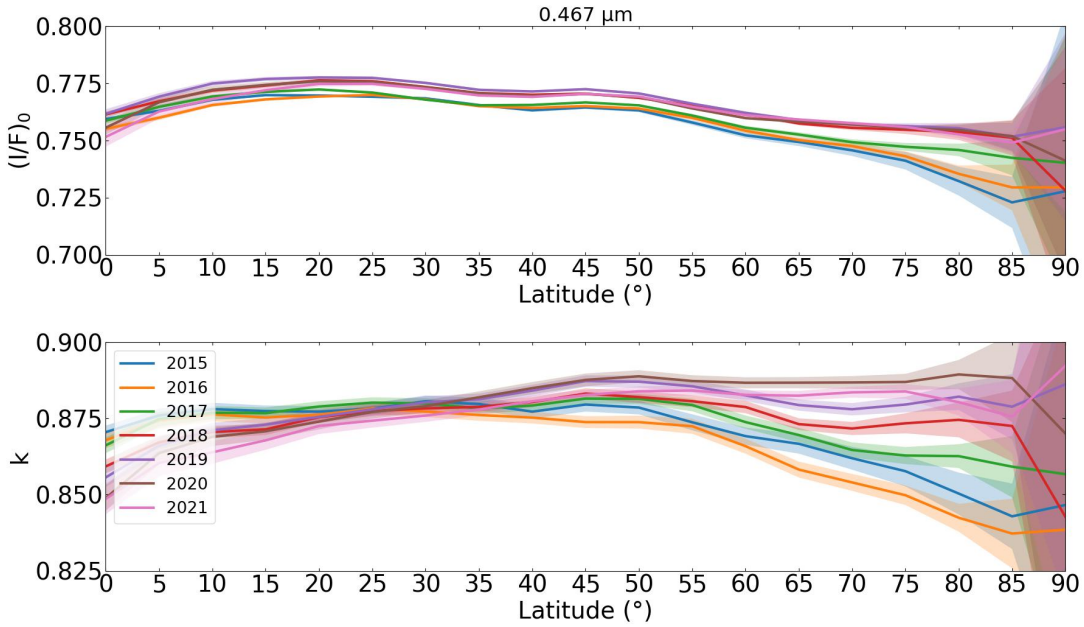


Figure 4.2: Plots of the fitted Minnaert parameters $\left(\frac{I}{F}\right)_0$ and k against latitude in the 0.467-μm UVIS filter of the HST/WFC3 Uranus observations. A small but fairly consistent brightening across all latitudes is seen over the timespan of the data, with a slightly larger increase observed at high northern latitudes. Errors are shown to 3σ and have been scaled according to Eqn. 4.1. The legend applies to both plots.

This was attempted but did not produce physically plausible results near to the north pole when applied to later retrieval work. As a result, the scaling factor was chosen as the preferred method.

The fitted Minnaert parameter latitudinal profiles for the seven UVIS filters are presented in Figs. 4.2 – 4.8. It is useful to note the clear visible presence of the polar hood in the WFC3 images of Fig. 2.2 for the 0.619-μm, 0.657-μm, 0.763-μm and 0.845-μm filters, and also its visible absence in the 0.467-μm, 0.547-μm and 0.727-μm filters, providing a reference for the expected Minnaert parameter profiles. The latitudinal profiles appear to be well correlated with the polar hood, i.e., for filters in which the polar hood is clearly

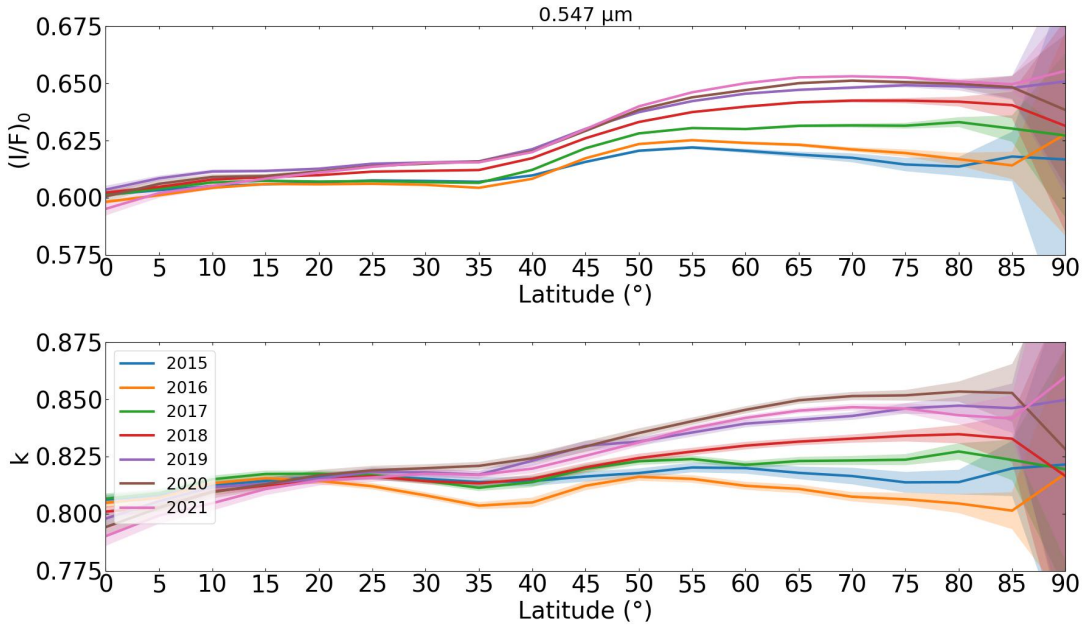


Figure 4.3: As Fig. 4.2 but for the 0.547-μm UVIS filter. Despite the polar hood not being clearly discernible from low latitudes in this filter (see Fig. 2.2), a clear increase in the Minnaert parameters is observed north of $\sim$45°N over time.

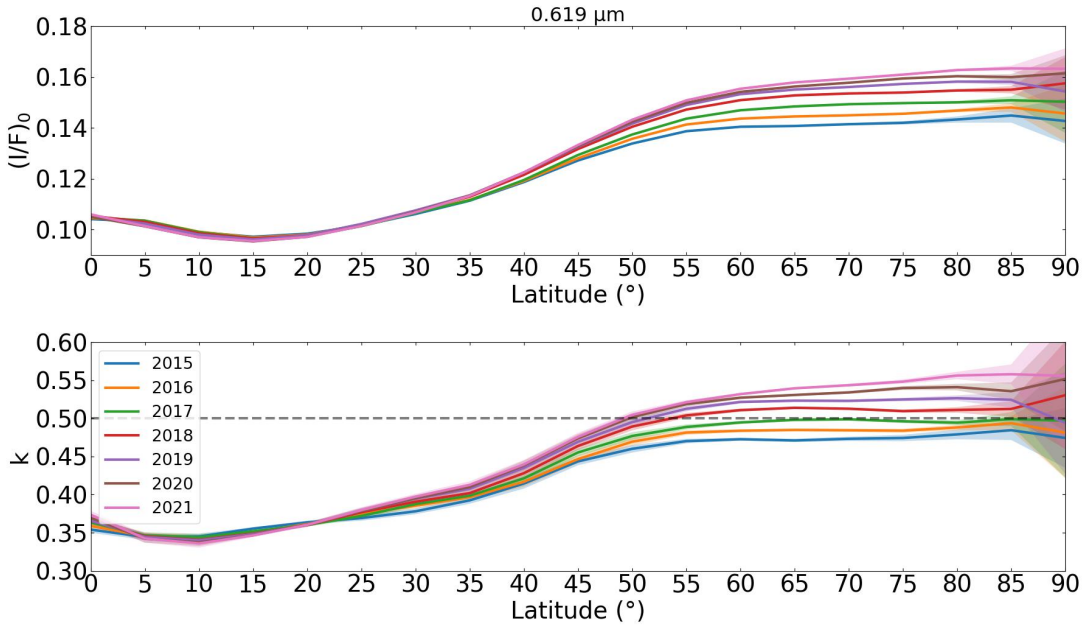


Figure 4.4: As Fig. 4.2 but for the 0.619-μm UVIS filter. A clear increase in the Minnaert parameters is observed north of $\sim$40°N over time. The black dashed line on the lower plot represents the transition point between limb-darkening ($k > 0.5$) and limb-brightening ($k < 0.5$).

discernible from low latitudes, the increase in $\left(\frac{I}{F}\right)_0$ over time at high northern latitudes is significantly more pronounced than that of mid- and equatorial latitudes. For example, the 0.845-μm filter image has an average increase in $\left(\frac{I}{F}\right)_0$ at 65°N of ∼0.0044/year; by contrast this value is only ∼0.00084/year at 30°N, a ∼5.25-fold difference. The filters in which the polar hood is not clearly discernible (e.g., 0.727 μm) show no comparable asymmetry in the change in $\left(\frac{I}{F}\right)_0$. The 0.547-$\mu$m filter image is the only exception to this.

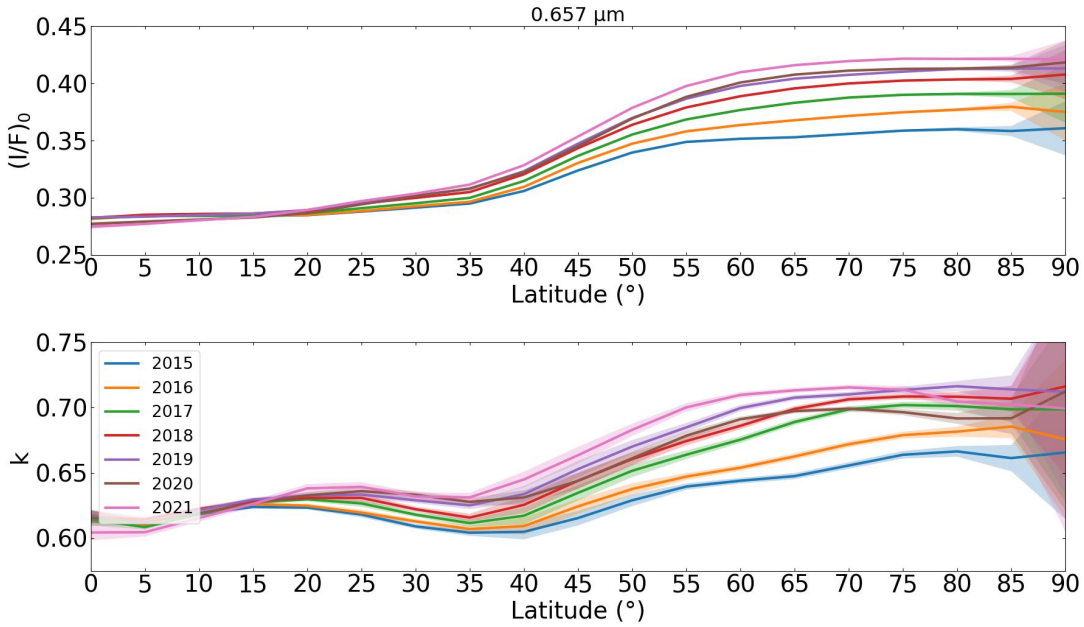


Figure 4.5: As Fig. 4.2 but for the 0.657-μm UVIS filter. A clear increase in the Minnaert parameters is observed north of ∼40°N over time.

The results returned from this simple analysis provide clear evidence for a temporal brightening of the north polar hood. In addition, due to the Minnaert model's ability to provide a measure of brightness that is independent of viewing angle, $\left(\frac{I}{F}\right)_0$, evidence is provided for the predominant contributors to the temporal brightening originating from changes in the cloud-top CH_4 VMR (i.e., atop the ∼5 bar deep haze layer in the chosen

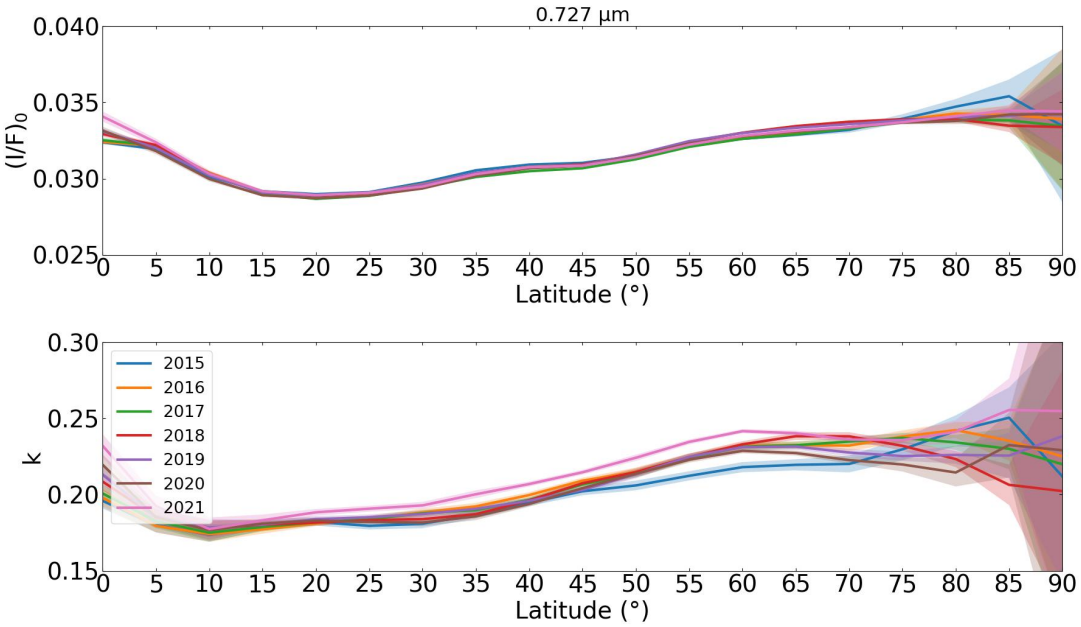


Figure 4.6: As Fig. 4.2 but for the 0.727-μm UVIS filter. No clear, simple trend is observed in the Minnaert parameters over time.

model) and/or changes in the vertical aerosol layers (i.e, changes in scattering and/or optical properties). This rules out any *apparent* brightening effects stemming from the changing viewing geometry combined with the polar depletion in CH_4, meaning that as Uranus' orbit progresses and its north pole points more directly towards the Sun, and therefore the Earth, the path length of the light is reduced. This results in less CH_4 absorption over time as northern summer solstice is approached and the viewing geometry continues to change, leading to an apparent brightening. The 0.467-μm and 0.727-μm filters probe high up in the troposphere ($\lesssim$ 1 bar) and show no clear signature of a consistent brightening at north polar hood latitudes ($\sim$45 – 90°N). The 0.467-μm filter does, however, appear to reveal a signature of change linked to the evolution of the hood in the k profile, via a temporal increase. In contrast, the five other filters, probing deeper in the atmosphere down to pressures of a few bars (coinciding with the pressure levels of the

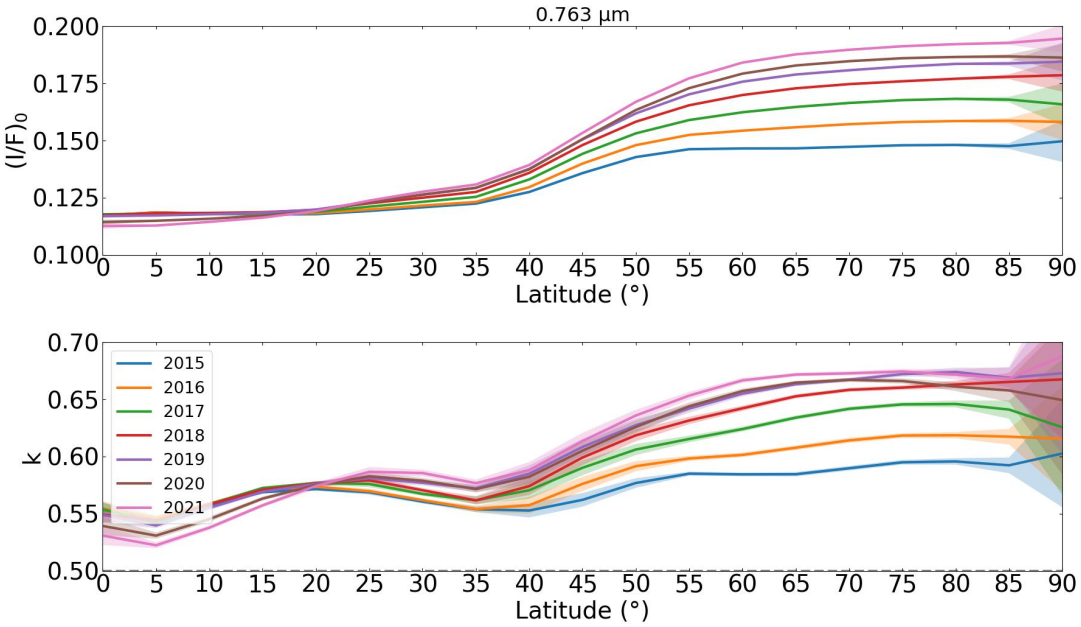


Figure 4.7: As Fig. 4.2 but for the 0.763-μm UVIS filter. A clear increase in the Minnaert parameters is observed north of $\sim$40°N over time.

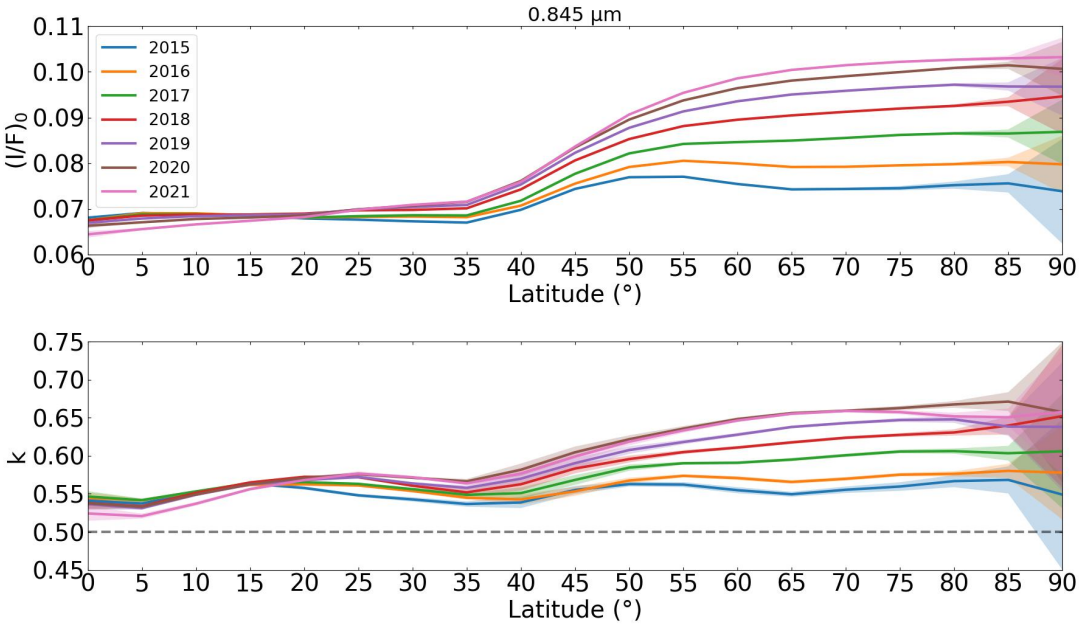


Figure 4.8: As Fig. 4.2 but for the 0.845-μm UVIS filter. A trend of a relatively large increase in the Minnaert parameters is observed north of $\sim$45°N over time. The black dashed line on the lower plot represents the transition point between limb-darkening ($k > 0.5$) and limb-brightening ($k < 0.5$)

aerosol layers within our model and the pressure sensitivity to cloud-top CH_4 VMR), reveal a clear and consistent brightening at polar hood latitudes. The 0.547-μm filter probes the highest altitudes (i.e., the lowest pressure range) of these five other filters and appears to mark the detectable vertical upper extent of the brightening of the polar hood using this dataset.

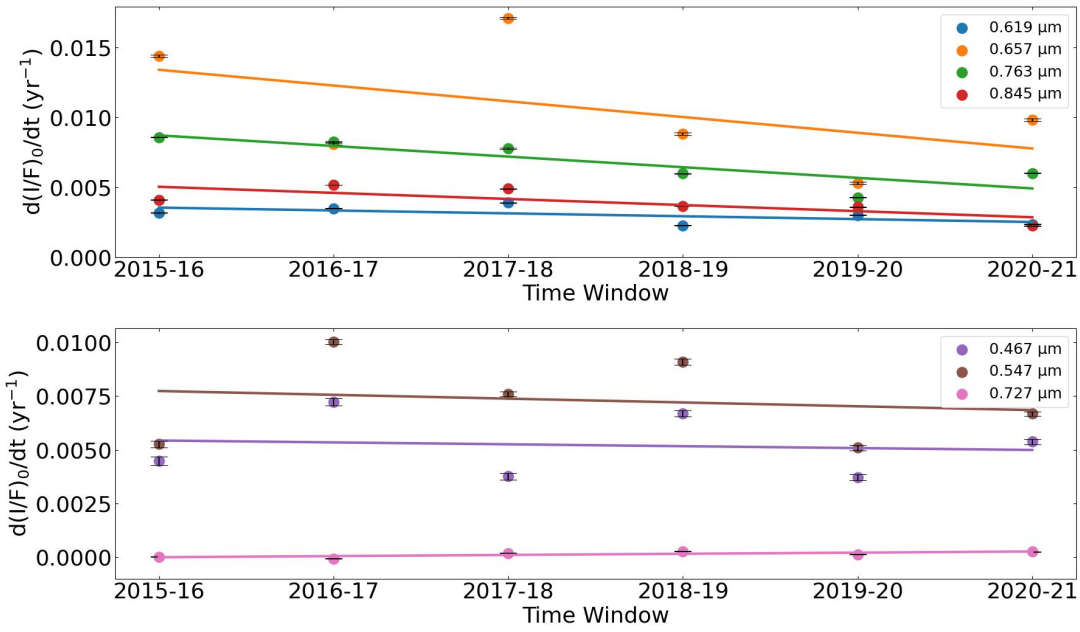


Figure 4.9: Plots of the average rate of change in $\left(\frac{I}{F}\right)_0$ against time. Datapoints are calculated from the average change across polar hood latitudes (45 – 90°N) between consecutive years of observation. Plots are separated by the filters in which the hood is visibly discernible (*top*) and in which it is not (*bottom*) (see Fig. 2.2). Linear least-squares fits for each filter are also included, displaying trends of a decrease in the rate of brightening with time in the filters for which the hood is visibly discernible (0.619, 0.657, 0.763 and 0.845 μm), and trends of a virtually constant rate of brightening in comparison for those in which it is not (0.467 and 0.727 μm). The 0.547-μm filter is the exception to this, capturing the signal of temporal brightening at polar hood latitudes despite the hood not being visibly discernible (see Fig. 2.2), and therefore also showing a trend of a decrease in the rate of brightening over time. Equations of the lines of best fit are given in Table 4.2.

Close inspection of Figs. 4.3, 4.4, 4.5, 4.7 and 4.8 appears to reveal a trend of a decrease in the degree of brightening at high northern latitudes as time progresses. In order to explore this, the average change in brightness [i.e., the change in $\left(\frac{I}{F}\right)_0$] over polar hood latitudes, i.e., 45 – 90°N, was calculated between successive years for each UVIS filter and plotted accompanied by linear least-squares fits (Fig. 4.9). A tentative slowing in the rate of brightening (i.e., negative gradients in the linear fits) is indeed observed for the filters in which the hood is clearly discernible from low latitudes, suggesting that the physical change(s) responsible for the temporal brightening of the hood, and thus, the underlying mechanism(s) involved, could be slowing with time. The filters in which the hood is not clearly discernible from low latitudes show tenuous trends by comparison (an order of magnitude difference), with the exception of the 0.547-μm filter. The equations for the lines of best fit are provided in the caption of Fig. 4.9 for comparison.

Table 4.2: Table presenting the Minnaert parameters $\mu\mu_0$ and $\mu\frac{I}{F}$ of retrievals on the 2015 HST/WFC3 observation.

Wavelength (μm)	Equation of line of best fit
0.467	$y = -8.818 \times 10^{-5}x + 542.8 \times 10^{-5}$
0.547	$y = -1.777 \times 10^{-4}x + 77.33 \times 10^{-4}$
0.619	$y = -2.061 \times 10^{-4}x + 35.33 \times 10^{-4}$
0.657	$y = -1.127 \times 10^{-3}x + 13.4 \times 10^{-3}$
0.727	$y = 5.357 \times 10^{-5}x - 0.5562 \times 10^{-5}$
0.763	$y = -7.597 \times 10^{-4}x + 87.04 \times 10^{-4}$
0.845	$y = -4.362 \times 10^{-4}x + 50.24 \times 10^{-4}$

4.2 CH_4 Retrievals with HST/STIS

Due to the nature of the HST/WFC3 observations, i.e., images captured with filters containing a range of wavelengths that have been convolved, we do not have the spectral resolution to directly retrieve the latitudinally-dependent cloud-top CH_4 VMR using

Karkoschka and Tomasko [2009]'s method utilising CIA (see Section 1.3.6.1). Therefore, before carrying out a latitudinal retrieval analysis with the HST/WFC3 dataset, it was necessary to choose a fixed *a priori* latitudinal profile for cloud-top CH_4 VMR. This could of course be obtained from the literature, however, in the interest of consistency, the ideal scenario would be to retrieve the profile using the preferred vertical aerosol model of this investigation. In order to achieve this, data with the necessary spectral resolution was sought after, resulting in the acquisition of an archival HST/STIS observation captured in 2015 [Sromovsky et al., 2019] described in Section 2.2.

Before carrying out a latitudinal retrieval analysis on the data, a vertical profile for the CH_4 VMR also needs to be assumed. In this instance, a simple 'step' model, similar to that of Irwin et al. [2021], was adopted. This model possesses a variable 'deep' CH_4 VMR, limited to 100% relative humidity above the condensation level, with a limiting stratospheric VMR of 1×10^{-4}. The advantage of using this model comes in the form of the resulting mean CH_4 VMR in the region of sensitivity ($\sim$2 – 5 bar), i.e., the cloud-top region, providing a parameter that is easily interpreted and useful for comparison with previous studies. This is opposed to the arguably more physically plausible descended profile (e.g., Sromovsky et al. [2011], Karkoschka and Tomasko [2011], Sromovsky et al. [2019]). This model instead has a smooth reduction in CH_4 VMR from the tropopause value to the deep value, parameterised by exponent vx determining the shape of the curve, and P_d the pressure depth at which the VMR equals to the uniform deep value.

We again employed the Minnaert limb-darkening model, allowing the efficient modelling

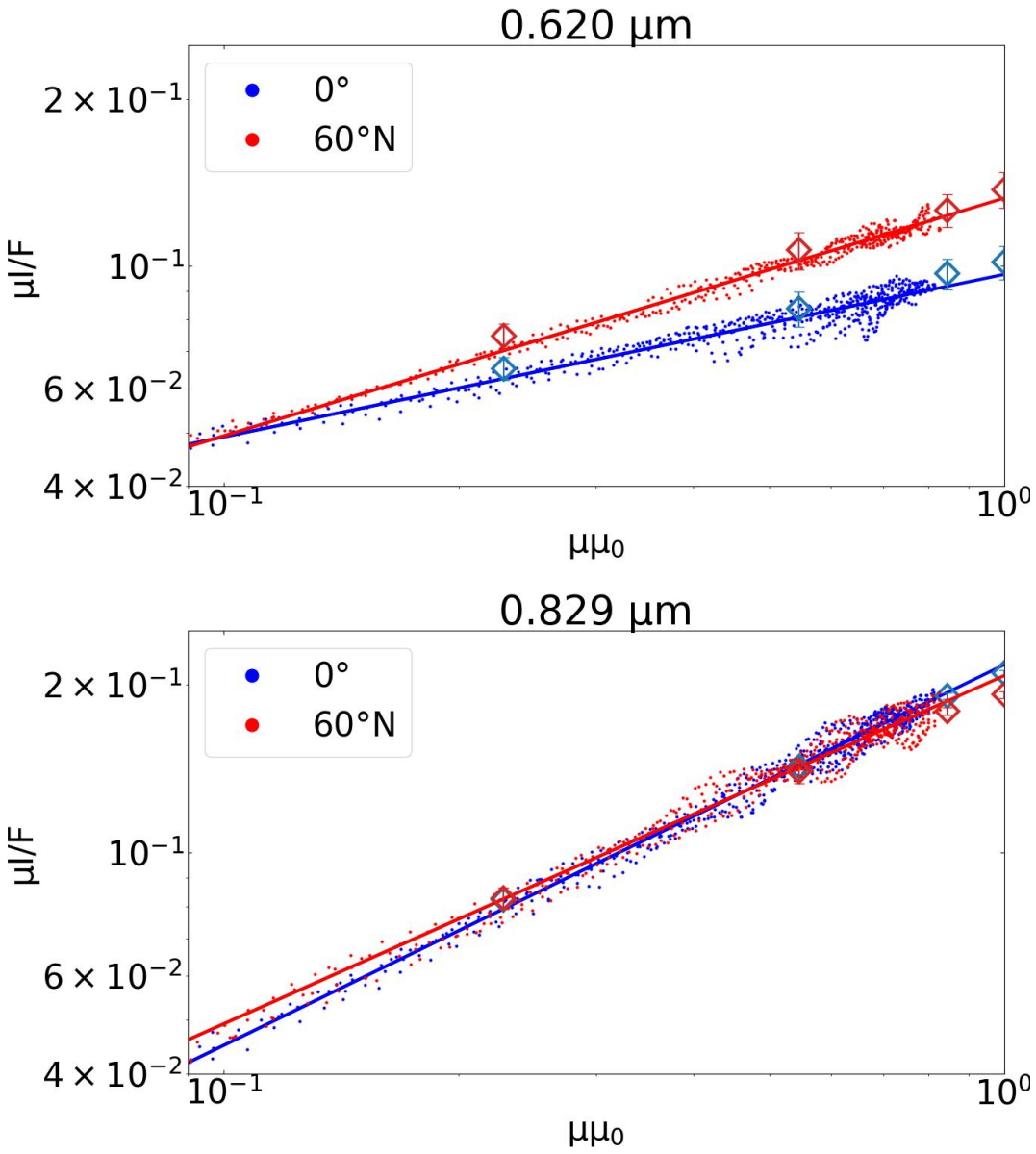


Figure 4.10: Minnaert plots showing the linear fits to the 2015 HST/STIS data at 0.620 μm and 0.829 μm at two 10°-wide latitude bands centred at 0° (blue) and 60°N (red). Solid lines represent the fits to each latitude band. Diamonds represent the simulated reflectivity values from our best-fit model to the data at 0° (blue) and 60°N (red) for the four zenith angles in the NEMESIS quadrature scheme lying within the $\mu\mu_0 > 0.09$ range (0.0°, 21.145°, 42.3729° and 61.45°), demonstrating that they obey the linear Minnaert relation. The equations of the linear fits in log space, in the form $\mu\frac{I}{F} = \left(\frac{I}{F}\right)_0 \mu\mu_0^k$, are as follows; for 0.620 μm, $\mu\frac{I}{F} = 0.096\mu\mu_0^{0.293}$ at 0°, and $\mu\frac{I}{F} = 0.132\mu\mu_0^{0.429}$ at 60°N; for 0.829 μm, $\mu\frac{I}{F} = 0.217\mu\mu_0^{0.684}$ at 0°, and $\mu\frac{I}{F} = 0.208\mu\mu_0^{0.626}$ at 60°N.

Table 4.3: Table presenting the Minnaert parameters $\mu\mu_0$ and $\mu\frac{I}{F}$ of retrievals on the 2015 HST/STIS observation in Fig. 4.10.

Wavelength (μm)	Latitude (°)	$\mu\mu_0$	$\mu\frac{I}{F}$	$\Delta\mu\frac{I}{F}$
0.620	0.0	1.000	0.1015	0.0070
0.620	0.0	0.846	0.0967	0.0061
0.620	0.0	0.546	0.0836	0.0060
0.620	0.0	0.228	0.0652	0.0031
0.829	0.0	1.000	0.2098	0.0028
0.829	0.0	0.846	0.1910	0.0025
0.829	0.0	0.546	0.1424	0.0058
0.829	0.0	0.228	0.0821	0.0030
0.620	60.0	1.000	0.1372	0.0102
0.620	60.0	0.846	0.1259	0.0086
0.620	60.0	0.546	0.1066	0.0083
0.620	60.0	0.228	0.0745	0.0040
0.829	60.0	1.000	0.1919	0.0029
0.829	60.0	0.846	0.1793	0.0026
0.829	60.0	0.546	0.1400	0.0068
0.829	60.0	0.228	0.0827	0.0036

of centre-to-limb variations of the observations, using the same latitudinal sampling as in Section 4.1 (i.e., 10° width, 5° step size). The fitted Minnaert parameters $\left(\frac{I}{F}\right)_0(\lambda)$ and $k(\lambda)$ were then used to generate reconstructed radiance spectra at two chosen viewing zenith angles, 0.0° and 61.45°, corresponding to two of the five zenith angles in the Gauss-Lobatto scheme used within NEMESIS. The larger angle was chosen such that it is sufficient to fully capture the observed limb-darkening (or limb-brightening) behaviour, whilst simultaneously aligning with one of the five angles in NEMESIS' Gauss-Lobatto scheme to avoid the need for any interpolation [Irwin et al., 2021]. NEMESIS retrievals were then set up using these Minnaert-reconstructed spectra as the 'measured' spectral observations to be fitted. Using Eqn. 3.23, we can reproduce the observations at any other zenith angle, assuming that the Minnaert model holds at all other zenith angles in our Gauss-Lobatto zenith-angle quadrature scheme, which Irwin et al. [2021] found to

be a good assumption for their analysis of VLT/MUSE Neptune observations. This is demonstrated in Fig. 4.10 displaying Minnaert fits to the 2015 observation.

NEMESIS incorporates Raman scattering and polarisation effects, which is important at wavelengths $\lesssim 0.55$ μm in the atmosphere of Uranus. In order to account for the downstream effects of these phenomena on the reflectivity spectrum stemming from UV wavelengths outside of our wavelength range (i.e, < 0.3 μm), the reflectivity at 0.3 μm was extrapolated to 0.2 μm, using a 0.001 μm interval (setting each reflectivity value to that at 0.3 μm). These reflectivity values were multiplied by the solar spectrum at the corresponding wavelength and given very large fractional errors ($> 100\%$) to prevent NEMESIS from attempting to fit to this wavelength range and skewing the retrievals, but allowing the effects of Raman scattering and polarisation to be approximated.

Before carrying out retrieval work, the unknown systematic errors involved in the retrieval problem need to be estimated, including those stemming from the Lucy-Richardson spatial deconvolution [Richardson, 1972, Lucy et al., 1974] applied to the HST/STIS observation (a Bayesian-based iterative technique for generating estimates to the solutions of rectification and deconvolution problems), the inhomogeneous aerosol structure, and the CH_4 absorption k-table parameters [Irwin et al., 2022]. Ordinarily, these are accounted for by adding a degree of forward-modelling noise. However, as our 'measured' spectra are Minnaert reconstructions, we also need a reliable way in which to assume the errors on these 'measurements'. As a result, the same treatment carried out by Irwin et al. [2022] was implemented, i.e., assuming the measurement errors to be $\frac{1}{50}$ of the peak reflectivity in 0.1-μm wide wavelength bins stepped by 0.05 μm, encompassing the errors associated with the aforementioned unknown systematic uncertainties as well. This error treatment resulted in fits with the desired $\chi^2_\nu \sim 1$ for retrievals on the

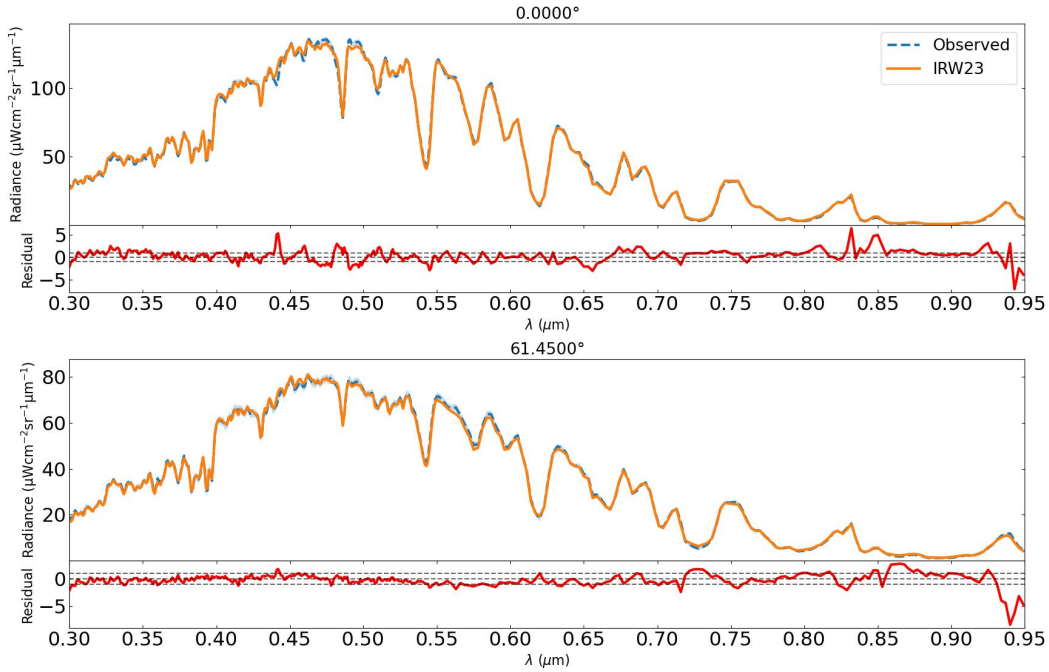


Figure 4.11: Plot of disc-averaged radiance against wavelength for the 2015 HST/STIS observation at the two chosen Minnaert zenith angles (0.0°, 61.45°), displaying the spectral fit to the disc-averaged reconstructed Minnaert spectrum of the Irwin et al. [2022, 2023a] (IRW23) aerosol model for Uranus. The fit has a reduced-χ^2 value of 1.16. Note, residuals are divided by the error on the measured spectrum.

disc-averaged observation. This fit is displayed in Fig. 4.11.

With a good quality fit for the disc-averaged spectrum confirmed, a latitudinal retrieval analysis was then carried out, fitting to the spectra extracted at each individual latitude band with the scaling factor of Eqn. 4.1 applied to the errors. The free parameters of the retrieval were set as: the integrated opacity of the deep haze (τ_1), the integrated opacity (τ_2) and pressure (p_2) of the 1 – 2-bar haze, the integrated opacity of the extended haze (τ_3), and the cloud-top CH_4 VMR (f_{CH_4}). The fractional *a priori* errors for these parameters were all set to 100%. In addition, the imaginary refractive index spectrum of each aerosol layer, defining the absorption profile of its aerosols with wavelength, was also allowed to vary with 10% fractional *a priori* errors (the real part of the refractive

index was set to 1.4 at 0.8 μm for each layer). Tables 4.4 and 4.5 detail the parameter setup for each of the retrievals run on the different latitude bands.

Table 4.4: Table detailing the parameter setup for the latitudinal retrieval analysis carried out using the 2015 HST/STIS observation, excluding the imaginary refractive index spectra. The *a priori* were sourced from the holistic aerosol model [Irwin et al., 2022]. All errors are set to 100% of the stated *a priori* values.

Parameter	*a priori*	*a priori* error
τ_1	5.0	5.0
τ_2	3.0	3.0
p_2 (bar)	1.45	1.45
τ_3	0.03	0.03
CH_4 VMR	0.03	0.03

Table 4.5: As Table 4.4 but for the imaginary refractive index spectra. The *a priori* were sourced from the holistic aerosol model [Irwin et al., 2022]. All errors were set to 10% of the stated *a priori* values.

Wavelength (μm)	n_{i1} *a priori*	n_{i2} *a priori*	n_{i3} *a priori*
0.3	3.8787×10^{-4}	8.5886×10^{-3}	3.3104×10^{-3}
0.4	2.1858×10^{-5}	1.4420×10^{-3}	1.5055×10^{-3}
0.5	9.9988×10^{-7}	1.0737×10^{-3}	2.5441×10^{-4}
0.6	2.3038×10^{-4}	1.8630×10^{-5}	2.9869×10^{-4}
0.7	9.6592×10^{-4}	8.3692×10^{-4}	4.7860×10^{-4}
0.8	6.8759×10^{-5}	5.0314×10^{-3}	7.9636×10^{-4}
0.9	3.0435×10^{-4}	3.8393×10^{-3}	2.6048×10^{-3}
1.0	6.2646×10^{-4}	1.2903×10^{-2}	1.1394×10^{-3}

Spectral fits of these retrievals for latitude bands representing equatorial and polar regions are displayed in Fig. 4.12.

The retrieved latitudinal profile of cloud-top CH_4 VMR from the 2015 STIS observation is shown in Fig. 4.13. We assume that this profile is valid for all years in our HST/WFC3 dataset (i.e., 2015 – 2021) in line with the assertion of a general temporal stability in the CH_4 latitudinal profile by Sromovsky et al. [2019]. The latitudinal profile for cloud-top

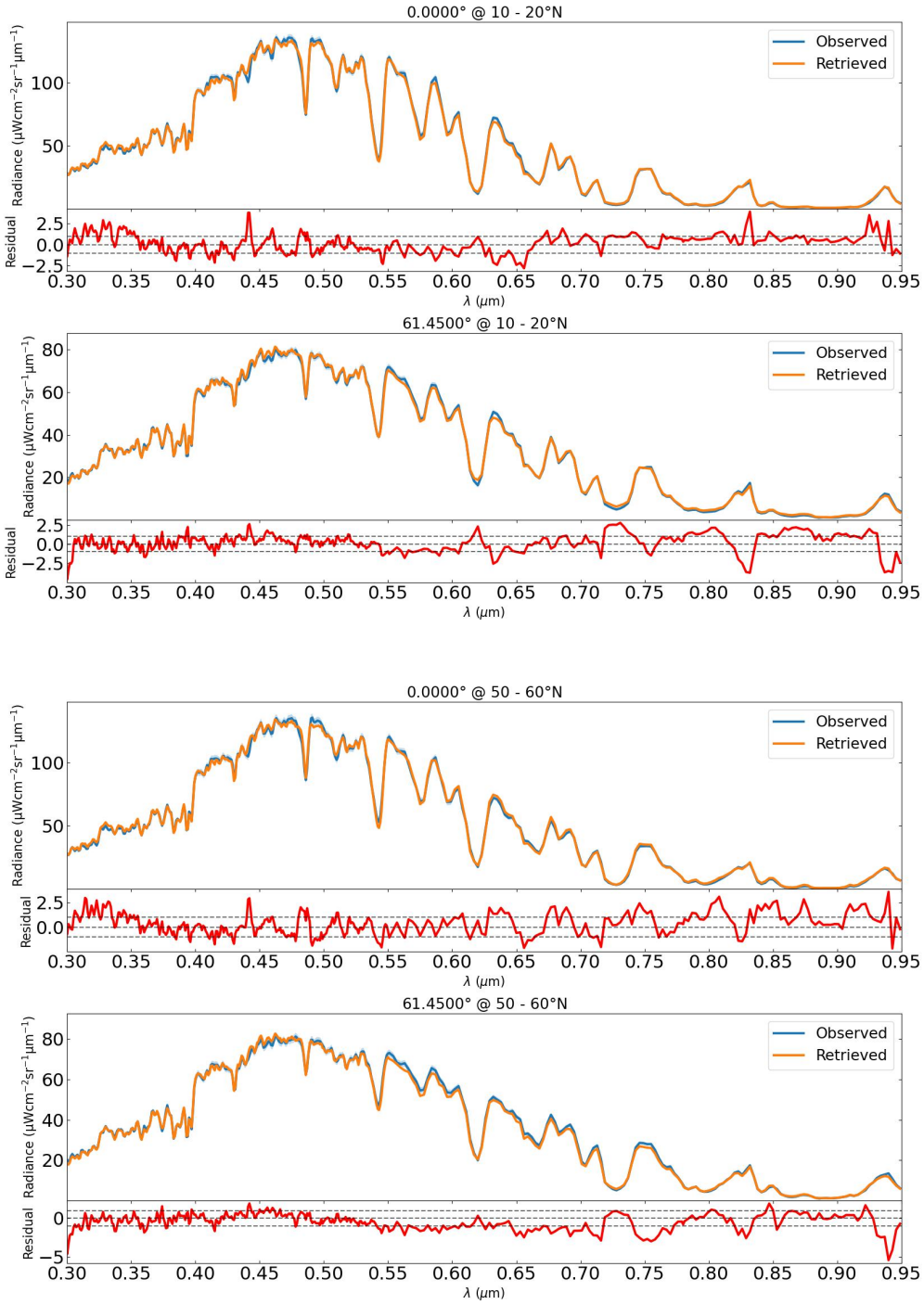


Figure 4.12: Plots of radiance against wavelength showing the spectral fits at the two chosen Minnaert zenith angles (0.0°, 61.45°) for retrievals carried out on the 2015 STIS observation at representative latitude bands of 10 – 20°N (top) & 50 – 60°N (bottom). Note, residuals are divided by the error on the measured spectrum.

CH_4 VMR in Fig. 4.13 was therefore fixed as the *a priori* profile for all years in our latitudinal retrieval analysis with the HST/WFC3 dataset.

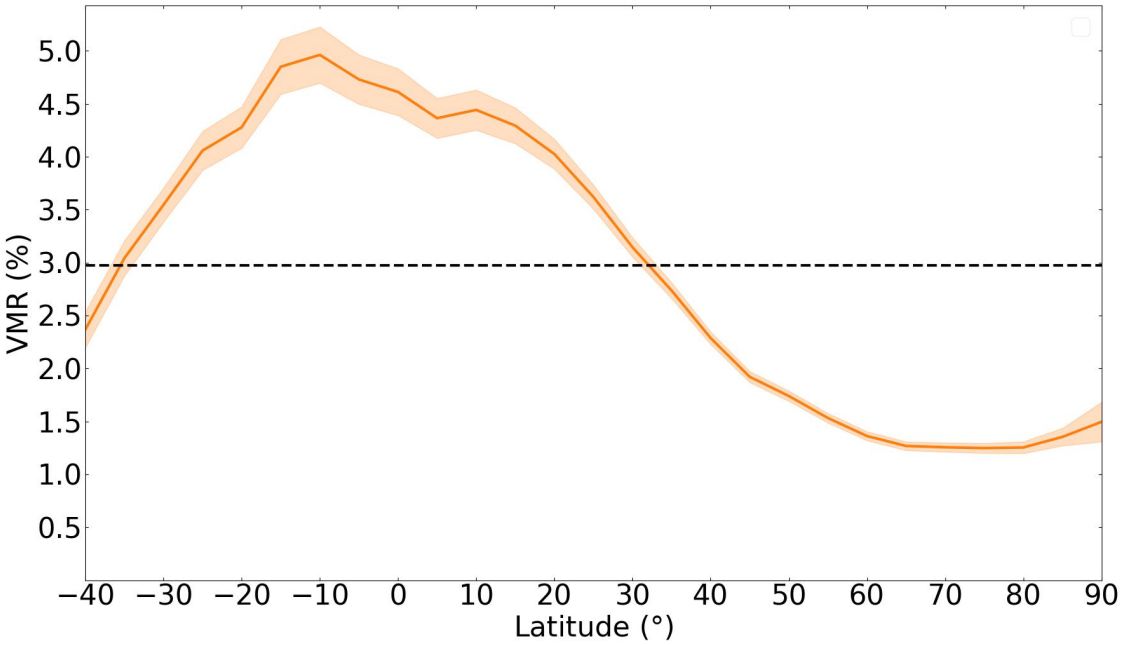


Figure 4.13: Plot of CH_4 volume mixing ratio against latitude retrieved from the 2015 STIS observation. The established equator-to-pole negative gradient in VMR is clearly observed. The black dashed line denotes the *a priori* value of 3.0% from the Irwin et al. [2022] model.

4.3 Latitudinal Retrievals

4.3.1 HST/WFC3

With an *a priori* profile for the cloud-top CH_4 VMR in hand, a latitudinal retrieval analysis of the HST/WFC3 dataset was commenced. The *a priori* imaginary refractive index spectra of each aerosol layer were fixed to that retrieved with the 2015 HST/STIS observation at each individual latitude band. Reconstructed spectra were produced from the Minnaert parameters obtained in Section 4.1 at zenith angles of 0.0° and 61.45°. Due to

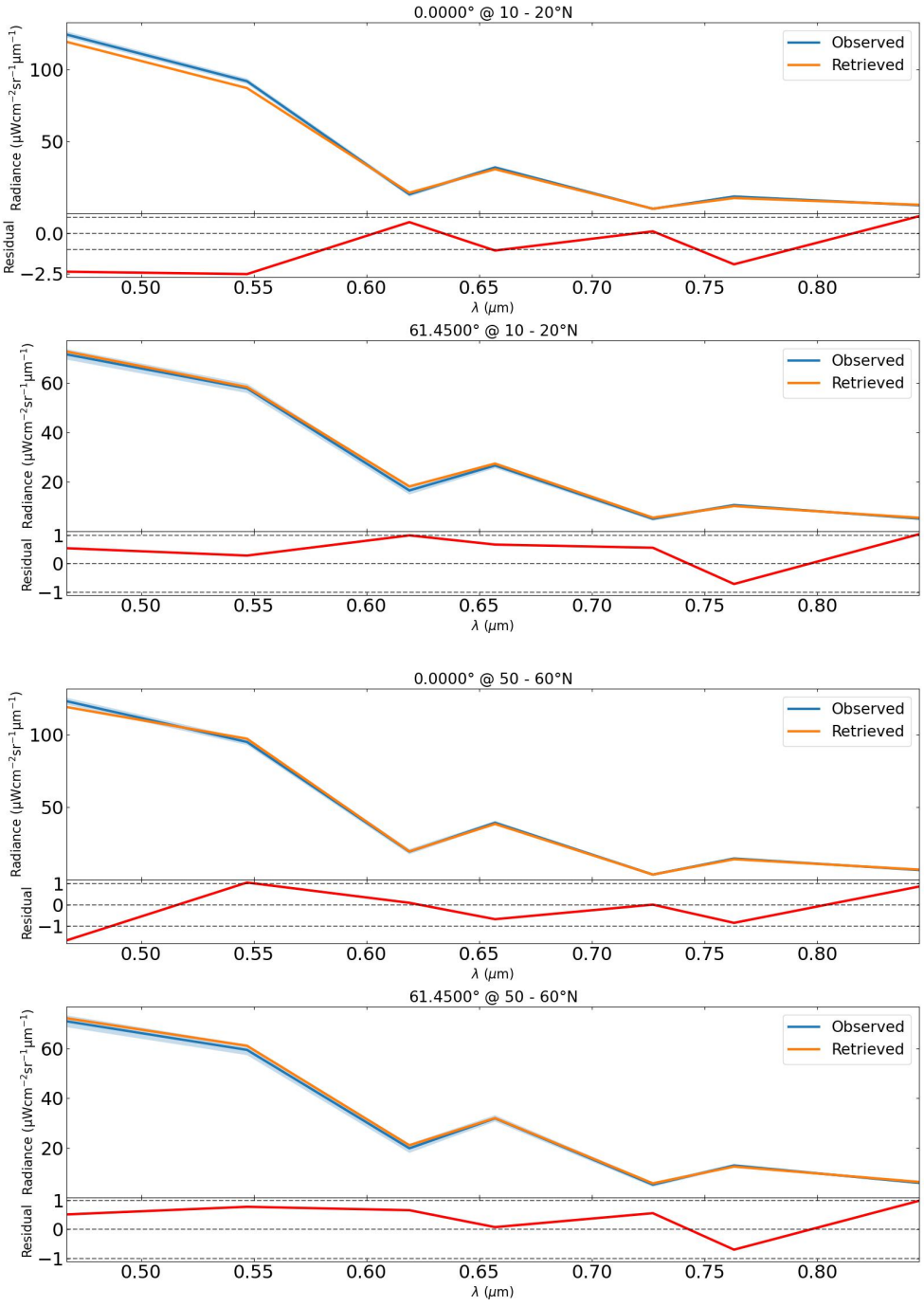


Figure 4.14: Spectral fits at the two chosen zenith angles (0.0°, 61.45°) retrieved using the 2015 HST/WFC3 observations at representative low latitude, 10 – 20°N (*top*), and high latitude, 50 – 60°N (*bottom*), bands. Reduced-χ^2 values for the retrievals are $\sim$1.53 and $\sim$0.66 respectively. Note, residuals are divided by the error on the measured spectrum.

the lack of spectral coverage in the dataset, the measurement errors were obtained by utilising the disc-averaged 2015 HST/STIS observation. Similar to Section 4.2, the errors were assumed to be $\frac{1}{50}$ of the peak reflectivity within 0.1-μm width wavelength bins, stepped by 0.05 μm, but in this case only within the wavelength range of each individual UVIS filter. The scaling factor from Eqn. 4.1 was then applied to the measurement errors.

A latitudinal retrieval analysis was then carried out for the entire dataset with the free parameters chosen as the: aerosol-1 integrated opacity (τ_1), aerosol-2 integrated opacity (τ_2) & base pressure (p_2), and aerosol-3 integrated opacity (τ_3). The *a priori* values were identical to those in Table 4.4, with the fractional *a priori* errors also set to 100%. The resulting spectral fits at representative low and high latitudes for the 2015 dataset are displayed in Fig. 4.14. Comparable fits were obtained for retrievals carried out on the rest of the dataset (2016 – 2021).

The resulting retrieved latitudinal profiles for the chosen free parameters are displayed for all years in Fig. 4.15, and for the 2015 & 2021 datasets only in Fig. 4.16 for easy temporal comparison. Inspection of these two figures returns a simple solution for the observed temporal brightening of the polar hood. The integrated opacity of the 1 – 2-bar haze layer (τ_2) is the only parameter seen to vary within the vertical aerosol model within error across the dataset, and only at latitudes coincident with the polar hood. The average increase seen in τ_2 between 45 – 90°N is 1.2 $\pm$ 0.3 (increasing from 2.9 $\pm$ 0.2 to 4.1 $\pm$ 0.2, i.e., $\sim$41% increase) at 0.8 μm, from 2015 to 2021. All other retrieved profiles for the free parameters are consistent with no change across time and latitude in the northern hemisphere.

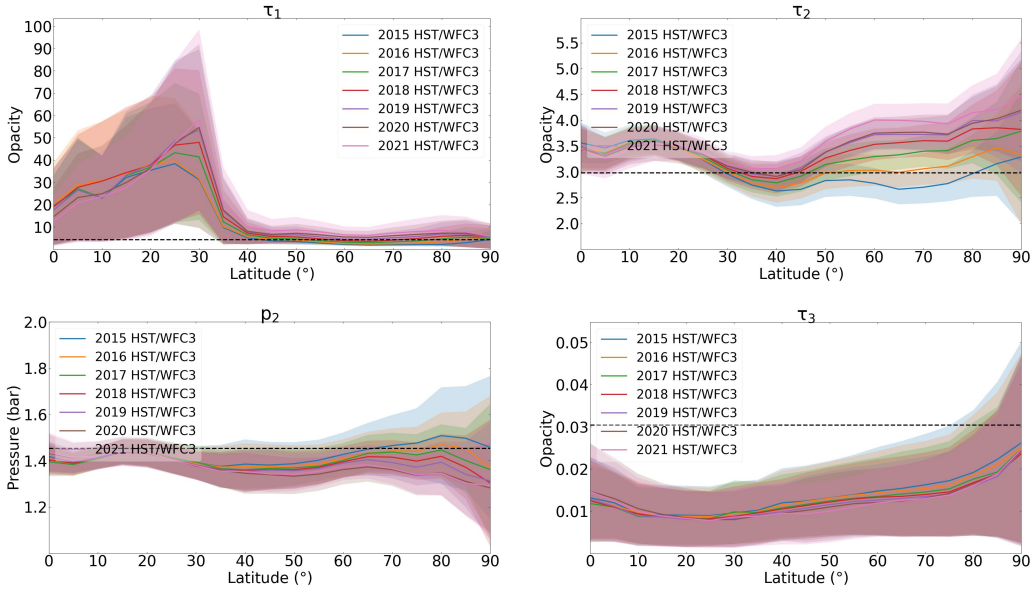


Figure 4.15: Latitudinal parameter profiles for the vertical aerosol model in the northern hemisphere retrieved using the entire HST/WFC3 dataset, including: aerosol-1 integrated opacity (τ_1), aerosol-2 base pressure (p_2) and integrated opacity (τ_2), and aerosol-3 integrated opacity (τ_3). The black dashed lines represent the *a priori* values for each parameter informed from the Irwin et al. [2022] holistic model.

Note the large retrieved values of the integrated opacity of the deep haze (τ_1) were a consistent feature of all retrievals on the HST/WFC3 dataset, along with the sharp increase at $\sim$30°N. This likely arises from τ_1 being strongly correlated with the imaginary refractive index spectrum of the 1 – 2-bar haze and the CH_4 VMR, meaning a change in the *a priori* values for these two parameters will significantly affect the resulting retrieved τ_1 profile. Both of these parameters are fixed for the above retrievals, due to a lack of spectral resolution in the dataset, likely resulting in the large values retrieved for the τ_1 profile as a compensatory response to the inability of the correlated parameters to vary. Note, the values retrieved at the equator ($\sim$15 – 20) are observationally indistinguishable from the values retrieved at the peak near 30°N ($\sim$30 – 60).

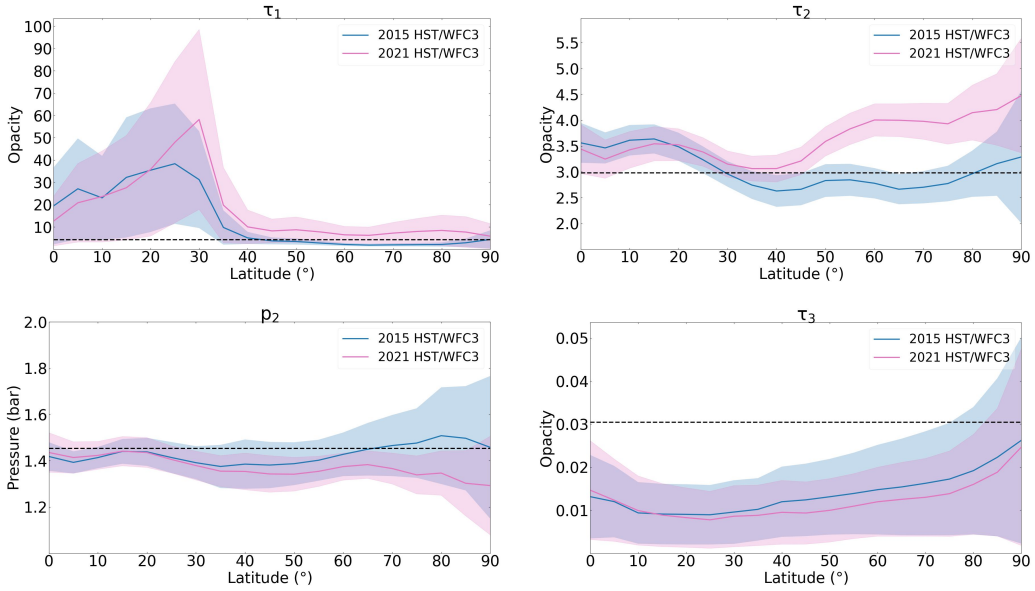


Figure 4.16: As Fig. 4.15 for the 2015 & 2021 HST/WFC3 observations only. This plot demonstrates the overall change over the 6-year timespan of the data, showing an increase in τ_2 northwards of $\sim$45°N as the only definitive change.

As previously alluded to, the WFC3 instrument's limited spectral resolution results in an inability to reliably retrieve changes in the cloud-top CH_4 VMR or the imaginary refractive index spectra of the aerosol layers within our model. As the n_i spectra describe the optical properties of aerosols (i.e., how absorbing or reflecting they are as a function of wavelength), and a reduction in polar cloud-top CH_4 VMR being a possible explanation for the main cause of the brightening, these remain important pieces of the puzzle that need to be accounted for.

Before embarking on these retrievals, we adopted Sromovsky et al. [2019]'s conclusion of a 'general stability' in the latitudinal CH_4 VMR profile and assumed it to hold across the timespan of this dataset. In the interest of completeness, if we now discard this assumption and assert that the polar cloud-top CH_4 VMR could be decreasing over time, how would this effect the retrieval results presented in this section?

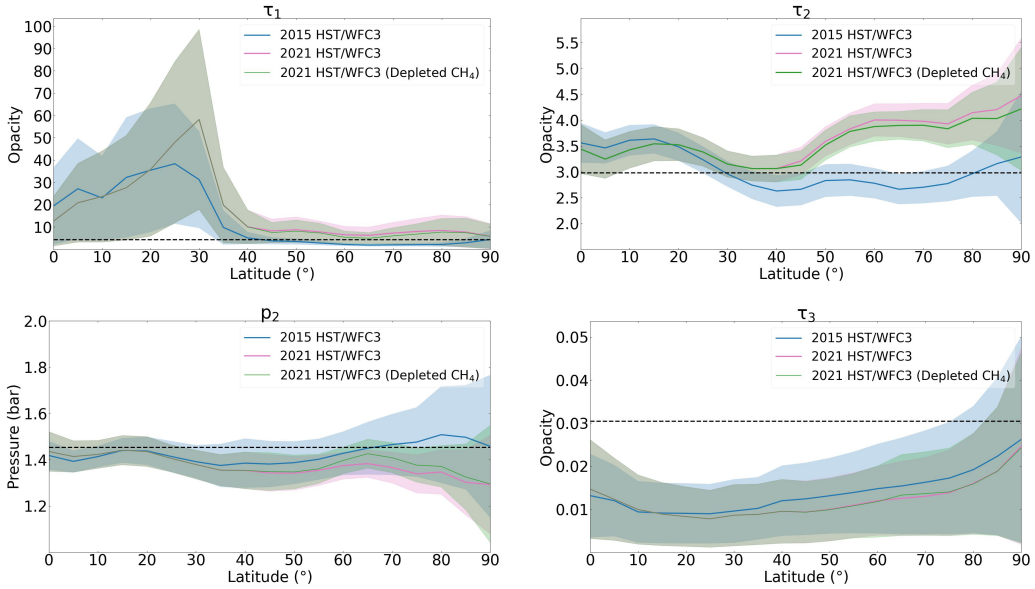


Figure 4.17: As Fig. 4.16 with the addition of a retrieval on the 2021 observations with a moderately chosen 20% reduction in polar cloud-top CH_4 VMR between 45 – 90°N. A relatively small reduction in τ_2 north of 45°N is observed as predicted. All other parameter profiles are practically identical to those of Fig. 4.16 within error.

In theory, a further reduction in polar cloud-top CH_4 VMR, would account for some degree of the polar hood brightening that has been attributed to the 1 – 2-bar haze layer's increase in integrated opacity (τ_2). As a result, a slightly smaller increase in the retrieved τ_2 would be expected between the 2015 and 2021 HST/WFC3 observations. In order to test this prediction, retrievals were run for the 2021 HST/WFC3 observations with a moderately chosen 20% reduction in polar cloud-top CH_4 VMR between 45 – 90°N. The resulting retrieved latitudinal profile of τ_2 is shown in Fig. 4.17, with a comparison to the original 2021 retrieved profile and the 2015 retrieved profile. The predicted small reduction in τ_2 north of 45°N, when compared to no CH_4 depletion, is indeed observed, accompanied by a small reduction in p_2, with the other retrieved profiles seen to be identical, practically speaking, to those in Fig. 4.16. We therefore assert with confidence

that the question of stability in the cloud-top CH_4 VMR, in line with the degree of change probed, does not have a major bearing on the conclusions of these results.

4.3.2 HST/STIS

The HST/STIS dataset, possessing relatively high spectral resolution, provides an ideal set of complementary observations from which we can hold the results of the HST/WFC3 retrieval analysis described in Section 4.3.1 up to scrutiny. A second observation of Uranus, captured by STIS in 2012 [Sromovsky et al., 2014], was analysed with the same aerosol model [Irwin et al., 2022, 2023a] from Section 4.2, yielding very good fits that could be compared with the 2015 STIS retrievals and used to explore temporal variations. Fits at two representative latitudes bands for the 2012 observation are given in Fig. 4.18, carried out in an identical manner to those of Section 4.2.

With sound fits to both STIS observations in hand, we could now carry out a simple comparative forward-model analysis using the observations, with the goal of determining whether or not the spectral fingerprint of the polar hood's brightening observed between them could be reproduced by an increase in τ_2 alone (found as the solution from HST/WFC3 retrievals in Section 4.3.1). The spectral fingerprint of the brightening is displayed in Fig. 4.19, with Fig. 4.20 showing the same comparison at equatorial latitudes (20°S – 20°N), revealing no such brightening between the observations within error at equatorial latitudes. Inspection of Fig. 4.19 reveals a clear increase in radiance between the two polar spectra longwards of $\sim$0.6 μm, with a relatively large degree of brightening observed at wavelengths dominated by hydrogen CIA ($\sim$0.818 – 0.832 μm), suggesting that the main source of the brightening originates from aerosol layer changes as opposed to a reduction in cloud-top CH_4 VMR, which would not produce a significant brighten-

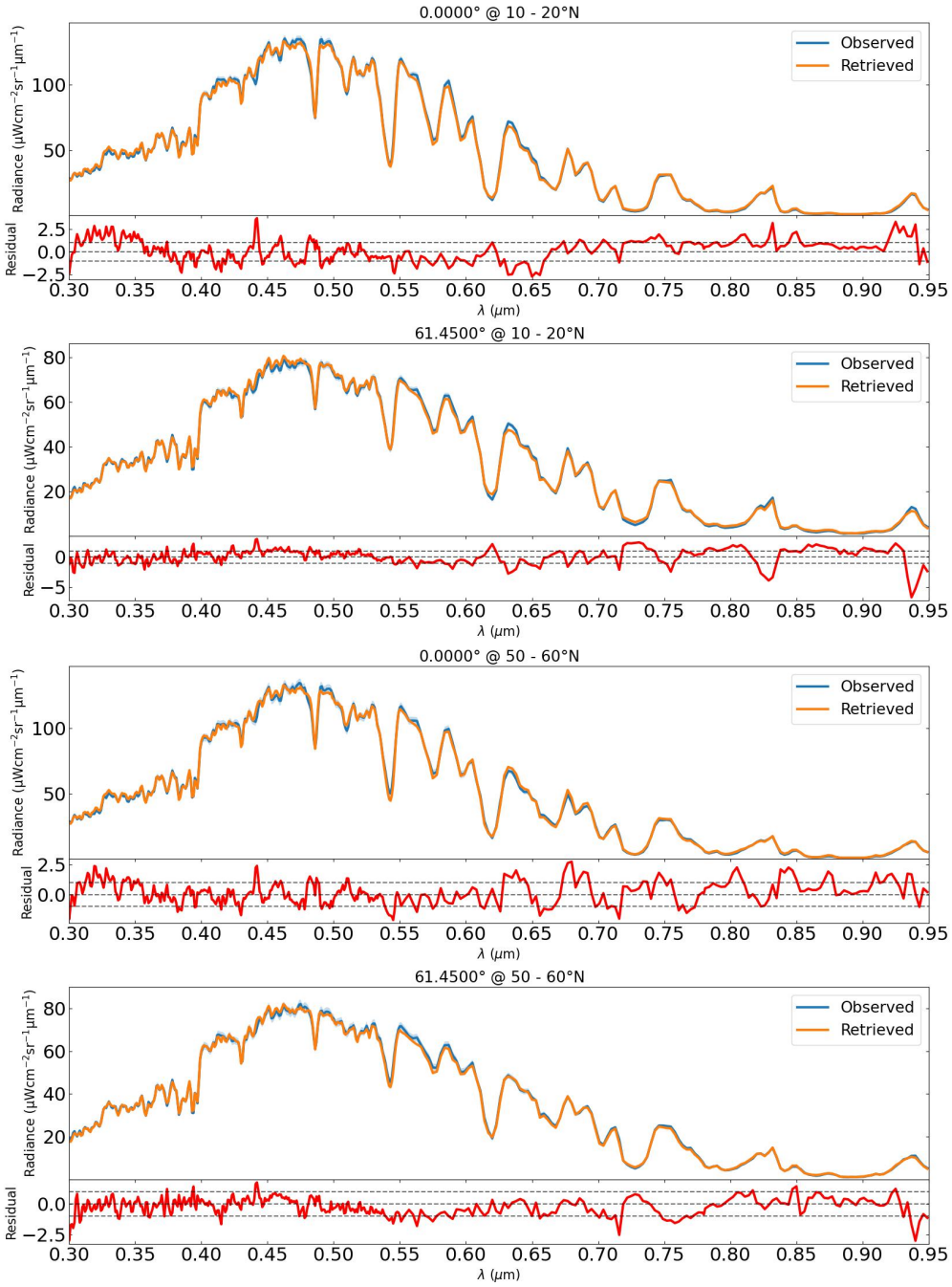


Figure 4.18: Plots of radiance against wavelength showing the spectral fits at the two chosen Minnaert zenith angles (0.0°, 61.45°) for retrievals carried out on the 2012 STIS observation at representative latitude bands of 10 – 20°N (top) & 50 – 60°N (bottom). Note, residuals are divided by the error on the measured spectrum.

ing at hydrogen-dominated wavelengths (see Fig. 4.21).

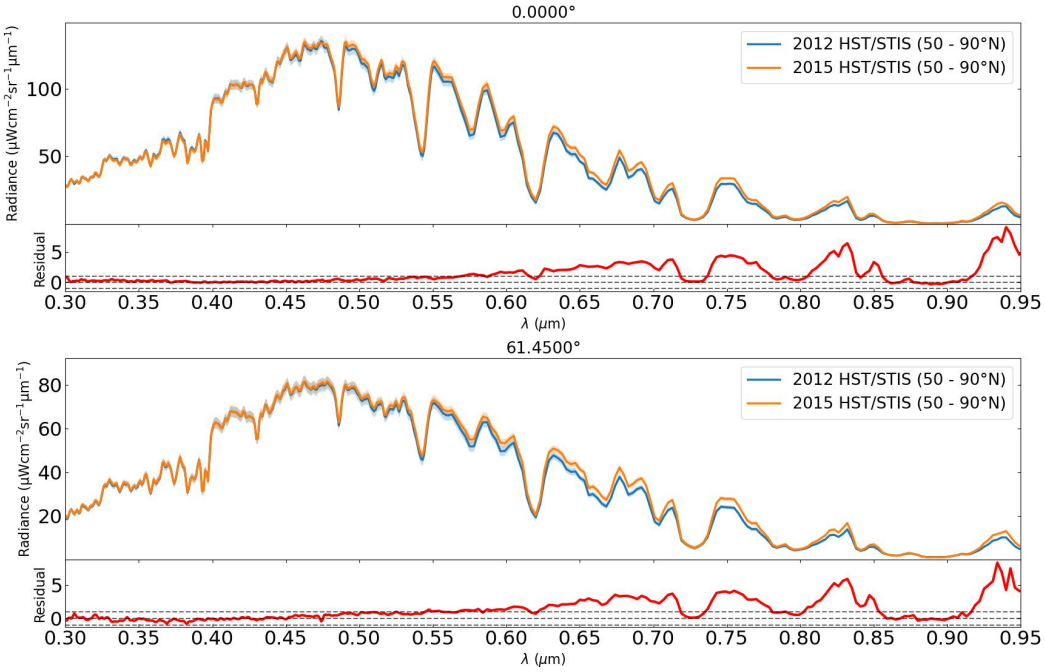


Figure 4.19: Plot of the 2012 and 2015 HST/STIS polar spectra extracted between 50°N and 90°N for our two chosen Minnaert zenith angles (0.0°, 61.45°). A clear increase in the radiance (i.e., a brightening) is observed longwards of ∼0.6 μm between the two spectra. The residuals provide a spectral fingerprint of this brightening. Note, residuals are divided by the error on the measured 2012 spectrum.

The forward-model analysis was carried out using NEMESIS by creating an initial template model with all parameters fixed to the values retrieved with the 2012 observation at polar latitudes (50 – 90°N). The model's values for different combinations of parameters were then altered and a forward model was run, with the resulting radiance spectrum plotted with the template model spectrum to identify the resulting changes, before comparing this to the spectral signature of the brightening (Fig. 4.19). This simple analysis has the additional advantage of highlighting any other potential parameter changes within our model that could be responsible for the spectral signature of the polar hood brightening, in the case that our HST/WFC3 solution was found to be inadequate. Upon testing

the obtained result of an increase in τ_2 alone, it was found to be an insufficient change to match the spectral signature observed in Fig. 4.19. The increase in τ_2, though producing a brightening at continuum wavelengths longward of $\sim$0.6 μm, results in a short-wave darkening that is not observed in the STIS spectra. The forward-model spectrum for this scenario is shown in Fig. 4.22.

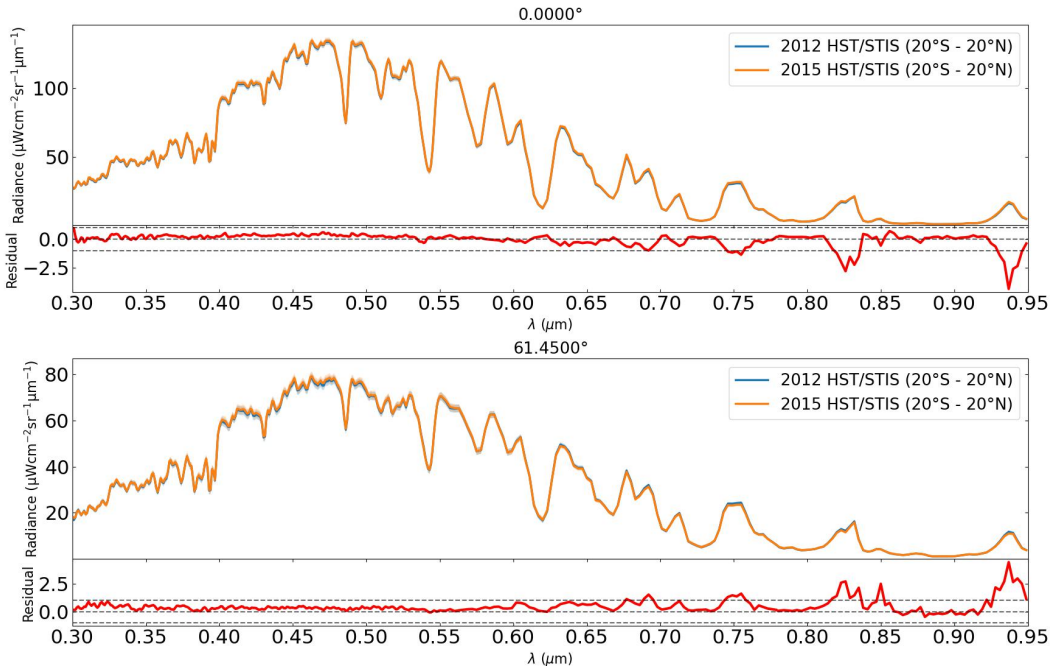


Figure 4.20: As Fig. 4.19 but for the equatorial region (20°S – 20°N). Almost no difference is observed between the two spectra within error. Note, residuals are divided by the error on the measured 2012 spectrum.

In order to be thorough, forward models for all combinations of parameters were tested, including changes in the imaginary refractive index spectra of the aerosol-1 and aerosol-3 layers. These included combinations with an increase in τ_2, as well as those without increasing τ_2. The simplest forward model returning the best spectral match to the observed brightening was found to be an increase in τ_2, in combination with a decrease in the imaginary refractive index spectrum of aerosol-2 (n_{i2}) at all wavelengths. This

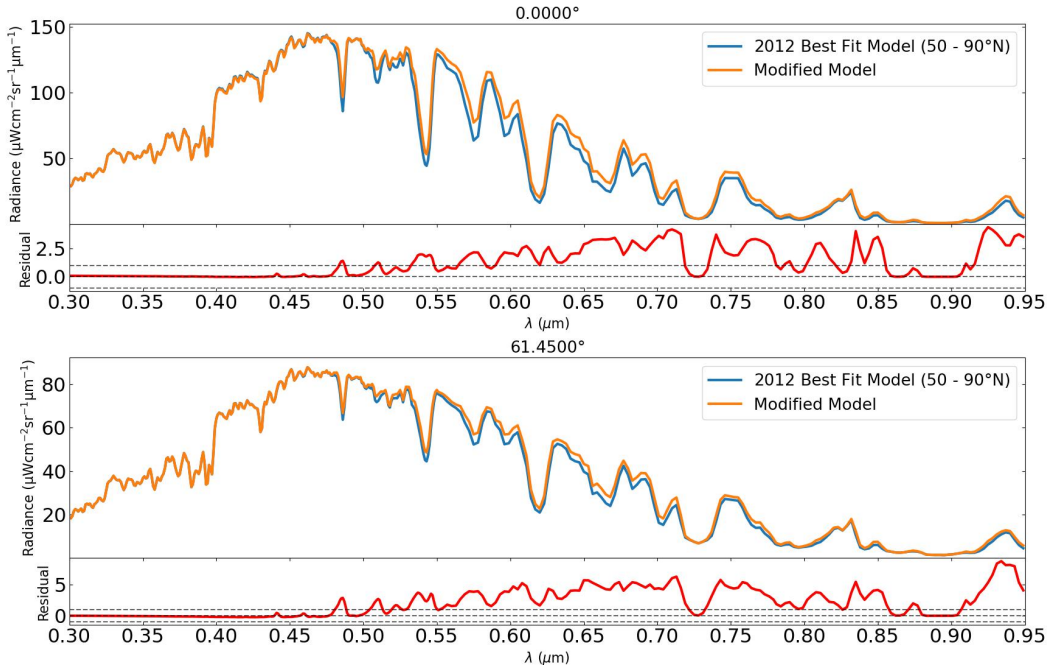


Figure 4.21: A comparison of the retrieved spectrum of the best-fit model at polar latitudes (50 – 90°N) carried out on the 2012 HST/STIS observation, to a forward model spectrum produced from a modified version of the best-fit model, testing a 50% decrease in cloud-top CH_4 VMR. A general brightening is observed longwards of ∼0.475 μm, but notably, residuals reveal minimal brightening at wavelengths dominated by hydrogen CIA (0.818 – 0.832 μm) in contrast to Fig. 4.19. Residuals are divided by the error on the best-fit model's measured spectrum.

solution preserves the brightening longwards of ∼0.6 μm produced by the increase in τ_2, with the decrease in n_{i2}, leading to more reflective aerosols, contributing to this long-wave brightening whilst simultaneously counteracting the short-wave darkening seen in Fig. 4.22. The spectrum for this forward model is displayed in Fig. 4.23.

With this comparative forward-model analysis in hand, latitudinal retrieval analyses were then conducted using both STIS observations. These were performed in an identical manner to the retrieval analysis of Section 4.2, but in this case, with n_{i2} as the only imaginary refractive index spectrum free to vary. The *a priori* values for n_{i1} and n_{i3} were

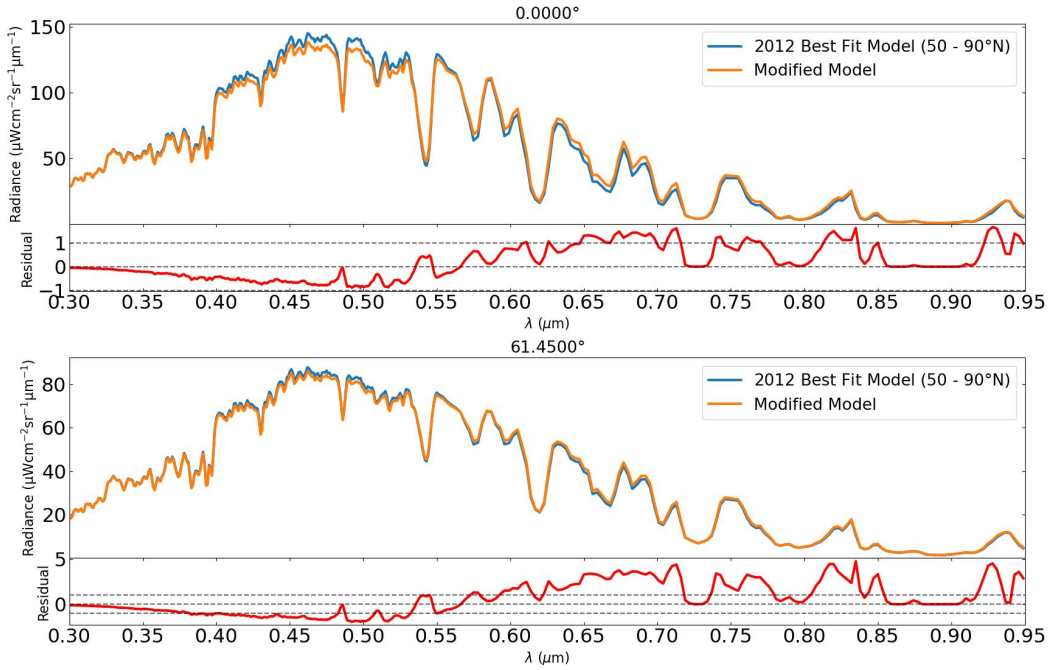


Figure 4.22: A comparison of the retrieved spectrum of the best-fit model at polar latitudes (50 – 90°N) carried out on the 2012 HST/STIS observation, to a forward model spectrum produced from a modified version of the best-fit model, testing a 41% increase in the integrated opacity of aerosol-2 (τ_2). The residuals show a clear difference in profile from those of Fig. 4.19, suggesting that an increase in τ_2 alone is insufficient to account for the observed polar hood brightening. Note, residuals are divided by the error on the best-fit model's measured spectrum.

fixed to those retrieved with the disc-averaged observations for all latitude bands. The resulting retrieved latitudinal profiles for the free parameters, excluding the imaginary refractive index spectra, are projected onto synthetic HST/STIS images of Uranus' full disc (the half-disc of the observations has been mirrored to create a full disc) to visually demonstrate the smoothly varying profiles at all visible latitudes in Figs. 4.24 & 4.25. The observed variations in the latitudinal profiles of τ_1, τ_2, and cloud-top CH_4 VMR are in line with proposed circulation models (e.g., Fletcher et al. [2020], see Fig. 1.9), being consistent with downwelling at high latitudes in both the middle and upper troposphere, resulting in depletions at high latitudes relative to low latitudes. The τ_3 profile shows

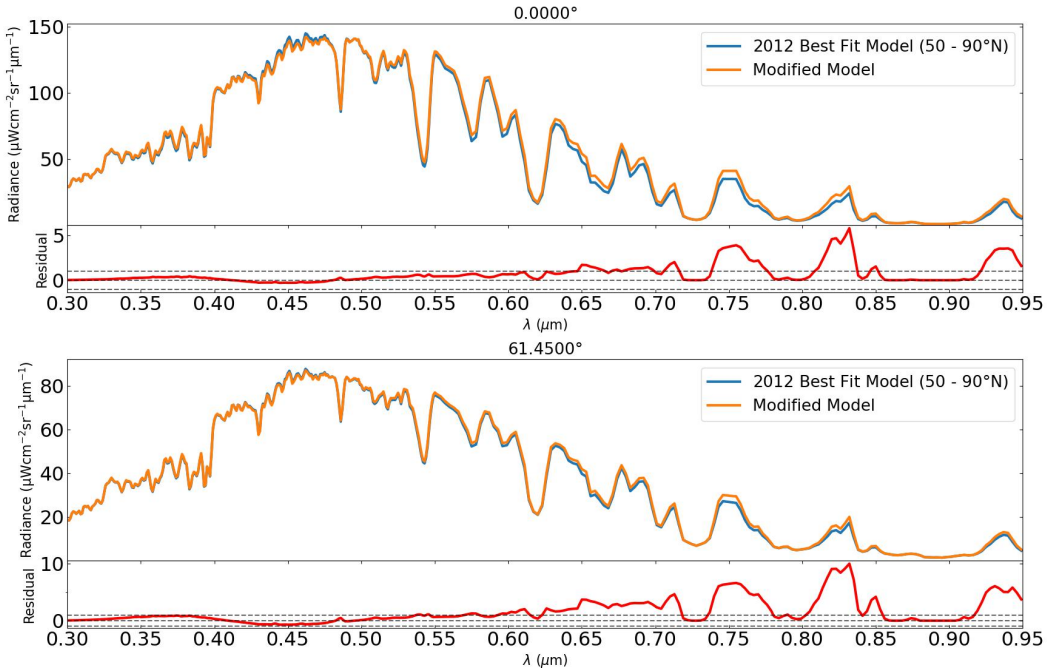


Figure 4.23: A comparison of the retrieved spectrum of the best-fit model at polar latitudes (50 – 90°N) carried out on the 2012 HST/STIS observation, to a forward model spectrum produced from a modified version of the best-fit model, testing a 33% increase in the integrated opacity of aerosol-2 (τ_2) in combination with a ∼33% decrease in the imaginary refractive index spectrum of aerosol-2 at all wavelengths. The residuals display a close match to those from Fig. 4.19. Note, residuals are divided by the error on the best-fit model's measured spectrum.

a concentration of haze at the equator, which smoothly decreases as we move toward the poles. Evidence for the upper tropospheric (0.1 – 1 bar) and stratospheric ($p < 0.1$ bar) circulations suggests upwelling at the midlatitudes and downwelling at the poles and equator [Roman et al., 2020, Fletcher et al., 2020]. The observed concentration of haze at the equator in our τ_3 profile suggests a transport of haze from higher latitudes, in line with the circulation described above. However, we do not see a concentration of haze at the north pole, which would also be expected. The reduction in constraint of our retrievals in the polar region may be partly responsible for this. However, speculatively speaking, this could be a sign of a faster rate of downwelling at the pole compared to the

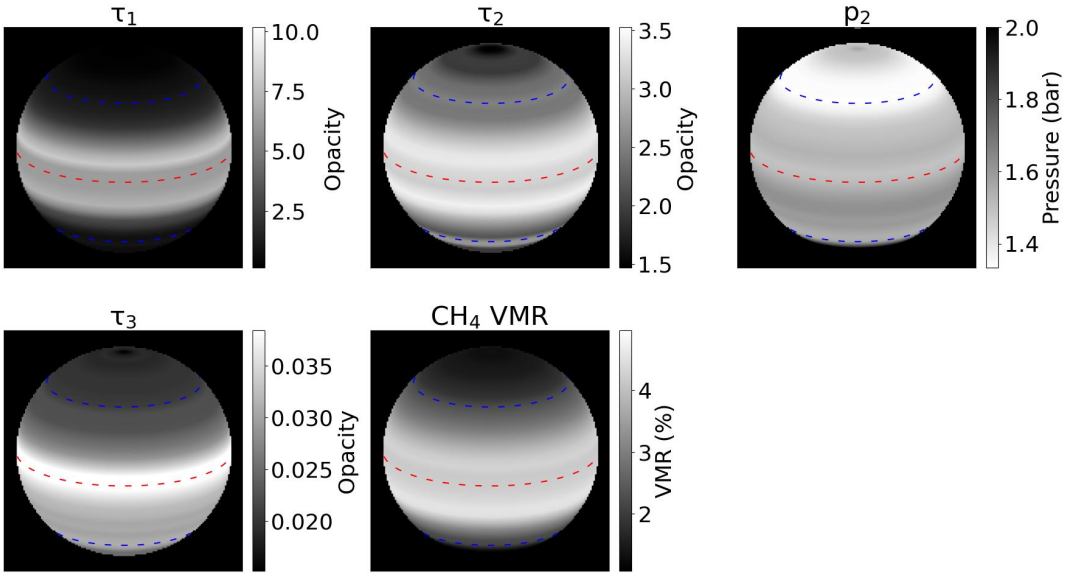


Figure 4.24: Synthetic images displaying the retrieved profiles of the free parameters (excluding the aerosol-2 imaginary refractive index spectrum shown in Fig. 4.28) from the 2012 HST/STIS retrievals: aerosol-1 integrated opacity (τ_1), aerosol-2 integrated opacity (τ_2) & pressure (p_2), aerosol-3 integrated opacity (τ_3), and cloud-top CH_4 VMR. The north pole is located near the top of the disc, the red dashed line represents the equator and the blue dashed lines represent $\pm 45°$. Note, the sharp decrease in τ_2 at the pole is likely an artefact.

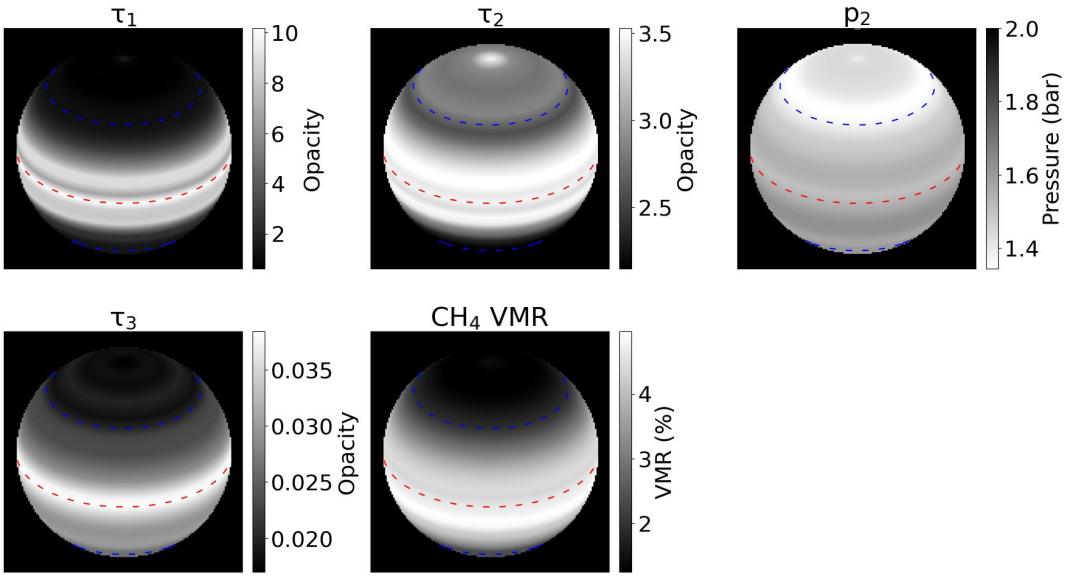


Figure 4.25: As Fig. 4.24 but displaying the retrieved profiles from the 2015 HST/STIS retrievals (the aerosol-2 imaginary refractive index spectrum is shown in Fig. 4.28). A comparison of the τ_2 image with that of Fig. 4.24 reveals an increase in the north polar region over time. Note, the sharp increase in τ_2 at the pole is likely an artefact.

equator, which could be due to the convergence of any haze transported polewards to a much smaller region than at the equatorial belt.

The retrieved latitudinal profiles are also plotted in Fig. 4.26 comparing the two sets of retrievals in the northern hemisphere only (latitudinal profiles for the retrieved aerosol-2 imaginary refractive index spectra are shown later in Fig. 4.28). A very similar increase in the 1 – 2-bar haze integrated opacity (τ_2), to that seen from the previous WFC3 retrievals (see Fig. 4.17), is observed north of 45°N (coincident with north polar hood latitudes). In this case, the average increase in τ_2 north of 45°N is 1.09 $\pm$ 0.08 at 0.8 μm ($\sim$33% increase). The two profiles for CH_4 VMR are seen to be largely similar, both displaying a reduction from equator to pole. However, though small, there is a distinct and consistent reduction observed between $\sim$40°N and 80°N, reducing by an average of 0.0019 $\pm$ 0.0003 ($\sim$10% decrease). This suggests that a small contribution to the observed temporal brightening is indeed due to a further depletion in polar cloud-top CH_4 VMR over time, and provides evidence against Sromovsky et al. [2019]'s conclusion of a general stability in the latitudinal profile.

At present, the behaviour of the polar cloud-top CH_4 VMR in the northern hemisphere is not entirely clear over short ($\leq$ 1 yr) or long timescales ($\geq$ a few years). It is plausible that there may be a degree of interseasonal variability in the cloud-top CH_4 VMR over either of these timescales in this dynamically active region. With only two datapoints in time captured 3 years apart available for comparison for the current season here, retrievals on a third observation, also obtained during Uranus' approach to northern summer solstice in 2030, and with comparable spectral resolution, would allow the cloud-top CH_4 VMR profile to be probed further, and the conclusion of a general stability to be further scrutinised.

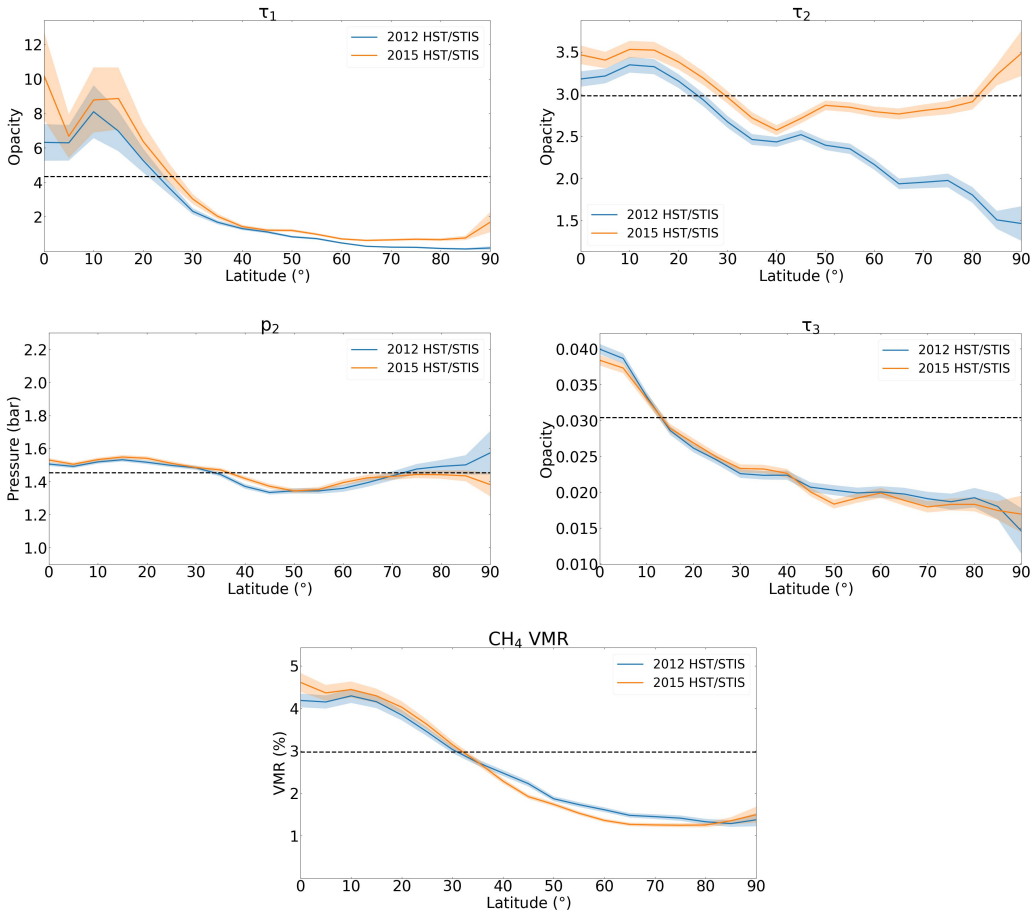


Figure 4.26: Retrieved latitudinal profiles of the free parameters (except the aerosol-2 imaginary refractive index spectrum shown in Fig. 4.28) from the 2012 and 2015 HST/STIS observations: aerosol-1 integrated opacity (τ_1), aerosol-2 integrated opacity (τ_2) & pressure (p_2), aerosol-3 integrated opacity (τ_3), and cloud-top CH_4 VMR. Comparisons of the two profiles reveal increases in τ_1 and τ_2 north of 45°N, and a decrease in cloud-top CH_4 VMR between ∼40 – 80°N. The black dashed lines represent the *a priori* values for each parameter informed from the Irwin et al. [2022] holistic model.

If retrieval work on new observations were to reveal a further reduction in polar cloud-top CH_4 VMR, it would suggest that the observed trend from our retrieval work is a consistent one over time, hinting at some kind of dynamical change, likely linked to the

orbital phase (i.e., a seasonal phenomenon). On the contrary, if an *increase* in cloud-top CH_4 VMR with respect to the profile retrieved using the 2015 HST/STIS observation in this work were retrieved, support for the picture of a 'general stability' in the latitudinal profile would be concluded, suggesting a degree of interseasonal variability about some mean profile. The acquisition of an observation of Uranus with the VLT/MUSE instrument in 2021 enables this very question to be explored, which will be presented later in Chapter 5. Additionally, an increase in the integrated opacity of aerosol-1 (τ_1) by an average of 0.6 $\pm$ 0.1 at 0.8 μm north of 45°N is observed, incident with polar hood latitudes. Note a small increase in τ_1 just south of the polar hood is also observed between $\sim$25 – 40°N, which could or could not be related to the thickening at polar hood latitudes.

When analysing this retrieved thickening over time, a marked difference is observed. For the region south of the hood located between $\sim$25 – 40°N, the average retrieved increase in τ_1 is $\sim$20%, whereas north of 45°N, coincident with the hood, the average increase is almost 3 times as large at $\sim$56%. An increase in τ_1 is observed in the retrieved profile as we move towards the pole, starting at a $\sim$23% increase at 30°N, and ending with a $\sim$79% increase at 90°N. It is plausible that this could be a signal of a change in the vertical motion of the circulation at the pole [Akins et al., 2023], or an increased dynamical transport of haze polewards at aerosol-1 pressure levels ($p \sim 4$ – 7 bar). It is worth noting that these two regions of thickening are separated by a region of no change in the integrated opacity of aerosol-1. This region lies within the two latitude bands that simultaneously capture the boundary of the polar hood and the darker midlatitudes (bands centred at 40°N & 45°N).

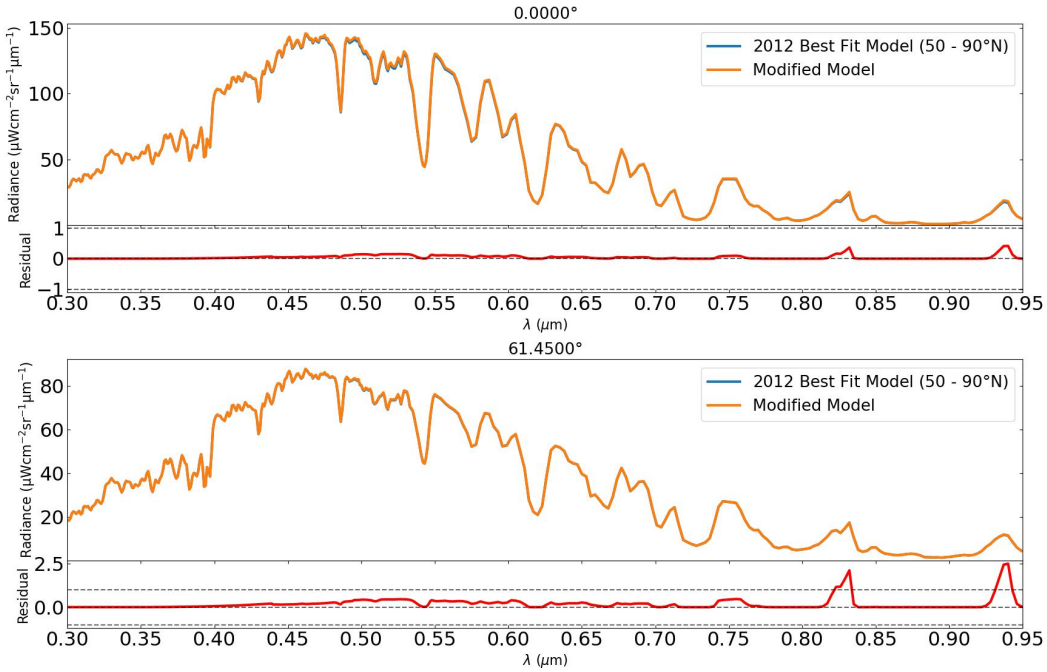


Figure 4.27: Plot comparing the best-fit model retrieved spectrum to the 2012 HST/STIS observation at polar latitudes (50 – 90°N) with a forward model spectrum of a modified version of this model, testing a 56% increase in the integrated opacity of the deep haze (τ_1) only. We see from the residuals that there is only significant change to the spectrum in two narrow regions between 0.8 – 0.95μm at 61.45°. Note, residuals are divided by the error on the best-fit model's measured spectrum.

To test whether or not this thickening of the deep haze is significant, a forward model with a 56% increase in τ_1 was run (matching the average retrieved increase north of 45°N) and compared to the best-fit model at polar latitudes. The resulting spectra are displayed in Fig. 4.27, and are seen to be largely the same. However, at the long end of the wavelength range ($>$ 0.8 μm), two spikes in radiance (brightness) are observed in CH_4 absorption windows at the 61.45° zenith angle. When compared to the residuals in Figs. 4.19, 4.22 & 4.23, we see that this contribution is very localised and small compared to the changes in aerosol-2, and therefore very unlikely to be a significant factor in the hood's observed brightening.

The retrieved latitudinal profiles for the imaginary refractive index spectra of aerosol-2 (n_{i2}), displayed in Fig. 4.28, show a marked decrease between the 2012 and 2015 observations in the 0.7, 0.8, 0.9 & 1.0 μm wavelength channels north of $\sim$40°N, with the largest change occurring for the majority of these channels at 60°N. These decreases in n_{i2} denote less absorption by the aerosols, i.e., an increase in the single-scattering albedo and more reflective aerosols, at these wavelengths within the 1 – 2-bar haze layer localised to the north polar hood. For the other four wavelength channels, 0.3 μm, 0.4 μm, 0.5 μm and 0.6 μm, no clear temporal trends are observed.

A comparison of the profiles within Figs. 4.16 & 4.17 obtained from the HST/WFC3 dataset with those of Fig. 4.26 (shown in Fig. 4.29) reveals several notable similarities and differences. In particular, a comparison of the 2015 retrieved profiles of each dataset proves useful in spotting any discrepancies. With the two sources of data possessing different properties (e.g., spectral resolution), as well as being captured and processed in completely different manners, we expect some variation in the retrieved profiles despite them being temporally close. It can be seen that very similar profiles for the opacity (τ_2) and pressure (p_2) of the 1 – 2-bar haze are retrieved, with HST/STIS showing slightly more variation in p_2. However, noticeable differences are observed in the profiles of the deep haze opacity (τ_1) and the extended haze opacity (τ_3). Although similar in shape, the latitudinal variations of the τ_1 profiles show two marked differences. Firstly, the consistently observed peak in opacity is shifted equatorwards by $\sim$10° in the case of HST/STIS, lying at $\sim$15°N. This could be a result of the underlying differences between the data collection and processing (e.g., stepping the STIS slit across the disc resulting in Uranus rotating by >45° during observation). Secondly, the magnitude of the retrieved values for τ_1 are seen to be much larger for HST/WFC3, approximately 3 – 4$\times$ those ret-

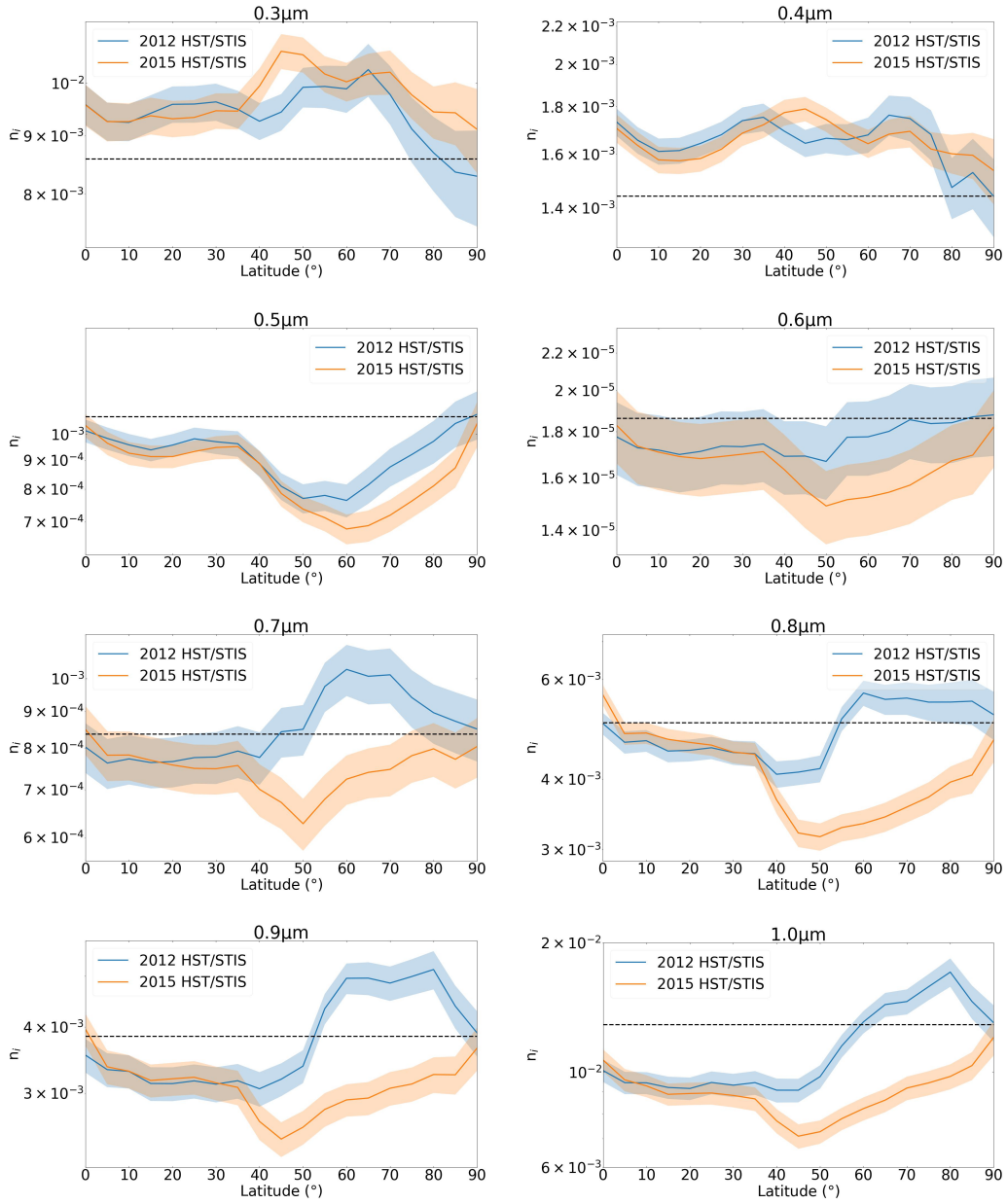


Figure 4.28: Retrieved latitudinal profiles of the aerosol-2 imaginary refractive index spectrum (n_{i2}) at each wavelength interval from our 2012 & 2015 HST/STIS retrievals. A clear decrease in n_{i2} is observed north of ∼40°N for wavelengths longwards of ∼0.7 μm. A decrease in n_{i2} is also seen at 0.5 μm between ∼60°N and 80°N. For the most part, the largest reduction occurs for the latitude band centred at 60°N. The black dashed lines represent the *a priori* values.

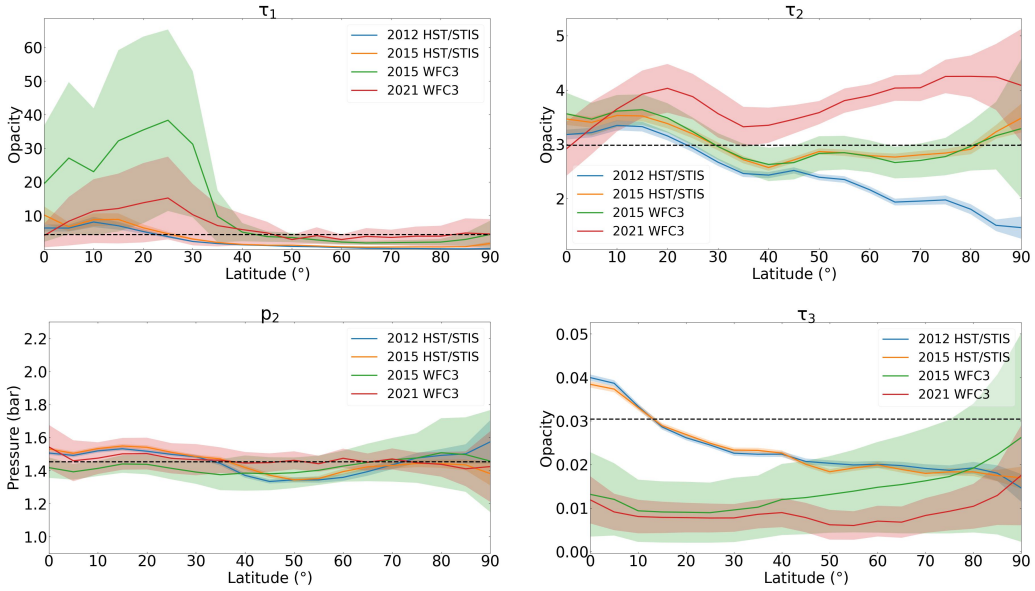


Figure 4.29: A comparison of the latitudinal parameter profiles for the vertical aerosol model in the northern hemisphere retrieved using the HST/STIS dataset and the 2015 & 2021 HST/WFC3 datasets: aerosol-1 integrated opacity (τ_1), aerosol-2 base pressure (p_2) and integrated opacity (τ_2), and aerosol-3 integrated opacity (τ_3). The black dashed lines represent the *a priori* values for each parameter informed from the Irwin et al. [2022] holistic model.

rieved for HST/STIS at their maxima. It was revealed from the HST/STIS that a strong correlation exists between τ_1, the CH_4 VMR, and the 1 – 2-bar haze imaginary refractive index spectrum. In the HST/STIS retrievals, these correlated parameters are free to vary when fitting to the much higher resolution spectra. As a result, much better constraint is achieved on the τ_1 profile, which, no longer attempting to compensate for a lack of freedom in these correlated parameters, leads to smaller opacity values. Note that the retrieved opacity values at low latitudes are large enough such that they are observationally indistinguishable between the datasets and therefore not contradictory.

The retrieved extended haze opacity (τ_3) profiles exhibit the most significant differences between the two 2015 observations. A concentration of haze is observed at the equa-

tor in the case of HST/STIS, which smoothly reduces towards the pole where it reaches a minimum, whereas the observed variation for the HST/WFC3 profile is the opposite. We see a roughly flat profile at low latitudes which begins to smoothly increase in the midlatitudes, reaching its maximum value at the pole, where it tends back towards the *a priori*. A solution to this discrepancy is found from penultimate retrievals run on the HST/STIS dataset, where the additional parameters that appear to contribute to the polar hood brightening (i.e., CH_4 VMR and n_{i2}) and τ_1 were individually fixed, as well as the case where all three of these parameters were simultaneously fixed. In each of these scenarios, the variation in the τ_3 profile was observed to be virtually identical, consistent with the profile in the final retrieval shown in Fig. 4.26, suggesting that the HST/STIS results present a more reliable profile. In addition, scanning the 0.727 μm UVIS filter images in Fig. 2.2, which probes pressure levels at high altitudes in the atmosphere ($\lesssim$ 1 bar), one observes a bright band encircling equatorial latitudes for both datasets, signifying a concentration of haze here compared to other latitudes, casting further doubt on the HST/WFC3 retrieved τ_3 profiles. It should be noted that the large errors on the 2015 WFC3 τ_3 profile means that it is also consistent with large opacity at the equator reducing towards a minimum at the pole. The lack of clear agreement between the retrieved latitudinal variations is likely the result of the WFC3 retrieval compensating for a lack of freedom in fixed parameters (i.e., n_{i2} and CH_4 VMR) combined with the limited spectral resolution of the data providing less constraint.

Finally, the retrieved n_{i2} wavelength spectra are displayed at representative tropical and polar latitudes in Fig. 4.30 for convenient comparison of the change over latitudes with time. The laboratory n_i wavelength spectra of Mahjoub et al. [2012] for Titan aerosol analogues (tholins), seeded in different concentrations of CH_4 gas, are also included for

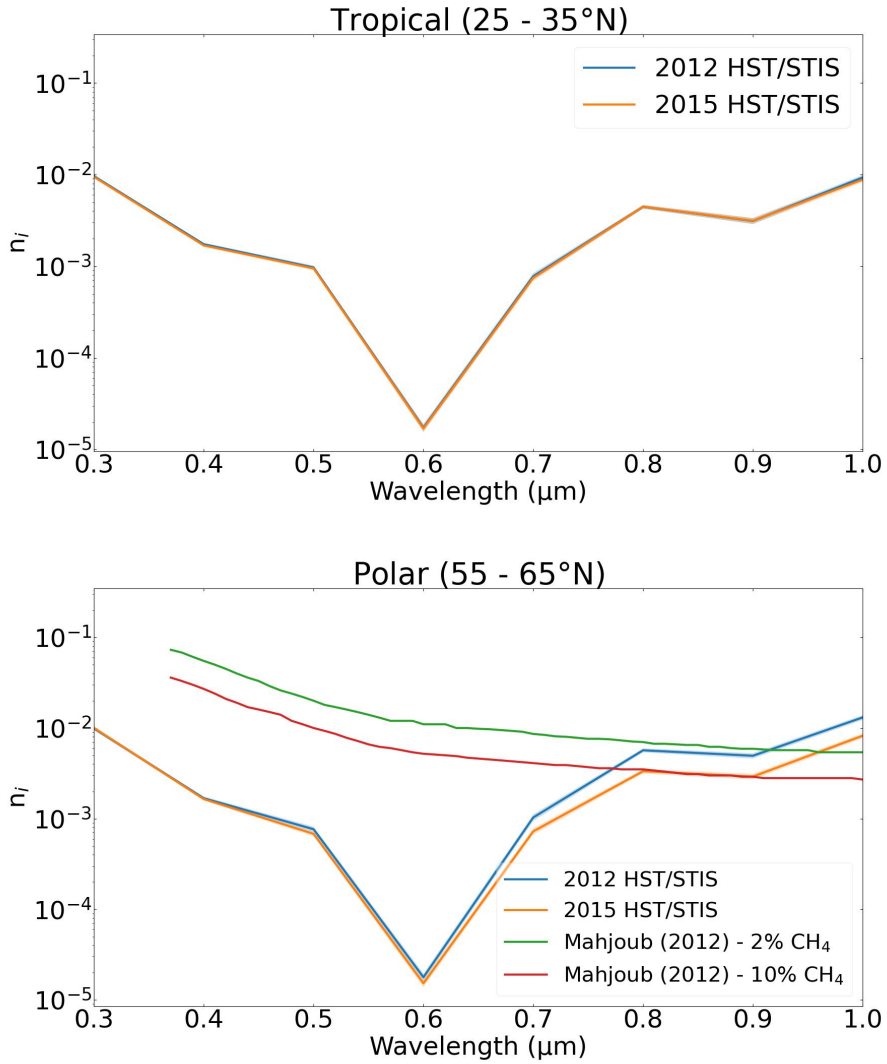


Figure 4.30: Comparison of the retrieved aerosol-2 imaginary refractive index spectra (n_{i2}) against wavelength at representative tropical (25 – 35°N) and polar (55 – 65°N) latitudes from the 2012 and 2015 HST/STIS retrievals. A polar reduction in n_{i2} is observed over time for wavelengths longwards of ∼0.6 μm. The laboratory n_i spectra of Mahjoub et al. [2012]'s Titan aerosol analogues (tholins), seeded in environments with concentrations of 2% and 10% CH_4 gas, are also included for comparison, for which higher CH_4 gas concentrations lead to reduced n_i (i.e., more reflective particles) at all wavelengths. The HST/STIS n_i spectra show a reduction by a comparable degree at long wavelengths where instead a relatively small *decrease* in CH_4 VMR is observed. This highlights the complex nature of *in situ* atmospheric processes and the interplay between the parameters involved.

comparison. It is important to note that with only two HST/STIS observations (i.e., two snapshots in time), it is difficult to assert with a high degree of confidence that the parameters uniquely probed by these retrievals (i.e., cloud-top CH_4 VMR & n_{i2}) reflect their trends over longer timescales. Further observations with comparable spectral resolution and spectral coverage are necessary to provide further context and support for our results, which is addressed in Chapter 5 using the VLT/MUSE dataset.

Viewing the results presented in this Chapter as a whole, a solution for the evolution of the north polar hood is obtained. Within the framework of the chosen vertical aerosol model [Irwin et al., 2022, 2023a], the main contributors to the temporal brightening of the hood were found to be:

1. A thickening of the 1 – 2-bar haze layer north of ∼45°N.
2. A decrease in the imaginary refractive index spectrum of the 1 – 2-bar haze north of ∼40°N and longwards of ∼0.6 μm.

4.4 Mechanisms

With a solution in hand for the physical changes responsible for the evolution of the polar hood, the focus is now turned to exploring the plausible mechanisms underlying these physical changes.

A thickening of the 1 – 2-bar haze layer north of ∼45°N could be predominantly caused by increased production and settling of haze particles at these latitudes, or alternatively by a transport of haze from low to high latitudes. The study of Toledo et al. [2019], employing microphysical simulations to constrain the structure, formation, and transport of haze within the atmosphere of Uranus, thus provides very useful constraints with which

to orient the search for a plausible mechanism. Their simulations returned timescales of $\gtrsim$ 30 years for haze particles to grow and settle out at pressures $>$ 0.1 bar, far too slow to account for the changes in haze structure observed in the northern hemisphere post-equinox (i.e., after 2007). This led Toledo et al. [2019] to conclude that atmospheric dynamics are likely the main factor responsible for the observed changes in the spatial and temporal distribution of haze over the poles. Additionally, the changes observed through equinox were faster than expected when considering radiative timescales [Conrath et al., 1990] and photochemical timescales [Moses et al., 2018]. One plausible mechanism put forward by Toledo et al. [2019] to explain the observed variations is a meridional stratospheric transport of haze particles.

Further work on the circulation of Uranus carried out by Fletcher et al. [2020] accounts for the results from studies of the zonal winds of Uranus, latitudinal variations, stratospheric chemical tracers, and many other considerations. This model (see their Fig. 8 for more details) is composed of several vertically stacked circulation cells, which includes a stratospheric meridional circulation producing downwelling at the equator and poles and upwelling at the midlatitudes. This type of circulation would enable a thickening of the 1 – 2-bar haze layer via the transport of haze particles from the midlatitudes to the poles, where upon descent, they would settle and accumulate at the 1 – 2-bar region of static stability [Irwin et al., 2022]. The stacked circulation model of Fletcher et al. [2020] is consistent with the findings of Toledo et al. [2019], as well as the other observational studies considered in its construction, and is also in line with the latitudinal variations found from earlier retrievals displayed in Figs. 4.24, 4.25 and 4.26. However, general circulation models of Uranus' atmosphere at the time of writing are scarce, and they are yet to produce results in support of proposed circulation models (e.g., Karkoschka and

Tomasko [2009], Sromovsky et al. [2014], Fletcher et al. [2020]), highlighting the need for further work in this area. Nonetheless, a stratospheric meridional circulation presents a good candidate for a plausible mechanism underlying the thickening of the 1 – 2-bar haze layer.

The retrieved reduction in polar cloud-top CH_4 VMR presents a curious result. As the season progresses and the northern hemisphere of Uranus receives increasing insolation (i.e., receives more energy over time), this would lead to a progressive heating of the north pole, likely causing a slowing of any meridional circulation that involves downwelling at high latitudes. Such an effect would be compounded by Uranus' low internal source of heat [Pearl et al., 1990], providing little energy, relatively speaking, to drive atmospheric dynamics from deeper within the atmosphere. As a result, changes in insolation are likely to have greater influence over the circulation. If there is indeed a reduction in the rate of downwelling at polar latitudes via heating, we would expect less depletion of the cloud-top CH_4 VMR, assuming that the depletion is the result of a tropospheric meridional circulation cell exhibiting downwelling at the poles. This is the exact opposite of the retrieval results presented in Section 4.3.2. However, this conflict can be resolved by proposing a scenario in which the stratospheric meridional circulation cell, put forward as the mechanism underlying the thickening of the 1 – 2-bar haze, undergoes this slowing effect via heating, but the tropospheric circulation cell below is not significantly affected (see Fig. 1.9). However, this would leave the cloud-top CH_4 VMR unchanged, requiring an alternative explanation for the retrieved reduction in VMR. It should be noted that at the time of writing, no significant changes in stratospheric temperature have yet been observed. Continuing the exploration of this model, the slowing of the stratospheric cell would lead to a reduction in the rate of haze transport polewards.

This would mean less haze particles downwelling and settling out over time at polar latitudes, seeding the 1 – 2-bar haze layer [Irwin et al., 2022]. If this is the case, a reduction in the rate of thickening of the aerosol-2 haze layer at high latitudes would be expected. To search for a signal of this effect, the average retrieved rate of change in τ_2 between consecutive years at polar hood latitudes (45 – 90°N) was calculated. This resulted in no definitive trend being observed in the rate of brightening over time, but did not rule it out (see Fig. 4.31). However, earlier in this Chapter (see Section 4.1) a decrease in the rate of brightening at polar hood latitudes was observed over the entire timespan of the HST/WFC3 dataset (see Fig. 4.9). This result provides plausibility for this scenario.

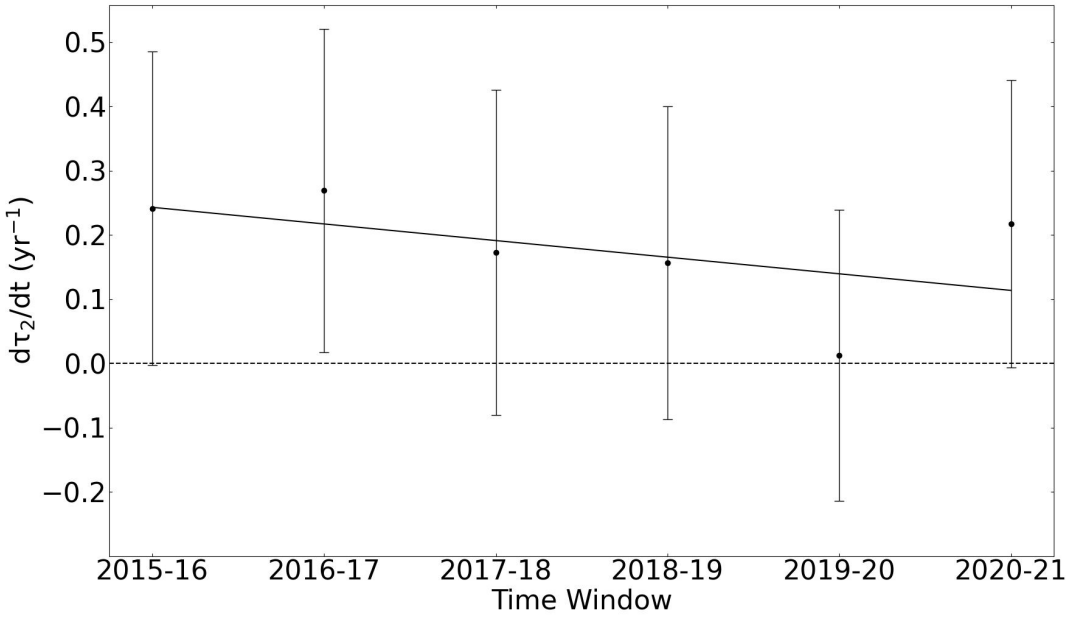


Figure 4.31: Plot showing the average rate of change in the integrated opacity of aerosol-2 (τ_2) from HST/WFC3 retrievals (τ_2 plot in Fig. 4.15) against each one-year time window considered. Datapoints were calculated by averaging the change in τ_2 across polar hood latitudes (45 – 90°N) between consecutive years. The linear best-fit line equation is given by: $d\tau_2/dt = -0.026t + 0.243$. The results are consistent with no change but do not rule out a slowing in the retrieved rate of thickening.

The 1 – 2-bar haze layer lies at pressure levels for which CH_4 is expected to condense in the atmosphere of Uranus. We therefore expect its aerosols to act as cloud condensation nuclei (CCN), i.e., surfaces readily available for CH_4 condensation to occur. This would lead to an accumulation of CH_4 ice, increasing the mass of the aerosols as CH_4 ice continues to condense. In addition to this increase in mass, the accumulation of CH_4 would in all likelihood lead to a change in the optical properties of the aerosols (e.g., causing them to be more reflective or absorbing at particular wavelengths). Unlike its sister planet Neptune, large blankets of CH_4 cloud are not observed within Uranus' atmosphere [Irwin et al., 2017, 2022]. A plausible explanation for their absence is that the aerosols rapidly reach a 'critical mass' as they accumulate CH_4 ice, whereby they begin to descend under gravity and precipitate out of the 1 – 2-bar haze layer [Irwin et al., 2022]. Estimates of CH_4 condensation in Ice Giant atmospheres put CH_4 ice particles at 1 – 2 bar growing to a size of $\sim$5 mm in as little as $\sim$100s [Carlson et al., 1988]. The precipitating CH_4 ice particles, falling deeper into the atmosphere where temperatures are increasing, would then sublimate, freeing the photochemical haze particles at their cores, which can then go on to act as CCN to seed H_2S condensation in the 4 – 7 bar region [Irwin et al., 2022]. It should be noted that the polar depletion in cloud-top CH_4 VMR would alter the CH_4 condensation level within the atmosphere, pushing it to higher altitudes (i.e., to a lower pressure) for the same temperature. Assuming significant condensation is still occurring, less condensation would take place at the same pressure compared to equatorial latitudes, i.e., the accumulation of CH_4 ice and precipitation of aerosols would be slower at high latitudes. In the extreme case, if the atmospheric circulation exhibits strong subsidence at the latitude in question, CH_4 condensation may be suppressed entirely. We therefore ask the question, what effect would a thickening of the 1 – 2-bar haze layer have on this process?

The thickening of the 1 – 2-bar haze layer at polar hood latitudes with time, via the accumulation of haze particles in this region. would provide an increasing number of CCN to seed CH_4 condensation. This would likely result in increasing numbers of aerosols precipitating out of the haze layer per unit of time, assuming a constant rate of condensation. An initial consequence of this increasing CH_4 condensation would be a progressive reduction in the surrounding CH_4 gas VMR, as it is transformed into CH_4 ice. Another consequence of this would be an increasing number of haze particles acting as CCN to seed H_2S condensation below. Therefore we have a plausible mechanism that can explain the retrieved reduction in polar cloud-top CH_4 VMR and the retrieved thickening of the deep haze layer found from HST/STIS retrievals. However, the decrease in polar cloud-top CH_4 VMR would likely counteract the increasing condensation, slowing down the rate of CH_4 condensation with time. This is not only due to a lower amount of CH_4 gas being readily available for condensation over time, but also due to this reduction in VMR resulting in the condensation level of CH_4 being shifted progressively higher into the atmosphere, compounded by a lower amount of latent heat from condensation being produced per unit of time. This reduction in the rate of condensation would likely result in the 1 – 2-bar aerosols growing more slowly in mass, causing them to remain within the layer for a longer period of time before precipitation occurs. These longer-lasting aerosols, being smaller in size for longer periods, could result in a change in the aerosol optical properties over time. This mechanism could explain the retrieved signature of a decrease in the imaginary refractive index (n_i) spectrum over time (i.e., an increase in single-scattering albedo and reflectivity of the aerosols).

This scenario is speculative as it is not currently known what the spectral identity of an increase in reflectivity of these aerosols would look like, and therefore how it would

match up to the retrieved signature of an increase in reflectivity longwards of $\sim$0.6μm. However, a study undertaken by Mahjoub et al. [2012] on the influence of CH_4 gas concentration on the measured n_i spectra when seeding Titan aerosol analogues (tholins) in the laboratory provides plausibility to this scenario. Increasing concentrations of CH_4 gas were found to cause a uniform decrease in the n_i spectrum over the 0.37 – 1.0 μm wavelength range of the tholins. A comparison of their n_i spectra with the retrieved spectra from the earlier HST/STIS retrievals was shown in Fig. 4.30, where it was noted that the change in CH_4 concentration is the opposite in our results (i.e., a similar decrease in n_i is seen for a relatively small *decrease* in CH_4 VMR). An increase from 2% to 10% in CH_4 gas concentration and a 0.0019 (or 0.19%) decrease in CH_4 VMR leading to comparable absolute changes in n_i suggests that other factors are likely more important in the case of Uranus' atmosphere. Further work modelling the spectral effects of CH_4 ice particles would be useful in exploring the plausibility of this explanation.

In conclusion, a scenario in which the thickening of the 1 – 2-bar aerosol layer leads to a decrease in polar cloud-top CH_4 VMR, which in turn slows down the rate of CH_4 condensation, to a degree whereby the number of particles precipitating out per unit of time is still increasing over time, simultaneously explains the reduction in polar cloud-top CH_4 VMR, the thickening of the deep haze layer, and the increase in reflectivity of the aerosols of the 1 – 2-bar haze layer. The proposed mechanism responsible for the retrieved physical changes, leading to a temporal brightening of the north polar hood, is a stratospheric meridional circulation exhibiting downwelling at the poles that is slowing down with time. This slowing is proposed to be due to a heating of the pole via increasing insolation of the northern hemisphere as the season progresses towards northern summer solstice. This is one of several plausible explanations, with more work certainly being

needed to provide evidence in support of this particular hypothesis, e.g., modelling of CH_4 ice particles and the detection of upper tropospheric/stratospheric heating.

4.5 Summary

The past ∼37 years of observation of the atmosphere of Uranus have tracked the evolution of its polar hood feature, firstly in the southern polar region and, a few years after Uranus passed through northern spring equinox, in the northern polar region, suggesting that this large long-lived feature is a seasonally-dependent phenomenon (i.e., it is governed by the orbital phase of Uranus). The results and analysis presented in this Chapter are in agreement with this picture of seasonal dependence, leading us to a solution with which to explain the observed post-equinox brightening of the north polar hood.

A Minnaert analysis carried out on the HST/WFC3 dataset confirmed an absolute brightening of the hood, ruling out any significant contributions from viewing geometry-related brightening effects. The observed depletion in cloud-top CH_4 VMR at polar latitudes [Karkoschka and Tomasko, 2009, Sromovsky et al., 2014, 2019], resulting in less absorption in the polar region, is one of the main contributors to the brighter appearance of the north polar hood when compared to equatorial latitudes [Toledo et al., 2018]. However, it was not entirely clear if this depletion also played a significant role in the observed brightening of the polar hood over time. Sromovsky et al. [2019], analysing HST/STIS and near-infrared images from Keck's Near Infrared Camera-2 (NIRC-2) instrument, refuted this as a significant source of the temporal brightening, finding wavelengths dominated by hydrogen absorption to also be increasing in brightness. The results in this Chapter provide further support for Sromovsky et al. [2019]'s conclusion, finding the spectral signature of the brightening to be mainly at wavelengths of low CH_4 absorption

or wavelengths dominated by hydrogen absorption (0.818 – 0.832 μm) (see Figs. 4.19 & 4.21), leading us to the same conclusion that changes in the aerosol layer scattering properties are the predominant cause of the brightening.

The HST/WFC3 & HST/STIS datasets presented an ideal complementary set of observations with which to carry out the analysis, providing both a wide temporal window and sufficient spectral resolution and coverage between them. Latitudinal retrieval analyses carried out on both of these datsets led to a solution for the evolution of the north polar hood. Within the framework of the chosen vertical aerosol model [Irwin et al., 2022, 2023a], it was found that the 1 – 2-bar haze layer (aerosol-2 layer) is the main contributor to the observed brightening of the north polar hood over time. This is due to a thickening of the layer north of $\sim$45°N and an increase in reflectivity of its aerosols north of 40°N and longwards of $\sim$0.6 μm. In addition, a small contribution to the brightening stemmed from a reduction in cloud-top CH_4 VMR north of $\sim$40°N.

Plausible mechanisms were then explored to explain these physical changes using the scientific literature as a guide to further constrain the possibilities. The temporal slowing of a stratospheric meridional circulation was chosen as a good candidate for the underlying mechanism, leading to a thickening of the 1 – 2-bar haze layer that slows with time, and plausibly, although speculatively, leading to a reduction in polar cloud-top CH_4 VMR, a thickening of the deep haze layer, and an increase in reflectivity of the 1 – 2-bar haze aerosols. This is one of many plausible explanations, with more work being needed to provide evidence in support of this hypothesis.

The main conclusions of this Chapter are as follows:

1. A Minnaert limb-darkening analysis of the HST/WFC3 dataset confirmed an ab-

solute brightening of the north polar hood, ruling out viewing geometry-related brightening effects as the main cause, with a provisional reduction in the rate of polar hood brightening with time also observed.

2. Latitudinal retrieval analyses on the HST/WFC3 & HST/STIS datasets find the main contributors to the brightening of the north polar hood, within the framework of the holistic Irwin et al. [2022, 2023a] vertical aerosol model, to be:

   - a thickening of the aerosol-2 layer - finding an average increase in integrated opacity of 1.09 $\pm$ 0.08 north of $\sim$45°N at 0.8 μm (a $\sim$33% average increase) between 2012 and 2015.

   - an increase in reflectivity of the aerosol-2 particles north of $\sim$40°N and longwards of $\sim$0.6 μm between 2012 and 2015.

3. HST/STIS retrievals also reveal a thickening of the deep haze (aerosol-1) layer, retrieving an average increase in integrated opacity of 0.6 $\pm$ 0.1 north of 45°N at 0.8 μm (i.e., a $\sim$56% average increase) between 2012 and 2015, and a small contribution to the hood brightening from an average decrease in cloud-top CH_4 mixing ratio of 0.0019 $\pm$ 0.0003 between 40°N and 80°N (a $\sim$10% decrease) between 2012 and 2015.

4. Our results are consistent with the temporal slowing of a stratospheric meridional circulation exhibiting downwelling at the poles.

Chapter 5

Variability within the Uranian Atmosphere

This Chapter builds upon the work presented in Chapter 4, and aims to address some of the scientific questions that arose within it. The work presented here expands upon the latitudinal retrieval analyses of the HST/WFC3 and HST/STIS datasets by incorporating a novel VLT/MUSE observation of Uranus, the first ever using the MUSE instrument, acquired in 2021. The attention turns from the north polar hood feature to general latitudinal and temporal variability within the atmosphere, with a focus on the cloud-top CH_4 volume mixing ratio (VMR).

5.1 Latitudinal Retrieval Analysis with VLT/MUSE

A VLT/MUSE observation of Uranus, the first ever captured using the MUSE instrument, was acquired in October 2021. The unique nature of the observation, the data reduction

and the deconvolution are described in detail in Section 2.3 of Chapter 2. Prior to commencing a latitudinal retrieval analysis, a comparison of the disc-averaged spectrum of the deconvolved 2021 MUSE observation and the disc-averaged HST/STIS observations was carried out. If the photometric calibration of the MUSE observation is accurate and the deconvolution is functioning correctly, we expect to see a fairly good match between the reflectivity values at short wavelengths, $\lambda < 0.55\mu$m, and the MUSE observation to show an enhanced signature of the polar hood brightening longwards of here (matching the spectral signature from Fig. 4.19). As an even greater proportion of the disc in the 2021 observation is covered by the north polar region, and thus the north polar hood, the disc-averaged spectrum should be dominated by this brightening signature. From the results of Chapter 4, which find the brightening of the polar hood to be mainly the result of changes in the scattering properties of the aerosol layer at 1 – 2 bar, we expect wavelengths of weak CH_4 absorption to have much larger reflectivity values and wavelengths of strong CH_4 to be similar in reflectivity between the observations. Fig. 5.1 displays this comparison, confirming the expected pattern, suggesting that the photometric calibration and deconvolution are functioning correctly. This is an important calibration check that will later allow for a direct comparison between the retrieval results of the datasets.

Before embarking on the latitudinal retrieval analysis, the best-fit atmospheric model found from retrievals on the HST/STIS observations of Chapter 4 (based on the aerosol model of Irwin et al. [2022, 2023a]) was tested on a retrieval of the Minnaert-reconstructed disc-averaged VLT/MUSE spectrum. Due to the new observations being captured with a different telescope and instrument, and due to the change in viewing geometry, coupled with the continued evolution of the north polar hood, it is likely that the best-fit model for STIS needs to be tweaked somewhat to achieve an ideal fit, i.e., a $\chi^2_\nu \simeq 1$. Therefore,

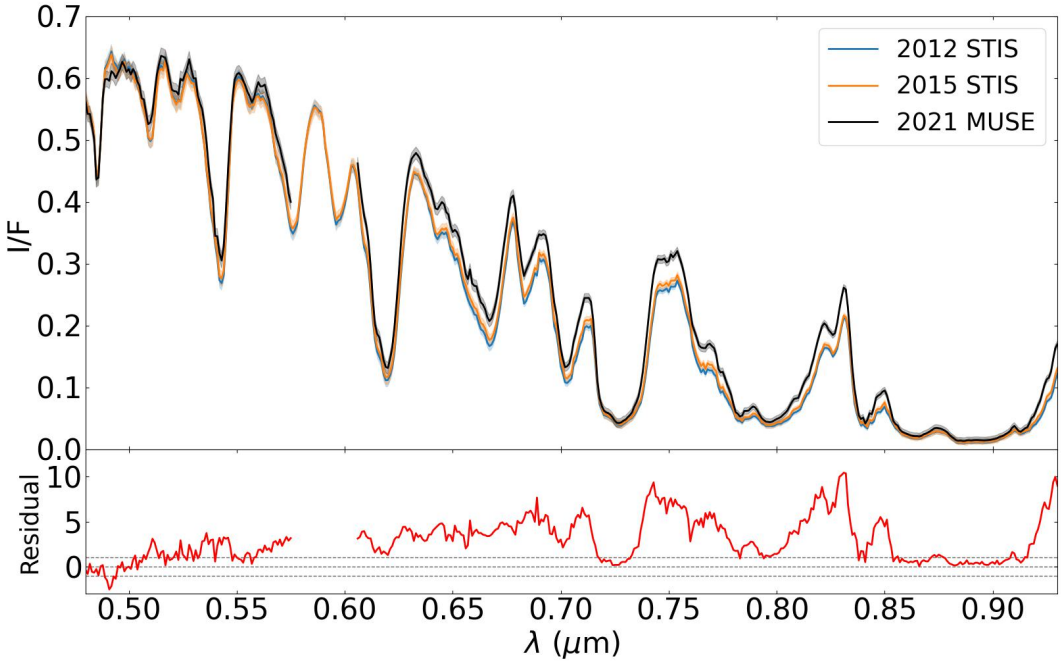


Figure 5.1: Plot comparing the disc-averaged reflectivity spectrum of the 2012 and 2015 HST/STIS observations with that of the 2021 VLT/MUSE observation. All three spectra are seen to be similar in the short-wave region at $\lambda \lesssim 0.55$ μm, with a large brightening observed in the 2021 spectrum at wavelengths longwards of this region. Residuals are between the 2015 STIS and 2021 MUSE disc-averaged spectra and have been divided by the error on the 2015 STIS disc-averaged spectrum.

the imaginary refractive index spectra from the best-fit STIS model were fixed, and the cloud opacities were allowed to vary with 100% fractional errors. The resulting fit was seen to be fairly good, but lacking at the short end of the wavelength range (Fig. 5.2).

A 'free' model was therefore run with 100% fractional errors on all parameters including the imaginary refractive index spectra of each aerosol layer within the spectral range covered by MUSE. A comparison of the best-fit STIS model and the new MUSE model is shown in Fig. 5.2. A comparison of the imaginary refractive index spectra for each aerosol layer between the two models is presented in Fig. 5.3. It can be seen that the n_i of the deep haze layer (aerosol-1) is largely the same as in the best-fit STIS model

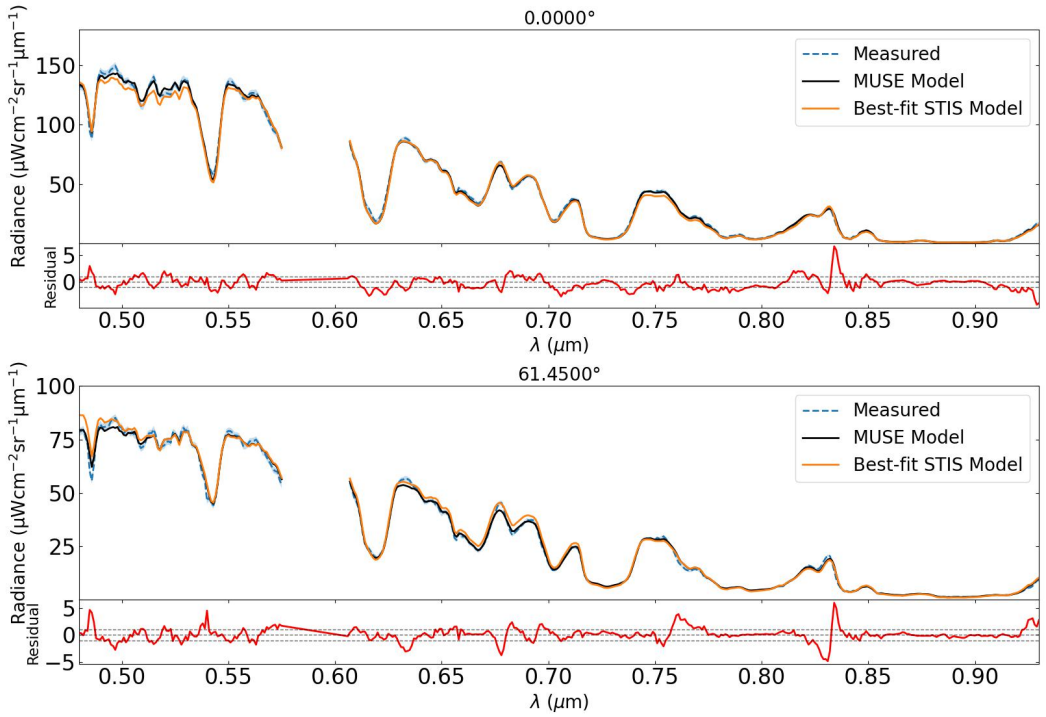


Figure 5.2: Plot comparing NEMESIS spectral fits to the disc-averaged 2021 VLT/MUSE Minnaert-reconstructed spectrum. The best-fit STIS model returned a $\chi^2_\nu \simeq 2.88$ and the new MUSE model returned a $\chi^2_\nu \simeq 1.22$, giving a slightly improved fit, particularly at the short-wave end of the spectral range. Residuals show the difference between the measured spectrum and the MUSE model divided by the error on the measured spectrum.

but with a notable increase at 0.9 μm. The n_i of the 1 – 2-bar haze layer (aerosol-2) is reduced compared to the STIS model at 0.5, 0.6, 0.8 and 0.9 μm, with it being unchanged at 0.4 and 0.7 μm. The n_i of the extended haze layer (aerosol-3) shows the most notable difference, presenting an increase by roughly an order of magnitude across all wavelengths compared to the STIS model. In physical terms, the deep haze aerosols are more absorbing at 0.9 μm, the 1 – 2-bar haze aerosols are more reflective at 0.5, 0.6, 0.8 and 0.9 μm (i.e., an increase in single-scattering albedo), and the extended haze aerosols are more absorbing across all wavelengths (i.e., a decrease in single-scattering

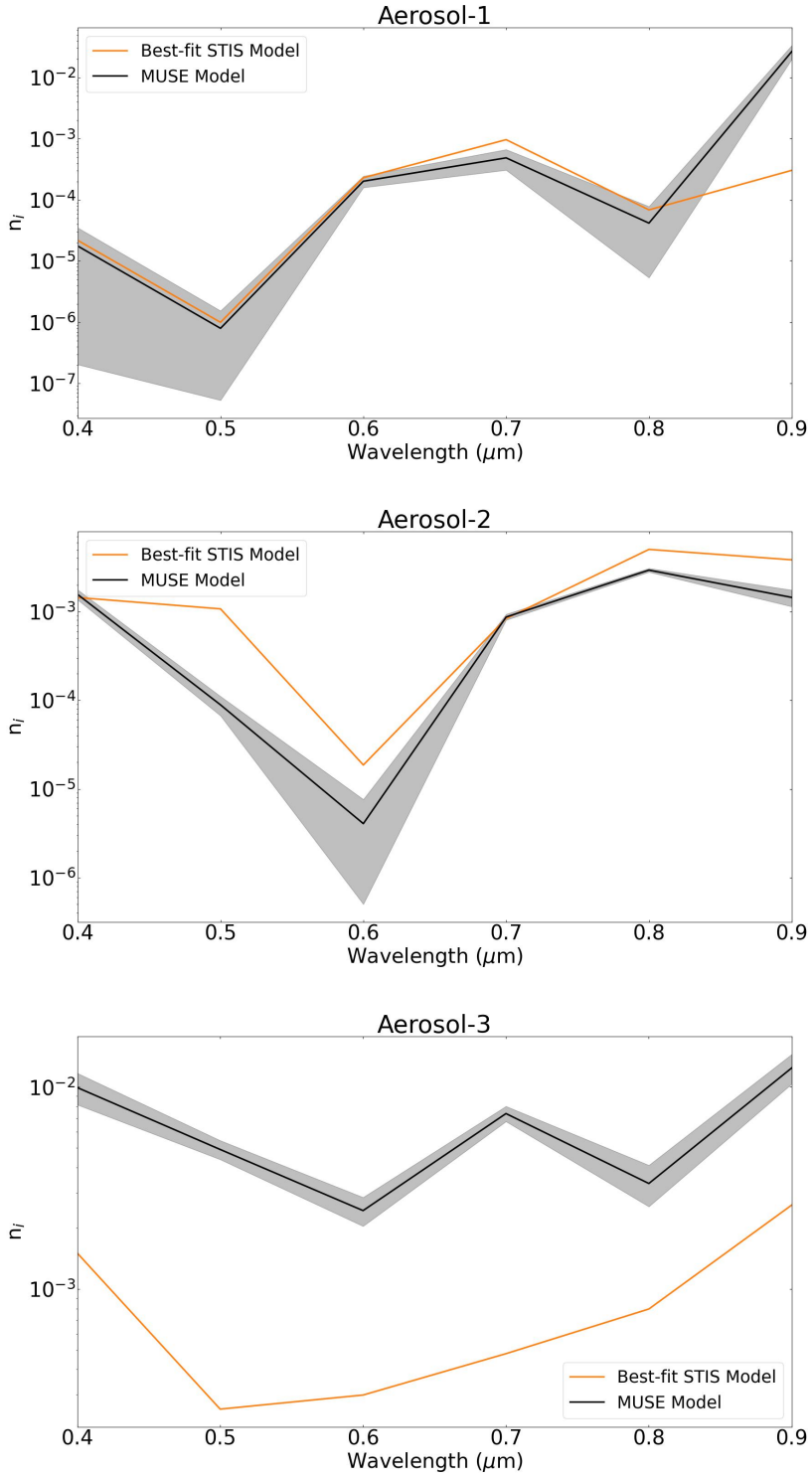


Figure 5.3: Plot comparing the imaginary refractive index spectra of the three aerosol layers in our vertical aerosol model, namely the deep haze layer (aerosol-1), the 1 – – 2-bar haze layer (aerosol-2) and the extended haze layer (aerosol-3). Spectra were retrieved using the Minnaert-reconstructed disc-averaged VLT/MUSE observation at the two chosen Minnaert zenith angles of 0.0° and 61.45°.

albedo) compared to the STIS n_i.

With these new n_i spectra in hand, a latitudinal retrieval analysis was then carried out on the MUSE observation. The Minnaert limb-darkening model was again employed to model the centre-to-limb variations of the observation, using the same latitudinal sampling as in Section 4.1 (i.e., 10°-width bands stepped by 5° across the disc). An example of the Minnaert plots produced is shown in Fig. 5.4 at representative wavelengths and latitude bands. The fitted Minnaert parameters $\left(\frac{I}{F}\right)_0(\lambda)$ and $k(\lambda)$ were again used to generate reconstructed radiance spectra at the two chosen viewing zenith angles of 0.0° and 61.45°. NEMESIS retrievals were then set up in an identical manner to the earlier HST/STIS retrievals of Section 4.3.2, for the relevant wavelength range, using the Minn-

Table 5.1: Table detailing the parameter setup for the latitudinal retrieval analysis carried out on the 2021 VLT/MUSE observation, excluding the imaginary refractive index spectra. The *a priori* were sourced from the holistic aerosol model [Irwin et al., 2022]. All errors are set to 100% of the stated *a priori* values.

Parameter	*a priori*	*a priori* error
τ_1	5.0	5.0
τ_2	3.0	3.0
p_2 (bar)	1.45	1.45
τ_3	0.03	0.03
CH_4 VMR	0.03	0.03

Table 5.2: As Table 5.1 but for the imaginary refractive index spectra. The *a priori* were sourced from the best-fit STIS model of Section 4.3.2. The n_{i1} and n_{i3} profiles remain fixed, whilst the errors on n_{i2} were set to 5% of the stated *a priori* values.

Wavelength (μm)	n_{i1} *a priori*	n_{i2} *a priori*	n_{i3} *a priori*
0.5	7.9755×10^{-7}	8.8852×10^{-5}	4.9060×10^{-3}
0.6	2.0206×10^{-4}	4.0638×10^{-6}	2.44430×10^{-3}
0.7	4.8704×10^{-4}	8.6931×10^{-4}	7.3861×10^{-3}
0.8	4.1792×10^{-5}	2.9377×10^{-3}	3.3291×10^{-3}
0.9	2.6635×10^{-2}	1.4458×10^{-3}	1.2431×10^{-2}

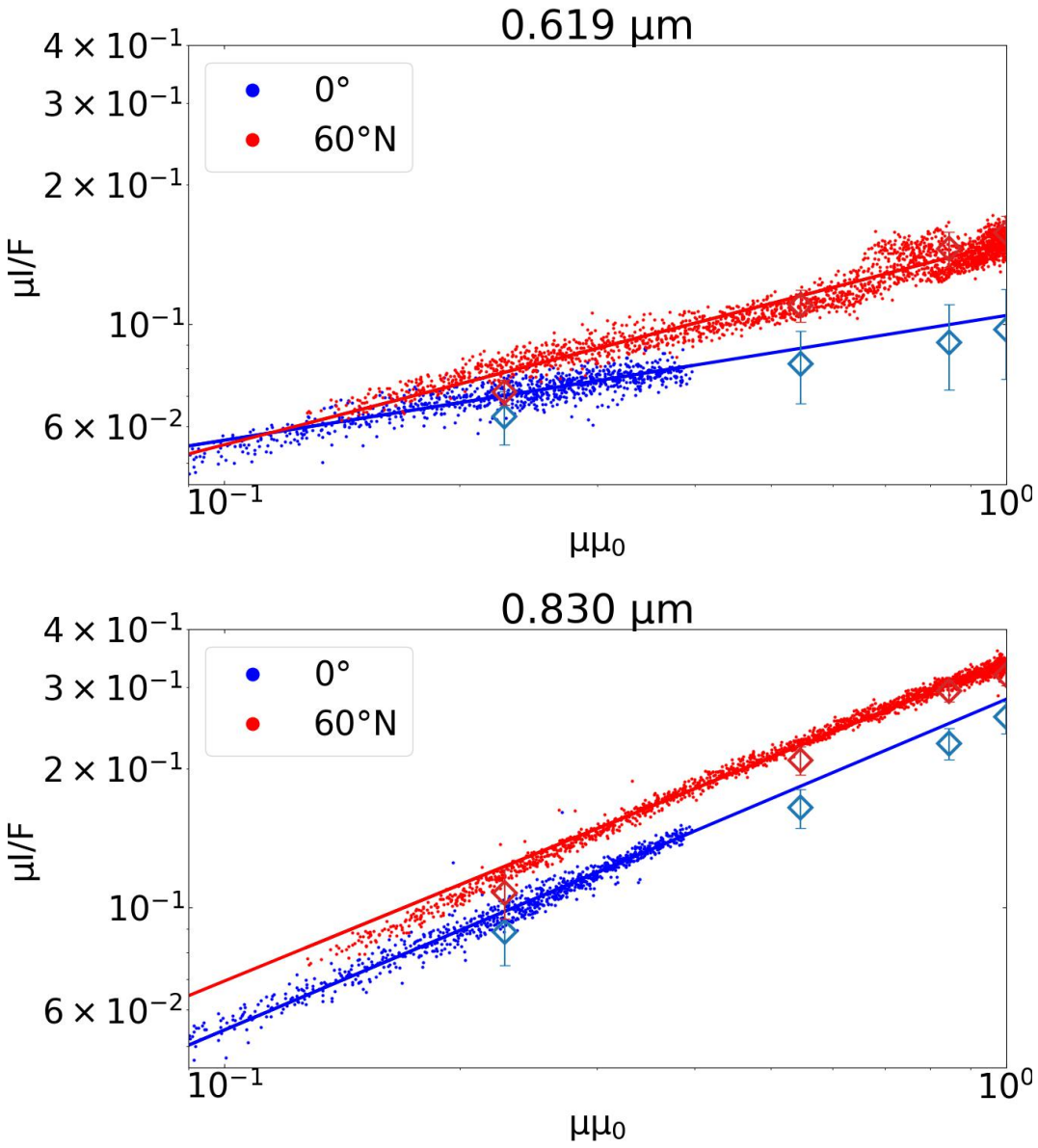


Figure 5.4: Minnaert plot showing the linear fits to the VLT/MUSE data at 0.619 μm and 0.830 μm at two 10°-wide latitude bands centred at 0° (blue) and 60°N (red). Solid lines represent the fits to each latitude band. Diamonds represent the simulated reflectivity values from our best-fit model to the data at 0° (blue) and 60°N (red) for the four zenith angles in the NEMESIS quadrature scheme lying within the $\mu\mu_0 > 0.09$ range (0.0°, 21.145°, 42.3729° and 61.45°), demonstrating that they obey the linear Minnaert relation. The equations of the linear fits in log space, in the form $\mu\frac{I}{F} = (\frac{I}{F})_0 (\mu\mu_0)^k$, are as follows; for 0.619 μm, $\mu\frac{I}{F} = 0.104(\mu\mu_0)^{0.270}$ at 0°, and $\mu\frac{I}{F} = 0.150(\mu\mu_0)^{0.437}$ at 60°N; for 0.830 μm, $\mu\frac{I}{F} = 0.282(\mu\mu_0)^{0.716}$ at 0°, and $\mu\frac{I}{F} = 0.341(\mu\mu_0)^{0.693}$ at 60°N.

Table 5.3: Table presenting the Minnaert parameters $\mu\mu_0$ and $\mu\frac{I}{F}$ of retrievals on the 2021 VLT/MUSE observation of Fig. 5.4.

Wavelength (μm)	Latitude (°)	$\mu\mu_0$	$\mu\frac{I}{F}$	$\Delta\mu\frac{I}{F}$
0.619	0.0	1.000	0.0974	0.0214
0.619	0.0	0.846	0.0910	0.0191
0.619	0.0	0.546	0.0818	0.0145
0.619	0.0	0.228	0.0631	0.0083
0.830	0.0	1.000	0.2586	0.0205
0.830	0.0	0.846	0.2266	0.0174
0.830	0.0	0.546	0.1643	0.0157
0.830	0.0	0.228	0.0884	0.0135
0.619	60.0	1.000	0.1573	0.0139
0.619	60.0	0.846	0.1453	0.0125
0.619	60.0	0.546	0.1097	0.0088
0.619	60.0	0.228	0.0712	0.0044
0.830	60.0	1.000	0.3187	0.0169
0.830	60.0	0.846	0.2945	0.0159
0.830	60.0	0.546	0.2085	0.0144
0.830	60.0	0.228	0.1076	0.0131

aert-reconstructed spectra as the 'measured' spectral observations. The free parameters were again the integrated opacities of each of the aerosol layers (τ_1, τ_2 and τ_3), the pressure of the 1 – 2-bar haze (p_2), the cloud-top CH_4 VMR, and the imaginary refractive index spectrum of the 1 – 2-bar haze (n_{i2}) (real part set to 1.4). The n_i spectra for the deep haze and extended haze were fixed to the disc-averaged values seen in Fig. 5.3 for the MUSE model, where the real parts were both set to 1.4. All errors were set to 100% fractional errors except those for n_{i2}, which were set to 5%. Tables 5.1 and 5.2 detail the parameter setup for the retrievals. The retrieved latitudinal profiles of the free parameters in our model are displayed in Figs. 5.5 & 5.6, with the latter displaying the imaginary refractive index spectrum of the 1 – 2-bar haze layer.

The latitudinal variations observed in the northern hemisphere of Fig. 5.5 are a peak in

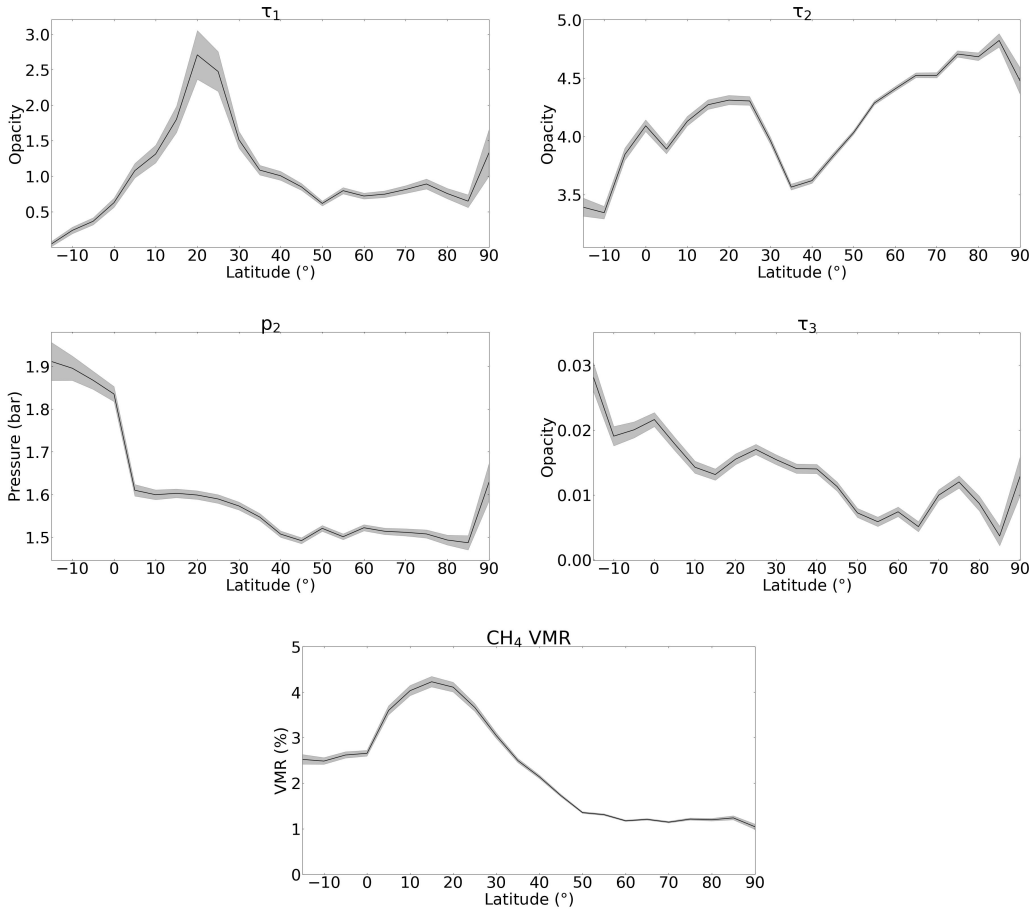


Figure 5.5: Retrieved latitudinal profiles of the free parameters (except the aerosol-2 imaginary refractive index spectrum shown in Fig. 5.6) from the 2021 VLT/MUSE retrievals at all visible latitudes, namely: aerosol-1 integrated opacity (τ_1), aerosol-2 integrated opacity (τ_2) & pressure (p_2), aerosol-3 integrated opacity (τ_3), and cloud-top CH_4 VMR. Note that several of the parameters display significant shifts south of $\sim$5°N (e.g., p_2, τ_1, and CH_4 VMR), suggesting that these changes are artefacts of the retrieval, likely a result of the lack of zenith angle coverage at these southern latitudes, i.e., a lack of constraint.

then sharply increases north of 40°N, τ_3 largest at the equator and reducing towards the pole, and a reduction in cloud-top CH_4 from equator to pole. These are very similar to the variations observed in the northern hemisphere from Chapter 4's HST/STIS and

HST/WFC3 retrievals (Section 4.3). A direct comparison of the latitudinal profiles between the three datasets, at all visible latitudes, will be undertaken later in Section 5.2. Note the sharp changes in the latitudinal profiles of Fig. 5.5 southwards of 5°N are artefacts of the retrieval, largely attributed to a lack of zenith angle coverage towards the edge of the disc.

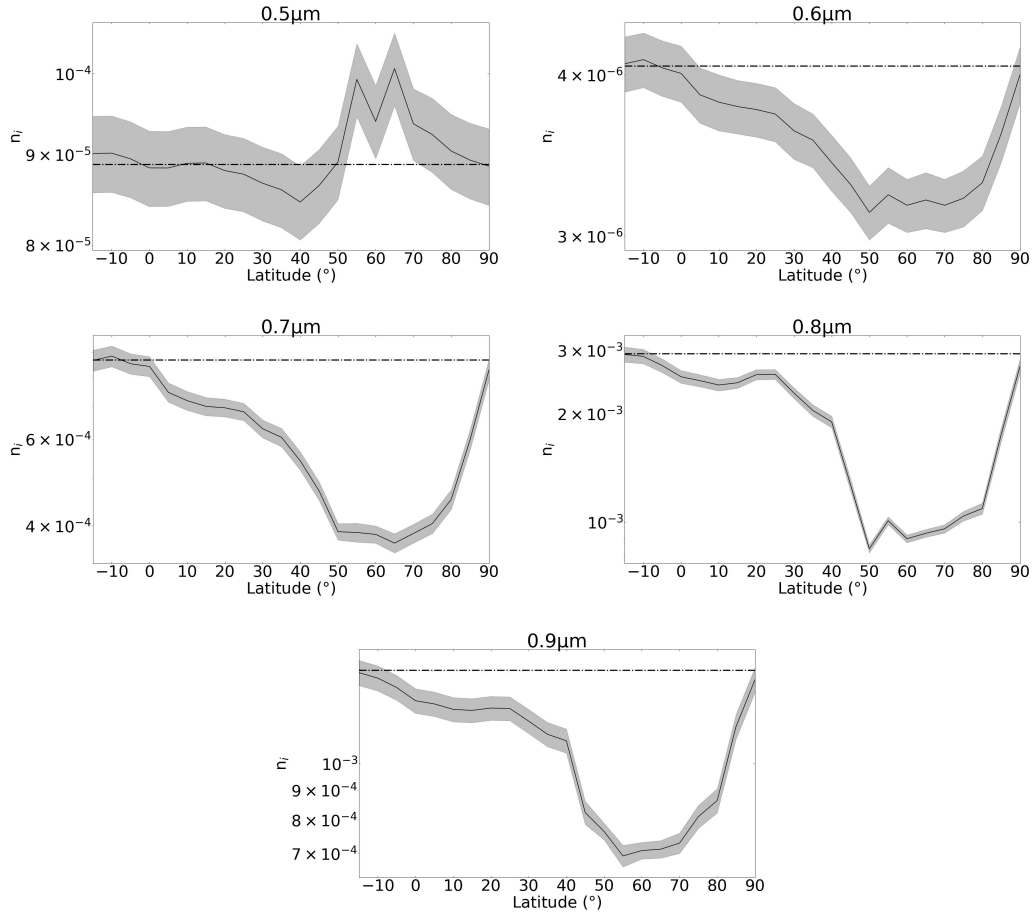


Figure 5.6: Retrieved latitudinal profiles of the aerosol-2 imaginary refractive index spectrum (n_{i2}) at 0.1 μm wavelength intervals at all visible latitudes from our 2021 VLT/MUSE retrievals. A clear decrease in n_{i2} is observed north of ∼40°N for wavelengths longwards of ∼0.6 μm. A relatively small increase in n_{i2} is also observed north of ∼40°N at 0.5 μm. The black dashed-dotted lines represent the *a priori* values.

The latitudinal variations of Fig. 5.6 present a reduction in n_i north of ~40°N for $\lambda \geq$ 0.6 μm, with latitudes south of this observed to have much less variability in n_i. This is similar to the patterns observed for the HST/STIS retrievals of Section 4.3.2, for which a comparison will be made later in Section 5.2.3. In contrast, a relatively small increase in n_i is observed at latitudes north of ~40°N at 0.5 μm, with a relatively stable profile observed south of this. Again, note the tendency of the profiles to increase southwards of 5°N due to edge effects. The free parameters of Fig. 5.5 are also projected onto Uranus' disc in Fig. 5.7 to visually demonstrate the retrieved latitudinal variations.

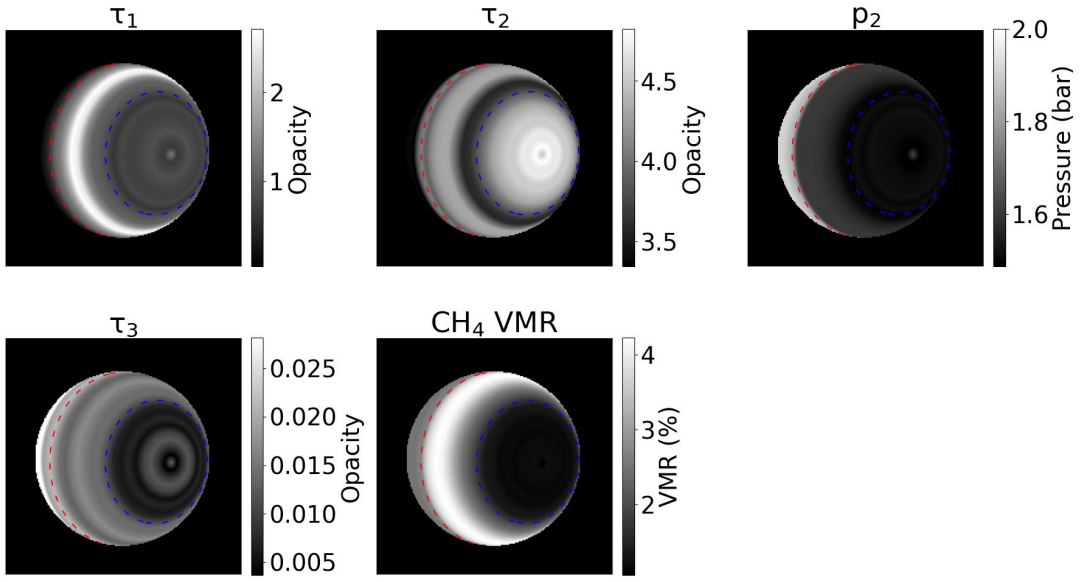


Figure 5.7: Retrieved latitudinal profiles of the free parameters of Fig. 5.5 from the 2021 VLT/MUSE retrievals for all visible latitudes projected onto Uranus' disc (except the imaginary refractive index spectrum of aerosol-2), namely: aerosol-1 integrated opacity (τ_1), aerosol-2 integrated opacity (τ_2) & pressure (p_2), aerosol-3 integrated opacity (τ_3), and cloud-top CH_4 VMR. The north pole is located at the right-hand side of the disc, the red dashed line represents the equator and the blue dashed line represents ±45°N.

The *a priori* constraint on n_{i2} is half of what it was for the HST/STIS latitudinal retrieval

analyses of Chapter 4, using 5% fractional errors compared to the former 10%. This was a result of the need to tune the retrievals to produce smooth, physically plausible n_{i2} latitudinal profiles. Using the former 10% fractional error led to wild, unphysical oscillations in the profiles in the northern hemisphere at each wavelength interval. Several *a priori* fractional errors between 10% and 1% were tested, with 5% providing the best balance of smooth latitudinal variation whilst not restricting the movement of the spectra from the *a priori*. To ensure that this new *a priori* constraint on the n_{i2} retrieved profile was not too restrictive, a bracket retrieval analysis was performed. The *a priori* profile of the retrieval displayed in Fig. 5.6 was multiplied by 5 to create the 'large' bracket and

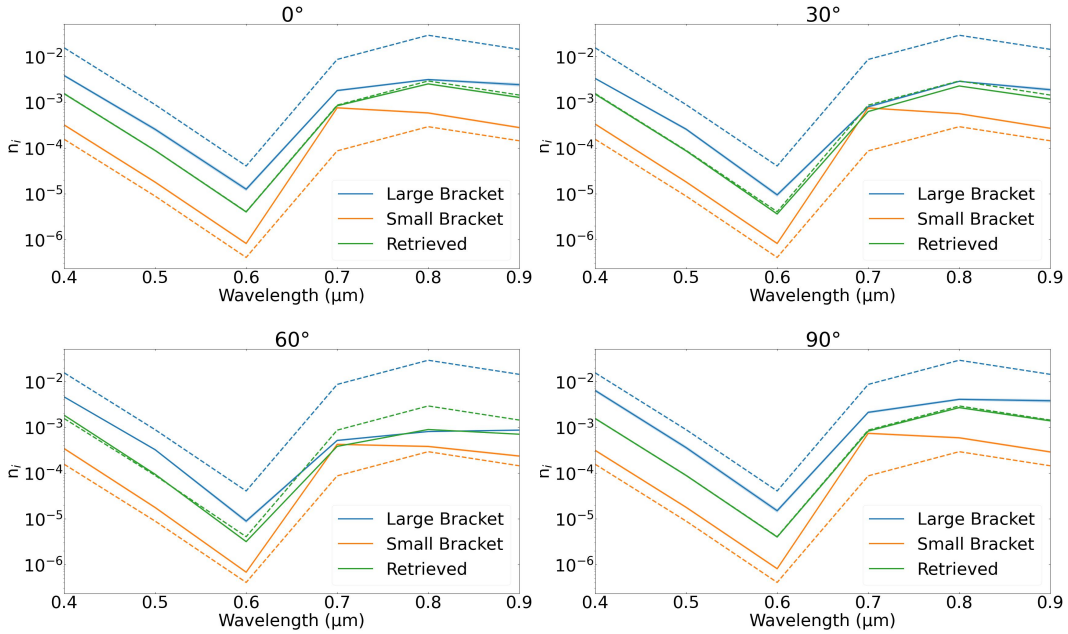


Figure 5.8: Retrieved imaginary refractive index spectra of the aerosol-2 layer at representative latitude bands (labelled by the central latitude). The n_{i2} spectra of the bracket retrieval analysis are compared to the best-fit retrieved n_{i2} spectrum. Solid lines represent the retrieved spectra and dashed lines of the same colour represent the corresponding *a priori* spectra. For each of the latitude bands displayed, the large and small brackets are seen to move away from their respective *a priori* spectra and tend towards the final retrieved spectrum.

by $\frac{1}{5}$ to create the 'small' bracket, with the fractional *a priori* errors held at 5%. Fig. 5.8 displays the retrieval results at four representative latitude bands, of width 10°, in the northern hemisphere.

For each of the latitude bands displayed, the retrieved spectra of the large and small bracket both tend towards the final retrieved spectrum, suggesting that the new *a priori* constraints are not too restrictive and that the retrieved profile is a reliable one. The reason underlying the need for this added constraint, when compared to the retrievals on the HST/STIS observations, however, is unclear. The MUSE spectrum does not appear to exhibit increased levels of noise compared to the STIS spectra, and the latitudinal profiles of the other free parameters in the retrievals show no correlated latitudinal oscillations (for MUSE retrievals using the 10% *a priori* error for n_{i2}).

5.2 Spatial & Temporal Variability

With latitudinal retrieval analyses for three independent datasets (HST/WFC3, HST/STIS and VLT/MUSE) now in hand, a comparative analysis of the retrieved latitudinal profiles of the free parameters probed was carried out, both spatially and temporally. Included in the comparison are both the 2012 and 2015 HST/STIS profiles of Chapter 4, the 2015 and 2021 HST/WFC3 profiles of Chapter 4, and the newly determined 2021 VLT/MUSE profiles presented in Section 5.1. In light of the conclusions of Chapter 4, i.e., a retrieved reduction in polar cloud-top CH_4 VMR and polar n_{i2} over time, the 2021 HST/WFC3 latitudinal retrieval analysis was ran again with the n_{i2} and CH_4 VMR at each latitude band fixed to that retrieved with the 2021 VLT/MUSE observation, with the n_i spectra for the deep haze (aerosol-1) and the extended haze (aerosol-3) fixed to that determined from retrievals on the disc-averaged 2021 VLT/MUSE observation.

5.2.1 Aerosol-2 Pressure

Fig. 5.9 shows a comparison between the retrieved profiles of the 1 – 2-bar haze (aerosol-2) central pressure.

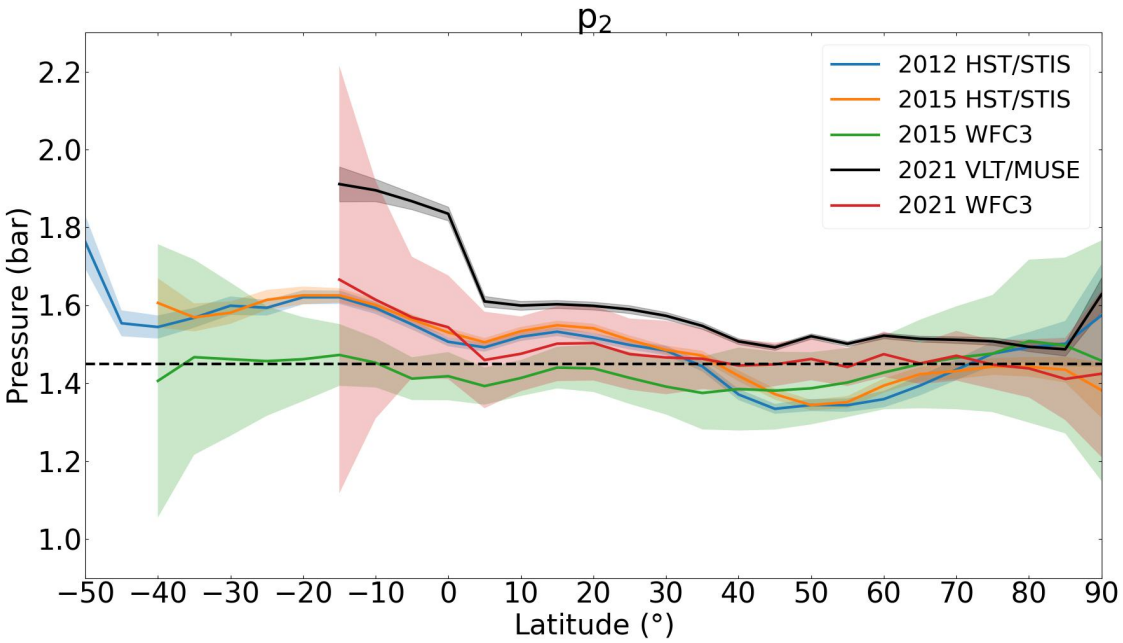


Figure 5.9: A comparison of the retrieved latitudinal profiles of the aerosol-2 layer's central pressure (p_2) for all visible latitudes of each labelled dataset. The black dashed line represents the *a priori* value of 1.45 bar.

We see significant overlap between each of the retrieved profiles across northern latitudes, with the exception of the VLT/MUSE profile, with minimal latitudinal variation. The equatorial and southern latitudes display the largest degree of latitudinal variation within each of the profiles, and the largest divergence of the profiles from one another. A degree of this variation is undoubtedly due to the aforementioned edge effects at these latitudes lying near to the disc's edge and lacking in zenith angle coverage. The VLT/MUSE profile shows the largest difference from the other four profiles, being slightly larger than its 2021 HST/WFC3 counterpart profile, though both display the same latitudinal varia-

tion of increasing pressure towards the equator. Ignoring the artefact of a sharp increase in p_2 southwards of 5°N in the VLT/MUSE profile, and accounting for an inevitable variation due to the different telescopes and/or instruments used, not to mention differing deconvolution algorithms, the profiles appear to be largely consistent with minimal spatial and temporal variation.

The comparison suggests that the vertical position of the 1 – 2-bar haze layer is stable over time and latitude. This comes as no surprise when considering Irwin et al. [2022]'s conclusion that this aerosol layer lies within a region of static stability, meaning that after vertical perturbations are experienced, it is favourable for the haze layer to return to its original altitude. This region of static stability is produced by Uranus' temperature decreasing more slowly than the lapse rate with altitude here, in addition to a significant change in mean molecular weight ($\sim$20%) across the CH_4 condensation level [Irwin et al., 2022]. The results presented above appear to be consistent with this picture.

As we are assuming that this 1 – 2-bar haze layer is composed of photochemical haze particles and CH_4 ice, it is important to consider the effects of the latitudinally variable CH_4 VMR, as well as any changes in temperature with latitude, on the aerosol layer's altitude. If we assume that the temperature profile in the the 1 – 5 bar region does not vary significantly with latitude, then the polar depletion in CH_4 will lead to the CH_4 condensing at higher altitudes (lower pressures), which could result in a higher and thinner haze. Temperature variations with latitude in the 1 – 2-bar region are unknown at present, however, we can speculate on the possible scenarios and relate these to the effects of the depletion in polar CH_4 VMR. If the temperature is decreasing with latitude towards the pole, this would result in CH_4 condensing at lower altitudes, counteracting the effect of the polar depletion in CH_4 VMR. This could explain the fair degree of latitudinal

stability we observe in the central pressure of this aerosol layer. If the temperature is increasing with latitude towards the pole, however, this would cause the opposite effect and result in CH_4 condensing at higher altitudes, compounding the effect of the polar depletion in CH_4 VMR and pushing the CH_4 condensation level even higher within the atmosphere, likely resulting in an even higher and thinner haze. This assumes that a significant portion of the haze's opacity is indeed due to CH_4 ice. If this were not the case, i.e., the condensation of CH_4 ice onto the haze particles did not significantly change the opacity of this layer, the reduced polar CH_4 VMR shifting the condensation level to higher altitudes would still shift the mean molecular weight gradient to higher altitudes, which could result in an upwards shift in the region of static stability. A reduction in temperature could counteract this effect, but it may be the case that the shift in the mean molecular weight gradient is not significant enough to outweigh the temperature-lapse rate effect in this region. Of course we cannot ignore the fact that the depletion in polar CH_4 VMR itself may reduce the significance of this mean molecular weight gradient in contributing to the region of static stability.

5.2.2 Aerosol Opacity

Attention now turns to the integrated opacities of the three haze layers. Here, it is important to bear in mind the correlation between the integrated opacities (τ), the imaginary refractive index spectra (n_i), and the cloud-top CH_4 VMR, meaning that a change in one of these parameters will cause a change in the other two, all other things being equal.

5.2.2.1 Aerosol-1

Fig. 5.10 displays the retrieved latitudinal profiles of the deep haze integrated opacity

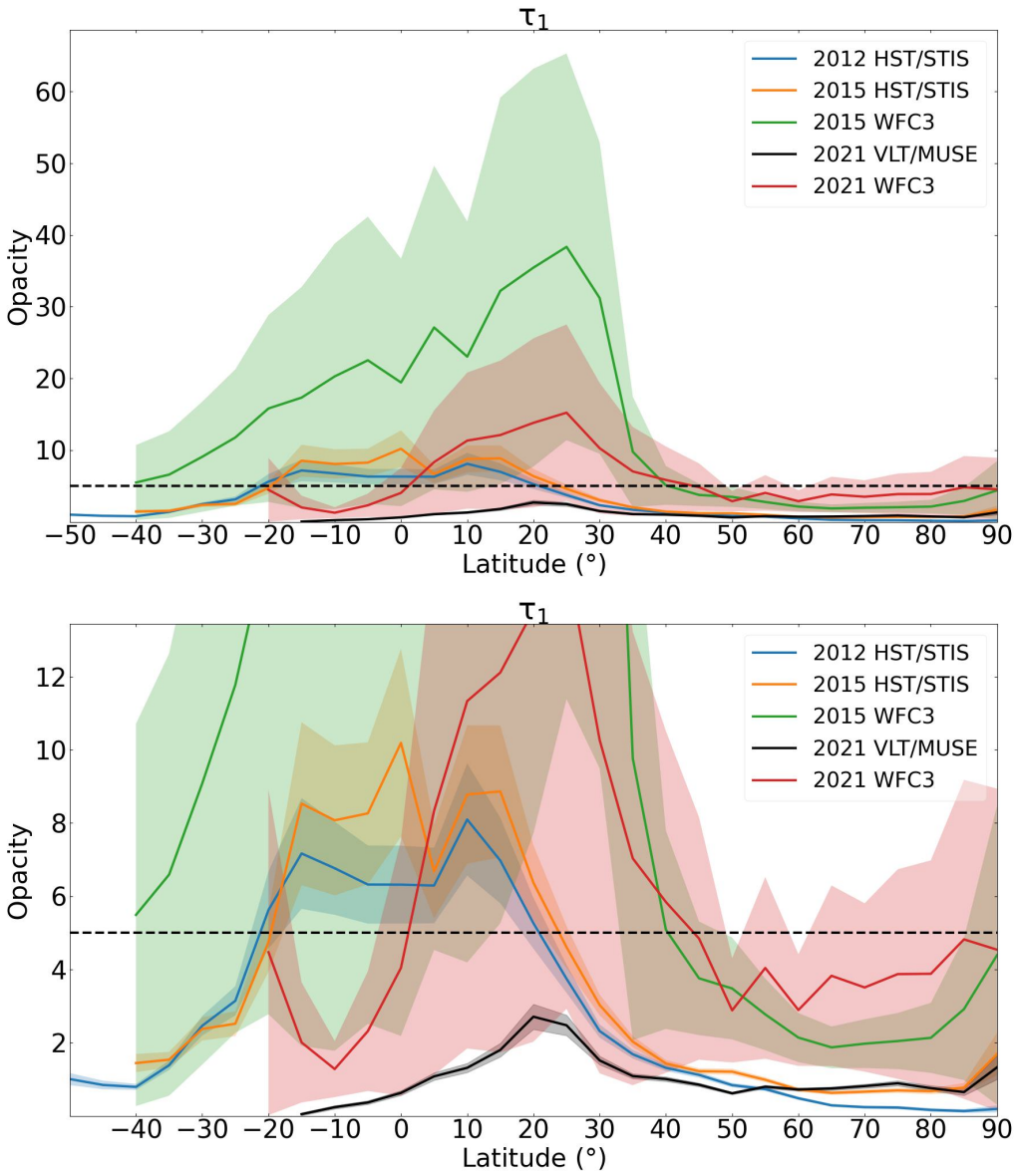


Figure 5.10: A comparison of the retrieved latitudinal profiles of the integrated opacity of the deep haze (aerosol-1) (τ_1) at 0.8 μm, displayed at all visible latitudes for each labelled dataset. The full opacity range is shown in the top plot, with a zoomed in view in the bottom plot to reveal smaller scale latitudinal variations. The black dashed line represents the *a priori* value of 5.0.

(τ_1). The profiles exhibit a number of similarities and differences. Firstly, each profile tends to a maximum at low latitudes, with the opacity falling off toward the poles. Each

profile displays a roughly symmetrical variation, about the maximum for the WFC3 & MUSE profiles, and about the equator for the STIS profiles. The WFC3 & MUSE profiles peak at ∼20 – 25°N, whereas the STIS profiles peak at ∼0 – 10°N. As previously mentioned in Section 4.3.2, this discrepancy could be a result of the underlying differences between the datasets.

At high northern latitudes, there appears to be a trend of increasing opacity over time. In this respect, the WFC3 profiles have large errors and are also consistent with no change over time. However, the STIS profiles show an unambiguous increase with time north of ∼45°N, with the MUSE profile also being consistent with this picture, despite its peak opacity being only $\sim\frac{1}{3}$ that of the STIS profiles.

The most notable feature of Fig. 5.10 is the large spread in the peak magnitude of τ_1 across the datasets, ranging from ∼3 for the 2021 MUSE profile up to ∼38 for the 2015 WFC3 profile. Although these opacities are observationally indistinguishable, the large spread suggests that the τ_1 profile is not very well constrained in any of our latitudinal retrieval analyses. This is not entirely surprising due to the aerosol-1 layer being the deepest of the hazes in our vertical aerosol model, meaning sunlight must travel through the aerosol-3 and aerosol-2 layers prior to reaching it. The scattering and absorption that occurs in these two overlying layers, in addition to gaseous absorption, results in the aerosol-1 layer receiving the least light of the three, contributing to the top region of this haze layer being the deepest pressure that is able to be probed for the studied wavelength range (i.e., the two-way transmission from space reaches unity here). In light of this, not much can be reliably said about the absolute opacities of the 'true' τ_1 profile, however, the consistent nature of the latitudinal variations across the profiles provides confidence in this respect.

The general latitudinal variations of large τ_1 at low or equatorial latitudes are consistent with previous studies of dynamics and latitudinal variations in atmospheric composition [Fletcher et al., 2020, Molter et al., 2021], suggesting a tropospheric meridional circulation below the haze layers of our vertical aerosol model ($\gtrsim$ 7 bar) exhibiting upwelling at low latitudes and downwelling at high latitudes.

5.2.2.2 Aerosol-2

Fig. 5.11 compares the retrieved latitudinal profiles of the 1 – 2-bar haze integrated opacity (τ_2).

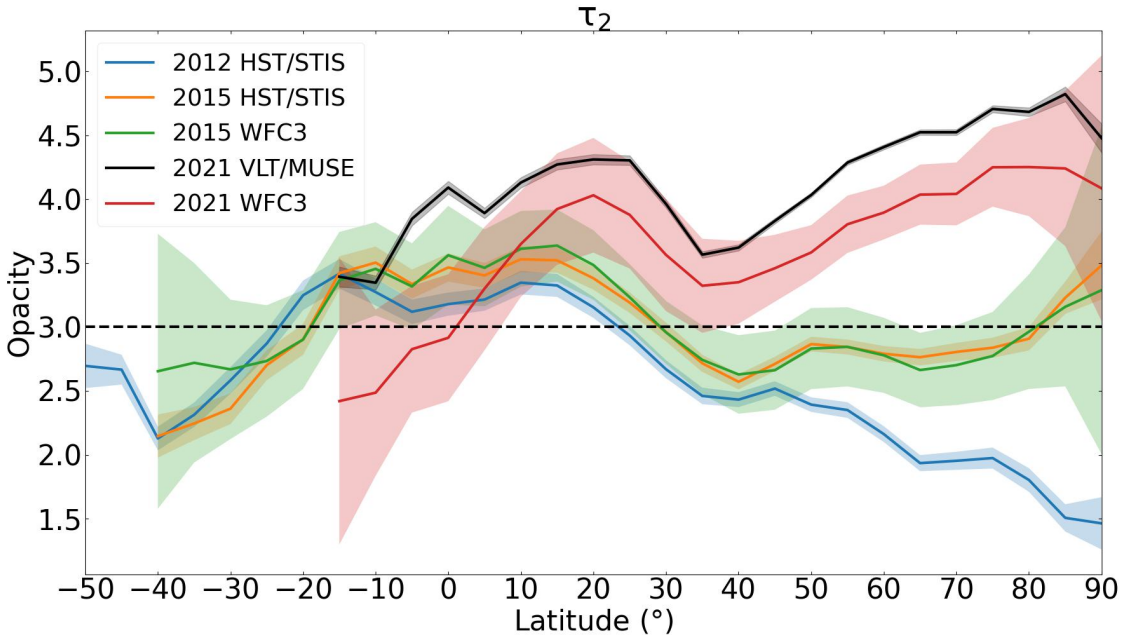


Figure 5.11: A comparison of the retrieved latitudinal profiles of the aerosol-2 layer's integrated opacity (τ_2) at 0.8 μm, displayed for all visible latitudes of each labelled dataset. The black dashed line represents the *a priori* value of 3.0.

Similar to the retrieved profiles for p_2, the τ_2 profiles show very good consistency across the datasets. Firstly, a comparison of the 2015 STIS and 2015 WFC3 profiles shows

them to be in complete agreement. The 2021 MUSE and 2021 WFC3 profiles, though displaying the same latitudinal variations, are not in complete agreement, with the MUSE profile returning slightly larger opacities. In general, the opacity is large at low and equatorial latitudes and falls off toward the midlatitudes. The variation northwards of the midlatitudes ($\sim$40°N) exhibits a temporal dependence. The general latitudinal variation is similar to that of τ_1 up to the midlatitudes. When considering the conclusion of Chapter 4 that a stratospheric transport and settling of haze from above leads to the increase in opacity at high northern latitudes, this variation at low latitudes hints at a meridional circulation cell at the pressure level of the aerosol-2 layer could be at play, exhibiting upwelling at low latitudes and downwelling at high latitudes. This would likely be the same circulation cell purported to produce the latitudinal gradient in cloud-top CH_4 VMR [Sromovsky et al., 2011, 2014, Fletcher et al., 2020].

The brightening of the north polar hood, studied in Chapter 4, enters the picture here, with the temporal trend observed also present in the MUSE profile, i.e., an increase in opacity over time north of $\sim$40°N (coincident with latitudes at which the polar hood is present). Between 2012 and 2021, τ_2 approximately doubles at north polar latitudes. In addition, a relatively small increase in opacity at low latitudes is observed over time.

These results are consistent with those of Chapter 4, suggesting a poleward stratospheric transport and settling of haze within this region of static stability at 1 – 2 bar [Toledo et al., 2019, Fletcher et al., 2020, Irwin et al., 2022].

5.2.2.3 Aerosol-3

Fig. 5.12 compares the retrieved latitudinal profiles of the extended haze integrated opacity (τ_3).

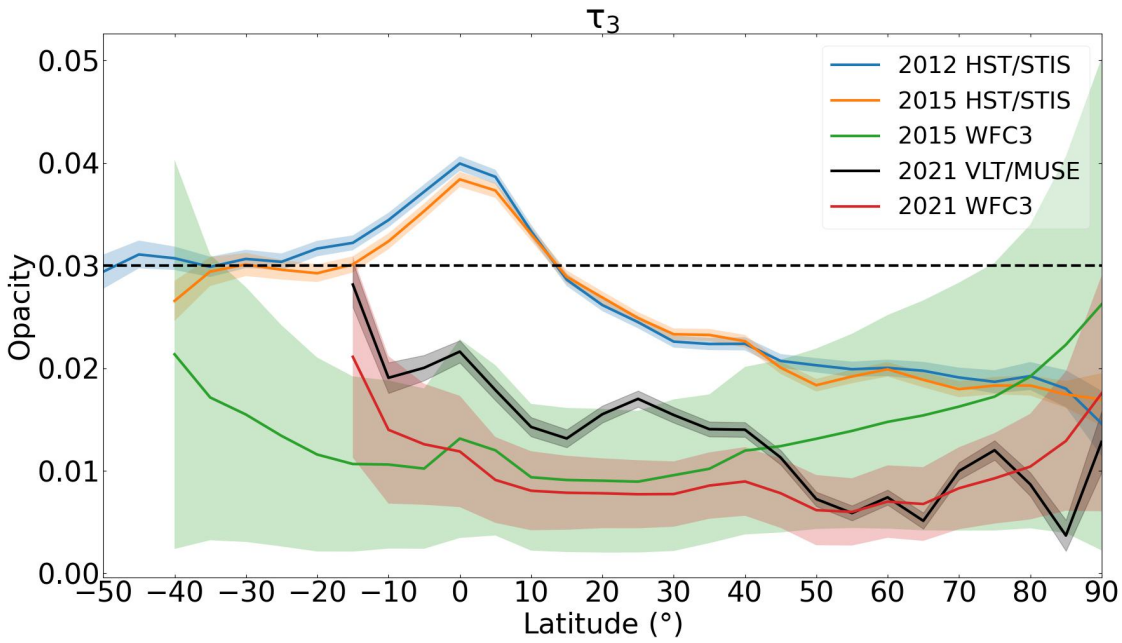


Figure 5.12: A comparison of the retrieved latitudinal profiles of the aerosol-3 layer's integrated opacity (τ_3) at 0.8 μm, displayed for all visible latitudes of each labelled dataset. The black dashed line represents the *a priori* value of 0.03.

The new VLT/MUSE τ_3 profile provides support for the conclusions regarding the differences between the STIS and WFC3 profiles. In Section 4.3.2, it was concluded that the latitudinal variation of the STIS profiles, i.e., τ_3 peaking at the equator and falling off toward the poles, was more reliable than the apparent WFC3 variation of increasing τ_3 toward the poles. The MUSE profile variation also exhibits large equatorial τ_3 that reduces as we move towards the north pole. This gives us increased confidence that this is indeed the 'true' variation. Note, both WFC3 profiles are also consistent with this latitudinal variation within error, circumventing any contradictions.

Temporally speaking, there appears to be minimal change in the τ_3 profile. The STIS profiles are largely consistent with each other, and the WFC3 profiles are largely consistent with no change. The 2021 MUSE and 2021 WFC3 profiles are largely consistent

north of 45°N, with the lack of agreement south of this attributed to differences in instruments, data reduction and deconvolution effects. However, as with the τ_1 profiles of Fig. 5.10, there is a notable difference in magnitude between the STIS profiles and the MUSE and WFC3 profiles, with the equatorial peak in magnitude roughly double for STIS (ignoring the sharp increase at 15°S for the MUSE profile attributed to edge effects). With these results suggesting that the latitudinal variations of the MUSE and STIS profiles are more reliable than those of the WFC3 profiles, the difference between the aerosol-3 imaginary refractive index spectra (n_{i3}) in the STIS best-fit model and the MUSE best-fit model would be the obvious choice for an explanation. However, with the MUSE best-fit model having larger n_i values at all wavelengths, the aerosols would be more absorbing and possess a smaller single-scattering albedo than for the STIS best-fit model. This would lead to the expectation of increased τ_3 for MUSE compared to the STIS profiles, the opposite of what is observed. The circumstances appear to be similar to those of Fig. 5.10 for τ_1, with the MUSE and STIS profiles displaying similar latitudinal variations but on different scales of magnitude. We can only attribute this oddity to the inherent differences between the datasets, their reduction processes, and their deconvolutions. As such, it is not entirely clear if the τ_3 profile is reducing with time, but the evidence here leans towards a fairly stable profile.

5.2.3 Aerosol-2 Imaginary Refractive Index Spectrum

Fig. 5.13 compares the retrieved latitudinal profiles of the 1 – 2-bar haze imaginary refractive index spectrum (n_{i2}), shown at 0.1 μm intervals for the overlapping STIS/MUSE wavelength range (0.5 – 0.9 μm).

As the *a priori* values (represented by the dashed/dashed-dotted lines) vary between the

two datasets, it is useful to compare the latitudinal variations only for the wavelength intervals in which they differ significantly. At 0.5 μm, there appears to be stable n_i at low and equatorial latitudes and a change at $\sim$40°N for all three profiles. At this point, the MUSE and STIS profiles exhibit opposite variations, with the STIS profiles having a small reduction and the MUSE profile having a small increase in n_i.

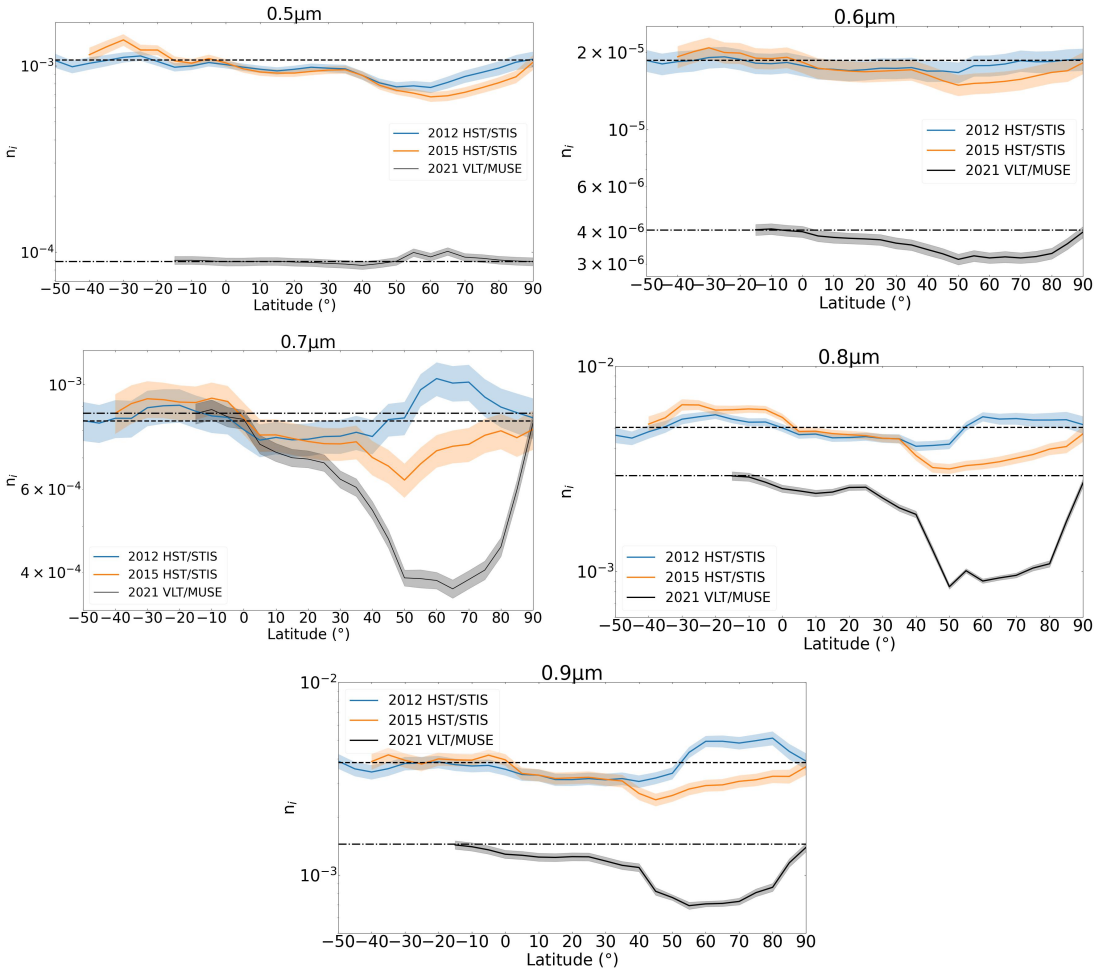


Figure 5.13: A comparison of the retrieved latitudinal profiles of the aerosol-2 layer's imaginary refractive index spectrum (n_{i2}), displayed for all visible latitudes for the 2012 & 2015 HST/STIS and 2021 VLT/MUSE datasets. The dashed black lines represent the *a priori* values for the STIS retrievals and the dashed-dotted black lines represent the *a priori* values for the MUSE retrievals.

The longer wavelength channels of 0.6, 0.7, 0.8 and 0.9μm all display consistent latitudinal variations, with relatively stable n_i at low and equatorial latitudes and a reduction north of $\sim$40°N. Temporally, the MUSE profile exhibits a continuation of the trend found to be partially responsible for the brightening of the north polar hood in Chapter 4, i.e., a further reduction in n_i resulting in increased single-scattering albedo. For example, in the 60 – 70°N latitude band at 0.8 μm, the single-scattering albedo increases from $\sim$0.958 in 2012, to $\sim$0.973 in 2015, and finally $\sim$0.991 in 2021. This provides further evidence and support for this being one of the main physical changes responsible for the observed evolution of the north polar hood.

The edge effects southwards of 5°N can again be observed leading to a slight increase in n_i at these latitudes in the MUSE profiles.

5.2.4 Cloud-top CH_4 VMR

Fig. 5.14 displays a comparison of the retrieved latitudinal profiles of cloud-top CH_4 VMR, i.e., the mean CH_4 VMR in the region of sensitivity ($\sim$2 – 5 bar), from the HST/STIS and VLT/MUSE retrievals.

Chapter 4 raised some unanswered questions in regard to the stability of the cloud-top CH_4 VMR in the atmosphere of Uranus. The results provisionally pointed towards to a temporal variation in the polar depletion of CH_4 VMR, coming in the form of a further reduction. However, due to the analysis only possessing two datapoints in time, it was not clear if this trend would be continued over time, or if further data would reveal a fluctuation about some 'mean' polar VMR profile. The successful acquisition of the VLT/MUSE observation in 2021 enabled this question to be further analysed.

Firstly, the general latitudinal variation observed in Fig. 5.14 is a peak in VMR at low

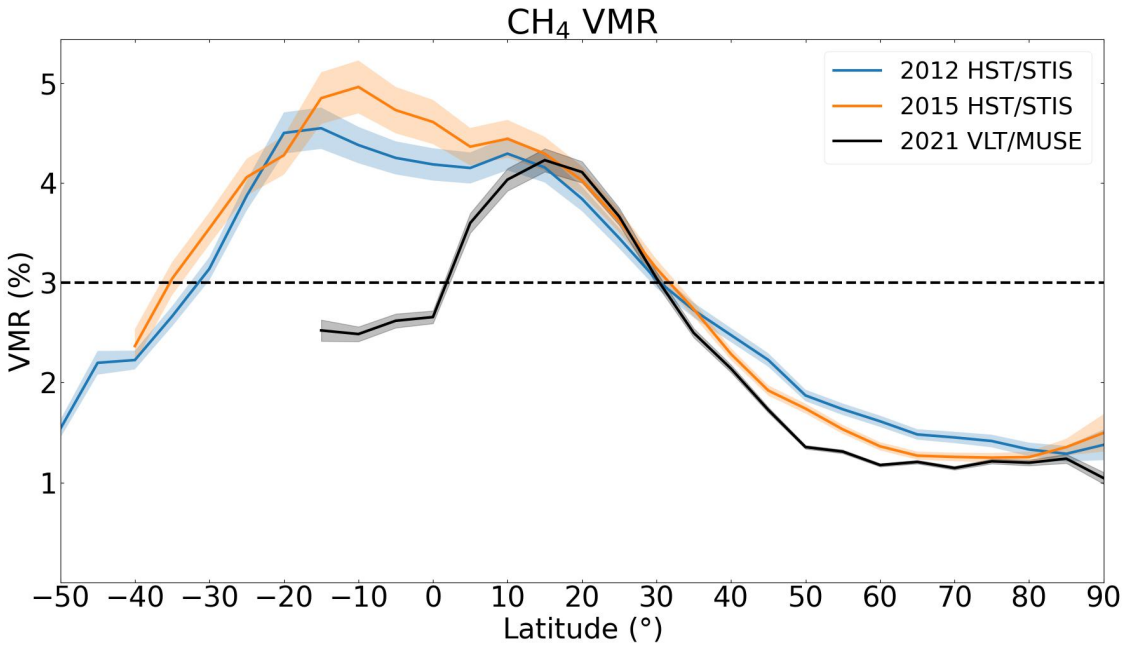


Figure 5.14: A comparison of the retrieved latitudinal profiles of the cloud-top CH_4 VMR, i.e., the mean CH_4 VMR in the region of sensitivity ($\sim$2 – 5 bar), for all visible latitudes of the 2012 & 2015 HST/STIS and 2021 MUSE datasets. The black dashed line represents the *a priori* value of 3.0%.

and equatorial latitudes that reduces in the midlatitudes and reaches a minimum near to the poles. The reduction here is by a factor of $\sim$3. It should again be noted that the MUSE profile is significantly affected by edge effects southwards of 5°N, similar to the profiles in Figs. 5.9, 5.10, 5.11, 5.12 & 5.13. This variation is consistent with that found in many previous studies [Karkoschka and Tomasko, 2009, Sromovsky et al., 2014, Irwin et al., 2017, Sromovsky et al., 2019, James et al., 2023]. Comparing the three profiles of Fig. 5.14, we see that the MUSE profile exhibits a further reduction in VMR north of $\sim$35°N, suggesting that this trend is indeed continued over time as the orbital phase of Uranus progresses (i.e., it is linked to Uranus' season). This provides evidence against Sromovsky et al. [2019]'s conclusion of a general stability in the latitudinal cloud-top

CH_4 VMR profile.

It is important to note here the difference in the treatment of the vertical CH_4 VMR profile between this work and that of Sromovsky et al. [2019]. Here, as stated in Section 4.2, a simple 'step' model is used with variable 'deep' CH_4 VMR limited to 100% relative humidity above the condensation level and a limiting stratospheric VMR of 1 $\times 10^{-4}$. Sromovsky et al. [2019] opt for a 'descended' CH_4 VMR profile [Sromovsky et al., 2011] in which the VMR smoothly decreases from the tropopause value to the deep value with the shape of the curve determined by the exponent vx, which varies with latitude. This vertical profile is more complex than the simple step model but is arguably the more physically plausible of the two. The advantage of using the step model is that it returns the mean CH_4 VMR in the region of sensitivity ($\sim$2 – 5 bar), which can easily be interpreted. In order to provide further support for our conclusion of a variable cloud-top CH_4 VMR profile in the polar region, it would be useful to carry out latitudinal retrieval analyses using the descended profile treatment for each dataset.

5.3 Summary

The successful procurement of the first ever observation of Uranus captured with the VLT/MUSE instrument provided an ideal dataset to further the analysis of this thesis and address some of the unanswered questions brought to the forefront in Chapter 4. With the MUSE instrument possessing sufficient spectral resolution and spectral range to directly retrieve cloud-top CH_4 VMR and the imaginary refractive index spectra, this not only affords the opportunity to test the conclusions of Chapter 4, but also allows for a general comparison of latitudinal and temporal variability within the atmosphere of Uranus.

A comparison of the VLT/MUSE and HST/STIS disc-averaged observations was carried out, ensuring that the data reduction and deconvolution of the MUSE observation were functioning as expected. The best-fit model from the disc-averaged STIS analysis was then tested on the disc-averaged MUSE spectrum and was found to fit quite poorly at very short wavelengths, leading to a new model being fit to the disc-averaged MUSE observation in order to retrieve new imaginary refractive index spectra for each of the three aerosol layers, improving the overall fit. With a new disc-averaged best-fit model in hand, the MUSE observation was Minnaert-analysed and a latitudinal retrieval analysis was carried out in an identical manner to those of HST/STIS in Section 4.3.2, with τ_1, τ_2, p_2, τ_3, cloud-top CH_4 VMR and n_{i2} free to vary.

A comparative analysis of each of the free parameters in our retrievals was then undertaken, looking at the latitudinal and temporal variability between the retrieved profiles of the 2015 & 2021 HST/WFC3, the 2012 & 2015 HST/STIS, and the 2021 VLT/MUSE datasets. The literature was then consulted to explore the consistency of the results with previous work. It was found that the central pressure level of the 1 – 2-bar haze (aerosol-2) showed very little latitudinal or temporal variability, exhibiting stability in both respects. This result is in agreement with Irwin et al. [2022]'s conclusion that this haze layer lies within a region of static stability, resulting in the haze returning to its original altitude upon experiencing vertical perturbations. The effects of the latitudinally-dependent cloud-top CH_4 VMR, as well as potential latitudinal variations in temperature, were explored to give plausible scenarios that could explain this observed stability. The deep haze (aerosol-1) integrated opacity proved the most variable in magnitude between the three datasets, hinting at a lack of constraint in our retrievals, likely due to this being the deepest lying aerosol layer, as well as its cross-correlation to the other

free parameters. However, a consistent latitudinal variation was observed, with large opacity at low and equatorial latitudes, falling off quickly in the midlatitudes, and relatively small opacity in the polar regions, exhibiting a roughly symmetrical profile with respect to the peak value in opacity. Temporally, we see signs of a continued increase in τ_1 (originally observed in Section 4.3.2) at polar hood latitudes ($\sim$45 – 90°N) from the VLT/MUSE profile. However, due to the difference in magnitude between the different datasets a reliable temporal comparison is difficult. The results were found to be consistent with models of the dynamics of Uranus' atmosphere [Fletcher et al., 2020, Molter et al., 2021].

The trends observed for the 1 – 2-bar haze (aerosol-2) integrated opacity, and the imaginary refractive index of this same layer, exhibit a continuation of the temporal trends observed from Chapter 4, i.e., an increase in τ_2, and a decrease in n_{i2} longwards of 0.6μm, at north polar hood latitudes ($\sim$45 – 90°N), from the VLT/MUSE retrievals. These results provide further evidence and support for the conclusion that the brightening of the north polar hood is indeed predominantly due to a thickening of this haze layer and its aerosols becoming more reflective at longer wavelengths. For τ_2, the general latitudinal variation appears to be similar to that of τ_1, i.e., large opacity at low and equatorial latitudes that begins to fall off in the midlatitudes, but in this case a temporal dependence north of $\sim$40°N is observed. After consideration of the conclusions of Chapter 4, this hinted at a tropospheric meridional circulation cell in the 1 – 2 bar pressure region, exhibiting upwelling at low latitudes and downwelling at high latitudes, likely the same circulation responsible for the latitudinal gradient in cloud-top CH_4 VMR. This provides further support for the notion that the temporal thickening north of 40°N requires an alternative explanation, which we attribute to a poleward stratospheric meridional transport

and settling of haze. The extended haze (aerosol-3) opacity latitudinal variations provided support for the proposed notion that the WFC3 profiles are less reliable than those of STIS and MUSE, i.e., that the true variation is large opacity at the equator, which falls off toward the poles. No clear temporal trend was able to be determined due to the offset in magnitude of the profiles, likely a result of the inherent differences between the processing of the datasets, in addition to the differing aerosol-3 imaginary refractive index spectra between the STIS and MUSE best-fit models. However, the evidence does suggest a spatial and temporal stability in the profile.

Finally, the cloud-top CH_4 VMR displayed a consistent latitudinal variation of peak VMR at low and equatorial latitudes, reducing in the midlatitudes, and reaching a minimum at the poles. This is consistent with previous studies [Karkoschka and Tomasko, 2009, Sromovsky et al., 2014, Irwin et al., 2017, Sromovsky et al., 2019, James et al., 2023]. Temporally, we observe a further reduction in VMR at high latitudes (north of 35°N) from the MUSE profile, providing evidence in conflict with Sromovsky et al. [2019] conclusion of a general stability in the profile. Further retrievals testing the arguably more physically plausible 'descended' vertical profile for CH_4 VMR of Sromovsky et al. [2019] were suggested to further this analysis.

The main conclusions of this Chapter are as follows:

1. We find the altitude of 1 – 2-bar haze layer (aerosol-2) to be very stable with respect to latitude and time, in agreement with Irwin et al. [2022]'s assertion that it lies in a region of static stability.

2. Further evidence for the solution found for the brightening of the north polar hood is provided from analysis of the 2021 VLT/MUSE observation, showing a further

thickening in the 1 – 2-bar haze, and a further decrease in the imaginary refractive index spectrum longwards of 0.6 μm, at polar hood latitudes ($\sim$45 – 90°N). For example, for the 60 – 70°N latitude band at 0.8 μm, the single-scattering albedo increases from $\sim$0.958 $\pm$ 0.002 in 2012, to $\sim$0.973 $\pm$ 0.002 in 2015, and finally $\sim$0.9918 $\pm$ 0.0002 in 2021.

3. We find a tentative stability in the extended haze's integrated opacity both latitudinally and temporally.

4. A further reduction in polar cloud-top CH_4 VMR is observed from retrievals carried out on the 2021 VLT/MUSE observation, suggesting that this is a continuous temporal trend and linked to the orbital phase of Uranus, i.e., linked to the season. This result provides evidence in conflict with Sromovsky et al. [2019]'s conclusion of a general stability in the profile.

Chapter 6

Conclusions & Future Work

In this Chapter, a complete summary of the work and key findings presented in this thesis is first given. Section 6.1 summarises the work of Chapter 4 on Uranus' north polar hood, and Section 6.2 summarises the work of Chapter 5 on general latitudinal and temporal variability within the Uranian atmosphere. This is followed by a discussion of the results and conclusions of this thesis in their entirety in Section 6.3, focusing on the degree to which they address the scientific questions asked at the outset, and any new scientific questions that arise as a result. Lastly, useful avenues for future work, building upon the work of this thesis, are explored in Section 6.4.

6.1 Uranus: The North Polar Hood

Two sets of Hubble Space Telescope (HST) observations of Uranus were obtained in order to probe the evolution of Uranus' north polar hood. Firstly, a dataset provided by the Outer Planet Atmospheres Legacy (OPAL) program [Simon et al., 2015] consisting

of yearly full-disc Wide-Field Camera 3 (WFC3) images spanning 2015 – 2021 and captured in seven visible/NIR spectral UVIS filters (centred at 0.467 μm, 0.547 μm, 0.619 μm, 0.657 μm, 0.727 μm, 0.763 μm and 0.845 μm). Secondly, an archival dataset, initially acquired by Sromovsky et al. [2014, 2019], was used consisting of two half-disc Space Telescope Imaging Spectrograph (STIS) observations captured in 2012 and 2015 in the visible/NIR, spanning $\sim$0.3 – 1.0 μm. The complementary nature of these datasets, i.e., one having very good temporal resolution (WFC3) and the other having very good spectral resolution (STIS), enables a comparative analysis to be carried out, holding the respective results up to scrutiny.

An initial analysis was carried out by fitting the Minnaert limb-darkening model [Minnaert, 1941] (Eqn. 3.24) to the entire HST/WFC3 dataset. Each of the seven filter images within each year's dataset were split into latitude bands of width 10° and stepped across the entire visible disc in 5° increments. The Minnaert model was applied to each of these latitude bands individually for the seven filters in each year's dataset, producing the Minnaert parameters as functions of wavelength, i.e., the nadir reflectivity $\left(\frac{I}{F}\right)_0(\lambda)$, and the limb-darkening parameter, $k(\lambda)$. Comparative plots of the profiles for each year in each of the seven filters revealed large increases in $\left(\frac{I}{F}\right)_0$ and k over time at north polar hood latitudes ($\sim$45 – 90°N) for the 0.547-μm, 0.619-μm, 0.657-μm, 0.763-μm and 0.845-μm filters, compared to low latitudes. These filters probe pressures of $\gtrsim$ 1 bar within the Uranian atmosphere. The 0.467-μm and 0.727-μm filters, which probe pressures $\lesssim$ 1 bar, show no comparable increase in $\left(\frac{I}{F}\right)_0$. The images captured by these two filters show no visible signs of the hood (see Fig. 2.2), and therefore suggest that the brightening observed in the other five filters is indeed linked to the hood, which appears to be vertically constrained to be below $\sim$1 bar. However, the 0.467-μm filter

does exhibit comparable increases in k over time to the filters displaying a brightening, suggesting that it does capture some change linked to the hood. These initial results confirmed that the brightening of the north polar hood reported in previous studies [Toledo et al., 2019, Sromovsky et al., 2019] is largely a 'true' brightening, i.e., due to physical changes within the atmosphere, as opposed to being largely the result of any viewing geometry-related apparent brightening effects linked to the polar depletion in cloud-top CH_4 VMR [Karkoschka and Tomasko, 2009, Sromovsky et al., 2014, Irwin et al., 2017, Sromovsky et al., 2019]. The two leading candidates that could be responsible for this brightening effect are thus changes in the polar cloud-top CH_4 VMR and/or changes in the atmosphere's aerosol layers. Lastly, a comparison of the rate of brightening per year revealed signs of a slowing down in the brightening of the hood, suggesting that the physical changes, and their underlying mechanisms, could be slowing with time.

The holistic vertical aerosol model of Irwin et al. [2022, 2023a] for Uranus was then employed in order to carry out a latitudinal retrieval analysis on this same HST/WFC3 dataset. The lack of spectral resolution in the WFC3 dataset means that a latitudinal profile of cloud-top CH_4 mixing ratio cannot be reliably retrieved using the method of Karkoschka and Tomasko [2009], which utilises hydrogen CIA-dominated wavelengths near to 0.8 μm to distinguish cloud-top altitude variations from cloud-top CH_4 VMR variations. The HST/STIS dataset, possessing sufficient spectral resolution to retrieve cloud-top CH_4 VMR, was therefore acquired, and a fit to the 2015 disc-averaged observation was made employing the holistic aerosol model and confirming its quality (χ^2_ν = 1.16). A latitudinal retrieval analysis was then run on the 2015 observation, due to its temporal proximity to the first set of HST/WFC3 observations (also captured in 2015), splitting the disc into 10°-wide latitude swaths stepped by 5° across the visible disc, with

the free parameters chosen as the integrated opacity of the deep haze (τ_1), the integrated opacity (τ_2) and central pressure (p_2) of the 1 – 2-bar haze layer, the integrated opacity of the extended haze (τ_3), the cloud-top CH_4 VMR, all given 100% fractional errors, and the imaginary refractive index spectra of each aerosol layer, given 10% fractional errors. The resulting retrieved cloud-top CH_4 VMR profile was then fixed for each year of the proceeding WFC3 retrievals, adopting Sromovsky et al. [2019]'s conclusion of a general stability in the cloud-top CH_4 VMR over time. The imaginary refractive index spectrum for each aerosol layer was also fixed to that retrieved with the 2015 HST/STIS observation for the WFC3 retrievals.

Latitudinal retrievals were then carried out on the entire WFC3 dataset, again splitting the disc into 10°-wide swaths stepped by 5° across the disc, with the same free parameters and fractional errors, bar the cloud-top CH_4 VMR and imaginary refractive index spectra. These revealed an unambiguous increase in the integrated opacity of the 1 – 2-bar haze layer (τ_2) from 2.9 $\pm$ 0.2 to 4.1 $\pm$ 0.2 at 0.8 μm, an increase of 1.2 $\pm$ 0.3 or $\sim$41%, at polar hood latitudes ($\sim$45 – 90°N), suggesting that a thickening of this layer is the primary cause of the polar hood brightening. The assumption at the outset of a general stability in the cloud-top CH_4 VMR latitudinal profile over time was then discarded in order to explore the degree to which our results depended on this. A moderately chosen 20% reduction in CH_4 VMR (with respect to the fixed *a priori* values at these latitude bands) from 2015 to 2021 between 45°N and 90°N was tested, revealing minimal reductions in the retrieved values of τ_2 and the pressure of the 1 – 2-bar haze layer (p_2), suggesting that the results do not significantly depend on the stability of the cloud-top CH_4 VMR latitudinal profile, with respect to a moderate change. The solution of a thickening of the 1 – 2-bar haze layer was then held up to scrutiny by utilising

the superior spectral resolution of the HST/STIS dataset. A good quality fit to the 2012 disc-averaged STIS observation was achieved using the same vertical aerosol model applied to the 2015 disc-averaged observation. A comparative forward model analysis was then carried out by fixing all parameters in our best-fit model at polar latitudes for the 2012 observation (50 – 90°N) and testing an increase in τ_2 only. The difference between this forward model spectrum and the best-fit spectrum was compared to the difference between the measured spectra at the same polar latitudes between the 2012 and 2015 observations, revealing the spectral fingerprint of the brightening. It was concluded that an increase in τ_2 alone, though producing a brightening longwards of 0.6 μm, was insufficient to match the spectral signature of the brightening observed, due to a darkening at short wavelengths. A comparative latitudinal retrieval analysis between the 2012 and 2015 STIS observations, which possess a superior spectral resolution to the WFC3 observations, enabling the cloud-top CH_4 VMR and imaginary refractive index spectra to be reliably retrieved, was therefore carried out to more thoroughly explore a solution to the brightening of the hood.

The comparative forward model analysis also produced a simple solution that resulted in a good match to the spectral fingerprint of the polar hood brightening, namely an increase in τ_2 in combination with a decrease in the imaginary refractive index spectrum of the 1 – 2-bar haze layer (n_{i2}) at all wavelengths. Therefore, the comparative latitudinal STIS retrievals were given the same free parameters as the earlier 2015 STIS latitudinal retrievals, with the same fractional *a priori* errors, but now fixing the imaginary refractive index spectra of the deep haze and the extended haze to the values retrieved with the disc-averaged observation. The results revealed a similar trend to that found from the HST/WFC3 retrievals, finding an average increase in τ_2 of 1.09 $\pm$ 0.08 at 0.8 μm

(a $\sim$33% increase) north of 45°N. Additionally, a reduction in cloud-top CH_4 VMR by 0.0019 $\pm$ 0.0003 ($\sim$10% decrease) was observed between 40 – 80°N, hinting that Sromovsky et al. [2019]'s conclusion of a general stability in the latitudinal profile may not hold true over certain timescales. An increase in the integrated opacity of the deep haze (τ_1) was also retrieved at polar hood latitudes. After a forward model analysis, it was deemed not to be a significant factor in the brightening of the polar hood. Finally, a reduction in n_{i2} was found longwards of 0.6 μm and north of $\sim$45°N, indicating an increase in single-scattering albedo, i.e., more reflective aerosols in the 1 – 2-bar haze at these wavelengths.

A comparison between the 2015 HST/WFC3 and 2015 HST/STIS retrieved latitudinal profiles for the free parameters common to both models (i.e., τ_1, τ_2, p_2 and τ_3) was then carried out to assess their compatibility, and to explore any contradictions between them. The latitudinal variations of the opacity and pressure of the 1 – 2-bar aerosol layer were seen to be very compatible, displaying almost identical profiles. The integrated opacity profiles of the deep haze displayed similar latitudinal trends but at very different scales of magnitude, with the peak values for the WFC3 profile being $\sim$4$\times$ larger than that of STIS. The most likely explanation for this difference was given as the WFC3 retrieval compensating for the lack of freedom in correlated parameters, i.e., the cloud-top CH_4 VMR and aerosol-2 imaginary refractive index spectrum. The peak in opacity of the two profiles also differed by 10° of latitude. This was attributed as likely arising from the underlying differences in the acquisition of the two datasets and their reduction processes (e.g., the STIS slit being stepped across the disc, leading to Uranus rotating by $> 45°$ during observation). The extended haze integrated opacity profiles displayed the clearest contradiction, with the STIS profile displaying a concentration of haze at the equator,

reducing smoothly towards the north pole, and the WFC3 profile seemingly displaying the opposite latitudinal variation. This apparent inconsistency was probed by running retrievals on the STIS observation, selectively fixing the CH_4 VMR, n_{i2} and τ_1, as well as fixing all of them simultaneously. Each scenario produced a similar variation in τ_3, giving us confidence that this latitudinal variation is trustworthy. This latitudinal distribution of upper atmospheric haze is also consistent with 0.727 μm WFC3 observations, which probe high up in the atmosphere ($p \lesssim 1$ bar), displaying a visible band of enhanced reflectivity at the equator (see Figs. 2.2 & 4.6). The cloud-top CH_4 VMR and imaginary refractive index spectra being fixed for the WFC3 retrievals, combined with its limited spectral resolution, was given as the best explanation for this difference. However, within error, the WFC3 profiles are consistent with the STIS latitudinal variation, eliminating any contradictions.

A comparison of the retrieved n_{i2} spectra at tropical and polar latitudes was then presented, comparing these to the n_i spectra of Mahjoub et al. [2012]'s tholins seeded in different concentrations of CH_4 gas. Opposite trends were observed in the Mahjoub et al. [2012] spectra, i.e., an increase in CH_4 concentration leading to a decrease in n_i, suggesting that more complex processes are responsible for the retrieved reduction in n_{i2}. It was concluded that the main physical changes responsible for the brightening of the north polar hood were a thickening of the 1 – 2-bar haze (aerosol-2), and a decrease in its imaginary refractive index spectrum longwards of 0.6 μm, between 45 – 90°N.

Mechanisms were then explored in some detail to explain the retrieved physical changes, using the literature as a guide. One plausible solution that could explain all of the changes we see is a stratospheric meridional circulation exhibiting downwelling at the poles, resulting in a poleward transport of haze, which then settles out in the 1 – 2-bar haze

layer, causing it to thicken over time. This circulation would also be weakening over time, perhaps due to a heating of the polar region via the increasing insolation as Uranus' orbit continues to approach summer solstice in 2030. Other plausible solutions exist, e.g., an upwelling of material from below the polar hood, with further evidence being required to identify which of these is the most likely scenario.

6.2 Uranus: Spatial & Temporal Variability

A novel VLT/MUSE observation of Uranus, acquired in October 2021, was employed to explore the question of variability within the Uranian atmosphere further. The disc-averaged observation was first compared to the 2012 and 2015 HST/STIS disc-averaged observations, confirming that the calibration, reduction and deconvolution of the MUSE observation were carried out correctly. This was evident from the short-wave ($\lambda \lesssim 0.55$ μm) reflectivity values matching very well between the three disc-averaged spectra, but the MUSE disc-averaged spectrum showing an enhanced signature of the polar hood brightening at wavelengths longwards of this; an expected outcome of the polar hood covering a larger portion of the disc.

The best-fit atmospheric model determined from retrievals on the disc-averaged HST/STIS observations was then applied to the disc-averaged MUSE observation to confirm whether or not a comparable quality of fit could be achieved. Despite a reasonably good fit being obtained ($\chi^2_\nu \simeq 2.88$), the short-wave region of the MUSE spectrum was poorly fitted. As a result, an improved model was sought by running a 'free' retrieval on the disc-averaged MUSE spectrum with all of the parameters probed in our model (τ_1, τ_2, p_2, τ_3, CH_4 VMR, n_{i1}, n_{i2} and n_{i3}) free to vary with 100% fractional errors, with the intent to find new imaginary refractive index spectra to form the base model from which latitudi-

nal retrievals could then be performed. The new best-fit model improved the quality of the fit to the disc-averaged MUSE spectrum, producing a $\chi^2_\nu \simeq 1.22$. The new retrieved n_i spectra were compared to those of the HST/STIS best-fit model, revealing similar n_{i1} and n_{i2} spectra, but a large increase in the n_{i3} spectrum at all wavelengths, indicating a reduction in the single-scattering albedo, i.e., more absorbing aerosols in the extended haze layer.

A latitudinal retrieval analysis was then carried out on the VLT/MUSE observation using the new best-fit MUSE aerosol model, with free parameters τ_1, τ_2, p_2, τ_3 and CH_4 VMR, all with 100% fractional errors, and n_{i2} with 5% fractional errors. The retrieved latitudinal profiles revealed similar variations to those found from retrievals on the HST/STIS observations, namely large τ_1 at low latitudes reducing towards the pole, large τ_2 at low latitudes that reduces toward the midlatitudes before sharply increasing north of 40°N, large τ_3 at the equator that reduces towards the pole, and finally large CH_4 at the equator that reduces towards the pole. The n_{i2} latitudinal profiles also displayed similar variations to those retrieved from the HST/STIS observations, namely fairly stable n_i south of 40°N and a relatively large reduction in n_i north of here for the longer wavelengths ($\lambda \gtrsim 0.6$ μm). An explanation for the increased *a priori* constraint on the n_{i2} spectrum was then given, with a bracket retrieval run to demonstrate the reliability of the retrieved profile and to justify the increase of constraint, eliminating unphysical latitudinal variations. The most plausible explanation for the underlying need for this increase in constraint was unclear. The MUSE spectrum did not appear to exhibit increased levels of noise compared to the STIS spectra, and the latitudinal profiles of the other free parameters in the retrievals showed no corresponding oscillations within the same latitude bands as the n_{i2} latitudinal profiles (for MUSE latitudinal retrievals carried out using the 10% *a priori*

error for n_{i2}).

With latitudinal profiles for the HST/WFC3, HST/STIS and VLT/MUSE observations in hand, spanning 2012 – 2021, a comparative analysis of the profiles was then embarked upon, using the previous results of Chapter 4 and the scientific literature as a guide, identifying any underlying patterns or inconsistencies, and drawing conclusions from these. Included in the analysis were the 2012 & 2015 STIS profiles, the 2015 & 2021 WFC3 profiles only, and the 2021 MUSE profiles. With a reduction in polar cloud-top CH_4 VMR and polar n_{i2} observed over time from the results of Section 5.1 and Chapter 4, the 2021 WFC3 latitudinal retrievals were run again, fixing the cloud-top CH_4 VMR and n_{i2} latitudinal profiles to those retrieved with the MUSE observation in Section 5.1, with the n_{i1} and n_{i3} spectra fixed to those retrieved with the disc-averaged MUSE observation (Fig. 5.3).

Firstly, the central pressure of the 1 – 2-bar haze (aerosol-2) was analysed. Significant overlap between all five latitudinal profiles was observed, suggesting temporal stability in the profile. The latitudinal variations were observed to be minimal for each profile when ignoring edge effects. The slight inconsistency between the 2021 WFC3 and 2021 MUSE profiles was largely attributed to the difference in instruments, data reductions and the deconvolution of the MUSE observation. The results were seen to be consistent with Irwin et al. [2022]'s assertion that this haze layer lies in a region of static stability, caused by the temperature decreasing more slowly than the lapse rate here, and a gradient in mean molecular weight of $\sim$20% across the CH_4 condensation level, which is predicted to lie within this pressure range. An exploration of the effects of the observed gradient in cloud-top CH_4 VMR, and any potential latitudinal temperature variations, on the pressure level of the aerosol layer was then undertaken. Assuming the opacity of this haze layer

has significant contributions from CH_4 ice, it was concluded that the polar depletion in CH_4 VMR, leading to a vertically higher CH_4 condensation level, would tend to lower the central pressure of the haze layer (i.e., push it to higher altitudes), all other things being equal. In this scenario, a lower temperature in the polar region was suggested to likely counteract the effect of the polar CH_4 depletion by lowering the altitude of the CH_4 condensation level, leading to less change in the central pressure of the haze with latitude, i.e., more latitudinal stability. In contrast, increased polar temperatures were suggested to likely produce the opposite effect, tending to push the condensation level to even higher altitudes, and thus moving the central pressure of the haze layer to even lower pressures (higher altitudes), working against latitudinal stability. In the scenario that CH_4 ice does not significantly contribute to the opacity of this haze layer, the depletion in CH_4 would still lead to the CH_4 condensation level being pushed to higher altitudes, shifting the gradient in mean molecular weight with it. Lower polar temperatures could counteract this effect, but the depletion in polar CH_4 VMR itself may diminish the contribution of the mean molecular weight gradient to the region static stability.

A comparison of the profiles for the integrated opacities of the three aerosol layers was then carried out. The deep haze (aerosol-1) opacity presented similar latitudinal variations, with large opacity at low latitudes falling off toward the poles, exhibiting roughly symmetrical profiles about their maxima. The WFC3 and MUSE profiles were seen to peak in opacity at $\sim$20 – 25°N, whereas the STIS profiles peaked at $\sim$0 - 10°N. These differences were attributed likely being due to the underlying differences in the datasets and their reduction processes. At high northern latitudes, a trend of increasing opacity over time between the STIS and MUSE profiles was observed, despite the offset in magnitude between the profiles, with the two WFC3 profiles being consistent with no

change over time. The clear difference in magnitude between the profiles of the different datasets was then discussed. With the spread in peak opacity ranging from $\sim$3 for the 2021 MUSE profile up to $\sim$38 for the 2015 WFC3 profile, it was concluded that the τ_1 profile is not very well constrained in any of our latitudinal retrieval analyses. However, due to these peak opacities being observationally indistinguishable, they are not contradictory. The lack of constraint in τ_1 was attributed to it being the deepest lying haze layer of our model, therefore receiving the least amount of sunlight of the three layers in our aerosol model. It was therefore concluded that only the consistent latitudinal variation observed in each of the profiles could be inferred with some confidence. This latitudinal variation of large τ_1 at low and equatorial latitudes was seen to be consistent with the results and conclusions of previous studies suggesting a tropospheric meridional circulation exhibiting upwelling at low latitudes and downwelling near the poles [Fletcher et al., 2020, Molter et al., 2021].

The 1 – 2-bar haze (aerosol-2) integrated opacity profiles display very consistent latitudinal variations. The 2015 WFC3 and 2015 STIS profiles were seen to be in complete agreement across all visible latitudes. The 2021 WFC3 and 2021 MUSE profiles, however, despite displaying the same latitudinal variation, were seen to exhibit only partial agreement, with the MUSE profile returning slightly larger opacity values. The general latitudinal variation was observed to be large opacity at low and equatorial latitudes, falling off toward the midlatitudes, and then having a temporal dependence north of $\sim$40°N. The opacity was then seen to consistently increase over time at these high northern latitudes, in line with the conclusion of Chapter 4, i.e., that this is one of the main causes of the brightening of the north polar hood. The latitudinal variation up to the midlatitudes was seen to be similar to that of τ_1, suggesting a similar tropospheric merid-

ional circulation cell could be at work at these pressure levels (exhibiting upwelling at low latitudes and downwelling at high latitudes), pointing to an alternative explanation for the observed temporal increase in opacity north of ∼40°N (attributed to a poleward stratospheric transport and settling of haze in Chapter 4 [Toledo et al., 2019]). It was noted that the suggested tropospheric meridional circulation cell affecting the 1 – 2 bar region could be the very same circulation cell proposed to be responsible for the polar depletion in cloud-top CH_4 VMR [Sromovsky et al., 2011, 2014, Fletcher et al., 2020].

The extended haze (aerosol-3) opacity profile for MUSE, displaying large opacity at the equator that reduces towards the pole, provided further support for the conclusion that this is indeed the 'true' latitudinal variation, which was reached after a comparison between the WFC3 and STIS profiles in Section 4.3.2 of Chapter 4. It was noted that the WFC3 profiles are also consistent with this trend within error, avoiding any direct contradictions between the profiles. Comparison of the STIS profiles showed very little temporal change, and comparison of the WFC3 profiles suggested the same conclusion. The 2021 WFC3 and 2021 MUSE τ_3 profiles were seen to be largely consistent north of 45°N, with the lack of agreement south of here attributed to the different instruments, data reduction methods and deconvolution of the MUSE observation. Again, we observed a difference in magnitude between the profiles, with the STIS profiles being roughly double the opacity of the MUSE profile at the equator. It was suggested that this difference could be a result of the differing imaginary refractive index spectra between the two best-fit models, however, with the single-scattering albedo of these aerosols being found to be lower in the MUSE best-fit model, we would expect a higher retrieved opacity for MUSE, not lower. The inconsistency here pointed toward the inherent differences between the STIS and MUSE datasets (data collection, data reduction and deconvolu-

tion algorithms), meaning no reliable temporal comparison could be made between their profiles. The evidence from the STIS profiles suggests a fairly stable profile over time.

A comparative analysis of the 1 – 2-bar haze (aerosol-2) imaginary refractive index spectra was then carried out between the STIS and MUSE profiles. Putting to one side the differences between the n_{i2} *a priori* of the STIS and MUSE models, a comparison of the latitudinal variations revealed stable n_i at 0.5 μm at low and equatorial latitudes, with a small decrease in the STIS profiles, and a small increase in the MUSE profile, observed north of ∼40°N. The longer wavelength channels of 0.6, 0.7, 0.8 and 0.9 μm were seen to display consistent variations between the three profiles, namely relatively stable n_i at low and equatorial latitudes, with a decrease in n_i north of ∼40°N. Analysis of the temporal trend revealed an enhanced reduction in n_{i2} at high northern latitudes, continuing the trend observed in Chapter 4. This provided further support for the conclusion that this reduction is partially responsible for the temporal brightening of the north polar hood. It was noted that a reduction in n_i leads to an increase in single-scattering albedo, which for the 60 – 70°N latitude band at 0.8 μm, increases from ∼0.958 in 2012, to ∼0.973 in 2015, and finally ∼0.991 in 2021.

Finally, a comparison of the cloud-top CH_4 VMR, i.e., the mean CH_4 VMR in the region of sensitivity (∼2 – 5 bar), for the STIS and MUSE profiles was undertaken. Ignoring the edge effects seen in the MUSE profiles southwards of 5°N, we observed good agreement between the three profiles at low northern latitudes, with each profile displaying the same latitudinal variation of large VMR at low and equatorial latitudes that reduces toward the poles. The MUSE profile was seen to extend the observed trend of a reduction in polar CH_4 VMR between the STIS profiles across time, exhibiting a reduction north of ∼35°N. This suggested the temporal trend is related to the orbital phase of Uranus,

and thus linked to the season. This result provided evidence against Sromovsky et al. [2019]'s conclusion of a general stability in the latitudinal cloud-top CH_4 VMR profile. The differences between the treatment of the vertical CH_4 profile between this work and that of Sromovsky et al. [2019] were pointed out, with this being one of the main differences that could potentially explain the differing conclusions regarding the stability of the profile.

6.3 Conclusions & Discussion

The main conclusions of this thesis can be summarised as follows:

1. The observed temporal brightening of Uranus' north polar hood is confirmed to be a 'true' brightening caused by physical changes within the atmosphere, as opposed to any viewing geometry-related effects.

2. Provisional signs of a slowing in the temporal brightening of the north polar hood is observed between 2015 and 2021.

3. The previously observed latitudinal dependence of cloud-top CH_4 VMR [Karkoschka and Tomasko, 2009, Sromovsky et al., 2014, Irwin et al., 2017, Sromovsky et al., 2019] within Uranus' atmosphere is confirmed, exhibiting a slightly larger reduction here by a factor of $\sim$3 from the equator to the north pole.

4. The temporal brightening of Uranus' north polar hood is confirmed to be predominantly caused by changes in the aerosol scattering properties of the atmosphere, as opposed to variations in cloud-top CH_4 VMR.

5. Within the framework of the holistic aerosol model for Uranus [Irwin et al., 2022,

2023a], we find changes in the 1 – 2-bar haze (aerosol-2) layer to be predominantly responsible for the brightening of the north polar hood, via:

- A thickening, i.e., an increase in the integrated opacity, of this haze layer north of ∼45°N.
- A reduction in the haze's imaginary refractive index spectrum longwards of 0.6 μm and north of ∼40°N, leading to an increase in single-scattering albedo and more reflective aerosols at these wavelengths.

6. A consistent reduction in polar cloud-top CH_4 VMR, north of ∼40°N, is observed between 2012 to 2021.
7. Stability is observed in the altitude of the 1 – 2-bar (aerosol-2) haze layer both temporally and latitudinally between 2012 and 2021.
8. The latitudinal variations in the integrated opacities of the deep haze (aerosol-1), 1 – 2-bar haze (aerosol-2), and extended haze (aerosol-3) layers are consistent with a stacked circulation cell model (e.g., Fletcher et al. [2020]), describing the dynamics of the Uranian atmosphere.

We now return to the scientific questions asked at the outset of this thesis, assessing the degree to which the conclusions above address each of these, and discussing any new questions that arise as a result.

The first of these questions was **what physical changes, if any, are responsible for the observed temporal brightening of Uranus' north polar hood?** The answer to this question was found to be predominantly changes in the aerosol scattering properties of the 1 – 2-bar haze (aerosol-2) layer of the Irwin et al. [2022, 2023a] holistic aerosol model for Uranus. Specifically, north of ∼45°N an increase in its integrated opacity (i.e., a

thickening of the haze), and north of ∼40°N a reduction in its imaginary refractive index spectrum longwards of 0.6 μm (i.e., an increase in single-scattering albedo), over time. In addition to these changes, a reduction in polar cloud-top CH_4 VMR also provided a minor contribution to the temporal brightening.

This solution naturally leads to the next scientific question; **what is the underlying mechanism driving the physical changes, if any, responsible for the temporal brightening of Uranus' north polar hood?** A definitive answer to this question could not be found from our results alone. However, by combining our results with additional constraints provided by the scientific literature, a plausible mechanism was proposed that could be responsible for the physical changes outlined above. This was given as a poleward stratospheric meridional transport and settling of haze [Toledo et al., 2019] within the 1 – 2-bar haze layer, where a region of static stability is found [Irwin et al., 2022]. This circulation would lead to the temporal thickening of the 1 – 2-bar haze, as well as altering the rate of condensation of CH_4 within this layer. This in turn would lengthen the lifetime of the aerosols within it, such that it would lead to a reduction in the imaginary refractive index spectrum at long wavelengths. Additionally, if further evidence supports the provisional signs of a slowing in the temporal brightening, a slowing of this stratospheric meridional circulation could explain this observation, which could be caused by a heating of the pole within the stratosphere due to increasing insolation in the polar region as the season progresses towards northern summer solstice in 2030. This is just one of a number of possible solutions, though, and more evidence is needed to determine whether this is the correct interpretation. Useful work to probe this scenario would include observations of the distribution of stratospheric hydrocarbons with latitude, with polar concentrations being expected for the proposed circulation cell. In addition, ob-

serving temporal variations in the north polar stratospheric temperature (e.g., using the James Webb Space Telescope's Mid-IR Instrument) could rule out the proposed heating of the north pole purported to result in a slowing of the circulation. The temporal reduction in polar cloud-top CH_4 mixing ratio was attributed to a tropospheric meridional circulation cell exhibiting upwelling at low and equatorial latitudes and downwelling at high and polar latitudes, previously favoured in the literature [Karkoschka and Tomasko, 2009, Sromovsky et al., 2011, 2014, 2019, Fletcher et al., 2020].

The subsequent scientific question addresses general variability within the Uranian atmosphere, asking **how do the aerosol layers of Uranus' atmosphere change with latitude and time?** This question is an important one when considering the development of the literature on this topic. Until Karkoschka and Tomasko [2009]'s landmark paper revealing latitudinal variability in the cloud-top CH_4 VMR within the Uranian atmosphere, it was largely thought that the observed latitudinal variations in reflectivity were mainly a result of changes in the altitudes of the tops of the aerosol layers, and that CH_4 VMR was relatively stable with latitude (e.g., Sromovsky and Fry [2007], Irwin et al. [2007]). Our results confirm the latitudinal variation in cloud-top CH_4 VMR, whilst also revealing latitudinal variations within each of the aerosol layers in our model. Temporal trends were also found, with some only being provisional. The deep haze (aerosol-1) layer, which was fixed at a central pressure of 5 bar in our model, exhibited large integrated opacity at low and equatorial latitudes that fell off toward the poles, displaying a roughly symmetrical profile about the peak in opacity. This describes a thicker haze at low latitudes and a thinner haze at high latitudes, suggesting upwelling at equatorial latitudes and downwellng at the poles. Temporally, a provisional increase in integrated opacity north of $\sim$45°N was also observed. The 1 – 2-bar haze (aerosol-2) layer exhibited a

strong degree of stability in its central pressure, both latitudinally and temporally, in line with Irwin et al. [2022]'s assertion that this layer lies in a region of static stability. The latitudinal variation of the integrated opacity displayed large values at equatorial and low latitudes, falling off toward the poles. However, north of ∼40°N a temporal dependence was observed, with the opacity increasing over time. This trend hints at an underlying circulation similar to that suggested by the aerosol-1 latitudinal variations, i.e., upwelling at the equator and downwelling at the poles, with the temporal increase in opacity seen at high latitudes originating from some other mechanism (attributed to the aforementioned stratospheric meridional transport and settling of haze). The imaginary refractive index spectrum of this haze also shows very consistent latitudinal variations, with stable n_i values found at low latitudes and a temporal dependence observed north of ∼40°N, where decreasing values are observed over time. Finally, the extended haze (aerosol-3) layer, with fixed base pressure of 1.6 bar in our model, was observed to exhibit a latitudinal variation in the integrated opacity of large values at equatorial latitudes falling off toward the poles. A provisional temporal stability in the profile was concluded. The latitudinal variations and temporal trends observed in this work provide clues regarding the dynamics of the Uranian atmosphere, conjuring up questions about its underlying circulation patterns at different pressure levels.

The final two scientific questions asked at the outset of this thesis were in regard to the cloud-top CH_4 VMR, the first of which being; **is the latitudinal profile of cloud-top CH_4 VMR stable over long timescales ($\gtrsim$ 3 years)?** The answer to this question was found to be no. The cloud-top CH_4 VMR north of ∼40°N was observed to be reducing over time, enhancing the existing polar depletion. The consistent reduction with time suggests a link to the orbital phase of Uranus, i.e., the season. This result is contrary to

Sromovsky et al. [2019]'s conclusion of a general stability in the latitudinal profile of cloud-top CH_4 VMR. This reduction over time then begs the question of how the cloud-top CH_4 VMR varies over an entire Uranian orbit? Would the same phenomenon be observed on the approach to southern summer solstice? And would we observe a corresponding increase in polar VMR on the approach to equinox after Uranus passes through northern summer solstice in 2030? This result leads onto the final scientific question of this thesis; **does the depletion in polar cloud-top CH_4 VMR exhibit interseasonal variability?** We find the answer to this question to be yes. We observe a reduction in polar cloud-top CH_4 mixing ratio over time during northern spring. This leads to the question, what is the underlying cause of this interseasonal variability? And is it related to the underlying cause of the latitudinal gradient in cloud-top CH_4 VMR itself?

6.4 Future Work

There are many avenues with which to extend the work that has been carried out in this thesis. Firstly, a very simple extension of this work can be achieved by acquiring a 2021 HST/STIS observation obtained by Erich Karkoschka, Lawrence Sromovsky and Patrick Fry, which is currently being reduced and analysed. This observation was made using the same methodology that captured the 2012 and 2015 HST/STIS observations used in this thesis. Adding a latitudinal retrieval analysis of this observation would enable two important things: 1) a like-for-like direct comparison to the 2012 and 2015 retrieved profiles, in particular for τ_1 and τ_3 where our retrievals exhibit less constraint and temporal comparisons proved difficult, and 2) a comparison to the 2021 WFC3 and 2021 MUSE profiles to explore agreements and inconsistencies between the three datasets, in particular cloud-top CH_4 VMR with MUSE. This would be a fairly straightforward analysis to

carry out that would provide an additional level of confidence to the conclusions of this thesis, were the profiles to be in line with those presented here.

The next suggestion would be to continue tracking the development of Uranus and its north polar hood by acquiring another VLT/MUSE observation, captured in the run up to northern summer solstice in 2030. Tracking the latitudinal trends in the parameters of our model over longer timescales via a latitudinal retrieval analysis would enable a further probing of the observed tentative slowing in the brightening of the north polar hood with time. In addition, a further tracking of the observed reduction in polar cloud-top CH_4 VMR can be carried out. As mentioned at the end of Section 5.2.4, in order to further solidify the retrieved reduction in cloud-top CH_4 VMR, it would be useful to carry out the retrievals of this investigation treating the vertical profile of CH_4 VMR with the 'descended' profile approach, from which Sromovsky et al. [2019] concluded a general stability in its latitudinal profile, as opposed to the simple step model used in this work. As this treatment results in a more physically plausible vertical profile, observing the same temporal trend in the retrieved profiles would add more weight to the disagreement of a general stability in the latitudinal profile.

The retrieved latitudinal profiles of the aerosol layer properties provided hints for the circulation of Uranus' atmosphere, suggesting upwelling and downwelling at either high or low latitudes in different pressure regions. However, most of the work on the dynamics of Uranus' atmosphere has constructed circulation models based on results from the scientific literature, e.g., latitudinal variations in molecules such as CH_4, or H_2S/NH_3 inferred from brightness temperature variations, stratospheric chemical tracers, zonal winds, and many other considerations (e.g., Fletcher et al. [2020]). However, general circulation models (GCMs) of Uranus' atmosphere at the time of writing are scarce. The

construction of a robust GCM to model the dynamics of the Uranian atmosphere would be extremely useful in putting the results of this investigation, as well as many others, in context. With a dedicated orbiter and probe mission to Uranus, providing *in situ* data on the circulation and dynamics, still a distant possibility, the best avenue available to make progress in this area would be a robust GCM.

Some smaller additional avenues to explore include seeking out an alternative source for CH_4 absorption coefficients to Karkoschka and Tomasko [2010]. Many spectroscopic databases exist such as HITRAN [Rothman et al., 2005], ExoMol [Tennyson and Yurchenko, 2012] and TheoReTS [Rey et al., 2016, 2018], containing high resolution absorption lines for various molecules. However, as these are intended for exoplanet spectroscopy, the wavelength ranges are typically limited to the IR ($\gtrsim 0.8$ μm) due to the high temperatures found in the inflated atmospheres of hot Jupiters (meaning thermal emission dominates). Thus, they do not cover the visible wavelength range used in this work where the absorption lines become much weaker. Until the absorption lines are provided for the visible wavelength range, the only option for incorporating them would be to stitch these absorption coefficients together with those of Karkoschka and Tomasko [2010], leading to a discontinuity at the crossover wavelength. As a degree of the systematic error in our retrieval stems from these absorption coefficients, finding an improved set would be a useful pursuit.

One final smaller avenue to pursue would be testing some more recent temperature profiles of the atmosphere of Uranus. The work in this thesis uses the F1 temperature profile of Lindal et al. [1987], obtained from *Voyager 2* radio occultation measurements. However, more recent temperature profiles are available, such as Orton et al. [2014a]'s obtained using the Spitzer space telescope, which can be applied to our model and a

comparison of the results from the profiles carried out. This analysis would be similar to that carried out by Irwin et al. [2018], for which no significant differences were observed, and Sromovsky et al. [2019]. Though this analysis would be unlikely to produce any significant changes to the results presented in this thesis, presenting this result would only serve to make them more robust.

As with any scientific investigation, it seems that answering one question inexorably leads to several more being asked. With much still to learn about the planet Uranus, including its formation history, its evolution, and its atmospheric dynamics, continued observation is key to uncovering the many mysteries that this planet holds close to its chest, obscuring them from prying eyes.

Bibliography

A. Akins, M. Hofstadter, B. Butler, A. J. Friedson, E. Molter, M. Parisi, and I. de Pater. Evidence of a Polar Cyclone on Uranus From VLA Observations. *Geophysical Research Letters*, 50(10), 2023.

B. A. Archinal, C. H. Acton, M. F. A'hearn, A. Conrad, G. J. Consolmagno, T. Duxbury, D. Hestroffer, J. L. Hilton, R. L. Kirk, S. A. Klioner, D. Mccarthy, K. Meech, J. Oberst, J. Ping, P. K. Seidelmann, D. J. Tholen, P. C. Thomas, and I. P. Williams. Report of the IAU Working Group on Cartographic Coordinates and Rotational Elements: 2015. *Celest Mech Dyn Astr*, 130(22), 2018.

S. K. Atreya. Uranus photochemistry and prospects for Voyager 2 at Neptune. *Advances in Space Research*, 10(1):113–119, 1990.

S. K. Atreya, M. H. Hofstadter, J. H. In, O. Mousis, K. Reh, and M. H. Wong. Deep Atmosphere Composition, Structure, Origin, and Exploration, with Particular Focus on Critical *in situ* Science at the Icy Giants. *Space Science Reviews*, 216(1), 2020.

R. Bacon, M. Accardo, L. Adjali, H. Anwand, S. Bauer, I. Biswas, J. Blaizot, D. Boudon, S. Brau-Nogue, J. Brinchmann, P. Caillier, L. Capoani, C. M. Carollo, T. Contini, P. Couderc, E. Daguisé, S. Deiries, B. Delabre, S. Dreizler, J. Dubois, M. Dupieux,

C. Dupuy, E. Emsellem, T. Fechner, A. Fleischmann, M. François, G. Gallou, T. Gharsa, A. Glindemann, D. Gojak, B. Guiderdoni, G. Hansali, T. Hahn, A. Jarno, A. Kelz, C. Koehler, J. Kosmalski, F. Laurent, M. Le Floch, S. J. Lilly, J.-L. Lizon, M. Loupias, A. Manescau, C. Monstein, H. Nicklas, J.-C. Olaya, L. Pares, L. Pasquini, A. Pécontal-Rousset, R. Pelló, C. Petit, E. Popow, R. Reiss, A. Remillieux, E. Renault, M. Roth, G. Rupprecht, D. Serre, J. Schaye, G. Soucail, M. Steinmetz, O. Streicher, R. Stuik, H. Valentin, J. Vernet, P. Weilbacher, L. Wisotzki, and N. Yerle. The MUSE second-generation VLT instrument. *Ground-based and Airborne Instrumentation for Astronomy III*, 7735:773508, 2010.

K. H. Baines and J. T. Bergstralh. The structure of the Uranian atmosphere: Constraints from the geometric albedo spectrum and H_2 and CH_4 line profiles. *Icarus*, 65(2-3): 406–441, 1986.

K. H. Baines and H. B. Hammel. Clouds, Hazes, and the Stratospheric Methane Abundance in Neptune. *Icarus*, 109(1):20–39, 1994.

K. H. Baines, M. E. Mickelson, L. E. Larson, and D. W. Ferguson. The Abundances of Methane and Ortho/Para Hydrogen on Uranus and Neptune: Implications of New Laboratory 4-0 H_2 Quadrupole Line Parameters. *Icarus*, 114(2):328–340, 1995.

J. Bally, R. S. Sutherland, D. Devine, and D. Johnstone. Externally Illuminated Young Stellar Environments in the Orion Nebula: Hubble Space Telescope Planetary Camera and Ultraviolet Observations. *The Astronomical Journal*, 116(1):293–321, 1998.

R. E. Bandy, C. Lakshminarayan, R. K. Frost, and T. S. Zwier. Direct detection of C_4H_2 photochemical products: Possible routes to complex hydrocarbons in planetary atmospheres. *Science*, 258(5088):1630–1633, 1992.

N. M. Batalha, J. F. Rowe, S. T. Bryson, T. Barclay, C. J. Burke, D. A. Caldwell, J. L. Christiansen, F. Mullally, S. E. Thompson, T. M. Brown, A. K. Dupree, D. C. Fabrycky, E. B. Ford, J. J. Fortney, R. L. Gilliland, H. Isaacson, D. W. Latham, G. W. Marcy, S. N. Quinn, D. Ragozzine, A. Shporer, W. J. Borucki, D. R. Ciardi, T. N. Gautier, M. R. Haas, J. M. Jenkins, D. G. Koch, J. J. Lissauer, W. Rapin, G. S. Basri, A. P. Boss, L. A. Buchhave, J. A. Carter, D. Charbonneau, J. Christensen-Dalsgaard, B. D. Clarke, W. D. Cochran, B.-O. Demory, J.-M. Desert, E. Devore, L. R. Doyle, G. A. Esquerdo, M. Everett, F. Fressin, J. C. Geary, F. R. Girouard, A. Gould, J. R. Hall, M. J. Holman, A. W. Howard, S. B. Howell, K. A. Ibrahim, K. Kinemuchi, H. Kjeldsen, T. C. Klaus, J. Li, P. W. Lucas, S. Meibom, R. L. Morris, A. Prša, E. Quintana, D. T. Sanderfer, D. Sasselov, S. E. Seader, J. C. Smith, J. H. Steffen, M. Still, M. C. Stumpe, J. C. Tarter, P. Tenenbaum, G. Torres, J. D. Twicken, K. Uddin, J. Van Cleve, L. Walkowicz, and W. F. Welsh. Planetary Candidates Observed by Kepler. III. Analysis of the First 16 Months of Data. *The Astrophysical Journal Supplement Series*, 204 (2):24, 2013.

A. P. Boss. Rapid Formation of Outer Giant Planets by Disk Instability. *The Astrophysical Journal*, 599(1):577–581, 2003.

A. P. Boss. Testing Disk Instability Models for Giant Planet Formation. *The Astrophysical Journal*, 661(1):L73–L76, 2007.

A. P. Boss, G. W. Wetherill, and N. Haghighipour. Rapid Formation of Ice Giant Planets. *Icarus*, 156:291–295, 2002.

G. Boué and J. Laskar. A Collisionless Scenario for Uranus Tilting. *The Astrophysical Journal*, 712(1):L44–L47, 2010.

R. Bourtembourg. Was uranus observed by hipparchus. *Journal for the History of Astronomy*, 44(4):377–387, 2013.

C. Briceño, A. K. Vivas, N. Calvet, L. Hartmann, R. Pacheco, D. Herrera, L. Romero, P. Berlind, G. Sánchez, J. A. Snyder, and P. Andrews. The CIDA-QUEST large-scale survey of Orion OB1: Evidence for rapid disk dissipation in a dispersed stellar population. *Science*, 291(5501):93–96, 2001.

A. Calamida, J. Mack, J. Medina, C. Shahanan, V. Bajaj, and S. Deustua. New time-dependent WFC3 UVIS inverse sensitivities. *Instrument Science Report WFC3 2021-4*, 3:1–33, 2021.

A. Calamida, V. Bajaj, J. Mack, M. Marinelli, J. Medina, A. Pidgeon, V. Kozhurina-Platais, C. Shanahan, and D. Som. New Photometric Calibration of the Wide Field Camera 3 Detectors. *The Astronomical Journal*, 164(2):32, 2022.

B. E. Carlson, W. B. Rossow, and G. S. Orton. Cloud Microphysics of the Giant Planets. *Journal of the Atmospheric Sciences*, 45(14):2066–2081, 1988.

T. Cavalié, R. Moreno, E. Lellouch, P. Hartogh, O. Venot, G. S. Orton, C. Jarchow, T. Encrenaz, F. Selsis, F. Hersant, and L. N. Fletcher. The first submillimeter observation of CO in the stratosphere of Uranus. *Astronomy & Astrophysics*, 562:33, 2014.

T. Cavalié, O. Venot, F. Selsis, F. Hersant, P. Hartogh, and J. Leconte. Thermochemistry and vertical mixing in the tropospheres of Uranus and Neptune: How convection inhibition can affect the derivation of deep oxygen abundances. *Icarus*, 291:1–16, 2017.

B. Conrath, D. Gautier, R. Hanel, G. Lindal, and A. Marten. The Helium Abundance

of Uranus From Voyager Measurements. *Journal of Geophysical Research*, 92(A13): 15003–15010, 1987.

B. J. Conrath, P. J. Gierasch, and S. S. Leroy. Temperature and circulation in the stratosphere of the outer planets. *Icarus*, 83(2):255–281, 1990.

B. J. Conrath, D. Gautier, G. F. Lindal, R. E. Samuelson, and W. A. Shaffer. The Helium Abundance of Neptune From Voyager Measurements. *Journal of Geophysical Research*, 96(S01):907–925, 1991.

B. J. Conrath, P. J. Gierasch, and E. A. Ustinov. Thermal Structure and Para Hydrogen Fraction on the Outer Planets from Voyager IRIS Measurements. *Icarus*, 135(2):501–517, 1998.

R. G. Cosentino, R. Morales-Juberías, T. Greathouse, G. Orton, P. Johnson, L. N. Fletcher, and A. Simon. New Observations and Modeling of Jupiter's Quasi-Quadrennial Oscillation. *Journal of Geophysical Research: Planets*, 122(12):2719–2744, 2017.

I. de Pater and S. T. Massie. Models of the millimeter-centimeter spectra of the giant planets. *Icarus*, 62(1):143–171, 1985.

I. de Pater, P. N. Romani, and S. K. Atreya. Uranus deep atmosphere revealed. *Icarus*, 82(2):288–313, 1989.

I. de Pater, P. N. Romani, and S. K. Atreya. Possible microwave absorption by H_2S gas in Uranus' and Neptune's atmospheres. *Icarus*, 91(2):220–233, 1991.

I. de Pater, L. A. Sromovsky, P. M. Fry, H. B. Hammel, C. Baranec, and K. M. Sayanagi. Record-breaking storm activity on Uranus in 2014. *Icarus*, 252:121–128, 2015.

S. E. Dodson-Robinson and P. Bodenheimer. The formation of Uranus and Neptune in solid-rich feeding zones: Connecting chemistry and dynamics. *Icarus*, 207(1):491–498, 2010.

T. E. Dowling, A. S. Fischer, P. J. Gierasch, J. Harrington, R. P. Lebeau, and C. M. Santori. The Explicit Planetary Isentropic-Coordinate (EPIC) Atmospheric Model. *Icarus*, 132(2):221–238, 1998.

T. E. Dowling, M. E. Bradley, E. Colón, J. Kramer, R. P. LeBeau, G. C. Lee, T. I. Mattox, R. Morales-Juberías, C. J. Palotai, V. K. Parimi, and A. P. Showman. The EPIC atmospheric model with an isentropic/terrain-following hybrid vertical coordinate. *Icarus*, 182(1):259–273, 2006.

T. Dubos, S. Dubey, M. Tort, R. Mittal, Y. Meurdesoif, and F. Hourdin. DYNAMICO-1.0, an icosahedral hydrostatic dynamical core designed for consistency and versatility. *Geoscientific Model Development*, 8(10):3131–3150, 2015.

T. Encrenaz, E. Serabyn, and E. W. Weisstein. Millimeter Spectroscopy of Uranus and Neptune: Constraints on CO and PH_3 Tropospheric Abundances. *Icarus*, 124(2):616–624, 1996.

T. Encrenaz, H. Feuchtgruber, S. K. Atreya, B. Bézard, E. Lellouch, J. Bishop, S. Edgington, T. De Graauw, M. Griffin, and M. F. Kessler. ISO observations of Uranus: The stratospheric distribution of C_2H_2 and the eddy diffusion coefficient. *Astron. Astrophys*, 333:43–46, 1998.

T. Encrenaz, E. Lellouch, P. Drossart, H. Feuchtgruber, G. S. Orton, and S. K. Atreya. First detection of CO in Uranus. *Astronomy & Astrophysics*, 413:5–9, 2004.

R. J. Fétick, T. Fusco, B. Neichel, L. M. Mugnier, O. Beltramo-Martin, A. Bonnefois, C. Petit, J. Milli, J. Vernet, S. Oberti, and R. Bacon. Physics-based model of the adaptive-optics-corrected point spread function: Applications to the SPHERE/ZIMPOL and MUSE instruments. *Astronomy Astrophysics*, 628:1–11, 2019.

H. Feuchtgruber, E. Lellouch, T. De Graauw, B. Bé Zard, T. Encrenaz, and M. Griffink. External supply of oxygen to the atmospheres of the giant planets. *Nature*, 389, 1997.

F. M. Flasar, B. J. Conrath, P. J. Gierasch, and J. A. Pirraglia. Voyager Infrared Observations of Uranus' Atmosphere: Thermal Structure and Dynamics. *Journal of Geophysical Research*, 92(A13):11–15, 1987.

L. N. Fletcher, P. Drossart, M. Burgdorf, G. S. Orton, and T. Encrenaz. Neptune's atmospheric composition from AKARI infrared spectroscopy. *Astronomy & Astrophysics*, 514:17, 2010.

L. N. Fletcher, I. de Pater, G. S. Orton, M. D. Hofstadter, P. G. J. Irwin, M. T. Roman, D. Toledo, O. Mousis, D. H. Atkinson, and B. L. N. Fletcher. Ice Giant Circulation Patterns: Implications for Atmospheric Probes. *Space Science Reviews*, 216(21), 2020.

D. Foreman-Mackey, D. W. Hogg, D. Lang, and J. Goodman. emcee: The MCMC Hammer. *Publications of the Astronomical Society of the Pacific*, 125(925):306–312, 2013.

T. Fouchet, E. Lellouch, and H. Feuchtgruber. The hydrogen ortho-to-para ratio in the stratospheres of the giant planets. *Icarus*, 161(1):127–143, 2003.

R. Frelikh and R. A. Murray-Clay. The Formation of Uranus and Neptune: Fine-tuning in Core Accretion. *The Astronomical Journal*, 154(3):98, 2017.

A. Fruchter and M. Sosey. The MultiDrizzle Handbook. *HST Data Handbooks*, (v3.0), 2009.

R. Garland. Modelling the spectra of brown dwarfs. *PhD thesis, University of Oxford, Oxford*, 2018.

M. Ghil, M. R. Allen, M. D. Dettinger, K. Ide, D. Kondrashov, M. E. Mann, A. W. Robertson, A. Saunders, Y. Tian, F. Varadi, and P. Yiou. Advanced spectral methods for climatic time series. *Reviews of Geophysics*, 40(1):3–1–3–41, 2002.

J. F. Giovannelli and A. Coulais. Positive deconvolution for superimposed extended source and point sources. *Astronomy and Astrophysics*, 439(1):401–412, 2005.

R. M. Goody and Y. L. Yung. *Atmospheric Radiation: Theoretical Basis*. Oxford University Press Inc., 1989.

S. Guerlet, A. Spiga, M. Sylvestre, M. Indurain, T. Fouchet, J. Leconte, E. Millour, R. Wordsworth, M. Capderou, B. Bézard, and F. Forget. Global climate modeling of Saturn's atmosphere. Part I: Evaluation of the radiative transfer model. *Icarus*, 238: 110–124, 2014.

H. B. Hammel, K. Rages, G. W. Lockwood, E. Karkoschka, and I. de Pater. New Measurements of the Winds of Uranus. *Icarus*, 153(2):229–235, 2001.

H. B. Hammel, L. A. Sromovsky, P. M. Fry, K. Rages, M. Showalter, I. de Pater, M. A. van Dam, R. P. Lebeau, and X. Deng. The Dark Spot in the atmosphere of Uranus in 2006: Discovery, description, and dynamical simulations. *Icarus*, 201:257–271, 2009.

W. K. Hastings. Monte Carlo sampling methods using Markov chains and their applications. *Biometrika*, 57(1):97, 1970.

R. Helled and P. Bodenheimer. The Formation of Uranus and Neptune: Challenges and Implications for Intermediate-Mass Exoplanets. *The Astrophysical Journal*, 789(1): 69, 2014.

R. Helled, N. Nettelmann, and T. Guillot. Uranus and Neptune: Origin, Evolution and Internal Structure. *Space Science Reviews*, 216(3), 2020.

B. E. Hesman, G. R. Davis, H. E. Matthews, and G. S. Orton. The abundance profile of CO in Neptune's atmosphere. *Icarus*, 186(2):342–353, 2007.

P. G. Irwin. *Giant Planets of Our Solar System: Atmospheres, Composition, and Structure*. Springer Science & Business Media, 2009.

P. G. Irwin, N. A. Teanby, R. de Kok, L. N. Fletcher, C. J. Howett, C. C. Tsang, C. F. Wilson, S. B. Calcutt, C. A. Nixon, and P. D. Parrish. The NEMESIS planetary atmosphere radiative transfer and retrieval tool. *Journal of Quantitative Spectroscopy and Radiative Transfer*, 2008.

P. G. Irwin, N. A. Teanby, and G. R. Davis. Vertical cloud structure of Uranus from UKIRT/UIST observations and changes seen during Uranus' northern spring equinox from 2006 to 2008. *Icarus*, 203(1):287–302, 2009.

P. G. Irwin, N. A. Teanby, and G. R. Davis. Revised vertical cloud structure of Uranus from UKIRT/UIST observations and changes seen during Uranus' Northern Spring Equinox from 2006 to 2008: Application of new methane absorption data and comparison with Neptune. *Icarus*, 208(2):913–926, 2010.

P. G. Irwin, N. A. Teanby, G. R. Davis, L. N. Fletcher, G. S. Orton, S. B. Calcutt, D. S. Tice, and J. Hurley. Further seasonal changes in Uranus' cloud structure observed by Gemini-North and UKIRT. *Icarus*, 218(1):47–55, 2012.

P. G. Irwin, D. S. Tice, L. N. Fletcher, J. K. Barstow, N. A. Teanby, G. S. Orton, and G. R. Davis. Reanalysis of Uranus' cloud scattering properties from IRTF/SpeX observations using a self-consistent scattering cloud retrieval scheme. *Icarus*, 250:462–476, 2015.

P. G. Irwin, L. N. Fletcher, P. L. Read, D. Tice, I. de Pater, G. S. Orton, N. A. Teanby, and G. R. Davis. Spectral analysis of Uranus' 2014 bright storm with VLT/SINFONI. *Icarus*, 264:72–89, 2016.

P. G. Irwin, M. H. Wong, A. A. Simon, G. S. Orton, and D. Toledo. HST/WFC3 observations of Uranus' 2014 storm clouds and comparison with VLT/SINFONI and IRTF/Spex observations. *Icarus*, 288:99–119, 2017.

P. G. Irwin, J. Dobinson, A. James, D. Toledo, N. A. Teanby, L. N. Fletcher, G. S. Orton, and S. Pérez-Hoyos. Latitudinal variation of methane mole fraction above clouds in Neptune's atmosphere from VLT/MUSE-NFM: Limb-darkening reanalysis. *Icarus*, 357, 2021.

P. G. Irwin, N. A. Teanby, L. N. Fletcher, D. Toledo, G. S. Orton, M. H. Wong, M. T. Roman, S. Pérez-Hoyos, A. James, and J. Dobinson. Hazy Blue Worlds: A Holistic Aerosol Model for Uranus and Neptune, Including Dark Spots. *Journal of Geophysical Research: Planets*, 127(6), 2022.

P. G. Irwin, N. A. Teanby, L. N. Fletcher, D. Toledo, G. S. Orton, M. H. Wong, M. T. Roman, S. Pérez-Hoyos, A. James, and J. Dobinson. Spectral determination of the

colour and vertical structure of dark spots in Neptune's atmosphere. *Nature Astronomy*, 2023a.

P. G. J. Irwin, N. A. Teanby, and G. R. Davis. Latitudinal Variations in Uranus' Vertical Cloud Structure from UKIRT UIST Observations. *The Astrophysical Journal*, 665(1): L71–L74, 2007.

P. G. J. Irwin, N. A. Teanby, G. R. Davis, L. N. Fletcher, G. S. Orton, D. Tice, and A. Kyffin. Uranus' cloud structure and seasonal variability from Gemini-North and UKIRT observations. *Icarus*, 212(1):339–350, 2011.

P. G. J. Irwin, D. Toledo, R. Garland, N. A. Teanby, L. N. Fletcher, G. A. Orton, and B. Bézard. Detection of hydrogen sulfide above the clouds in Uranus's atmosphere. *Nature Astronomy*, (2):420–427, 2018.

P. G. J. Irwin, J. Dobinson, A. James, M. H. Wong, L. N. Fletcher, M. T. Roman, N. A. Teanby, D. Toledo, G. S. Orton, S. Pérez-Hoyos, A. Sánchez-Lavega, A. Simon, R. Morales-Juberias, and I. de Pater. Latitudinal Variations in Methane Abundance, Aerosol Opacity and Aerosol Scattering Efficiency in Neptune's Atmosphere Determined From VLT/MUSE. *Journal of Geophysical Research: Planets*, 128(11), 2023b.

R. A. Jacobson. The Orbits of the Uranian Satelittes and Rings, the Gravity Field of the Uranian System, and the Orientation of the Pole of Uranus. *The Astronomical Journal*, 148(5):76, 2014.

A. James, P. G. J. Irwin, J. Dobinson, M. H. Wong, T. K. Tsubota, A. A. Simon, L. N. Fletcher, M. T. Roman, N. A. Teanby, D. Toledo, and G. S. Orton. The Temporal

Brightening of Uranus' Northern Polar Hood From HST/WFC3 and HST/STIS Observations. *Journal of Geophysical Research: Planets*, 128(10), 2023.

E. Karkoschka and M. Tomasko. The haze and methane distributions on Uranus from HST-STIS spectroscopy. *Icarus*, 202(1):287–309, 2009.

E. Karkoschka and M. G. Tomasko. Methane absorption coefficients for the jovian planets from laboratory, Huygens, and HST data. *Icarus*, 205(2):674–694, 2010.

E. Karkoschka and M. G. Tomasko. The haze and methane distributions on Neptune from HST-STIS spectroscopy. *Icarus*, 211(1):780–797, 2011.

J. A. Kegerreis, L. F. A. Teodoro, V. R. Eke, R. J. Massey, D. C. Catling, C. L. Fryer, D. G. Korycansky, M. S. Warren, and K. J. Zahnle. Consequences of Giant Impacts on Early Uranus for Rotation, Internal Structure, Debris, and Atmospheric Erosion. *The Astrophysical Journal*, 861(1):52, 2018.

J. Krist. Simulation of HST PSFs using Tiny Tim. *Astronomical Data Analysis Software and Systems IV*, 77, 1995.

A. A. Lacis and V. Oinas. A description of the correlated k distribution method for modeling nongray gaseous absorption, thermal emission, and multiple scattering in vertically inhomogeneous atmospheres. *Journal of Geophysical Research: Atmospheres*, 96(D5):9027–9063, 1991.

E. Lellouch, R. Moreno, G. S. Orton, H. Feuchtgruber, T. Cavalié, J. I. Moses, P. Hartogh, C. Jarchow, and H. Sagawa. Astrophysics New constraints on the CH_4 vertical profile in Uranus and Neptune from Herschel observations. *Astronomy & Astrophysics*, 579 (A121):121–126, 2015.

K. Levenberg. A Method for the Solution of Certain Non-Linear Problems in Least Squares. *Quarterly of Applied Mathematics*, 2(2):164–168, 1944.

Y. Lian and A. P. Showman. Generation of equatorial jets by large-scale latent heating on the giant planets. *Icarus*, 207(1):373–393, 2010.

G. F. Lindal. The Atmosphere of Neptune: An Analysis of Radio Occultation Data Acquired with Voyager 2. *The Astronomical Journal*, 103(3):967–982, 1992.

G. F. Lindal, J. R. Lyons, D. N. Sweetnam, V. R. Eshleman, D. P. Hinson, and G. L. Tyler. The atmosphere of Uranus: Results of radio occultation measurements with Voyager 2. *Journal of Geophysical Research*, 92(A13):14987–15001, 1987.

G. F. Lindal, J. R. Lyons, D. N. Sweetnam, V. R. Eshleman, D. P. Hinson, and G. L. Tyler. The atmosphere of Neptune: Results of radio occultation measurements with the Voyager 2 spacecraft. 17(10):1733–1736, 1990.

L. B. Lucy, Lucy, and L. B. An iterative technique for the rectification of observed distributions. *Astronomical Journal*, 79(6):745, 1974.

A. Mahjoub, N. Carrasco, P. R. Dahoo, T. Gautier, C. Szopa, and G. Cernogora. Influence of methane concentration on the optical indices of titan's aerosols analogues. *Icarus*, 221(2):670–677, 2012.

M. S. Marley and C. P. McKay. Thermal Structure of Uranus' Atmosphere. *Icarus*, 138 (2):268–286, 1999.

D. W. Marquardt. An Algorithm for Least-Squares Estimation of Nonlinear Parameters. *Journal of the Society for Industrial and Applied Mathematics*, 11(2):431–441, 1963.

Y. Miguel and A. Vazan. Interior and Evolution of the Giant Planets. *Remote Sensing*, 15(3):1–22, 2023.

G. Milcareck, S. Guerlet, A. Spiga, J. Leconte, D. Bardet, F. Montmessin, and A. Boissinot. GCM simulations of Uranus and Neptune: general circulation and eddy activity. *Europlanet Science Congress 2021*, 2021.

B. Militzer, W. B. Hubbard, S. Wahl, J. I. Lunine, E. Galanti, Y. Kaspi, Y. Miguel, T. Guillot, K. M. Moore, M. Parisi, J. E. P. Connerney, R. Helled, H. Cao, C. Mankovich, D. J. Stevenson, R. S. Park, M. Wong, S. K. Atreya, J. Anderson, and S. J. Bolton. Juno Spacecraft Measurements of Jupiter's Gravity Imply a Dilute Core. *The Planetary Science Journal*, 3(8):185, 2022.

M. Minnaert. The reciprocity principle in lunar photometry. *The Astrophysical Journal*, 93(2):403, 1941.

M. I. Mishchenko and L. D. Travis. Gustav Mie and the Evolving Discipline of Electromagnetic Scattering by Particles. *Bulletin of the American Meteorological Society*, 89 (12):1853–1862, 2008.

E. M. Molter, I. de Pater, S. Luszcz-Cook, J. Tollefson, R. J. Sault, B. Butler, and D. de Boer. Tropospheric Composition and Circulation of Uranus with ALMA and the VLA. *The Planetary Science Journal*, 2(1):3, 2021.

J. I. Moses, K. Rages, and J. B. Pollack. An Analysis of Neptune's Stratospheric Haze Using High-Phase-Angle Voyager Images. *Icarus*, 113(2):232–266, 1995.

J. I. Moses, L. N. Fletcher, T. K. Greathouse, G. S. Orton, and V. Hue. Seasonal stratospheric photochemistry on Uranus and Neptune. *Icarus*, 307:124–145, 2018.

J. I. Moses, T. Cavalié, L. N. Fletcher, and M. T. Roman. Atmospheric chemistry on Uranus and Neptune. *Phil. Trans. R. Soc. A*, 378(2187), 2020.

O. Mousis, A. Aguichine, R. Helled, P. G. J. Irwin, and J. I. Lunine. The role of ice lines in the formation of Uranus and Neptune. *Phil. Trans. R. Soc. A*, 378(2187), 2020.

S. Müller, R. Helled, and L. Mayer. On the Diversity in Mass and Orbital Radius of Giant Planets Formed via Disk Instability. *The Astrophysical Journal*, 854(2):112, 2018.

N. Nettelmann, R. Helled, J. J. Fortney, and R. Redmer. New indication for a dichotomy in the interior structure of Uranus and Neptune from the application of modified shape and rotation data. *Planetary and Space Science*, 77:143–151, 2013.

J. W. Norwood and N. J. Chanover. Spatial and short-term temporal variations in Uranus' near-infrared spectrum. *Icarus*, 203(1):331–335, 2009.

G. S. Orton, D. K. Aitken, C. Smith, P. F. Roche, J. Caldwell, and R. Snyder. The spectra of Uranus and Neptune at 8-14 and 17-23 μm. *Icarus*, 70(1):1–12, 1987.

G. S. Orton, L. N. Fletcher, J. I. Moses, A. K. Mainzer, D. Hines, H. B. Hammel, F. J. Martin-Torres, M. Burgdorf, C. Merlet, and M. R. Line. Mid-infrared spectroscopy of Uranus from the Spitzer Infrared Spectrometer: 1. Determination of the mean temperature structure of the upper troposphere and stratosphere. *Icarus*, 243:494–513, 2014a.

G. S. Orton, J. I. Moses, L. N. Fletcher, A. K. Mainzer, D. Hines, H. B. Hammel, J. Martin-Torres, M. Burgdorf, C. Merlet, and M. R. Line. Mid-infrared spectroscopy of Uranus from the Spitzer infrared spectrometer: 2. Determination of the mean composition of the upper troposphere and stratosphere. *Icarus*, 243:471–493, 2014b.

N. Otsu. A threshold selection method from gray-level histograms. *IEEE Trans. on Systems, Man and Cybernetics*, 9(1):62–66, 1996.

C. Palotai and T. E. Dowling. Addition of water and ammonia cloud microphysics to the EPIC model. *Icarus*, 194(1):303–326, 2008.

J. C. Pearl and B. J. Conrath. The Albedo, Effective Temperature, and Energy Balance of Neptune, as Determined From Voyager Data. *Journal of Geophysical Research*, 96: 921–939, 1991.

J. C. Pearl, B. J. Conrath, R. A. Hanel, J. A. Pirraglia, and A. Coustenis. The albedo, effective temperature, and energy balance of Uranus, as determined from Voyager IRIS data. *Icarus*, 84(1):12–28, 1990.

S. Pérez-Hoyos, A. Sánchez-Lavega, J. F. Sanz-Requena, N. Barrado-Izagirre, O. Carrión-González, A. Anguiano-Arteaga, P. G. Irwin, and A. S. Braude. Color and aerosol changes in Jupiter after a North Temperate Belt disturbance. *Icarus*, 352, 2020.

E. A. Petigura, G. W. Marcy, J. N. Winn, L. M. Weiss, B. J. Fulton, A. W. Howard, E. Sinukoff, H. Isaacson, T. D. Morton, and J. A. Johnson. The California-Kepler Survey. IV. Metal-rich Stars Host a Greater Diversity of Planets. *The Astronomical Journal*, 155(2):89, 2018.

M. Podolak and R. Helled. What Do We Really Know About Uranus and Neptune? *The Astrophysical Journal*, 759(2):L32, 2012.

J. B. Pollack, K. Rages, S. K. Pope, M. G. Tomasko, P. N. Romani, and S. K. Atreya'.

Nature of the Stratospheric Haze on Uranus: Evidence for Condensed Hydrocarbons. *Journal of Geophysical Research*, 92(A13):37–52, 1987.

J. B. Pollack, O. Hubickyj, P. Bodenheimer, J. J. Lissauer, M. Podolak, and Y. Greenzweig. Formation of the Giant Planets by Concurrent Accretion of Solids and Gas. *Icarus*, 124(1):62–85, 1996.

C. C. Porco, R. A. West, A. Mcewen, A. D. D. Genio, A. P. Ingersoll, P. Thomas, S. Squyres, L. Dones, C. D. Murray, T. V. Johnson, J. A. Burns, A. Brahic, G. Neukum, J. Veverka, J. M. Barbara, T. Denk, M. Evans, J. J. Ferrier, P. Geissler, P. Helfenstein, T. Roatsch, H. Throop, M. Tiscareno, and A. R. Vasavada. Cassini Imaging of Jupiter's Atmosphere, Satellites, and Rings. *Science*, 299(5612):1541–1547, 2003.

K. Rages, J. B. Pollack, M. G. Tomasko, and L. R. Doose. Properties of scatterers in the troposphere and lower stratosphere of Uranus based on Voyager imaging data. *Icarus*, 89(2):359–376, 1991.

C. Reinhardt, A. Chau, J. Stadel, and R. Helled. Bifurcation in the history of Uranus and Neptune: the role of giant impacts. *MNRAS*, 492(4):5336–5353, 2020.

M. Rey, A. V. Nikitin, Y. L. Babikov, and V. G. Tyuterev. TheoReTS - An information system for theoretical spectra based on variational predictions from molecular potential energy and dipole moment surfaces. *Journal of Molecular Spectroscopy*, 327: 138–158, 2016.

M. Rey, A. V. Nikitin, B. Bézard, P. Rannou, A. Coustenis, and V. G. Tyuterev. New accurate theoretical line lists of $^{12}CH_4$ and $^{13}CH_4$ in the 0–13400 cm^{-1} range: Application to the modeling of methane absorption in Titan's atmosphere. *Icarus*, 303: 114–130, 2018.

W. H. Richardson. Bayesian-Based Iterative Method of Image Restoration. *JOSA*, 62 (1):55–59, 1972.

C. D. Rodgers. *Inverse methods for atmospheres: Theory and practice*. World Scientific, 2000.

M. T. Roman, L. N. Fletcher, G. S. Orton, N. Rowe-Gurney, and P. G. J. Irwin. Uranus in Northern Midspring: Persistent Atmospheric Temperatures and Circulations Inferred from Thermal Imaging. *The Astronomical Journal*, 159(2):45, 2020.

P. N. Romani and S. K. Atreya. Methane photochemistry and haze production on Neptune. *Icarus*, 74(3):424–445, 1988.

L. S. Rothman, D. Jacquemart, A. Barbe, D. C. Benner, M. Birk, L. R. Brown, M. R. Carleer, C. Chackerian, K. Chance, L. H. Coudert, V. Dana, V. M. Devi, J. M. Flaud, R. R. Gamache, A. Goldman, J. M. Hartmann, K. W. Jucks, A. G. Maki, J. Y. Mandin, S. T. Massie, J. Orphal, A. Perrin, C. P. Rinsland, M. A. Smith, J. Tennyson, R. N. Tolchenov, R. A. Toth, J. Vander Auwera, P. Varanasi, and G. Wagner. The HITRAN 2004 molecular spectroscopic database. *Journal of Quantitative Spectroscopy and Radiative Transfer*, 96(2):139–204, 2005.

R. Rufu and R. M. Canup. Coaccretion + Giant-impact Origin of the Uranus System: Tilting Impact. *The Astrophysical Journal*, 928(2):123, 2022.

V. S. Safronov. Sizes of the largest bodies falling onto the planets during their formation. *Soviet Astronomy*, 9:987–991, 1966.

A. Sanchez-Lavega, J. F. Rojas, and P. V. Sada. Saturn's Zonal Winds at Cloud Level. *Icarus*, 147(2):405–420, 2000.

M. Sankur and B. Sezgin. Survey over image thresholding techniques and quantitative performance evaluation. *Journal of Electronic Imaging*, 13(1):146–165, 2004.

K. M. Sayanagi and A. P. Showman. Effects of a large convective storm on Saturn's equatorial jet. *Icarus*, 187(2):520–539, 2007.

A. A. Simon, M. H. Wong, and G. S. Orton. First Results From the Hubble OPAL Program: Jupiter in 2015. *The Astrophysical Journal*, 812(1):55, 2015.

J. Skilling. Nested sampling for general Bayesian computation. *Bayesian Anal.*, 1(4): 833–859, 2006.

W. L. Slattery, W. Benz, and A. G. Cameron. Giant impacts on a primitive Uranus. *Icarus*, 99(1):167–174, 1992.

K. M. Soderlund, M. H. Heimpel, E. M. King, and J. M. Aurnou. Turbulent models of ice giant internal dynamics: Dynamos, heat transfer, and zonal flows. *Icarus*, 224(1): 97–113, 2013.

S. T. Sohn, D. Branton, J. Carlberg, J. H. Debes, S. E. Deustua, S. Lockwood, M. Maclay, T. R. Monroe, A. Riley, P. G. Sonnentrucker, and D. E. Welty. STIS Data Handbook. *STScI*, v7.0, 2011.

L. A. Sromovsky and P. M. Fry. Dynamics of cloud features on Uranus. *Icarus*, 179(2): 459–484, 2005.

L. A. Sromovsky and P. M. Fry. Spatially resolved cloud structure on Uranus: Implications of near-IR adaptive optics imaging. *Icarus*, 192(2):527–557, 2007.

L. A. Sromovsky and P. M. Fry. The methane abundance and structure of Uranus' cloud bands inferred from spatially resolved 2006 Keck grism spectra. *Icarus*, 193(1):252–266, 2008.

L. A. Sromovsky, S. S. Limaye, and P. M. Fry. Dynamics of Neptune's Major Cloud Features. *Icarus*, 105(1):110–141, 1993.

L. A. Sromovsky, P. G. Irwin, and P. M. Fry. Near-IR methane absorption in outer planet atmospheres: Improved models of temperature dependence and implications for Uranus cloud structure. *Icarus*, 182(2):577–593, 2006.

L. A. Sromovsky, P. M. Fry, H. B. Hammel, W. M. Ahue, I. de Pater, K. A. Rages, M. R. Showalter, and M. A. van Dam. Uranus at equinox: Cloud morphology and dynamics. *Icarus*, 203(1):265–286, 2009.

L. A. Sromovsky, P. M. Fry, and J. H. Kim. Methane on Uranus: The case for a compact CH_4 cloud layer at low latitudes and a severe CH_4 depletion at high-latitudes based on re-analysis of Voyager occultation measurements and STIS spectroscopy. *Icarus*, 215 (1):292–312, 2011.

L. A. Sromovsky, P. M. Fry, H. B. Hammel, I. de Pater, and K. A. Rages. Post-equinox dynamics and polar cloud structure on Uranus. *Icarus*, 220(2):694–712, 2012a.

L. A. Sromovsky, H. B. Hammel, I. de Pater, P. M. Fry, K. A. Rages, M. R. Showalter, W. J. Merline, P. Tamblyn, C. Neyman, J. L. Margot, J. Fang, F. Colas, J. L. Dauvergne, J. M. Gómez-Forrellad, R. Hueso, A. Sánchez-Lavega, and T. Stallard. Episodic bright and dark spots on Uranus. *Icarus*, 220(1):6–22, 2012b.

L. A. Sromovsky, E. Karkoschka, P. M. Fry, H. B. Hammel, I. de Pater, and K. Rages.

Methane depletion in both polar regions of Uranus inferred from HST/STIS and Keck/NIRC2 observations. *Icarus*, 238:137–155, 2014.

L. A. Sromovsky, I. de Pater, P. M. Fry, H. B. Hammel, and P. Marcus. High S/N Keck and Gemini AO imaging of Uranus during 2012–2014: New cloud patterns, increasing activity, and improved wind measurements. 2015.

L. A. Sromovsky, E. Karkoschka, P. M. Fry, I. de Pater, and H. B. Hammel. The methane distribution and polar brightening on Uranus based on HST/STIS, Keck/NIRC2, and IRTF/SpeX observations through 2015. *Icarus*, 317:266–306, 2019.

E. C. Stone and E. D. Miner. The Voyager 2 encounter with the Uranian system. *Science*, 233(4759):39–43, 1986.

M. G. Sussman. Modeling Seasonal Change on Uranus with the EPIC GCM. *PhD thesis, New Mexico State University, New Mexcio*, 2011.

J. Taylor. Impact of variable photospheric radius on exoplanet atmospheric retrievals. *Monthly Notices of the Royal Astronomical Society: Letters*, 513(1):L20–L24, 2022.

N. A. Teanby, P. G. J. Irwin, J. I. Moses, and R. Helled. Neptune and Uranus: ice or rock giants? *Phil. Trans. R. Soc. A*, 378(2187), 2020.

J. Tennyson and S. N. Yurchenko. ExoMol: Molecular line lists for exoplanet and other atmospheres. *Monthly Notices of the Royal Astronomical Society*, 425(1):21–33, 2012.

E. W. Thommes, M. J. Duncan, and H. F. Levison. The formation of Uranus and Neptune in the Jupiter-Saturn region of the Solar System. *Nature*, 402(6762):635–638, 1999.

E. W. Thommes, M. J. Duncan, and H. F. Levison. The Formation of Uranus and Neptune among Jupiter and Saturn. *The Astronomical Journal*, 123(5):2862–2883, 2002.

D. S. Tice, P. G. Irwin, L. N. Fletcher, N. A. Teanby, J. Hurley, G. S. Orton, and G. R. Davis. Uranus' cloud particle properties and latitudinal methane variation from IRTF SpeX observations. *Icarus*, 223(2):684–698, 2013.

D. Toledo, P. G. Irwin, N. A. Teanby, A. A. Simon, M. H. Wong, and G. S. Orton. Uranus's Northern Polar Cap in 2014. *Geophysical Research Letters*, 45(11):5329–5335, 2018.

D. Toledo, P. G. Irwin, P. Rannou, N. A. Teanby, A. A. Simon, M. H. Wong, and G. S. Orton. Constraints on Uranus's haze structure, formation and transport. *Icarus*, 333: 1–11, 2019.

S. Tomic, M. Beko, L. M. Camarinha-Matos, and L. B. Oliveira. Distributed Localization with Complemented RSS and AOA Measurements: Theory and Methods. *Applied Sciences*, 10(1):272, 2019.

K. Tsiganis, R. Gomes, A. Morbidelli, and H. F. Levison. Origin of the orbital architecture of the giant planets of the Solar System. *Nature*, 435(7041):459–461, 2005.

S. J. Weidenschilling and J. S. Lewis. Atmospheric and cloud structures of the Jovian planets. *Icarus*, 20(4):465–476, 1973.

P. M. Weilbacher, R. Palsa, O. Streicher, R. Bacon, T. Urrutia, L. Wisotzki, S. Conseil, B. Husemann, A. Jarno, A. Kelz, A. Pécontal-Rousset, J. Richard, M. M. Roth, F. Selman, and J. Vernet. The data processing pipeline for the MUSE instrument. *Astronomy Astrophysics*, 641:A28, 2020.

R. V. Yelle, J. C. McConnell, D. F. Strobel, and L. R. Doose. The far ultraviolet reflection

spectrum of Uranus: Results from the Voyager encounter. *Icarus*, 77(2):439–456, 1989.